University of Strathclyde

Department of Physics

Interpreting Optical Signals in shelf sea Environments

Jennifer Mairi Darley

A thesis presented in fulfilment of the requirements for the degree of Doctor of Philosophy

2014

Declaration

This thesis is the result of the author's original research. It has been composed by the author and has not been previously submitted for examination which has led to the award of a degree. The copyright of this thesis belongs to the author under the terms of the United Kingdom Copyright Acts as qualified by University of Strathclyde Regulation 3.50. Due acknowledgement must always be made of the use of any material contained in, or derived from, this thesis.

Signed: **Date:**

Contents

Abstract

Measurements of optically significant constituent (*OSCs*) concentrations in shelf seas can be used as sensitive indicators of ecosystem status and function. Measuring *OSC* concentrations is labour intensive and a method to improve data analysis would greatly enhance our ability to monitor shelf sea environments. One option is the inversion of optical signals to recover constituent concentrations, as instrumentation already exists for measuring optical properties *in situ*. The feasibility of inverting measurements of inherent optical properties (*IOPs*) to give constituent concentrations using linear matrix algebra is considered, as previous authors reported that this gave encouraging results. Two problems were identified when *IOP* inversion was tested using synthetic data. First, the results obtained degraded rapidly in response to increasing levels of noise. Second, the inversion process relied on accurate values for the specific inherent optical properties of the *OSCs* that were unlikely to be obtained in practice. A further difficulty was encountered in the long-term deployments of instrumentation for measuring *IOPs*, since the equipment proved to be very susceptible to fouling. Alternative methods for optical data analysis had to be proposed which were more resistant to noise and required fewer assumptions for analysis to be completed. Two promising lines of research were initiated. One involved combining *IOP* measurements with other available optical and hydrographic variables to study particle populations in Scottish sea lochs. The other employed signal processing techniques to derive information on sediment transport in Liverpool Bay from measurements of beam attenuation subjected to large amounts of biofouling. Both of these methods allow ecological information to be derived from optical data that has been gathered under sub-optimal conditions. They provide a foundation for the analysis of large scale optical data sets from planned ocean observing systems, which will deploy optical instruments on moorings, floats, ocean gliders and autonomous underwater vehicles.

Chapter 1 Introduction

1.1 Executive Summary

Measurements of the concentrations of phytoplankton, suspended mineral particles and dissolved coloured organic matter in shelf seas can be used as sensitive indicators of ecosystem status and function. The ability to gather information on these optically significant constituents (*OSCs*) without the current requirement for labour intensive sample analysis would greatly enhance our ability to monitor shelf sea environments. One attractive option for this purpose is the inversion of optical signals to recover constituent concentrations, since instrumentation already exists for measuring a wide range of optical properties *in situ*. This thesis begins by assessing the feasibility of inverting measurements of inherent optical properties (*IOPs*) to give constituent concentrations using linear matrix algebra, since previous authors reported that this technique gave encouraging results. However two significant problems were identified when this inversion strategy was tested on a synthetic data set. First, the results obtained degraded rapidly in response to the introduction of increasing levels of noise (representing likely measurement errors). Second, the inversion process relied on a degree of certainty in the knowledge of the specific inherent optical properties of the *OSCs* that was unlikely to be obtained in practice. A further difficulty was encountered in the long-term deployments of instrumentation for measuring *IOPs*, since the equipment proved to be very susceptible to fouling of the optical surfaces. It was therefore necessary to explore alternative methods which were more tolerant of measurement error and made fewer assumptions regarding the optical properties of the main *OSCs*. Two promising lines of research were initiated. One involved combining *IOP* measurements with other available optical signals (fluorescence and backscattering) and hydrographic variables (salinity and temperature) to study the vertical structure of particle populations in Scottish sea lochs. The other employed signal processing techniques (Fourier transform and cross correlation analysis) to derive information on sediment re-suspension and advection in Liverpool Bay from beam attenuation measurements

that were subject to high levels of bio-fouling. Both of these methods allow ecological information to be derived from optical data that has been gathered under sub-optimal conditions or in situations where a priori knowledge of specific optical properties is not available. They provide a foundation for the analysis of large scale optical data sets from planned ocean observing systems, which will deploy optical instruments on moorings, floats, ocean gliders and autonomous underwater vehicles.

1.2 Background

Shelf seas are relatively shallow waters over continental shelves occupying the regions between land and the open oceans. They are responsible for a significant fraction of global ocean productivity (Field et al., 1998). This productivity is a result of terrigenous nutrient input and seasonal cycles of vertical mixing and stratification establishing nutrient-rich surface waters conducive to phytoplankton growth and photosynthesis. As a result of their proximity to land, shelf seas are important to mankind for environmental and economic reasons. Acting as buffers between land and the open oceans, shelf seas are subject to many anthropogenic influences including fisheries, transport, tourism and sewage effluent. Legislation may be altered to account for the effects that human interaction has on shelf seas, and this in turn has implications for the sustainability of the marine environment (Llope et al., 2011; Möllmann et al., 2009; Oguz, 2005; Smith et al., 1999).

The optical properties of shelf seas have a direct influence on ecosystem function. For example, they determine the amount of solar radiation available for phytoplankton growth (Capuzzo et al., 2013) and this has an effect on the entire ecosystem since phytoplankton are a major food source for zooplankton, which are in turn a food source for fish (Timms & Moss, 1984).

In addition to the ecological importance of optical properties in determining underwater light fields, the measurement and analysis of these properties can yield information about processes occurring in shelf seas, and on factors which influence them. For example, they can serve as indicators for water quality, with spatial and temporal variation indicating changing levels of both pollution and eutrophication

(Le et al., 2013). Since optical properties can vary in response to meteorological forcing, monitoring temporal variation of the optical properties in an area can provide an indication of long term meteorological changes and the resulting ecosystem response. Variations in river flow, which would impact on the salinity of a water body, can be monitored using both spatial and temporal measurements of optical properties (Lahet & Stramski, 2010). Soil erosion from agriculture can also affect the optical properties of a shelf sea environment (Fabricus et al., 2013).

Significant effort has recently been directed toward the numerical modelling of ocean processes by coupling physical and biological sub-models (Doron et al., 2011; Los et al., 2008; Allen et al., 2007; Holt et al., 2005; Allen et al., 2001). In order to advance model development and to increase current understanding of these processes, biogeochemical oceanographic measurements with high spatial and temporal resolutions are required. Traditionally, distributions of *OSC* concentrations, such as chlorophyll-a (*CHL*), mineral suspended solids (*MSS*) and chromophoric dissolved organic material (*CDOM*) have been obtained by discrete water sampling followed by laboratory analysis. This process is labour intensive and results in poor spatial and temporal resolution, as well as poor coverage, when compared to physical oceanographic parameters such as temperature and salinity (Pegau et al., 2002).

A partial solution to this problem is offered by the estimates of biogeochemical and optical parameters that can be obtained from remotely sensed ocean colour (normalised water leaving radiance) data from various satellite sensors including MODIS Aqua and SeaWIFS (NASA) and MERIS (ESA) (Mitchell et al., 2014; Neil et al., 2012; Neil et al., 2011; Creanor & Cunningham, 2010; Platt et al., 2008; Dickey et al., 2006; Lee et al., 2002). This remote sensing data gives valuable insights into spatial and temporal distributions of biogeochemical parameters on a global scale, with some reservations. There are numerous operational issues regarding cloud cover, adjacency effects, atmospheric correction, and the calibration and validation of remote sensing products which require further investigation (Mitchell et al., 2014; Morel & Prieur, 1977; Gordon & McCluney, 1975). Moreover, it is not possible to evaluate the vertical structure of a water column using

remote sensing, and the depth range over which the satellite observed radiance originates is determined by water turbidity, which could restrict the observation of deep chlorophyll maxima (Cunningham et al., 2013). A further complication in the interpretation of remote sensing data is the increased optical complexity of coastal waters (relative to open ocean waters), which often results in the failure of algorithms developed for oceanic waters when they are applied to coastal regions (Robinson et al., 2008).

The biogeochemical properties of seawater may also be inferred from *in situ* optical measurements of various parameters regularly made during oceanographic research cruises. Frequently measured optical properties include the absorption, scattering, backscattering and beam attenuation coefficients, in addition to fluorescence from *CDOM* and *CHL*. The absorption, scattering and beam attenuation coefficients (together with the scattering phase function) comprise the inherent optical properties (*IOPs*) of seawater. *IOPs* are independent of the angular distribution of the underwater light field and are related to water composition by specific inherent optical properties (*SIOPs*) (Mobley, 1994). The existence of a formal relationship between *IOPs* and *OSC* concentrations suggests that *IOP* measurements are an obvious starting point for efforts to derive these concentrations from *in situ* optical signals. Submersible optical instruments typically allow measurements at spatial resolutions of the order of one metre, limited largely by the relative motion of the research vessel, instrument cage and seawater (Slade et al., 2010). The combination of relatively small size and low power consumption renders these instruments well suited to deployment on fixed moorings, autonomous underwater vehicles, towed bodies and ferry box systems in addition to depth profiling deployment using the winch on board a research vessel. These diverse deployment possibilities facilitate the collection of *IOP* time series and transects on varying spatial and temporal scales. If such data can be interpreted using *IOP* inversion techniques, significant insights into spatial and temporal distributions and variability in constituent concentrations and associated bio-physical processes may be gained.

However the use of *in situ* optical instrumentation is not without its limitations. Long term deployments in shallow waters have proved to be difficult due to fouling

of optical surfaces (Slade et al., 2010; Morrison & Sosik, 2002) which can skew the optical data, so that it is only reliable during the first few days (Slade et al., 2010). This increases the resource requirement as a research vessel must be sent to the mooring site to perform maintenance checks or regular instrument replacements (Morrison & Sosik, 2002). The most commonly used instrument for *IOP* measurements (the WET Labs *ac-s*) requires regular cleaning and calibration to monitor drift in the optical system to ensure data collected are a true measure of *IOPs* (WET Labs, 2006).

Calculating *OSC* concentrations from *IOP* measurements has been attempted previously by various authors (Schofield et al., 2004; Gallegos & Neale, 2002; Bricaud & Stramski, 1990; Morrow et al., 1989; Roesler et al., 1989). Each of these techniques makes a different set of assumptions and employs different mathematical techniques to partition the total absorption coefficient into contributions by constituents. So far no one method has been universally adopted, and each has both benefits and drawbacks. In this thesis an attempt is made to define an novel *IOP* inversion method for recovering *OSC* concentrations with as few assumptions as possible, and to compare the uncertainty in the results with previously published methods.

Despite the known operational challenges, the *ac-s* remains the most versatile instrument for the measurement of optical properties in shelf seas (Pegau et al., 1995). However accurate *IOP* and *SIOP* measurements are required in order to recover *OSC* concentrations from *ac-s* data and the instrument must be maintained in a clean and well-calibrated condition. These conditions are not easily met during long term deployments, and in such cases an alternative approach is required to obtain useful information from sub-optimal optical property measurements. The work within this thesis provides a novel method to tackle this problem by treating data from a long-term *ac-s* deployment as an un-calibrated optical signal, rather than as *IOP* data, and explores the use of signal analysis techniques to study tidally-driven changes in optical turbidity in the presence of high levels of baseline drift and long term noise. This allows changes in the time series to be monitored and recorded without the need for recovering accurate *IOP* values.

The measurement of *SIOPs* requires accurate information on both *IOPs* and *OSC* concentrations. *SIOP* determinations are therefore affected both by the uncertainties in *in situ IOP* measurements described above and by the accuracy with which the *OSC* concentrations are determined in the laboratory. For the purposes of numerical light field modelling, *SIOP* values are generally averaged over a given area of interest, which can mask any variability that may occur across the area or even within a single station profile. This can pose a problem for all *IOP* inversion methodologies, which rely on locally accurate *SIOP* values to recover the *OSC* concentrations. The extent of this problem can be assessed by deriving information on fine scale variability from measurements of hydrographic variables such as temperature and salinity, as well as optical measurements not utilised in the *IOP* inversion, such as fluorescence and backscattering. The use of such ancillary data is developed in this work to allow variations in optical properties and particle types to be examined on a station-by-station basis, and to provide useful information on the success or mode of failure of *IOP* inversion techniques.

Large parts of this thesis deal with the analysis of data when conventional techniques are not adequate. Two cases are looked at; the first is the examination of the *IOP* inversion results whose uncertainties are too large, making the recovered *OSC* concentrations themselves unusable. Individual stations are analysed to recover information on the population of particles with depth to determine spatial information on the particle populations within a water column. The second is the analysis of temporal *ac-s* data, where fouling has resulted in the *IOP* inversion techniques to be an inappropriate means of analysis. Instead, the use of the attenuation coefficient as a measure of turbidity, which when coupled with other measurements of an area, can give insights into the particle dynamics. Together these techniques can be used to determine the particle population dynamics of a region of interest, where standard processing and analysis techniques may currently fail.

1.3 The Inverse Problem

In general the forward problem, in a physical system, can be defined as the relationship between the physical properties and measurable quantities. In this case the forward problem is written as;

$$y = F(x), \tag{1.1}$$

where *x* are the properties, *y* the observables and *F* is the forward model. Generally *F* represents the governing equations that relate the model parameters to the observed data (i.e. the governing physics).

The meaning of inversion is "a general framework that is used to convert observed measurements into information about a physical object or system" (Press et al., 2007). By definition the inverse problem (*I*) is then;

$$x = I(y) \tag{1.2}$$

The inverse problem is commonly used throughout science and can be complicated by uncertainties in the observables and also by the nature (noninvertible, singular or over-constrained solutions) of the forward model. However within this thesis the observables are the *IOPs*, the properties are the constituents and the forward model is assumed to be linear in nature. Therefore the forward and inverse problem can be written as a matrix equation consisting of *SIOPs* in this case.

$$y = Fx \tag{1.3}$$

$$y = F^{-1}x \tag{1.4}$$

Largely in this work the discrete linear inverse problem described above is used. In the case of the over-constrained problem the direct inversion of the forward problem is more complex as the transform matrix is non-square and therefore does not have a unique inverse. In this case a least squares optimisation algorithm is applied in order to find the best solution.

1.4 Thesis Structure

This thesis can be divided into five sections: optical theory (Chapter 2), an outline of instrumentation, data collection and analysis (Chapter 3 & Chapter 4), the inversion methodologies (Chapter 5 & Chapter 6), a novel method for spatial analysis presented for the archive UK Shelf data set from the University of Strathclyde (Chapter 7), and a novel technique for the analysis of temporal optical data subjected to fouling presented for the Liverpool Bay Coastal Observatory (Chapter 8). An outline of these main sections is presented in Figure 1.1.

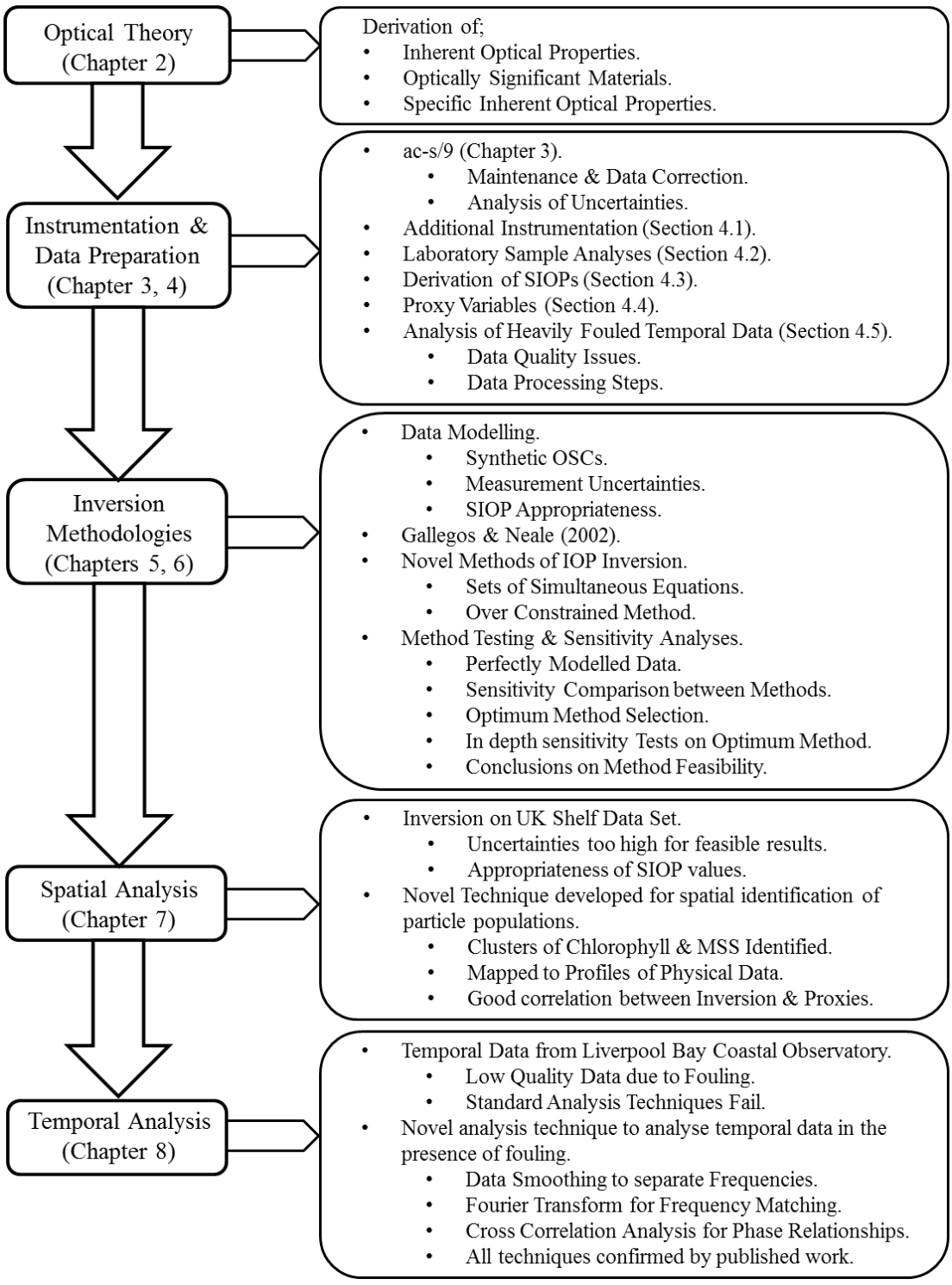

Figure 1.1: Diagram showing the five sections of this thesis (as the left-hand column) with the major sub-sections shown in the right-hand column.

1.4.1 Key Issues Addressed in this Thesis

1. Development of a randomly sampled set of *OSC* concentrations within a predetermined range, in order to create a modelled *IOP* data set. Careful consideration was given to the addition of measurement uncertainties in the *IOPs* and also to correct modelling of the variation and appropriateness of *SIOPs*, in order to determine how the *IOP* inversion will perform when applied to data measured by an *ac-9* in the field.

2. Selection of the optimum method of *IOP* inversion through rigorous testing with the modelled data subjected to measurement uncertainties. Several novel methods are presented and are compared to the method of Gallegos & Neale (2002). Novel methods presented include; sets of three simultaneous equations (many variations utilising absorption and attenuation wavelengths are presented) and the over constrained method, resulting from the use of all available *ac-9* data. The optimum method is defined as the least sensitive to measurement uncertainties.

3. Rigorous testing of the optimum method of *IOP* inversion then needs to be further characterised by more rigorous testing of the effect of measurement uncertainties in the modelled data set and also testing of the effect of using inappropriate *SIOPs* for the area of interest. This analysis is essential to understanding how the *IOP* inversion will perform when applied to the UK Shelf data set (University of Strathclyde).

4. Application of a novel method of spatial analysis to the *IOP* inversion results to further test limitations of the results. The use of additional optical data not utilised in the inversion techniques alongside proxy variables as measures *OSC* concentrations (with greater spatial resolution than the laboratory sampled *OSC* concentration measurements) to give insights to the particle population distributions and *OSC* concentrations within the spatial profile, to better understand and characterise the *IOP* inversion results. This methodology can also be used for spatial analysis where data quality is of

poor quality due to fouling of the instruments, giving rise to applications for large scale deployments of optical instruments (*AUVs* & Argo floats).

5. Development of a method of temporal analysis, whereby optical data may be used as a proxy for turbidity and can characterise sediment transport over both a tidal cycle and long term variations in an area of interest. This methodology would be applied where optical instrumentation is deployed for long time scales and fouling is an issue. Applications for this methodology include optical data on Argo floats and *AUVs* and the Global Ocean Observing System (*GOOS*).

Together the spatial and temporal analysis techniques can be used as effective tools for the analysis of data that would previously have been discarded due to the large degree of fouling. This would allow the expansion of optical instruments on long term deployments, potentially increasing our knowledge of both oceanic and coastal waters.

Chapter 2 Optical Theory

2.1 Inherent Optical Properties

Inherent optical properties (*IOPs*), such as (wavelength (λ) dependent) absorption (*a*(λ)), scattering (*b*(λ)), beam attenuation (*c*(λ)) and volume scattering function (*VSF*) control the way light propagates in natural waters (Mobley, 1994). *IOPs* are dependent only on the medium and are independent of the ambient light field. They can be defined by considering a thin layer of water illuminated by a collimated beam of monochromatic light incident perpendicular to the interface as in Figure 2.1.

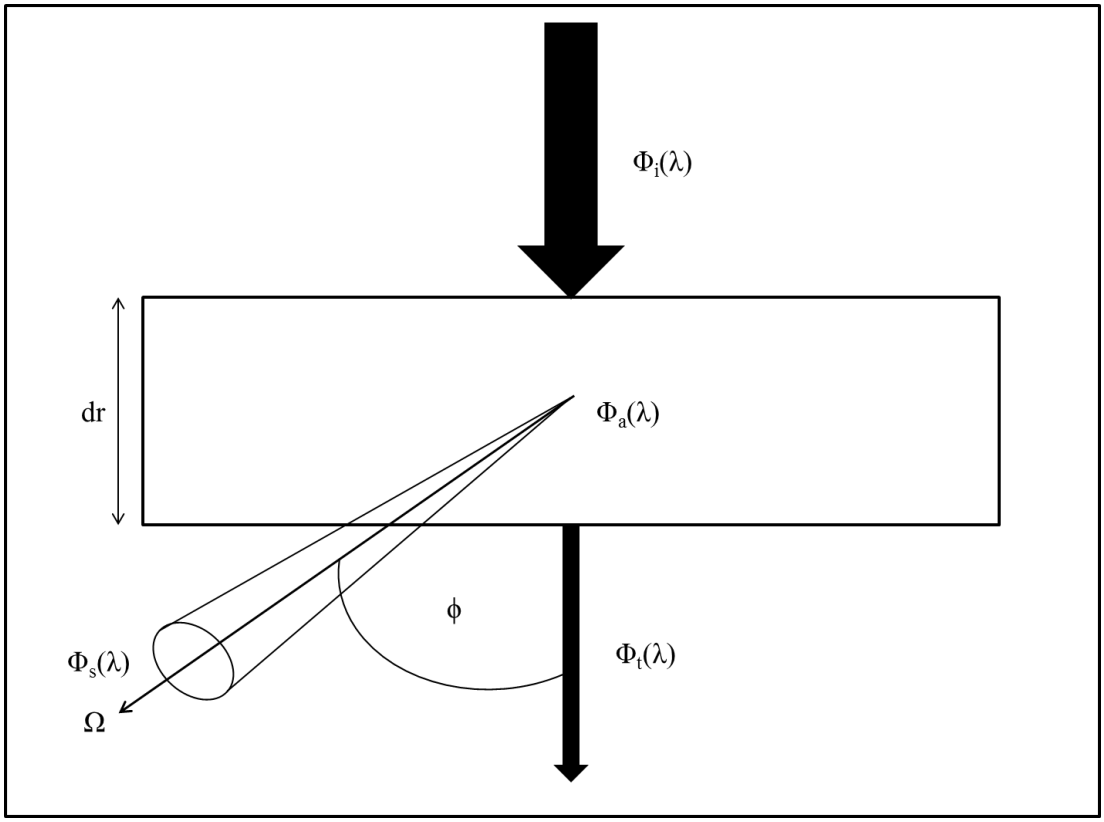

Figure 2.1: Diagrammatic representation of the interaction of a beam of monochromatic light incident at right angles on an infinitesimally thin layer of water (adapted from Mobley (1994)).

On passing through the thin layer, each photon comprising the beam may either be absorbed, scattered or pass through the medium with no loss of energy or change in direction. Assuming no inelastic interactions, the sum of the radiant flux absorbed

by the medium, Φ_a, scattered by the medium, Φ_s, and transmitted with no deviation, Φ_t, equals the radiant flux of the incident beam, Φ_i. The absorptance, A (λ), and scatterance, B(λ), of the water comprising the thin layer may be expressed as in Equations (2.1) & (2.2).

$$A(\lambda) = \frac{\Phi_a(\lambda)}{\Phi_i(\lambda)} \tag{2.1}$$

$$B(\lambda) = \frac{\Phi_s(\lambda)}{\Phi_i(\lambda)} \tag{2.2}$$

The absorption, scattering and beam attenuation coefficients are defined in Equations (2.3) - (2.5), in which *dr* is used to denote the thickness of the thin layer

$$a(\lambda) = \lim_{dr \to 0} \frac{A(\lambda)}{dr} \tag{2.3}$$

$$b(\lambda) = \lim_{dr \to 0} \frac{B(\lambda)}{dr} \tag{2.4}$$

$$c(\lambda) = a(\lambda) + b(\lambda) \tag{2.5}$$

The angular distribution of the scattered light is described by the volume scattering function (*VSF*) of the medium, $\beta(\phi, \lambda)$ (Kirk, 1994; Mobley, 1994);

$$\beta(\phi, \lambda) = \lim_{dr \to 0} \lim_{d\Omega \to 0} \frac{\Phi_s(\phi, \lambda)}{\Phi_i(\lambda) dr d\Omega} \tag{2.6}$$

where, $d\Omega$ is the solid angle. The shape of the *VSF* is often expressed as the scattering phase function ($\vec{\beta}(\phi, \lambda)$):

$$\vec{\beta}(\phi, \lambda) = \frac{\beta(\phi, \lambda)}{b(\lambda)} \tag{2.7}$$

A further quantity, describing the degree to which *in situ* attenuation is determined by scattering, the single scattering albedo, ω, is defined in Equation (2.8).

$$\omega(\lambda) = \frac{b(\lambda)}{c(\lambda)} \equiv \frac{b(\lambda)}{a(\lambda)+b(\lambda)} \tag{2.8}$$

2.2 Optically Significant Constituents

Morel & Prieur (1977) introduced an optical classification system to differentiate between ocean and coastal waters. If the optical properties of the waters were closely correlated with Chlorophyll then they were defined as oceanic or Case 1 waters. Otherwise they were coastal or Case 2 waters. Other than water, the main optically significant constituents (*OSCs*) in Case 2 waters are coloured dissolved organic matter (*CDOM*), phytoplankton cells and suspended mineral particles (*SPM*). Conventionally these are measured using proxy variables: *CDOM* is measured as the absorption coefficient of filtered samples at 440 nm, phytoplankton cells are measured as Chlorophyll-a (*CHL*) concentration and *SPM* as the dry weight of mineral suspended solids (*MSS*) per unit filtered volume (Kirk, 1994; Spinrad et al., 1994; Bukata et al., 1995). All example spectra presented in this section were collected and analysed by myself throughout the course of my research.

2.2.1 Absorption by Coloured Dissolved Organic Material

Coloured dissolved organic material (*CDOM*), also sometimes referred to as yellow substance or gelbstoff, may be a significant contributor to the total absorption coefficient in Case 2 waters. It has particularly strong absorption at blue wavelengths and its absorption spectrum can be described as an exponential function of wavelength, as in Equation (2.9) (Jerlov, 1975):

$$a_{CDOM}(\lambda) = a_{CDOM}(\lambda_r) \cdot \exp[-S(\lambda - \lambda_r)] \tag{2.9}$$

where S is a coefficient describing the exponential slope of $a(\lambda)$ and λ_r is a reference wavelength (Aas et al., 2005; Bricaud et al., 1981). Extensive studies of *CDOM* absorption have shown that the coefficient for the spectral slope can vary

from 0.01 to 0.02, with the majority of the values falling between 0.012 and 0.015 (Binding et al., 2003; Carder et al., 1989; Bricaud et al., 1981).

An example of a *CDOM* absorption spectrum is shown in Figure 2.2;

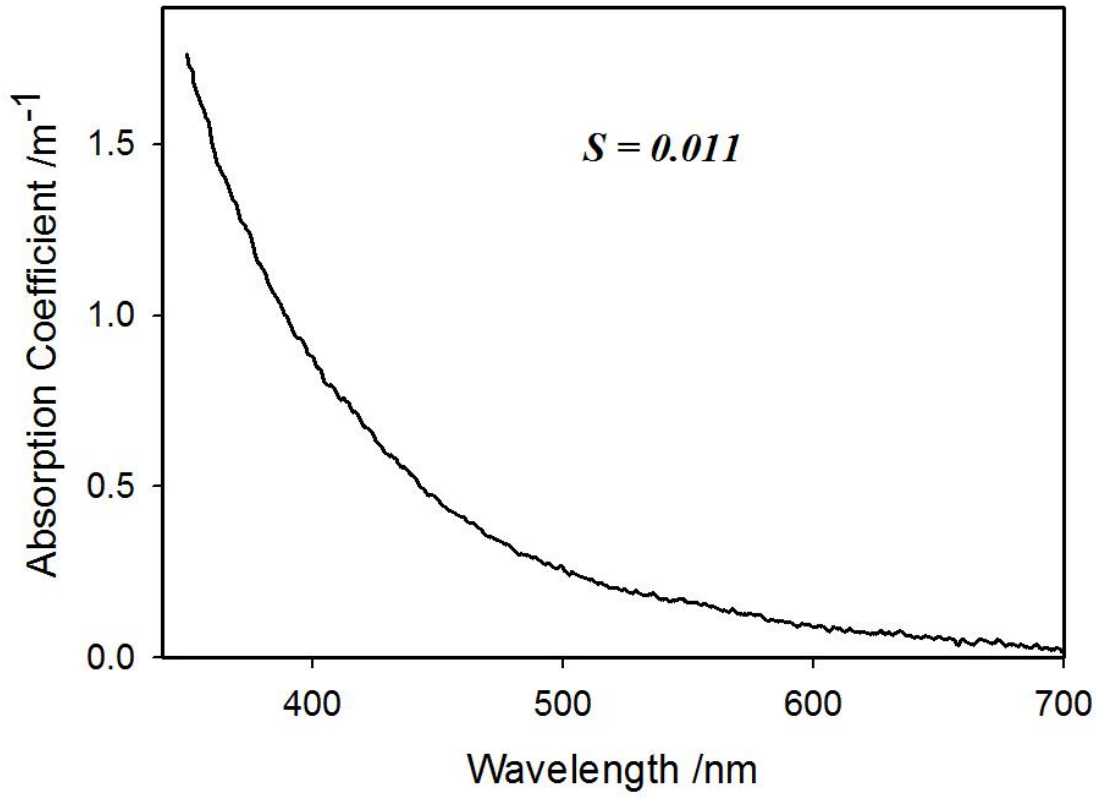

Figure 2.2: An example of a *CDOM* absorption spectrum for a sample taken from the Gareloch on 18th May 2010.

2.2.2 Phytoplankton

a Phytoplankton Absorption Coefficient

The absorption due to phytoplankton can be determined using the quantitative filter technique (*QFT*, described in detail in Chapter 4), where particles within a water sample are collected on a filter pad which is placed in a spectrophotometer. The total particulate absorption is first obtained and then the filter pad is bleached using sodium hypochlorite. Bleaching removes the pigment from the organic material (phytoplankton) leaving only mineral suspended solids (*MSS*). The filter is then scanned in the spectrophotometer again and the two spectra are subtracted to give phytoplankton absorption (Tassan & Ferrari, 1998; Kishino et al., 1985; Yentsch, 1962).

$$a_{ph}(\lambda) = a_t(\lambda) - a_{MSS}(\lambda) \tag{2.10}$$

where $a_{ph}(\lambda)$ is the absorption coefficient of phytoplankton, $a_t(\lambda)$ is the total absorption coefficient and $a_{MSS}(\lambda)$ is the absorption coefficient of *MSS*.

This technique has a degree of uncertainty due to the requirement for path length amplification correction (β factor) due to the highly scattering nature of the filter (Lohrenz et al., 2003; Tassan & Ferrari, 1998). Figure 2.3 shows an example of a phytoplankton absorption spectrum obtained using the *QFT*. In this example a beta factor of β = 1.73 was used (Neil et al., 2011).

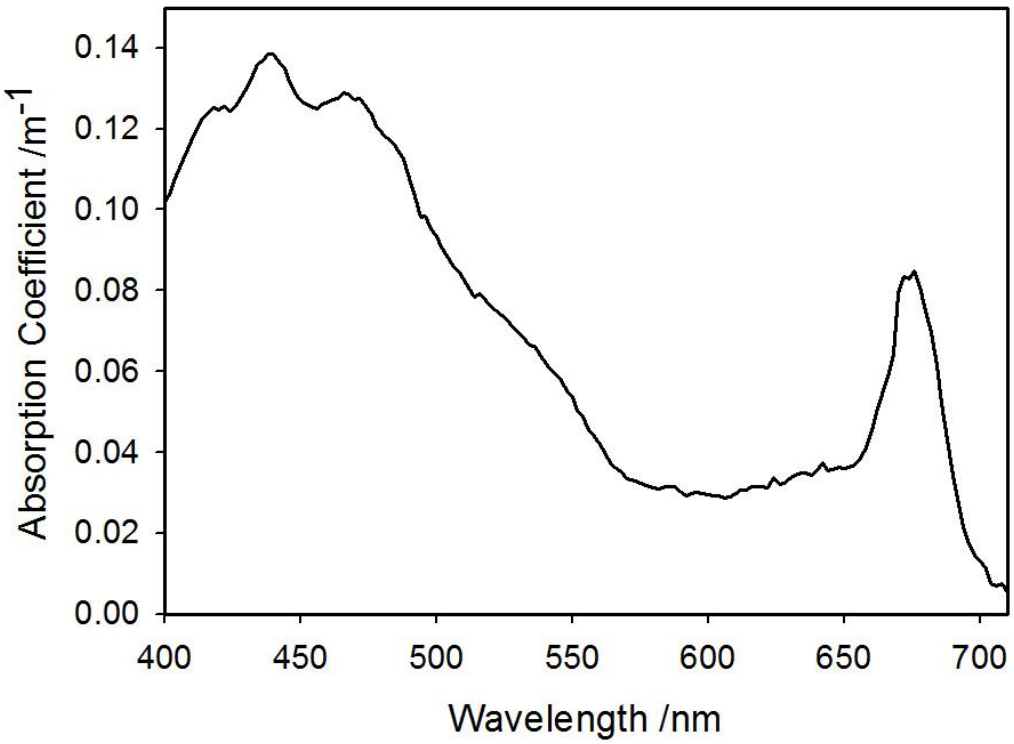

Figure 2.3: Phytoplankton absorption spectrum obtained using the *QFT* method. The sample was taken from Liverpool Bay on the 6th August 2001. For this example $\beta = 1.73$ (Neil et al., 2011).

b Phytoplankton Scattering Coefficient

Unlike absorption, the scattering coefficients for different classes of particulate material cannot be separated by laboratory analysis. Instead statistical methods have to be applied, which increases the level of uncertainty in the phytoplankton scattering coefficients. An example of a phytoplankton scattering spectrum is shown in Figure 2.4. Due to anomalous dispersion, phytoplankton scattering is lower around the main chlorophyll absorption peaks (Bricaud et al., 1983).

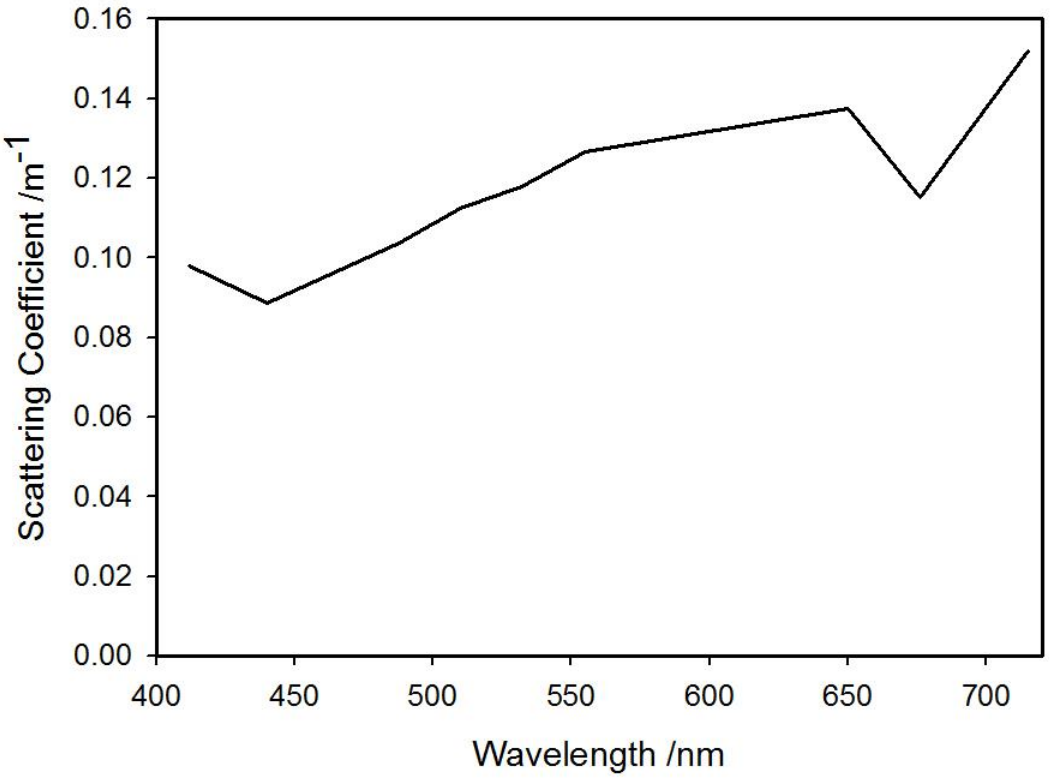

Figure 2.4: Phytoplankton scattering spectrum recovered using end-member analysis (Chapter 4) on the total scattering coefficient. This example is taken from Liverpool Bay on the 6th August 2001.

2.2.3 Mineral Suspended Sediment

a MSS Absorption Coefficient

The absorption coefficient for mineral suspended solids (*MSS*) is obtained using the quantitative filter technique (*QFT*). The *MSS* spectrum is that recorded by the spectrophotometer following the bleaching of phytoplankton pigments. *MSS* absorption spectra usually have a similar exponential shape to *CDOM* (Brown, 2010). An example of a *MSS* absorption spectrum is shown in Figure 2.5. In this example a beta factor of $\beta = 1.73$ was used (Neil et al., 2011).

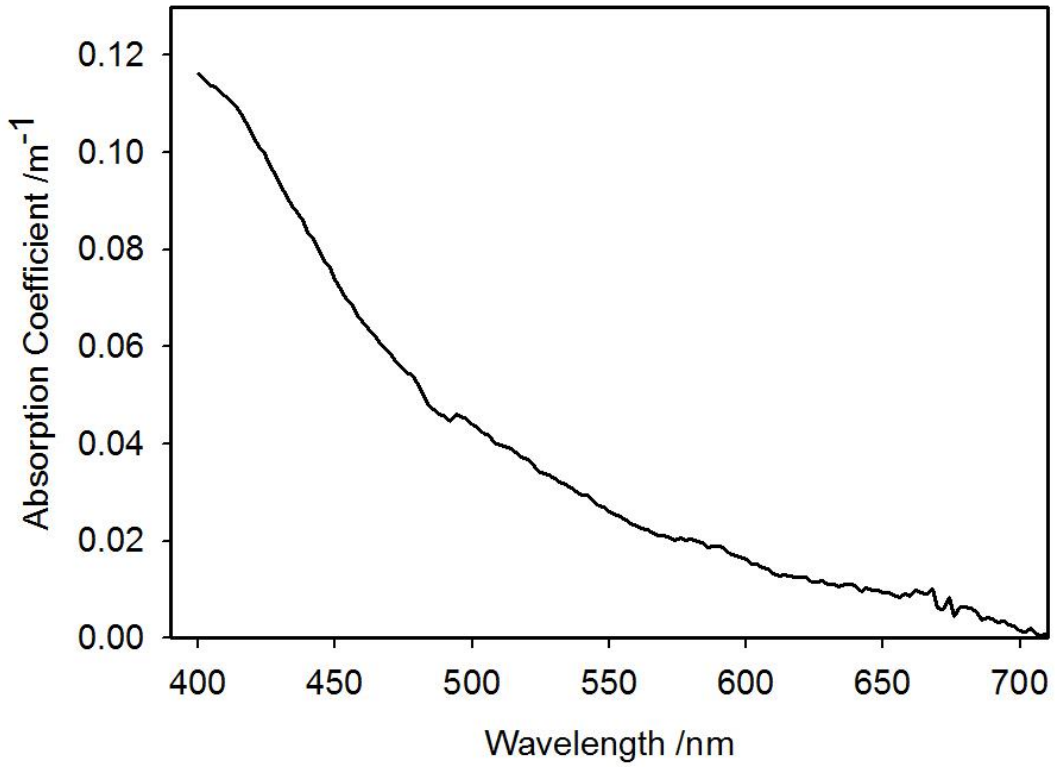

Figure 2.5: *MSS* absorption spectrum obtained using the *QFT* method. The sample was taken from Liverpool Bay on the 6th August 2001. In this example β = 1.73 (Neil et al., 2011).

b MSS Scattering Coefficient

As with phytoplankton scattering, *MSS* scattering cannot be determined by water sample analysis in the laboratory, and statistical analysis of field measurements is required. An example of a scattering coefficient spectrum for *MSS* is shown in Figure 2.6. However, with the large uncertainties associated with this method the shape of Figure 2.6 is uncertain.

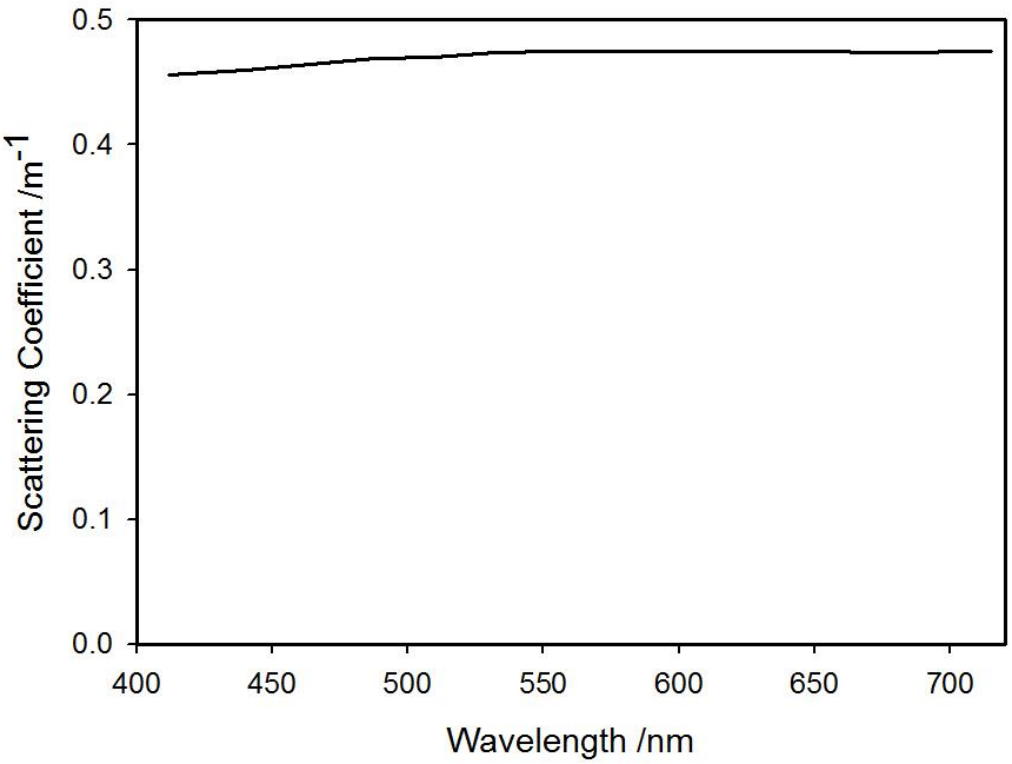

Figure 2.6: *MSS* scattering spectrum recovered using end-member analysis. This example is taken from Liverpool Bay on the 6th August 2001.

2.3 The Total Absorption Coefficient

The absorption of underwater light can be analysed by separating the total absorption into the contributions by individual components (Cannizzaro et al., 2008; Chami et al., 2006; Gallegos, 2005). Since the absorption by the different constituents is additive, the total absorption ($a_t(\lambda)$) as a function of wavelength can be written (Kirk, 1994):

$$a_t(\lambda) = a_w(\lambda) + a_{CDOM}(\lambda) + a_{CHL}(\lambda) + a_{MSS}(\lambda) \qquad (2.11)$$

where the subscripts *w*, *CDOM*, *CHL* & *MSS* represent water, coloured dissolved organic matter (*CDOM*), phytoplankton pigments (*CHL*) and mineral suspended solids (*MSS*), respectively (Doxaran et al., 2009; Cannizzaro et al., 2008). Values for a_w are commonly taken from Pope & Fry (1997).

2.4 The Total Scattering Coefficient

Scattering from suspended particles plays a key role in determining the propagation of light in the water column. It is therefore important to understand the spectral dependence of the scattering coefficient in natural waters, $b(\lambda)$, and the factors that might influence it. The wide variation in the characteristics of the particles in the water is a major contributor to the optical complexity of coastal waters (Peng et al., 2009).

The total scattering coefficient $b_t(\lambda)$ can be separated into contributions from individual components such as water and particulates. *CDOM* is taken to be a non - scattering substance and is therefore not included (Bricaud et al., 1981). Consequently, the spectral dependence of $b_t(\lambda)$ can be written as:

$$b_t(\lambda) = b_w(\lambda) + b_{CHL}(\lambda) + b_{MSS}(\lambda) \tag{2.12}$$

where the subscripts (*w, CHL & MSS*) are the same as those defined for the absorption coefficient. Values for b_w are commonly taken from (Smith & Baker, 1981).

The partitioning of the total absorption coefficient between constituents can be completed by laboratory sample analysis. However, it is not possible to physically separate constituents to measure the scattering coefficient for each constituent in the laboratory. Instead therefore, a method of deconvolution such as end-member analysis or multiple linear regression has to be employed (Stavn & Richter, 2008). This introduces additional uncertainty to the scattering coefficients.

2.5 The Backscattering Ratio

The scattering phase function defined in Equation (2.7) can be approximated by the ratio of scattering in the backwards direction to the total scattering coefficient (Equation (2.13));

$$\vec{\beta}(\phi,\lambda) \sim \frac{b_b(\lambda)}{b_t(\lambda)} \tag{2.13}$$

where $b_b(\lambda)$ is the backscattering coefficient and $b_t(\lambda)$ is the total scattering coefficient.

The backscattering ratio is a sensitive indicator of changes in the characteristics of particle populations in the marine environment (Loisel et al., 2007; Sullivan et al., 2005).

2.6 Specific Inherent Optical Properties

Specific inherent optical properties (*SIOPs*) express the *in situ* absorption and scattering coefficients of optically significant constituents per unit concentration. Total *in situ IOPs* may be expressed as the sum of the *SIOPs* multiplied by the corresponding constituent concentrations (Equations (2.14) & (2.15)). In order to derive the *SIOPs*, inherent optical properties and constituent concentrations must be measured both independently and concurrently. This has consequences for the estimates of the uncertainties in experimentally derived *SIOPs* since the fractional uncertainties in the contributing measurements are additive.

$$a_t(\lambda) = a_w(\lambda) + \sum_i [a_i^*(\lambda) \cdot X_i] \tag{2.14}$$

$$b_t(\lambda) = b_w(\lambda) + \sum_i [b_i^*(\lambda) \cdot X_i] \tag{2.15}$$

In Equations (2.14) & (2.15) the subscripts *t* & *w* are as previously defined, *i* is used to denote the constituent and *X* is used to denote constituent concentration.

A number of assumptions have to be made in order for Equations (2.14) & (2.15) to be valid. Firstly the measurement of proxy variables (*CDOM, CHL* & *MSS*) must adequately capture the optically relevant characteristics of the optically significant constituents (*OSCs*). Secondly, the contribution of the constituents should be linearly dependent on their concentrations. This is not necessarily the case for chlorophyll which has been shown to display a nonlinear dependence with concentration (Bricaud et al., 2004; 1995). Lastly the use of average *SIOPs* for an area does not allow for any variability within the area of interest. For example Brown (2010) published average *SIOPs* for the Irish Sea and adjacent waters but demonstrated that even within this restricted region considerable variability could be found (Figure 2.7).

Reasons for the variability of *SIOP* values in different regions include chemical composition in the case of *CDOM*, taxonomic composition and physiological status in the case of phytoplankton blooms and the formation and breaking up of aggregates in the case of suspended mineral particles.

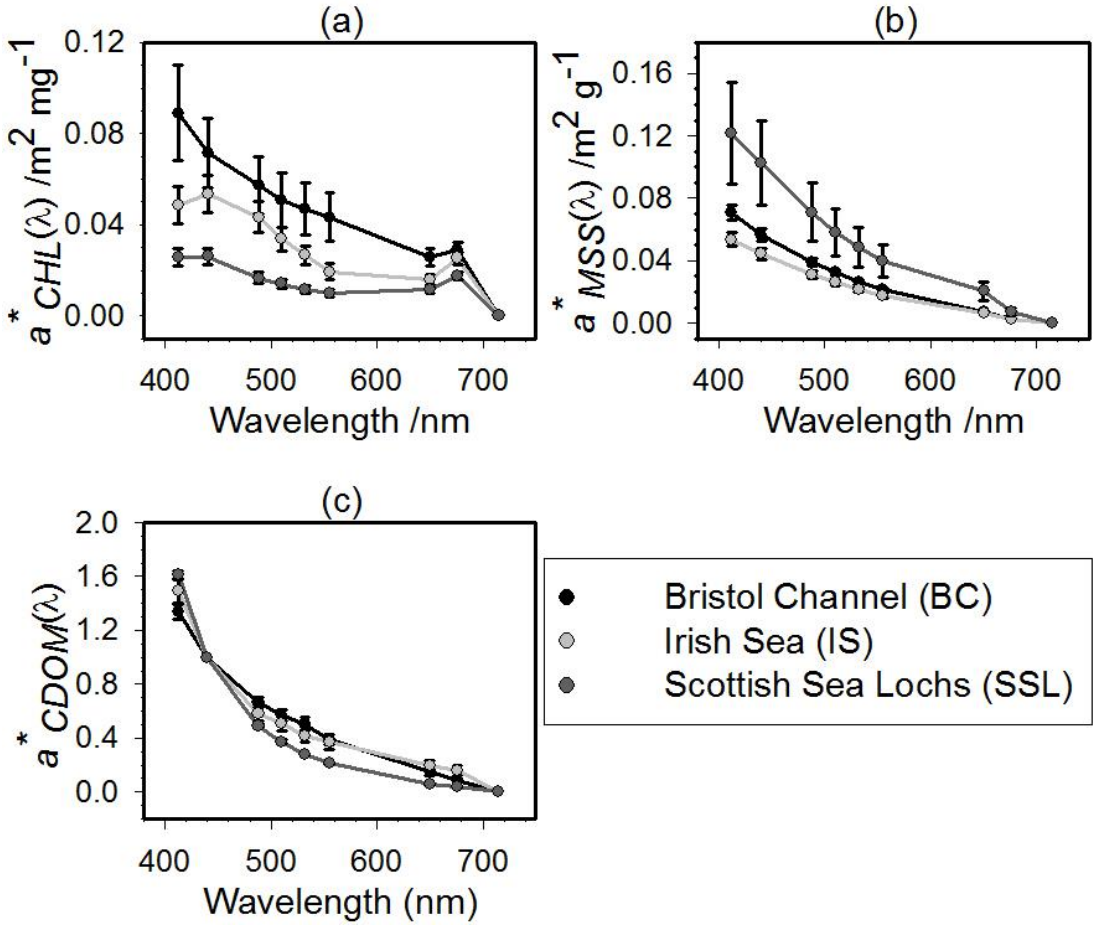

Figure 2.7: Plots of regional, regression derived, *SIOP* spectra (a) $a^*_{CHL}(\lambda)$, (b) $a^*_{MSS}(\lambda)$ and (c) $a^*_{CDOM}(\lambda)$. Error bars represent the 95% confidence intervals in the regression slopes (Brown, 2010).

2.7 Chapter Summary

1. For the purpose of constructing forward models, inherent optical properties are usually derived by summing the product of *SIOPs* and the corresponding constituent concentrations.

2. The derivation of *IOPs* involves two key assumptions. Firstly that the contribution of each constituent to the relevant *IOP* is a linear function of

concentration and secondly that the *SIOPs* for each constituent are known (and constant for a specific water body).

3. If the two assumptions above hold then the inversion of *IOPs* to recover constituent concentrations is a well-defined linear problem. This problem is formulated and considered further in Chapter 6.

Chapter 3 Instrumentation for Inherent Optical Property (*IOP*) measurements: The WET Labs Absorption / Attenuation Meter

The WET Labs 'ac' series of absorption/attenuation meters are instruments for making *in situ* inherent optical property (*IOP*) measurements, relative to a pure water standard. The original (*ac-9*) version measured the absorption and attenuation coefficients at nine discreet wavelengths. This was subsequently replaced by a hyper spectral version (*ac-s*). The principle of operation of both instruments is similar and is explained in the following sections. The terms *ac-s* and *ac-9* are used intermittently throughout this chapter, for clarity the term *ac-s* is used in the description of operations as the literature for the *ac-9* is no longer available. *ac-9* is used for the description of errors as the error analysis described was completed for *ac-9* instruments.

3.1.1 Hyper Spectral vs. Nine Wavebands

The *ac-9* simultaneously measures the absorption ($a_{ac\text{-}9}(\lambda)$) and beam attenuation $c_{ac\text{-}9}(\lambda)$ of a water sample in nine wavebands. The standard band-centre wavelengths are 412, 440, 510, 532, 555, 650, 676 and 715 nm. It is available with a path length of either 10 or 25 cm. The *ac-s* on the other hand has a spectral range between 400 nm and 730 nm with a resolution of 4 nm, resulting in between 80 and 90 output wavelengths. The specifications for both instruments are shown in Table 3.1.

A direct comparison of the two instruments was not possible for this work since no simultaneous deployment of the *ac-s* and *ac-9* was completed. Section 4.5 of this thesis outlines the analysis of an optical time series completed with an *ac-s*. However as part of that analysis, the *ac-s* wavelengths were binned using the information in Table 3.1 to obtain *ac-9* style wavebands. The binning of *ac-s* data into *ac-9* wavelengths was completed for two reasons. The first was the need for compatibility between the Liverpool Bay data measured with an *ac-s* (Section 4.5) and the archive data set for the UK shelf sea (Chapter 7). The second reason for

wavelength binning of *ac-s* data was to reduce the Liverpool Bay data to a manageable set of variables for use in *IOP* inversion methodologies. Figure 3.1 shows an example of an absorption spectrum for Liverpool Bay measured using an *ac-s* and subsequently binned to give *ac-9* wavebands.

Table 3.1: Specifications for *ac-9* and *ac-s* (WET Labs, 2006)

Specifications	***ac-9***	***ac-s***	
Spectral Range	412 – 715 nm	400 – 730 nm	
Band pass	10 nm/channel	15 nm/channel	
Path length	10 or 25 cm	10 or 25 cm	
Beam Cross-Section	8 mm	8 mm	
Linearity	≥ 99% R^2	≥ 99% R^2	
Output Wavelengths	9	80 – 90	
Accuracy	± 0.01 m^{-1}	± 0.01 m^{-1}	
Precision (typical values)	± 0.003 m^{-1} @ 6 Hz	450 – 730 nm	± 0.001 m^{-1} @ 4Hz
			± 0.0005 m^{-1} @ 1Hz
	± 0.001 m^{-1} @ 1 Hz	400 – 449 nm	± 0.005 m^{-1} @ 4Hz
			± 0.003 m^{-1} @ 1Hz
Dynamic Range	0.001 – 10 m^{-1}	0.001 – 10 m^{-1}	

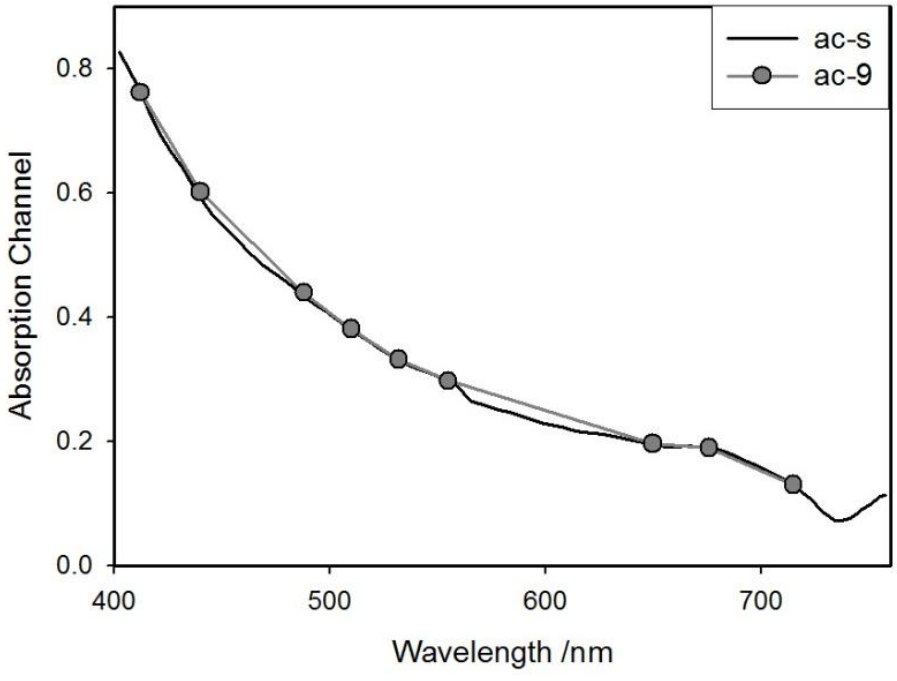

Figure 3.1: Spectral output from absorption channel from *ac-s* before and after wavelength binning (Section 4.5). This example was taken from Liverpool Bay to show the effect of deriving an *ac-9* type signal from *ac-s* measurements.

While the main spectral shape is captured by the *ac-9* wavebands, several details are missed, for example the dip in the absorption coefficient around 560 nm and the dip in the near-infrared caused by the temperature difference between the measured water and the calibration water are missed entirely by the *ac-9* wavebands.

3.2 Operation (WET Labs, 2006)

The *ac-s* measures the *in situ* non-water absorption and beam attenuation coefficients of sea water ($a_{ac\text{-}s}(\lambda)$ and $c_{ac\text{-}s}(\lambda)$, respectively). The non-water scattering coefficient, $b_{ac\text{-}s}(\lambda)$, is obtained using Equation (3.1).

$$b_{ac-s}(\lambda) = c_{ac-s}(\lambda) - a_{ac-s}(\lambda) \tag{3.1}$$

In addition to these optical measurements, the *ac-s* measures its own internal temperature and ambient pressure. Figure 3.2 shows a schematic diagram of the *ac-s* instrument. The lower housing contains the incandescent light sources and transmission optics for both channels. The upper housing contains the control and acquisition electronics, receiver optics and detectors. Between the pressure housings are support struts and two flow tubes which act as sample chambers, through which water is pumped by external pumps.

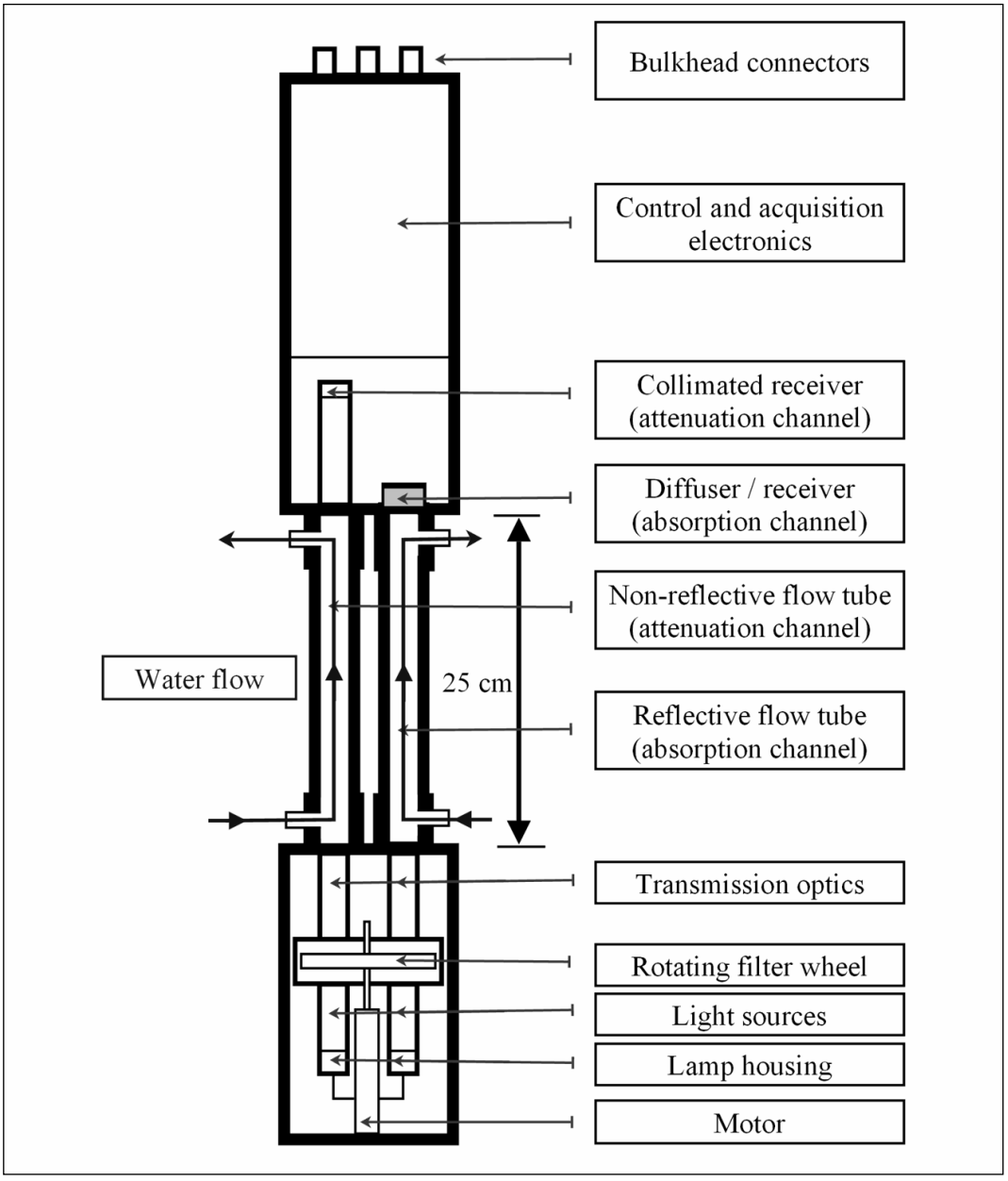

Figure 3.2: Schematic diagram of a WET Labs *ac-s* dual-beam spectrophotometer showing the major components (WET Labs, 2006).

3.2.1 Attenuation Channel Operation

Figure 3.3 shows a schematic of the attenuation channel optics and Table 3.2 lists the components.

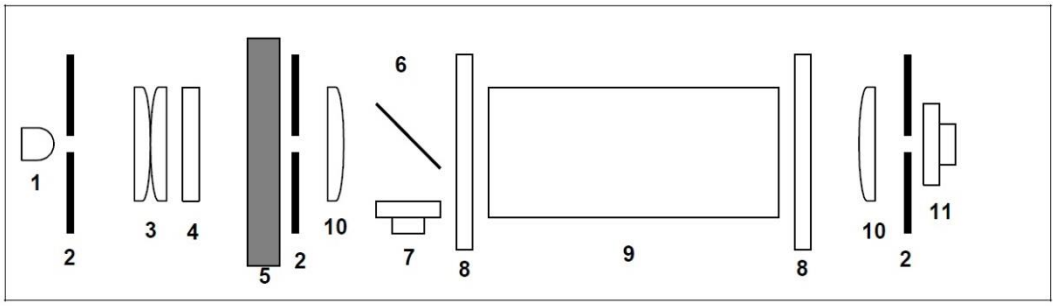

Figure 3.3: Schematic diagram of the attenuation tube of an *ac-s* (WET Labs, 2006).

Table 3.2: List of components in attenuation channel of the *ac-s*

Number	Component
1	Tungsten Bulb
2	1 mm Aperture
3	Lenses
4	IR Filter
5	Filter Wheel
6	Beam Splitter
7	Reference Detector
8	6mm Quartz Pressure Window
9	Flow Tube
10	Singlet Lens
11	Signal Detector

Light from an incandescent bulb passes through the 1 mm aperture. Light is then focussed through a filter section onto a second 1mm aperture creating a narrow band spectral output. The light then passes through a beam splitter creating primary and reference beams. The reference beam intensity is measured by the reference detector to compensate for long term lamp drift. The primary beam passes through the pressure window into the sample water volume. The flow tube for the attenuation channel is black to absorb scattered photons so that they do not contribute to the measured transmitted intensity. The measured light intensity therefore excludes light

that has been both scattered and absorbed by the water sample. Once through the water path, the light passes through another pressure window and is then refocused through a lens upon a receiver detector. A third 1 mm aperture is placed directly in front of the detector creating a 0.75º acceptance angle in water.

3.2.2 Absorption Channel Operation

Figure 3.4 shows a schematic of the attenuation channel optics and Table 3.3 lists the components.

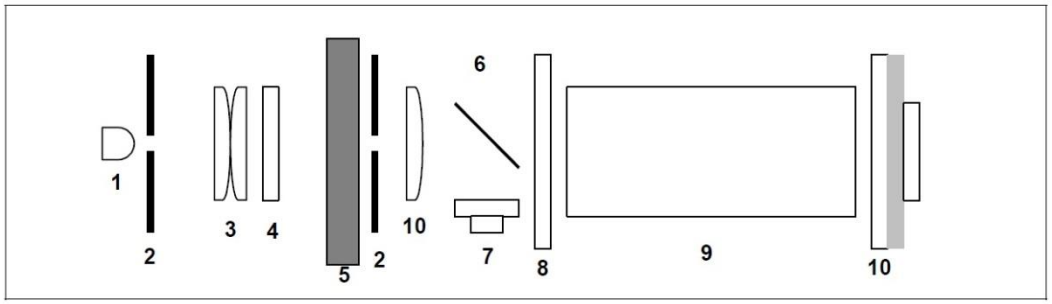

Figure 3.4: Schematic diagram of the absorption tube of an *ac-s* (WET Labs, 2006).

Table 3.3: List of components in absorption channel of the *ac-s*

Number	Component
1	Tungsten Bulb
2	1 mm Aperture
3	6 mm Aperture
4	38mm Singlet Lens
5	Interference Filter
6	Beam Splitter
7	Reference Detector
8	6mm Quartz Pressure Window
9	Reflective Flow Tube
10	Diffuser/Signal Detector

The beam splitter and aperture are identical to that of the attenuation channel. The absorption channel light is 45º out of phase with the attenuation channel. Light passing through the tube is absorbed both by the water and by any dissolved and

suspended particulate matter within the sample volume. Forward scattered light is reflected back into the water volume by the tube wall, which uses the principal of total internal reflection, and is then collected by a diffuse large area detector at the far end of the flow tube.

The reflective flow tube employs a clear quartz tube to create a thin volume of air along the outer perimeter of the tube. The absorption meter uses a reflective tube to collect scattered light. Because of the reflective tube and detector design, some of the light scattered at angles wider than 41.7 degrees (with respect to the optical axis) is lost.

3.3 Absorption/Attenuation Meter Limitations

3.3.1 Collection of Scattered Photons in the Absorption Tube

One source of error in the absorption coefficient measured by the *ac-9*, $a_{ac\text{-}9}(\lambda)$, arises from the incomplete collection of scattered photons in the absorption tube. A perfect design would ensure that every scattered photon (regardless of scattering angle) would be detected. Due to practical limitations of sensor geometry and fabrication, the *ac-9* meets neither of these conditions. Photons scattered at angles exceeding 41.7° relative to the optical axis are not subject to total internal reflection in the flow tube (Leymarie et al., 2010; WET Labs, 2006) and Monte Carlo simulations by Kirk (1992) and McKee et al. (2008) show that photons scattered in the backward direction are poorly detected. These factors contribute to the *ac-9* failing to detect a significant fraction of scattered photons in the absorption tube, resulting in an overestimation of the true absorption coefficient. Methods to correct this overestimation are outlined in Section 3.5.3.

3.3.2 The Collection Angle of the Detector in the Attenuation Tube

In the attenuation tube of the *ac-9*, there is a lens and a 1 mm aperture placed before the detector. This is used to focus the beam and exclude as much of the forward scattered light as possible. However, it is not possible to exclude all of the forward scattered light from the detector as the detector must be of finite size. The effect of

the collection angle on the measured attenuation is complex (Boss et al., 2009; Pegau et al., 1995; Voss & Austin, 1993; Jerlov, 1976). A correction to remove forward scattered light has been proposed (Voss & Austin, 1993) but due to the variation between instruments and the effect of particle size on the volume scattering function (*VSF*), none have yet fully solved the problem of acceptance angle on the attenuation coefficient (Pegau et al., 1995).

To correct the *ac-9* measured attenuation coefficient, Boss et al. (2009) suggest using the volume scattering function from a LISST instrument (Sequoia Scientific) calibrated using the method of Slade & Boss (2006) and integrating between the acceptance angle of the *ac-9* and that of the LISST. The scattering was then subtracted from the *ac-9* beam attenuation, assuming that the spectral difference between the instruments has a negligible effect (Equation (3.2))

$$c_{ac-9\,corrected} = c_{ac-9} - 2\pi \int_{\theta_{LISST}}^{\theta_{ac-9}} \beta \sin\theta \, d\theta \tag{3.2}$$

The data presented in this thesis are either archive data from the University of Strathclyde or, in the case of the Liverpool Bay time series, provided by colleagues at the National Oceanography Centre in Liverpool. Accompanying LISST measurements were not available and no correction of the attenuation coefficients for scattered light was made in this thesis.

3.4 Maintenance

3.4.1 Cleaning

After each use the *ac-9* must be thoroughly cleaned to remove any fouling resulting from deployment. In order to do this the steps below must be completed (WET Labs, 2006).

1. Remove the flow tube and all O-rings. Remove the sleeves from each flow tube and wash all the components in a mild detergent diluted in Ultrapure Milli-Q water (0.2 μm filtered, ultraviolet treated, distilled water) and rinse thoroughly with Milli-Q.

2. Dry the *ac-9* overnight to ensure it is completely dry. Note that dry Nitrogen gas can speed up this process.

3. Clean the windows and flow tubes of the *ac-9* using a small amount of Methanol and lint free paper to remove any streaks. Use dry Nitrogen to remove any lint from the windows and flow tubes.

4. Carefully reassemble the *ac-9* ensuring that the flow tubes are properly attached to the instrument.

To ensure that the *ac-9* is properly clean, turn the instrument on and leave to warm up for 15 minutes, then cover the nozzles with black tape and record a data sample for 10 minutes. The variation in each channel should be no more than ± 0.005 m^{-1} across the entire sample time. Repeat the cleaning process until there are 3 samples in a row where the variation across each data file is no more than ± 0.005 m^{-1}.

3.4.2 Calibration

Before every use, the *ac-9* must be calibrated in the laboratory to mitigate the effects of instrument drift. This is completed using the equipment shown in Figure 3.5.

Milli-Q water of known temperature should be placed in a container and manually pumped to a pressure in the region of 5–10 PSI. The tap connected to the output of

the *ac-9* flow tube is then opened to allow water to pass through the *ac-9*. Measurements are made for a period of 30–60 seconds to observe the average measured absorption or attenuation coefficient. This process should be completed for each *ac-9* flow tube in turn, and repeated. Repetition ensures that a stable signal is observed before any changes were made to existing calibration files. When stable signals are observed, the average values are then used to correct the existing instrument calibration coefficients. The measurements are repeated with the updated calibration coefficients. The aim of *ac-9* calibration is to obtain measurements of non-water absorption and attenuation coefficients, $a_{ac\text{-}9}(\lambda)$ and $c_{ac\text{-}9}(\lambda)$, of 0.000 ± 0.005 m^{-1} with pure water in each flow tube, following calibration (matching the manufacturers quoted instrument precision).

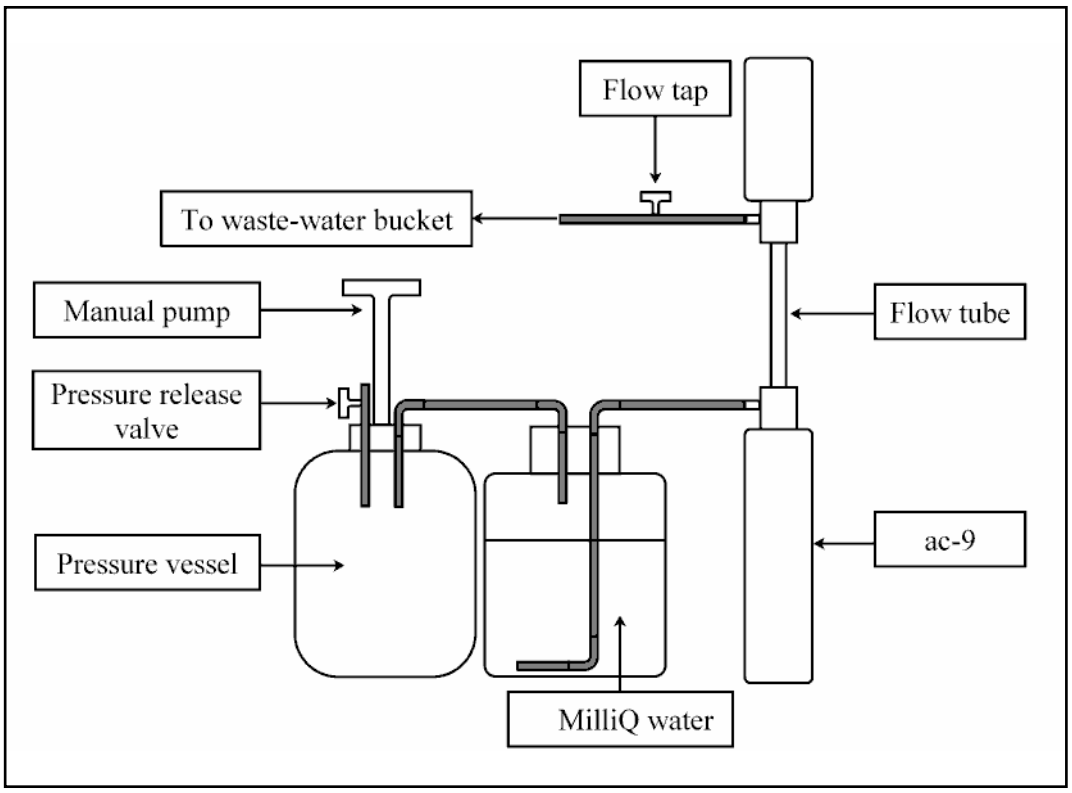

Figure 3.5: Diagram of *ac-9* calibration apparatus.

3.5 Data Processing

3.5.1 WET Labs Archive Program

The *ac-s* records all data in a binary format. Before the data can be analysed it must first be converted from binary into ASCII. This is completed with the dedicated WET Labs Archive Program (*WAP*) supplied with the instrument. The software can be used to separate data from all instruments logged by the WET Labs data logger (*DH-4*). *WAP* also applies the calibration coefficients to the *ac-9* data so that the post-processed data has already been calibrated. A step-by-step guide for operating the *WAP* software is given in the software manual (WETLabs, 2006a). The output files from *WAP* processing take the form *archive_21_ACS.xxx* where *xxx* is the file number from the *DH-4*.

3.5.2 Temperature and Salinity Corrections

Since the absorption spectrum of pure water is affected by the temperature and salinity of the water, the output data from the *ac-9* must be processed to take the temperature and salinity difference between the sample and the calibration water into account. In order for this correction to be completed accurately, a conductivity, temperature and depth meter (*CTD*) must be deployed alongside the *ac-9*.

Equations (3.3) & (3.4) are used to correct the absorption and attenuation data respectively;

$$a_{ac-9}^{TS}(\lambda) = a_{ac-9}(\lambda) - \Psi_T^a(T - T_t) - \Psi_S^a S \tag{3.3}$$

$$c_{ac-9}^{TS}(\lambda) = c_{ac-9}(\lambda) - \Psi_T^a(T - T_t) - \Psi_S^c S \tag{3.4}$$

where $a_{ac\text{-}9}^{TS}(\lambda)$ is the temperature and salinity corrected *ac-9* absorption, $a_{ac\text{-}9}(\lambda)$ is the uncorrected *ac-9* absorption, Ψ_T^a is the temperature correction coefficient for absorption, T is the measured temperature from the *CTD*, T_t is the calibration temperature of the *ac-9*, Ψ_S^a is the salinity correction coefficient for absorption, S is the salinity measured by the *CTD*, $c_{ac-9}^{TS}(\lambda)$ is the temperature and salinity corrected

ac-9 attenuation, $c_{ac\text{-}9}(\lambda)$ is the uncorrected *ac-9* attenuation and Ψ_S^c is the salinity correction coefficient for attenuation.

Equations (3.3) & (3.4) are taken from Pegau et al. (1997), who published values for the temperature and salinity coefficients for the standard *ac-9* wavelengths. The values for the coefficients were expanded for the *ac-s* (hyper spectral) by Sullivan et al. (2006).

3.5.3 Scattering Correction Theories

a Zaneveld et al. (1994)

The absorption tube in an *ac-9* is made reflective by a glass inner tube creating an air gap. In this design, light scattered at angles greater than 41.7° to the optic axis is not totally internally reflected and therefore does not reach the diffuser. This causes an overestimation of the absorption coefficient. The scattering correction proposed by Zaneveld et al. (1994) (Equation (3.5)) is widely used to correct this overestimation.

$$a_{ac-9}(\lambda) = a_{ac-9}^{TS}(\lambda) - b_{ac-9}^{TS}(\lambda)\left[\frac{a_{ac-9}^{TS}(715)}{b_{ac-9}^{TS}(715)}\right] \tag{3.5}$$

where $a_{ac-9}^{TS}(\lambda)$ is the temperature and salinity corrected absorption from the *ac-9* at wavelength λ, $b_{ac-9}^{TS}(\lambda)$ is the scattering calculated from the temperature and salinity corrected absorption and attenuation from the *ac-9* at wavelength λ. This correction sets $a_{ac\text{-}9}(715) = 0$. A ratio of the absorption to scattering at 715 nm is used to calculate the proportion of the absorption attributed to this overestimation at each wavelength. This is then subtracted from the absorption coefficient to correct for the overestimation.

b Issues with the Zaneveld et al. (1994) Method

The Zaneveld et al. (1994) method makes two key assumptions. The first of these is that the absorption coefficients of particulate and dissolved materials are negligible in the near infrared (i.e. $a_{ac\text{-}9}(715) = 0$). While initially this appeared to be a reasonable assumption (Stramski et al., 2004; Babin & Stramski, 2002), its validity

has been increasingly questioned, particularly in particle laden waters (Leymarie et al., 2010; Doxaran et al., 2009; Tzortziou et al., 2006; Tassan & Ferrari, 2003). Monte Carlo modelling by Leymarie et al. (2010) of the effect of infrared absorption by mineral particles on *ac-s* correction procedures suggests that $a_{ac\text{-}9}(\lambda)$ could be underestimated by as much as 5% at 412 nm and 50% at 676 nm in water where mineral particles are dominant. These results were based on the absorption coefficients of non-algal particles at 750 nm being 25% of the value at 440 nm which is at the upper end of the range reported by Tassan & Ferrari (2003) for marine sediments and considerably higher than the 5% suggested by Tzortziou et al. (2006). The uncertainties arising in $a_{ac\text{-}9}(\lambda)$ are clearly more pronounced in the red and near infrared wavebands, but there is still uncertainty regarding their magnitude.

The second assumption made by Zaneveld et al. (1994) was related to the wavelength dependence of the volume scattering function (*VSF*). They assumed that the *VSF* was wavelength independent. The validity of this assumption is still under debate (Whitmire et al., 2010; McKee et al., 2008), with current studies using an integrating cavity absorption meter attempting to disentangle the complexity in *VSF* determination (Röttgers & Gehnke, 2012).

3.6 Measurements made with an *ac-9*

3.6.1 Inherent Optical Property Measurements

Neither channel of the *ac-9* measures the absorption or attenuation coefficient directly, and these quantities are calculated by the manufacturer's supplied software (Section 3.5.1). Both channels of the *ac-9* measure the transmittance of the water enclosed in the sample tube using Equation (3.6), wherein T_R denotes transmittance, E_{SIG} and E_{REF} denote the irradiance detected by the signal and reference detectors, respectively.

$$T_R = \frac{E_{SIG}}{E_{REF}} \tag{3.6}$$

The absorption and beam attenuation coefficients are subsequently calculated using Equations (3.7) – (3.9) (absorption as an example) with $T_R(\lambda)$ from the corresponding *ac-9* channel.

$$a_{RAW}(\lambda) = -\frac{\ln\left(T_R(\lambda)\right)}{L_{FT}} \tag{3.7}$$

$$a_{UC}(\lambda) = a_{RAW}(\lambda) - \Delta aT_I \tag{3.8}$$

$$a_{ac-9}(\lambda) = a_{UC}(\lambda) - a_{CAL}(\lambda) \tag{3.9}$$

In these equations, L_{FT} denotes the flow tube length, ΔaT_I, denotes the temperature dependence of the electronics in the *ac-9*, subscripts *RAW*, *UC* and *ac-9* denote 'raw', 'un-calibrated' and '*ac-9* instrument output' respectively. The temperature correction term, ΔaT_I, is computed using the internal temperature sensor of the *ac-9* and applied automatically during data output (note that this temperature correction compensates for the temperature dependence of the instrument electronics, not the water temperature as discussed in Section 3.5.2). The symbol a_{CAL} is used to refer to the calibration coefficient for pure water determined during calibration and applied such that $a_{ac\text{-}9}(\lambda)$ is the non-water absorption coefficient of the water sampled, prior to correction for salinity, water temperature and scattering errors, as discussed in Section 3.5.2.

3.6.2 Uncertainties Associated with *ac-9* Measurements

The typical accuracy for the *ac-9* stated by the manufacturer (± 0.01 m^{-1}) was taken to be the random uncertainty in both $a_{ac\text{-}9}(\lambda)$ and $c_{ac\text{-}9}(\lambda)$ measurements. An alternative method of uncertainty quantification for *ac-9* measurements was developed by McKee et al. (2008) whereby signals from adjacent wavebands in each *ac-9* channel were compared using a residual analysis technique using the 510 and 532 nm wavebands. These are the most closely paired wavebands of the *ac-9*

instrument that are not situated near to local maxima or minima in either $a_{ac\text{-}9}(\lambda)$ or $b_{ac\text{-}9}(\lambda)$.

The adjacent waveband residual analysis technique is described in this paragraph using the non-water absorption coefficient, $a_{ac\text{-}9}(\lambda)$, as an example. Linear regression was used to regress $a_{ac\text{-}9}(510)$ against $a_{ac\text{-}9}(532)$, returning a gradient and offset, M_{LR} and C_{LR}, respectively. The dependent variable, $a_{ac\text{-}9}(510)$, was modelled from $a_{ac\text{-}9}(532)$, using this regression derived relationship, as expressed in Equation (3.10) (in which 'hat' notation, $\hat{a}$, is used to denote a modelled *IOP*). The residuals between the modelled and measured $a_{ac\text{-}9}(510)$, $Ra_{ac\text{-}9}(510)$, were calculated prior to determining the root mean squared error, $RMSE_{Raac\text{-}9(510)}$, of these residuals (Equations (3.11) & (3.12)). As these residuals, $Ra_{ac\text{-}9}(510)$, were the cumulative result of random uncertainties in data from both *ac-9* wavebands, it was necessary to partition $RMSE_{Raac\text{-}9(510)}$ to estimate the random uncertainty in a single waveband. Assuming that these wavebands were subject to random uncertainties of equal magnitude and using the equations of Taylor (1997), $RMSE_{Raac\text{-}9(510)}$ was partitioned between the channels as shown in Equations (3.13) & (3.14).

$$\hat{a}_{ac-9}(510) = [a_{ac-9}(532) \cdot M_{LR}] + C_{LR} \tag{3.10}$$

$$Ra_{ac-9}(510) = \hat{a}_{ac-9}(510) - a_{ac-9}(510) \tag{3.11}$$

$$RMSE_{Ra_{ac-9}(510)} = \sqrt{\frac{1}{N}\sum_{i=1}^{N}[Ra_{ac-9}(510)^2]} \tag{3.12}$$

$$\delta x_1 = \delta x_2 = \sqrt{\frac{1}{2}\delta y^2} \tag{3.13}$$

$$\delta a_{ac-9}(510) = \delta a_{ac-9}(532) = \sqrt{\frac{1}{2}\left(RMSE_{Ra_{ac-9}(510)}{}^2\right)} \tag{3.14}$$

Figure 3.6 shows scatterplots of the data from the adjacent wavebands of both the absorption and beam attenuation channels, above scatterplots of the corresponding

residuals, $Ra_{ac\text{-}9}(510)$ and $Rc_{ac\text{-}9}(510)$ described in the preceding paragraph. Using this residual analysis technique yielded estimates of the random uncertainties in $a_{ac\text{-}9}(510)$ and $c_{ac\text{-}9}(510)$ of ± 0.002 and ± 0.009 m^{-1}, respectively. This technique was repeated for the waveband pairs 532 and 555 nm, and 488 and 510 nm, with similar results. As a consequence of this and the common light sources and electronics used by all *ac-9* wavebands in each channel, the absolute random uncertainties across all *ac-9* wavebands were treated as equal to that of the 510 nm waveband. The residual analysis derived estimate of $\delta c_{ac\text{-}9}(510)$ = ± 0.009 m^{-1} was within 10% of the manufacturers specification (± 0.01 m^{-1}), however the estimate of $\delta a_{ac\text{-}9}(510)$ = ± 0.002 m^{-1} was significantly smaller than the manufacturers specification.

The likely reason for the discrepancy in the values calculated by McKee et al. (2008) and those quoted by the manufacturer is that the manufacturer's figure includes factors other than the noise inherent in the digitisation of the electronic signal. These could include uncertainties in the absorption correction procedure and small variations in the optics (particularly tube reflectivity) between *ac-9* instruments.

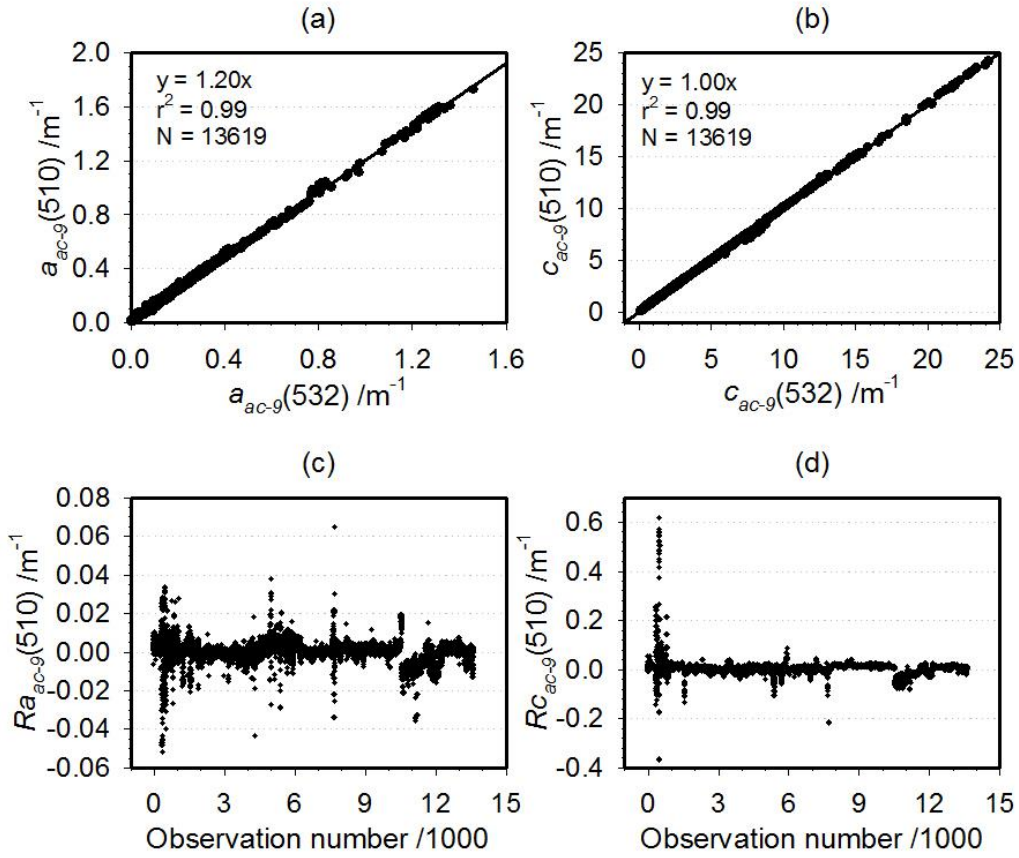

Figure 3.6: (a) Scatterplot of the in situ, non-water absorption coefficient, $a_{ac\text{-}9}(\lambda)$, from two adjacent *ac-9* wavebands (510 and 532 nm) for the entire UK shelf data set, (b) Similarly plotted in situ non-water beam attenuation coefficients, $c_{ac\text{-}9}(\lambda)$. Having modelled $a_{ac\text{-}9}(510)$ and $c_{ac\text{-}9}(510)$ from $a_{ac\text{-}9}(532)$ and $c_{ac\text{-}9}(532)$ respectively, residuals were calculated ($R_{aac\text{-}9}(510) = a_{ac\text{-}9}(510) - [a_{ac\text{-}9}(532)M_{LR} + C_{LR}]$). (c) The residual absorption coefficients at 510 nm, $R_{aac\text{-}9}(510)$. (d) The residual beam attenuation coefficients at 510 nm, $R_{cac\text{-}9}(510)$.

3.7 Noise in Typical *ac-s/9* Measurements

In order to measure the amount of noise in typical *ac-s/9* signals three sets of data with relatively constant signals were examined. First, calibration (*CAL*) data from the laboratory were used. Second, field data were taken from the Oban 2004 (*OB04*) cruise (Appendix B) where an *ac-9* was held at constant depth just below the surface. Third, data were taken from Liverpool Bay (*LB*) where an *ac-s* was permanently moored 5 m below the surface (Appendix A). The resulting signals in the 412 nm waveband for all three sets of data are shown in Figure 3.7.

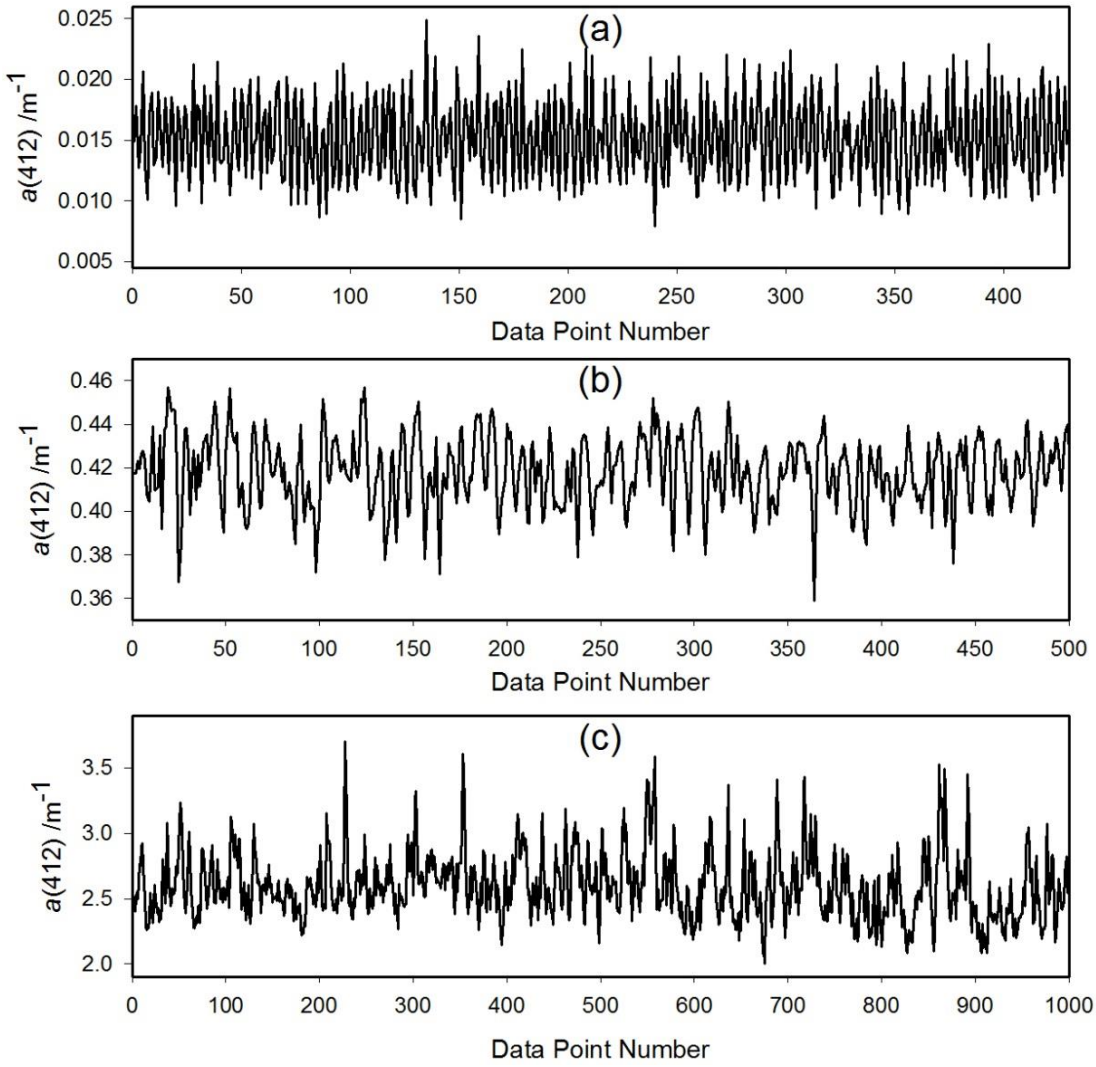

Figure 3.7: *ac-s/9* data used to measure noise in typical *ac-s/9* signals (a) *ac-9* Calibration file in the laboratory, (b) *ac-9* deployed during Oban 2004 Cruise (c) *ac-s* from Liverpool Bay July 2010. Notice in each example that the range of *a*(412) values varies significantly, with a range in the calibration file of 0.013 m^{-1}, the Oban 2004 cruise of 0.19 m^{-1} and in Liverpool Bay of 3.7 m^{-1}.

The laboratory calibration run gives a best case scenario as it was acquired in a controlled environment where the instrument was perfectly clean, the sample was pure water, and the noise should be a minimum. For the Oban 2004 data the water was relatively clear and the instrument properly cleaned and calibrated before deployment. In this case, the noise level should be typical for a well maintained instrument in coastal water. In Liverpool Bay, high particulate water coupled with long deployments of a poorly maintained instrument should give a worst case scenario for noise levels in an *ac-s*. By calculating the mean and standard deviation

of the data, typical noise levels can be determined. Table 3.4 shows the mean and the standard deviation for each set of data and for each wavelength.

Table 3.4: Mean and standard deviation of *ac-9* channels for three different data sets to measure typical noise values in *ac-s/9* data

$a_{ac\text{-}s}(\lambda)$		*CAL*	*OB04*	*LB*	$c_{ac\text{-}s}(\lambda)$		*CAL*	*OB04*	*LB*
412	**Mean**	0.015	0.561	1.421	**412**	**Mean**	0.066	1.160	2.380
	σ	0.004	0.061	0.478		**σ**	0.001	0.103	0.826
440	**Mean**	0.008	0.451	1.210	**440**	**Mean**	0.065	0.999	2.229
	σ	0.002	0.041	0.412		**σ**	0.001	0.082	0.781
488	**Mean**	0.011	0.338	0.935	**488**	**Mean**	0.062	0.907	2.076
	σ	0.001	0.025	0.325		**σ**	0.001	0.066	0.743
510	**Mean**	0.007	0.301	0.830	**510**	**Mean**	0.054	0.875	2.037
	σ	0.001	0.021	0.293		**σ**	0.001	0.062	0.728
532	**Mean**	0.007	0.278	0.751	**532**	**Mean**	0.054	0.869	1.994
	σ	0.002	0.018	0.268		**σ**	0.001	0.060	0.715
555	**Mean**	0.006	0.247	0.675	**555**	**Mean**	0.048	0.832	1.957
	σ	0.001	0.015	0.243		**σ**	0.001	0.058	0.700
650	**Mean**	0.005	0.137	0.540	**650**	**Mean**	0.040	0.709	1.821
	σ	0.001	0.010	0.206		**σ**	0.001	0.054	0.653
676	**Mean**	0.010	0.157	0.582	**676**	**Mean**	0.038	0.708	1.797
	σ	0.002	0.010	0.218		**σ**	0.001	0.054	0.648
715	**Mean**	-0.003	-0.122	0.385	**715**	**Mean**	0.027	0.471	1.728
	σ	0.001	0.008	0.158		**σ**	0.001	0.052	0.628

Taking average values across the wavelength channels and calculating the ratio of the standard deviation and the mean gives the typical percentage noise expected for each of the three different scenarios. The results are summarised in Table 3.5.

Table 3.5: Summary of typical noise values for the three characteristic data sets. Dividing the standard deviation by the mean gives the percentage error attributable to noise in *ac-s/9* data.

	CAL		*OB04*		*LB*	
	$a_{ac\text{-}9}(\lambda)$	$c_{ac\text{-}9}(\lambda)$	$a_{ac\text{-}9}(\lambda)$	$c_{ac\text{-}9}(\lambda)$	$a_{ac\text{-}s}(\lambda)$	$c_{ac\text{-}s}(\lambda)$
Mean	0.009	0.050	0.309	0.837	0.868	2.00
Standard Deviation	0.002	0.001	0.025	0.066	0.305	0.724
Percentage Error	**22%**	**2%**	**8%**	**8%**	**35%**	**36%**

The percentage noise values for the calibration data were high due to the low values being examined: a percentage noise level is not necessarily appropriate in this case.

The other two cases give typical noise levels of around 8% and 35%, and the difference shows the requirement of instrument maintenance, particularly in coastal regions which are dominated by sediment.

3.8 Chapter Summary

The measurement accuracy of the *ac-9* is limited by the failure of the absorption tube to collect photons scattered above 41.7º to the optic axis. This results in an overestimation of the absorption coefficient. The most commonly used correction procedure (Zaneveld et al., 1994) assumes that the absorption by particulate and dissolved matter at 715 nm is negligible and that the volume scattering function is independent of wavelength. Both of these assumptions are controversial with recent work indicating that there is significant near infrared absorption in particulate laden waters and that the volume scattering function is not necessarily independent of wavelength (Röttgers & Gehnke, 2012; Sokolov et al., 2010; Chami et al., 2006). At the time this work was completed, no convincing alternative was available, but a new method has recently been proposed by McKee et al. (2013) which utilises Monte Carlo simulations to correct the absorption coefficient. This method was not employed throughout this work due to the need for concurrent backscattering and independent robust absorption measurements. For the archive UK shelf data set, backscattering measurements were not always available and absorption measurements were only available for discrete depths. For Liverpool Bay there was no concurrent backscattering or absorption measurements available to implement this correction methodology. Future deployments which utilise submersible integrating-cavity absorption meters such as the HOBI Labs *a*-Sphere and TriOS OSCAR will make it possible to correct *ac-s/9* data in this manner.

Another limitation of the *ac-9* arises from the finite collection angle in the attenuation tube, which results in the collection of some forward scattered light leading to an underestimation of the attenuation coefficient. Attempts to characterise the extent of the underestimation have shown that the issue is dependent on the concentrations of optically significant materials within the water and also the size of particles within the water. Corrections proposed by (Boss et al., 2009) rely on

concurrent deployment of a LISST instrument to measure particle size and the volume scattering function. As the data presented in this thesis are mainly archive data from the University of Strathclyde, LISST data are not available to apply such corrections.

3.8.1 Summary of likely uncertainties in *ac-s* measurements

- Underestimation of absorption coefficients arising from the scattering correction method of Zaneveld et al. (1994). In the most unfavourable circumstances, this could lead to an uncertainty in the absorption coefficient of 5% at 412 nm and 50% at 676 nm.

- The acceptance angle of the attenuation channel detector. The ratio between the beam attenuation measured with an *ac-9* and a LISST in Boss et al. (2009) varied from 0.64 to 1.03, which suggested a 20 % variation in the *ac-9* measurements. However this analysis was completed using a 10 cm path length *ac-9* and is probably an over-estimate for the 25 cm path length instrument utilised in this thesis.

- The random uncertainties in *IOP* measurements from both an *ac-s* and an *ac-9* are quoted by the manufacturer to be of the order of ± 0.01 m^{-1}. Analysis of *ac-9* signals by McKee et al. (2008) in a controlled laboratory environment produced similar uncertainties for the beam attenuation coefficient but substantially lower values (of the order of ± 0.002 m^{-1} at 510 nm) for the absorption channel. However these figures were derived by analysing the noise with which signals were digitised rather than by comparison with known absorption and attenuation standards.

- Typical noise levels in *ac-s/9* data were calculated for three scenarios. Calibration data in the laboratory gave minimum absolute noise levels, of the order of 3.8×10^{-5} m^{-1}, but disproportionately high percentage noise figures (22% in the absorption channel) due to small values. Typical field data had noise levels of around 8%, while Liverpool Bay mooring data gave the worst results with noise levels around 35%.

Chapter 4 Ancillary Instrumentation, Water Sample Analysis & Temporal Data Analysis

As described in Chapter 3, the *ac-s* requires a *CTD* to be deployed simultaneously in order to correct for temperature and salinity differences between the water used for calibration and the water being sampled. Other instruments deployed in acquiring the data used in this thesis include an Acoustic Doppler Current Profiler (*ADCP*) to measure the current velocity at different depths, a WET Labs ECO-Fluorometer (*ECO*) to measure chlorophyll fluorescence and a HOBI Labs Hydroscat-2 backscattering meter (*HS2*) to measure particulate backscattering.

In addition, water sample analyses had to be completed in order to measure the concentration of optically significant constituents (*OSCs*). The *OSC* concentrations were then combined with inherent optical property (*IOP*) data to allow the calculation of specific inherent optical properties (*SIOPs*).

4.1 Instrumentation

4.1.1 Acoustic Doppler Current Profiler (*ADCP*)

In the Liverpool Bay time series (Appendix A) an Acoustic Doppler Current Profiler (*ADCP*) was mounted on the sea floor at the site of the *ac-s* deployment. The current velocity data from the *ADCP* were combined with the optical time series to draw conclusions about the dynamics of Liverpool Bay.

An *ADCP* uses the Doppler shift to measure the velocity of sound scatterers in water. A pulse of sound is emitted from the *ADCP* (in this case from the top as it was bottom mounted) and the particles in the water scatter the sound waves in all directions. The sound waves reflected in the backwards direction (towards the *ADCP*) are Doppler shifted. When the scatterers are moving away from the *ADCP*, the sound waves are Doppler shifted to a lower frequency proportional to the relative velocity between the *ADCP* and the scatterers. As the *ADCP* both sends and receives sound, the Doppler shift is doubled.

The Doppler shift only occurs when sound sources and receivers get closer to or further from one another – this is radial motion. On the other hand, angular motion changes the direction between the source and receiver, but not the distance separating them, and causes no Doppler shift. The velocity of the scatterers can be calculated from Equation (4.1) (assuming that the *ADCP* is stationary) using

$$V = \frac{CF_d}{2F_s \cos\theta} \tag{4.1}$$

where F_d is the Doppler shift frequency, F_s is the frequency of sound at zero velocity, V is the relative velocity, C is the speed of sound and θ is the angle between the acoustic beam and the relative velocity vector (Gordon, 1996). Figure 4.1 is a schematic showing the angle θ.

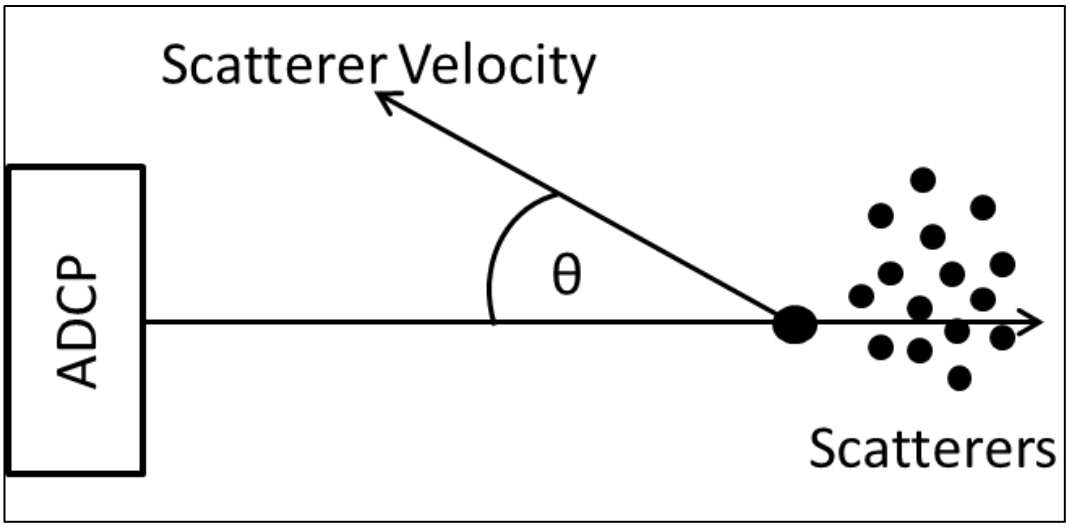

Figure 4.1: Schematic demonstrating the principles of operation for the *ADCP*

4.1.2 SeaBird SBE 19 plus *CTD*

The SBE 19 plus *CTD* instrument (Sea-Bird Electronics Inc., Washington, USA) measures the conductivity and temperature of seawater, together with ambient pressure (Seabird, 2008). A schematic diagram is included as Figure 4.2.

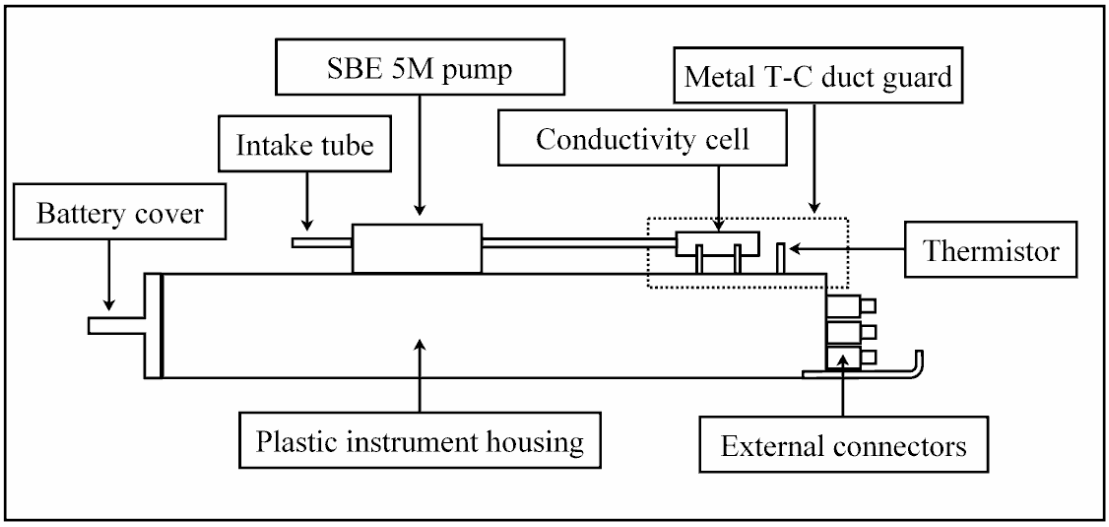

Figure 4.2: Schematic diagram of the Sea-Bird SBE 19*plus CTD* instrument.

The conductivity and temperature sensors are located under the metal 'T-C duct' guard with a small physical separation (approximately 2 cm) to minimise the effects of sample spatial inhomogeneity on the alignment of measurements from each sensor. Conductivity, temperature and pressure are measured using a high precision Wein-Bridge oscillator conductivity cell, an ultra-stable thermistor mounted in a bridge circuit and a Druck semiconductor strain-gauge, respectively. The instrument was supplied factory calibrated, and no further calibration was attempted in the laboratory. The manufacturers quoted specifications for the *CTD* are shown in Table 4.1.

Table 4.1: Manufactures' Specifications for the *CTD* (Seabird, 2008)

	Conductivity	Temperature	Pressure	A/D Inputs
Measurement Range	0 – 7 S/m	-5 to +35 °C	0 to full scale -- 1400/2000/4200/6800/10,500 m (2000/3000/6000/10,000/15,000 psia)	0 to +5 volts
Initial Accuracy	0.0003 S/m	0.001 °C	0.015% of full scale	0.005 volts
Typical Stability	0.0003 S/m	0.0002 °C per month	0.02% of full scale per year	0.001 volts per month
Resolution at 24 Hz	0.00004 S/m	0.0002 °C	0.001% of full scale	0.0012 volts
Time Response	0.065 s	0.065 s	0.015 s	5.5 Hz 2-pole Butterworth Low Pass Filter
Master Clock Error Contribution	0.00005 S/m	0.00016 °C	0.3 dbar with 6800 m (10,000 psia) pressure sensor	

The SBE 19plus *CTD* was connected to an external pump (Sea-Bird SBE5M) used to pump seawater through the instrument's 'T-C duct'. The *CTD* and *ac-s* instruments were typically plumbed in series. Where multiple pumps were used, these were all controlled and powered by the *CTD*. The manufacturer supplied software, *SeaSoft*, was used to configure and control the SBE 19plus and attached pumps. The instrument was configured to operate in profiling mode storing raw sensor voltages in hexadecimal format. The supplied software, SBE Data Processing, was used to convert these raw data from hexadecimal to ASCII to facilitate further processing.

4.1.3 WET Labs *ECO* Fluorometer

The Environmental Characterization Optics, or *ECO*, miniature fluorometer allows the user to detect signals generated by chlorophyll, *CDOM*, uranine, phycocyanin, or phycoerythrin by measuring the amount of fluorescence emission in a sample volume of water. In the case of this work, Chlorophyll fluorescence was measured. The *ECO* uses an LED to provide the excitation source (an interference filter is used to reject the small amount of out-of-band light emitted by the LED). The light from the source enters the water volume at an angle of approximately 55 – 60º with respect to the end face of the unit. Fluoresced light is received by a detector positioned so that the acceptance angle forms a 140º intersection with the source beam. An interference filter is used to discriminate against the scattered excitation light (WET

Labs, 2011). Figure 4.3 shows a schematic of the optical setup of the *ECO* Fluorometer.

Fluorescence counts are converted to concentrations using the manufacturer supplied scale factor. For chlorophyll, WET Labs derives the chlorophyll equivalent concentration (*CEC*) using a fluorescent proxy approximately equal to 25 µg/l of a *Thalassiosira weissflogii* phytoplankton culture.

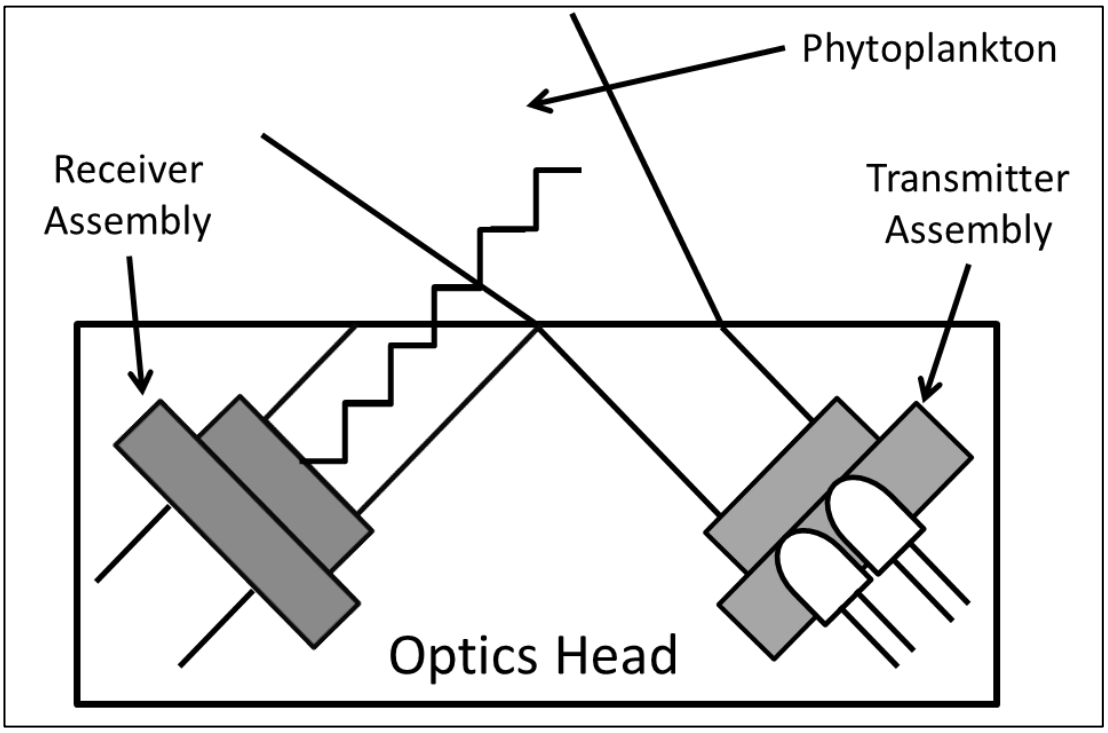

Figure 4.3: Schematics of the optical setup of the *ECO* Fluorometer

4.1.4 HOBI Labs Hydroscat-2 Backscattering Meter

The Hydroscat-2 (*HS2*) instrument (HOBI Labs, Washington, USA) measures the backscattering coefficient, $b_b(\lambda)$, at 470 and 676 nm together with chlorophyll-a (*CHL*) fluorescence at 676 nm and ambient pressure. A schematic diagram of the *HS2* is included as Figure 4.4.

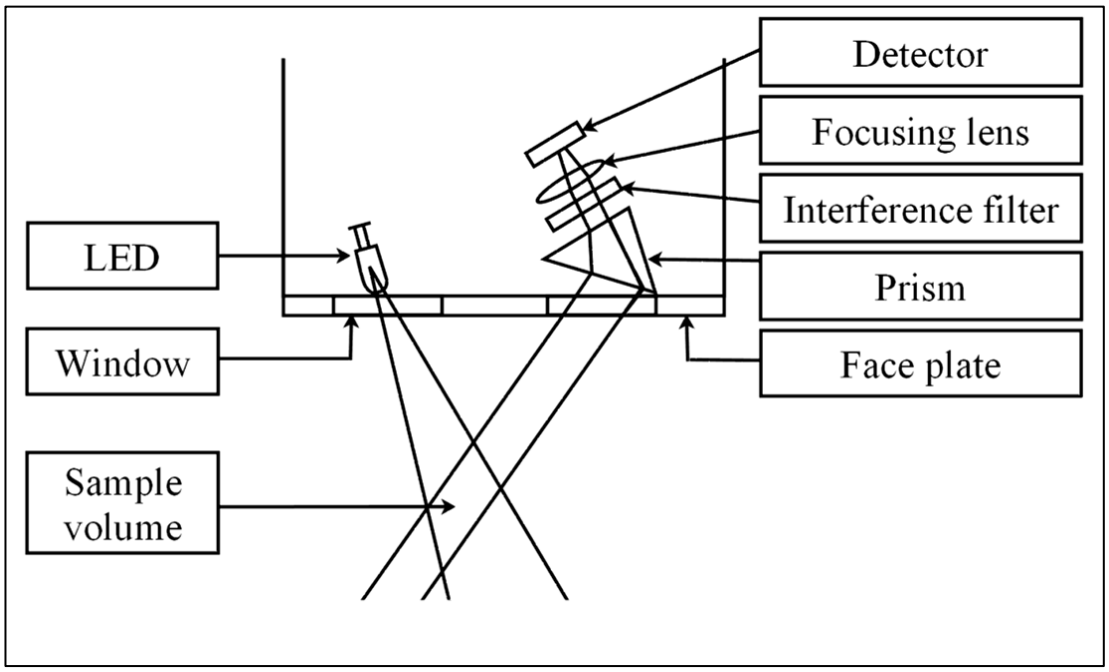

Figure 4.4: Schematic diagram of Hydroscat-2 optics (single channel).

The *HS2* consists of two independent channels each comprising an LED light source in the transmission side, with the reception optics comprising a prism, band pass interference filter, focussing lens and silicon detector. The emitted light enters the water at an angle of 20° to the normal. The prism bends the field of view of the detector toward the emitted beam, with the interference filter excluding all light outwith the desired spectral detection range. The lens focuses the received, filtered light onto the silicon detector. The fields of view of the detectors are coincident to facilitate the detection of chlorophyll fluorescence stimulated by the blue LED emission. In order to discriminate between stimulated red fluorescence and backscattered light emitted by the red LED, a system of source modulation is employed. The volume scattering function at 140° is estimated from the irradiance detected by the *HS2*, and the backscattering coefficient is subsequently calculated using the method of Maffione & Dana (1997).

4.2 Laboratory Analysis of Water Samples

Water samples for laboratory analysis were collected either as surface (bucket) samples, by a water bottle mounted on the ships winch, or by a *CTD*-mounted rosette sampler. Measurements of particulate, non-pigmented particulate and chromophoric dissolved organic matter absorption coefficient spectra were made, together with measurements of suspended particulate material (*SPM*) and photosynthetic pigment concentrations.

4.2.1 Coloured Dissolved Organic Material (*CDOM*)

Seawater samples were filtered through 25 mm diameter Gelman Supor 0.2 μm pore membrane filters into acid rinsed bottles using glass syringes and plastic filter holders to remove suspended particulate material from the samples. The filtrate was then placed into a 10 cm path length cuvette which was inserted in the sample chamber of Shimadzu UV-PC2501 spectrophotometer. An identical cuvette containing ultrapure Milli-Q water was placed in the spectrophotometer reference beam. The optical density (*OD*) of the sample relative to pure Milli-Q water was measured, in triplicate, at 1, 2 or 5 nm wavelength increments between 400 and 750 nm.

$$a_{CDOM}(\lambda) = \frac{2.303 \cdot OD(\lambda)}{L} \tag{4.2}$$

These optical densities were converted to absorption coefficients using Equation (4.2) in which *L* denotes the optical path length of the cuvette.

The resulting $a_{CDOM}(\lambda)$ values were corrected for scattering losses by subtracting $a_{CDOM}(700)$ from all $a_{CDOM}(\lambda)$ and disregarding $a_{CDOM}(\lambda > 700$ nm). The reason for this correction procedure differing from that applied to filter pad absorption spectra is that there is significant temperature dependence in the absorption by pure water between 710 and 750 nm. Choosing 700 nm as the wavelength at which to zero measured *CDOM* absorption coefficient spectra avoided this temperature dependent water absorption, while introducing a slight negative bias in $a_{CDOM}(\lambda)$ measurements. Due to its chemical complexity, $a_{CDOM}(440)$ was taken as a proxy for the

concentration of *CDOM*. The spectral slope of absorption by *CDOM*, *S*, was determined for each sample by fitting an exponential function to $a_{CDOM}(\lambda)$ across the wavelength range ($400 \leq \lambda \leq 555$ nm). This allowed $a_{CDOM}(\lambda)$ to be expressed as in Equation (4.3), in which λ_r denotes a reference wavelength (440 nm in our methodology).

$$a_{CDOM}(\lambda) = a_{CDOM}(\lambda_r) \cdot \exp[-S(\lambda - \lambda_r)] \quad (4.3)$$

The estimated error in measurements of *CDOM* concentration was ± 0.1 m^{-1}. This was intended to account for base line drift and random noise in the spectrophotometer, the potential (unrecorded) temperature differential between sample and reference cuvettes in the spectrophotometer, and the possible presence of significant concentrations of sub-0.2 μm particles in the *CDOM* sample.

4.2.2 Chlorophyll-a (*CHL*)

Samples for pigment concentration measurement were prepared by filtering seawater through 25 mm diameter Whatmann GF/F filters. Samples were prepared in triplicate. Immediately following filtration, the filters were placed in labelled plastic centrifuge tubes and frozen. In the laboratory, magnesium carbonate ($MgCaO_3$) neutralised 90% acetone solution was added to each centrifuge tube and the lid replaced. To allow pigment extraction to take place, the samples were placed in dark refrigeration overnight, after which they were centrifuged at 5600 rpm for a period of ten minutes. After centrifugation, 8 ml of the extracted pigment solution was placed in a 1 cm path length cuvette in the Shimadzu UVPC-2501 spectrophotometer with an identical cuvette of neutralised acetone solution in the reference beam. The optical density of the extracted pigment solution, relative to the neutralised acetone solution, was obtained between 400 and 750 nm. Following the measurement of optical density, 0.2 ml of 10% hydrochloric acid solution was added to the cuvette and the measurement repeated. Pigment concentrations were estimated using the trichromatic equations of Jeffrey & Humphrey (1975) (Equations (4.4) – (4.8)).

$$CHL_a = \frac{[11.85\ (OD(664) - OD(750)) - 1.54(OD(647) - OD(750)) - 0.08(OD(630) - OD(750))]V_e}{V_f L} \quad (4.4)$$

$$CHL_b = \frac{[-5.43\ (OD(664) - OD(750)) + 21.03(OD(647) - OD(750)) - 2.26(OD(630) - OD(750))]V_e}{V_f L} \quad (4.5)$$

$$CHL_c = \frac{[-1.67\ (OD(664) - OD(750)) - 7.60(OD(647) - OD(750)) + 24.52(OD(630) - OD(750))]V_e}{V_f L} \quad (4.6)$$

$$CHL_a = \frac{11.4K[(OD_o(665) - OD_o(750)) - (OD_a(665) - OD_a(750))]V_e}{V_f L} \quad (4.7)$$

$$PHAEO_a = \frac{11.4K[R(OD_o(665) - OD_o(750)) - (OD_a(665) - OD_a(750))]V_e}{V_f L} \quad (4.8)$$

where;

$$R = \frac{OD_o(665)}{OD_a(665)} \quad (4.9)$$

$$K = \frac{R}{R - 1} \quad (4.10)$$

The uncertainty in measurements of Chlorophyll (*CHL*) concentration, were estimated as ± 0.75 mg m^{-3} based on replicate measurements. Further discussions of the uncertainties in measured pigment concentrations may be found in Parsons et al. (1984) and Jeffrey et al. (1996).

where CHL_a, CHL_b, CHL_c and $PHAEO_a$ are the concentrations of Chlorophyll-a, b, c and Phaeopigment-a respectively, $OD(\lambda)$ is the optical density of the extracted pigment at wavelength λ, $OD_o(\lambda)$ and $OD_a(\lambda)$ are the optical densities of the extracted pigment before and after acidification, V_e is the extracted volume of pigment, V_f is the filtered volume and L is the path length of the cuvette.

4.2.3 Suspended Particulate Matter (*SPM*)

Whatmann 90 mm diameter GF/F glass-fibre filters were used for SPM concentration measurements. Prior to each cruise, filters were numbered, dried at 100 °C for a period of one hour and weighed three times to ensure an accurate dry weight (W_D), for each filter was recorded. At sea, large volumes of seawater were filtered through each GF/F using a purpose-built filter rig consisting of a vacuum vessel, two pumps connected in series, a glass frit and a sample vessel. The sample volume was typically 5 litres, with lower volumes filtered in highly turbid waters. After sample filtration, around 100 - 200 ml of Milli-Q ultrapure water was rinsed through the filters in an attempt to remove sea salt. The filters were subsequently dried for a period of one hour in a small oven at 100 °C and stored individually in polyethylene petri-dishes. In the laboratory the loaded filters were dried and weighed three times, as before, to determine the loaded weight (W_L). The filters were subsequently combusted for three hours in a laboratory furnace at a temperature of 500 °C, after which all organic material was assumed combusted. On removal from the furnace, filters were re-weighed three times to determine the weight after combustion (W_C). Between repeat weighings, the filters were placed in the laboratory oven to minimise the effect on filter weight by moisture absorption. The concentrations of organic, mineral and total suspended solids (denoted *OSS*, *MSS* and *TSS*, respectively) were calculated using Equations (4.11) – (4.13). In these equations, filtered volumes (V_F) are measured in cubic metres and filter weights (strictly masses) in grams, giving *SPM* concentrations in units of g m^{-3}.

$$TSS = \frac{(W_L - W_D)}{V_F} \tag{4.11}$$

$$OSS = \frac{(W_L - W_C)}{V_F} \tag{4.12}$$

$$MSS = \frac{(W_C - W_D)}{V_F} = TSS - OSS \tag{4.13}$$

The uncertainty in measured *MSS* was estimated to be approximately 0.75 g m^{-3} based on limited repeat measurements. The presence of potentially significant systematic errors in measurements of *MSS* was likely. These were thought to include

salt and water of hydration retention in the *SPM* filters (Stavn et al., 2009; Barillé-Boyer et al., 2003), loss of filter pad mass during combustion and potentially the loss of filter mass through rinsing. To some extent these systematic errors may cancel each other, limiting the final uncertainty. Repeat measurements and detailed analyses of the adopted procedure would be required in order to isolate each of these potential sources of error.

Mineral Suspended Solids (*MSS*) are operationally defined as the material remaining on a glass-fibre filter pad (through which seawater was filtered) after combustion at 500 °C for three hours. As a result, measurements of *MSS* were unable to discriminate suspended sediment particles such as clays and silts from mineral particles of biogenic origin such as amorphous silica from diatom cells or calcium carbonate from coccolithophores. Inorganic mineral particles such as quartz, clays and silts exhibit significantly different optical characteristics from biogenic silica (Stavn & Richter, 2008; Babin et al., 2003; Lide, 1997) and this has important implications for *SIOP* derivation and consequently *IOP* inversion.

In principle, a method to correct possible overestimation of *MSS* concentrations could be devised utilising the scattering to absorption coefficient ratio to estimate the fraction of the *MSS* concentration represented by each class of suspended mineral particle. A maximum value of $b_{ac\text{-}s}(\lambda) / a_{ac\text{-}s}(\lambda)$ would suggest that the corresponding *ac-9* observation contained no biogenic minerals and a minimum value of $b_{ac\text{-}s}(\lambda) / a_{ac\text{-}s}(\lambda)$ would indicate purely biogenic suspended minerals. Intermediate values of $b_{ac\text{-}s}(\lambda) / a_{ac\text{-}s}(\lambda)$ would determine the ratio of biogenic to non-biogenic mineral particles. The use of the wavelength 676 nm to determine the scattering to absorption coefficient ratio is recommended as this encompasses the Chlorophyll absorption maximum (emphasising the divergence in $b_{ac\text{-}s}(\lambda) / a_{ac\text{-}s}(\lambda)$). Once the fraction of the *MSS* concentration attributed to either class of mineral had been estimated, $b_{MSS}(\lambda) = b_{ac\text{-}9}(\lambda) - b_{CHL}(\lambda)$ would be partitioned between biogenic and non-biogenic minerals before the corresponding *MSS*-specific scattering coefficients were used to determine the concentration of each class of suspended minerals.

A drawback of the procedure described above is that it was not possible to validate the retrieved concentrations of biogenic and non-biogenic minerals for the data presented in this thesis; therefore the procedure was not implemented.

4.2.4 Filter Pad Absorption

In order to measure the spectral absorption coefficients of suspended particulate material and non-pigmented particulates, the quantitative filter pad technique (*QFT*) (Mitchell, 1990; Trüper & Yentsch, 1967; Yentsch, 1962) was employed. This technique involved concentrating particles from a natural sample onto glass-fibre filter pads, before measuring the absorption coefficient spectrum using a spectrophotometer. Variable sample volumes (between 50 and 1000 ml) were filtered onto Whatmann 25 mm diameter GF/F glass-fibre filters. Each sample was filtered in triplicate. The loaded filters were placed on glass slides immediately in front of the detector window of a Shimadzu UV-PC2501 spectrophotometer. A blank filter was wetted with 0.2 μm filtered seawater, placed on a glass slide and inserted in the path of the spectrophotometer reference beam. The optical density of the loaded filters, $OD_{FP}(\lambda)$, relative to that of the blank filters was measured between 400 and 750 nm at 1, 2 or 5 nm wavelength increments. The relationship between absorptance, $A(\lambda)$, and optical density is shown in Equation (4.14).

$$OD_{FP}(\lambda) = \log_{10}\left[\frac{1}{1 - A_{FP}(\lambda)}\right] = \log_{10}[1 - A_{FP}(\lambda)] \tag{4.14}$$

The overestimation of $OD_{FP}(\lambda)$ due to scattering losses was approximately corrected by subtracting $OD_{FP}(750)$, 750 nm being the longest available wavelength, from all $OD_{FP}(\lambda)$.

These measured optical densities were converted to total filter pad absorption coefficients, $a_{TFP}(\lambda)$, using Equation (4.15), in which A_F, V_F, and β, denote the effective area of the filter pad, the volume of the sample filtered, and the dimensionless path length amplification correction factor (Section 4.2.5), respectively.

$$a_{TFP}(\lambda) = \frac{(2.303 \cdot OD_{FP}(\lambda) \cdot A_F)}{\beta(\lambda) \cdot V_F} \quad (4.15)$$

Following the measurement of $a_{TFP}(\lambda)$, a small amount of hypochlorite bleach was applied to the filters to destroy the pigments, leaving non-pigmented material on the filters. The optical densities, and hence absorption coefficient spectra were measured as before, yielding bleached filter pad absorption coefficients, $a_{BFP}(\lambda)$. The absorption by extractable phytoplankton pigments, $a_{PHY}(\lambda)$, was subsequently estimated by subtracting $a_{BFP}(\lambda)$ from $a_{TFP}(\lambda)$.

4.2.5 Path Length Amplification Factor

The path length amplification factor (β factor) is defined as the increase in the mean optical path length travelled by photons through a loaded glass-fibre filter pad relative to the geometrical path length, or sample thickness. Path length amplification arises from scattering by the fibres of the filter pad and – to a lesser extent – particles embedded therein. As the mean photon optical path length cannot be measured, β is generally expressed as the ratio of the optical density of the sample embedded in a filter pad, $OD_{FP}(\lambda)$, to that of a similar sample in suspension, $OD_{SUS}(\lambda)$, shown in Equation (4.16).

$$\beta(\lambda) = \frac{OD_{FP}(\lambda)}{OD_{SUS}(\lambda)} \quad (4.16)$$

The requirement for β factor correction has been well documented, and a number of methods proposed for its correction (Röttgers & Gehnke, 2012; Lohrenz et al., 2003; Tassan et al., 2000; Lohrenz, 2000; Tassan & Ferrari, 1998; Arbones et al., 1996; Allali et al., 1995; Bricaud & Stramski, 1990; Mitchell, 1990).

Quoted ranges for the β factor are within the range of 1.5 –5 (Lohrenz, 2000; Tassan et al., 2000; Roesler, 1998; Arbones et al., 1996; Moore et al., 1995; Cleveland & Weidemann, 1993; Mitchell, 1990; Kishino et al., 1985), with the value β = 1.73 from Neil et al. (2011) being used throughout this work. This value was calculated by plotting the absorption coefficients measured in the laboratory (averaged over the 10 nm bandwidths covered by the *ac-9*) against the particulate absorption

coefficients measured at the same location *in situ* using an *ac-9*. The resultant graph was definitely linear (Figure 4.5) with a gradient derived by linear regression equal to β and a goodness of fit (R^2) equal to 0.9.

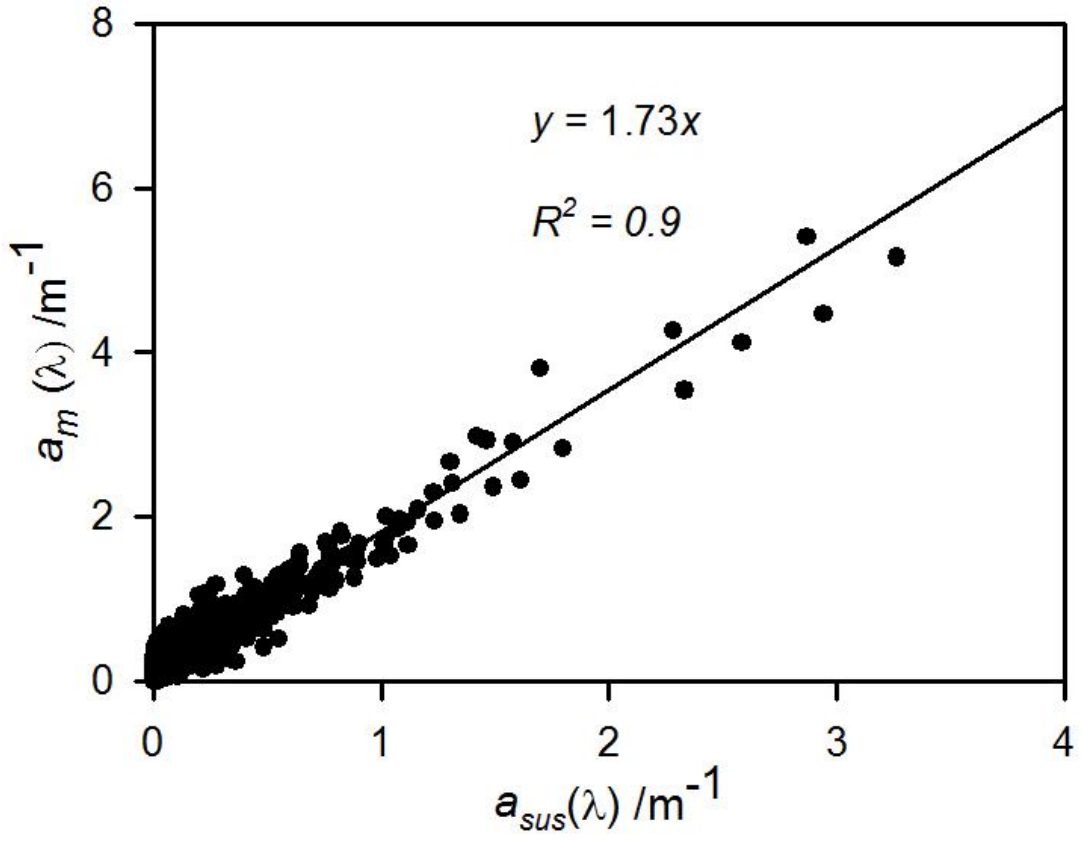

Figure 4.5: Apparent absorption coefficients of particles collected on filter pads, $a_f(\lambda)$, plotted against particulate absorption coefficients measured in situ using an *ac-9*, $a_{sus}(\lambda)$, for all 9 wavebands of the *ac-9*. The line, derived by linear regression, has a slope of $\beta = 1.73$ and coefficient of determination of $R^2 = 0.9$.

4.3 Derivation of Specific Inherent Optical Properties

4.3.1 Specific Absorption Coefficients

Specific absorption coefficients for phytoplankton and mineral suspended sediments ($a^*_{CHL}(\lambda)$ & $a^*_{MSS}(\lambda)$) were calculated by dividing the absorption coefficients ($a_{CHL}(\lambda)$ & $a_{MSS}(\lambda)$) obtained from the filter pad absorption analysis (Section 4.2.4) by the measured concentration of *CHL* and *MSS* (X_{CHL} & X_{MSS}) (Sections 4.2.2 & 4.2.3 respectively).

$$a^*_{CHL}(\lambda) = \frac{a_{CHL}(\lambda)}{X_{CHL}} \tag{4.17}$$

$$a^*_{MSS}(\lambda) = \frac{a_{MSS}(\lambda)}{X_{MSS}} \tag{4.18}$$

The specific absorption for *CDOM* is slightly more complex as the spectral dependence of absorption is defined by Equation (4.19) (Bricaud et al., 1981)

$$\frac{a(\lambda)}{a(440)} = \exp\big(-S(\lambda - 440)\big) \tag{4.19}$$

where $a(440)$ is the absorption coefficient at 440 nm and the exponent S serves as the equivalent of an *SIOP*.

4.3.2 Specific Scattering Coefficients

Before the specific scattering coefficients can be determined, the total scattering coefficient must first be separated into contributions by *MSS* and *CHL*. As discussed in Section 2.4, this cannot be conducted in a laboratory and statistical methods must be employed.

To separate the scattering coefficients of *CHL* and *MSS* end member analysis can be carried out. Plotting the *MSS* concentration against the *CHL* concentration for all stations it is possible to separate the stations into three categories (Figure 4.6). Group 1 stations are characterised by high *CHL* and low *MSS* concentrations, Group 2 stations are characterised by low *CHL* and high *MSS* concentrations and Group 3

stations are characterised by having a mixture of both *CHL* and *MSS*. By selecting the Group 1 and Group 2 stations the scattering coefficients can be estimated using the relative contributions of the constituents to the total. The specific scattering coefficients are then determined using Equations (4.20) & (4.21).

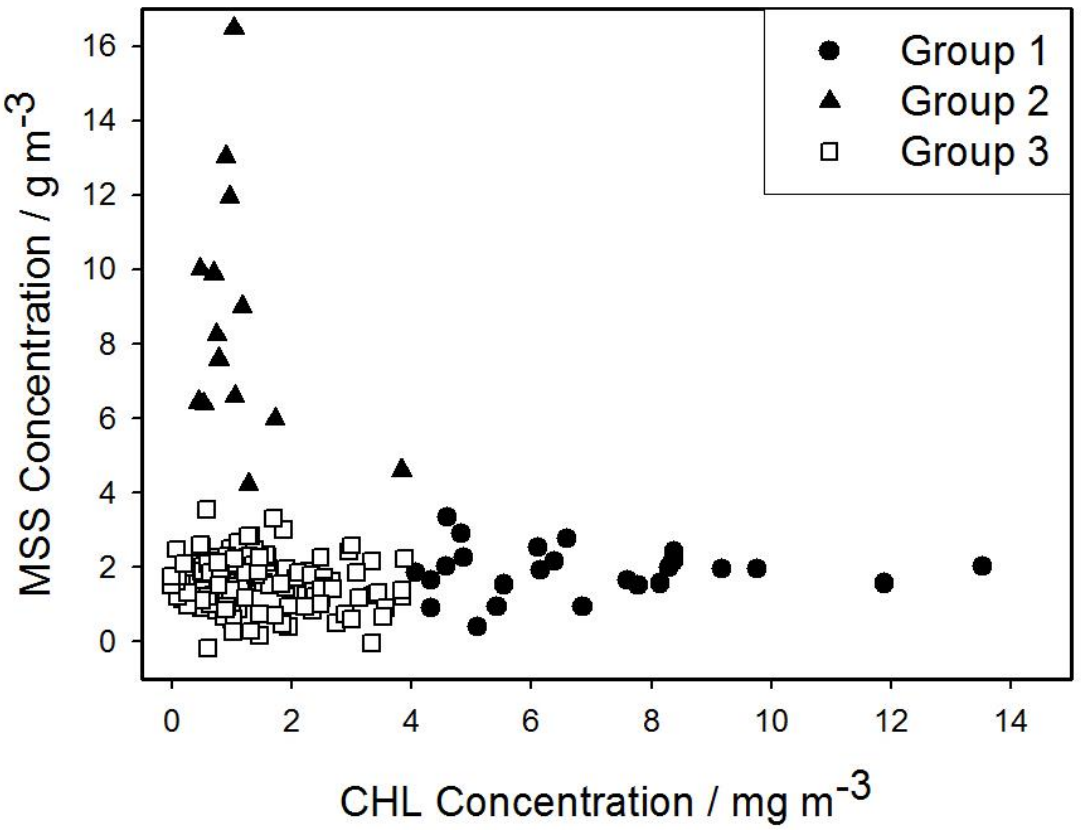

Figure 4.6: *MSS* concentration plotted against *CHL* concentration for all stations in Neil et al. (2011) where Group 1 was classified as high *CHL* low *MSS*, Group 2 as high *MSS* low *CHL* and group 3 as mixed stations.

The Group 3 stations were not classifiable as being dominated by either *CHL* or *MSS*. These stations are located in areas of the Irish Sea with depths greater than 30 m. The optical characteristics of these particles include a low backscattering ratio which suggests larger particles and absorption coefficients with 676 nm larger than 650 nm which suggests a significant chlorophyll peak. This suggests that a significant fraction of the *MSS* at these stations is in fact biogenic minerals in the form of diatom frustules, and that its contribution to absorption and scattering should logically be included in the phytoplankton-related *CHL* component.

$$b^*_{CHL}(\lambda) = \frac{b_{CHL}(\lambda)}{X_{CHL}} \tag{4.20}$$

$$b^*_{MSS}(\lambda) = \frac{b_{MSS}(\lambda)}{X_{MSS}} \tag{4.21}$$

4.3.3 *SIOPs* Utilised in this Work

The *SIOPs* utilised in this work for are taken from Neil et al. (2011) and are shown in Table 4.2. The values in Table 4.2 represent an average for the Irish Sea and adjacent areas and do not take into account regional variability (Section 2.6).

The *SIOPs* in Table 4.2 are used throughout this thesis in order to generate modelled *IOP* data to test the *IOP* inversion methods in Chapter 6. Also the *SIOPs* are used directly in the *IOP* inversion methods to recover the constituent concentrations both for modelled and real *IOP* data.

Table 4.2: Table of mean *SIOP* values ($\bar{x}$) and associated standard deviations (σ) averaged for the UK shelf sea (Neil et al., 2011). Note that the $c^*_i(\lambda)$ mean values are calculated from the other values using $c^*_i(\lambda) = a^*_i(\lambda) + a^*_i(\lambda)$ and standard deviations are added in quadrature.

λ /nm	$a^*_{CHL}(\lambda)$ **/m^2 mg^{-1}**		$b^*_{CHL}(\lambda)$ **/m^2 mg^{-1}**		$c^*_{CHL}(\lambda)$ **/m^2 mg^{-1}**		$a^*_{MSS}(\lambda)$ **/m^2 mg^{-1}**		$b^*_{MSS}(\lambda)$ **/m^2 mg^{-1}**		$c^*_{MSS}(\lambda)$ **/m^2 mg^{-1}**		$a^*_{CDOM}(\lambda)$ **/m^{-1}**
	$\bar{x}$	**σ**	$\bar{x}$	**σ**	$\bar{x}$	**σ**	$\bar{x}$	**σ**	$\bar{x}$	**σ**	$\bar{x}$	**σ**	$\bar{x}$
412	0.06	0.012	0.12	0.026	0.18	0.028	0.08	0.027	0.4	0.130	0.48	0.132	1.4
440	0.08	0.014	0.12	0.025	0.2	0.028	0.06	0.021	0.4	0.130	0.46	0.131	1
488	0.06	0.012	0.12	0.024	0.18	0.026	0.04	0.015	0.4	0.135	0.44	0.135	0.56
510	0.04	0.009	0.12	0.023	0.16	0.024	0.03	0.012	0.4	0.135	0.43	0.135	0.43
532	0.03	0.007	0.12	0.023	0.15	0.024	0.02	0.010	0.4	0.137	0.42	0.137	0.33
555	0.02	0.004	0.12	0.022	0.14	0.022	0.015	0.008	0.4	0.137	0.415	0.137	0.25
650	0.02	0.004	0.12	0.021	0.14	0.021	0.01	0.003	0.4	0.138	0.41	0.138	0.08
676	0.04	0.005	0.12	0.020	0.16	0.020	0.005	0.001	0.4	0.138	0.405	0.138	0.06
												$a^*_{CDOM}(\lambda)$ **Slope**	0.012
												$a^*_{CDOM}(\lambda)$ **Slope σ**	0.0033

4.4 The use of proxy variables as a measure of optically significant constituent (*OSC*) concentration

As the water sample analyses described in Section 4.2 can only be made at a finite number of depths for each station, assumptions have to be made about the profile of each *OSC* concentration. These assumptions can usually be justified by examining proxy variables for each *OSC* concentration. The proxy variables chosen are obtainable from instruments that can measure over an entire station profile.

CHL concentration can be represented to a first approximation by the fluorescence measured by the *ECO* fluorometer. This is subject to variation in *CHL* specific fluorescence yield particularly in the surface layer (Kromkamp et al., 2006; Kiefer et al., 1989; Lorenzen, 1966; Yensch & Menzel, 1963).

The optical backscattering coefficient at 676 nm ($b_b(676)$) measured by the *HS2* was chosen as a proxy for *MSS* concentration, since an increase in *MSS* concentration generally causes an increase in $b_b(\lambda)$ (Neil et al., 2011; Chen et al., 2010; Boss et al., 2009a; D'Sa et al., 2007; Lynch et al., 1994). Salinity was chosen as a proxy for *CDOM* (Geiger et al., 2011; Menon & Sangekar, 2010; Fang et al., 2009; Coble et al., 2004; Kowalczuk et al., 2003; Doerffer et al., 1999; Ferrari & Dowell, 1998; Vodacek et al., 1997). However the assumption of an inverse linear relationship between the two variables only holds if *CDOM* is a conserved quantity and there is a single freshwater source with unvarying concentration. These assumptions do not hold in the Scottish Sea Lochs (Chapter 7) or Liverpool Bay (Appendix A), which may cause problems when examining the results of the *IOP* inversion methodologies on field *ac-9* data.

4.5 Analysis Techniques and Data Processing of Temporal Optical Data subjected to Fouling (Liverpool Bay)

The data utilised for the temporal analysis in this thesis was collected from the Liverpool Bay Coastal Observatory (*COBS*). The optical data collected during the as part of the *COBS* deployments (July 2010 – November 2011) was badly fouled. Also due to the lack of instrument cleaning and calibration techniques to correct for the fouling could not be implemented. Therefore novel techniques of data processing and analysis were employed and are outlined in the following subsection.

4.5.1 The Liverpool Bay Coastal Observatory Deployments

The RV *Prince Madog* was used to service the moorings. This was completed every 4 - 6 weeks depending on the time of year. Spatial surveys were completed at the same time, which included *CTD* profiles and *SPM* analysis. For the optical instruments, there were periods where data were not collected due to instrument failure. The deployments dates and data recorded are shown in Table 4.3.

Table 4.3: The number of days of recorded and missing data from each *COBS* cruise.

***COBS* Cruise**	**Deployment Date**	**Number of Days**		
		Deployed	**Recorded**	**Missed**
71	7th July 2010	35	35	0
72	11th August 2010	48	48	0
73	28th September 2010	70	0	70
74	7th December 2010	35	35	0
75	12th January 2011	63	52	11
76	16th March 2011	34	34	0
77	18th April 2011	52	52	0
78	6th June 2011	48	48	0
79	25th July 2011	56	0	56
80	19th September 2011	50	0	50
	TOTAL	**491**	**304**	**187**

4.5.2 Data Quality Issues

The average length of deployment for the optical instruments in Liverpool Bay was six weeks (Table 4.3), and upon recovery the instruments were badly fouled. This affected the quality of the recovered data. Moreover since the *ac-s* was not

calibrated before and after deployment, readings at instrument switch-over cannot be relied upon as a starting point as these were not accurate measures of absorption or attenuation. Sadly, therefore, none of the *ac-s* data is usable for the intended purpose of measuring inherent optical properties (*IOPs*) to recover optically significant constituents (*OSCs*).

Figure 4.7 provides a closer look at the attenuation time series, and shows the issues caused by the lack of instrument maintenance outlined above. The large sections of missing data (already outlined in Table 4.3) are due to instrument failure or optical saturation, both caused by a lack of maintenance such as clogged pumps and fouling of the optics.

A clear baseline shift can be observed in the optical data, caused by a combination of instrument fouling and drift over the course of the deployment. During servicing the fouled *ac-s* is replaced with a cleaner instrument. This causes a "step-down" where the effects of fouling and drift are removed from the optical signal. Ordinarily these effects would be measured as part of the cleaning and calibration process described in Chapter 3 and the optical signal could be corrected accordingly.

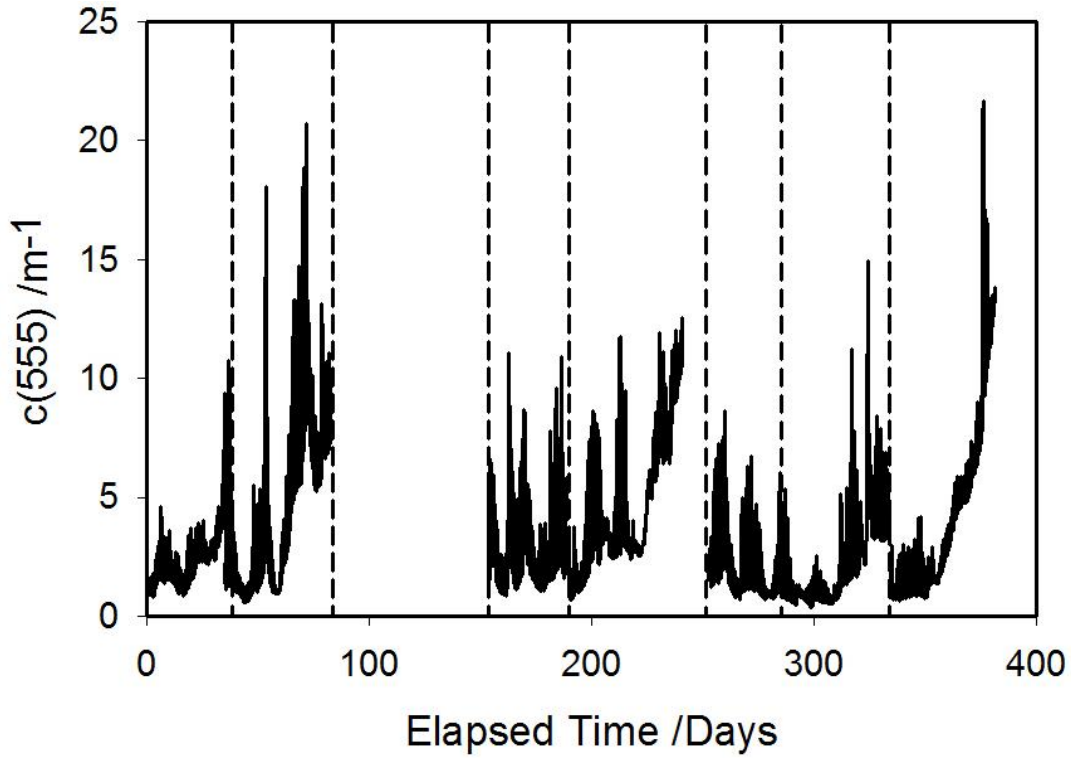

Figure 4.7: Time Series of $c_{ac\text{-}9}(555)$ to demonstrate the problem with the data collection. The dotted lines represent instrument switch over.

Despite these problems, analysis was still attempted for the optical data from Liverpool Bay and results are presented in this chapter. Before the data could be analysed however, certain features in the recovered data had to be considered, such as unphysical optical results and difficulties arising from the methodology used for instrument deployments.

4.5.3 Fouling Effects

Figure 4.8 shows that the absorption channel at 555nm has greater values than the attenuation channel at 555nm, which should not be observed as the attenuation is equal to the sum of absorption and scattering at each wavelength.

Due to the unphysical nature of these results, the scattering correction of the absorption tube of the *ac-s* using the method of Zaneveld et al. (1994) (outlined in Section 3.5.3) could not be applied and therefore absorption data from the *ac-s* could not be used. This meant that only the uncalibrated data from the *ac-9* attenuation

tube, which was subject to unknown amounts of fouling, was suitable for further analysis. These data were treated, therefore, as a semi-quantitative measure of turbidity rather than an inherent optical property.

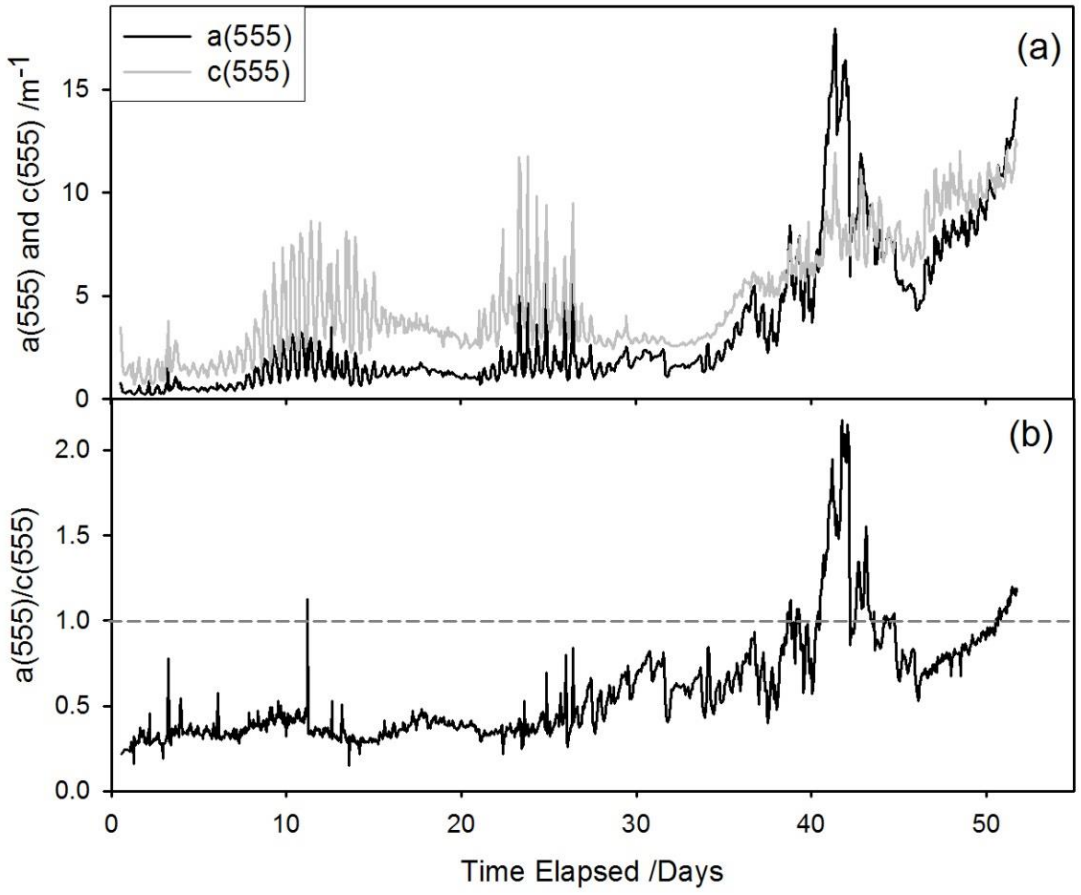

Figure 4.8: Optical results from *ac-s* during the *COBS* cruise 75 (12th January 2011 – 16th March 2011) showing (a) the absorption and attenuation tube output at 555nm with the absorption greater than attenuation and (b) the ratio of $a_{ac\text{-}9}(555)$ / $c_{ac\text{-}9}(555)$ to better observe the unphysical result towards the end of the deployment.

4.5.4 Wavelength Selection

The attenuation at 555nm was selected for further analysis. This wavelength was initially chosen to minimise the effects of chlorophyll-a on the data set (see below). However as Figure 4.9 demonstrates, all the attenuation channels were linearly correlated ($R^2 > 0.990$) and therefore the choice of wavelength was not important.

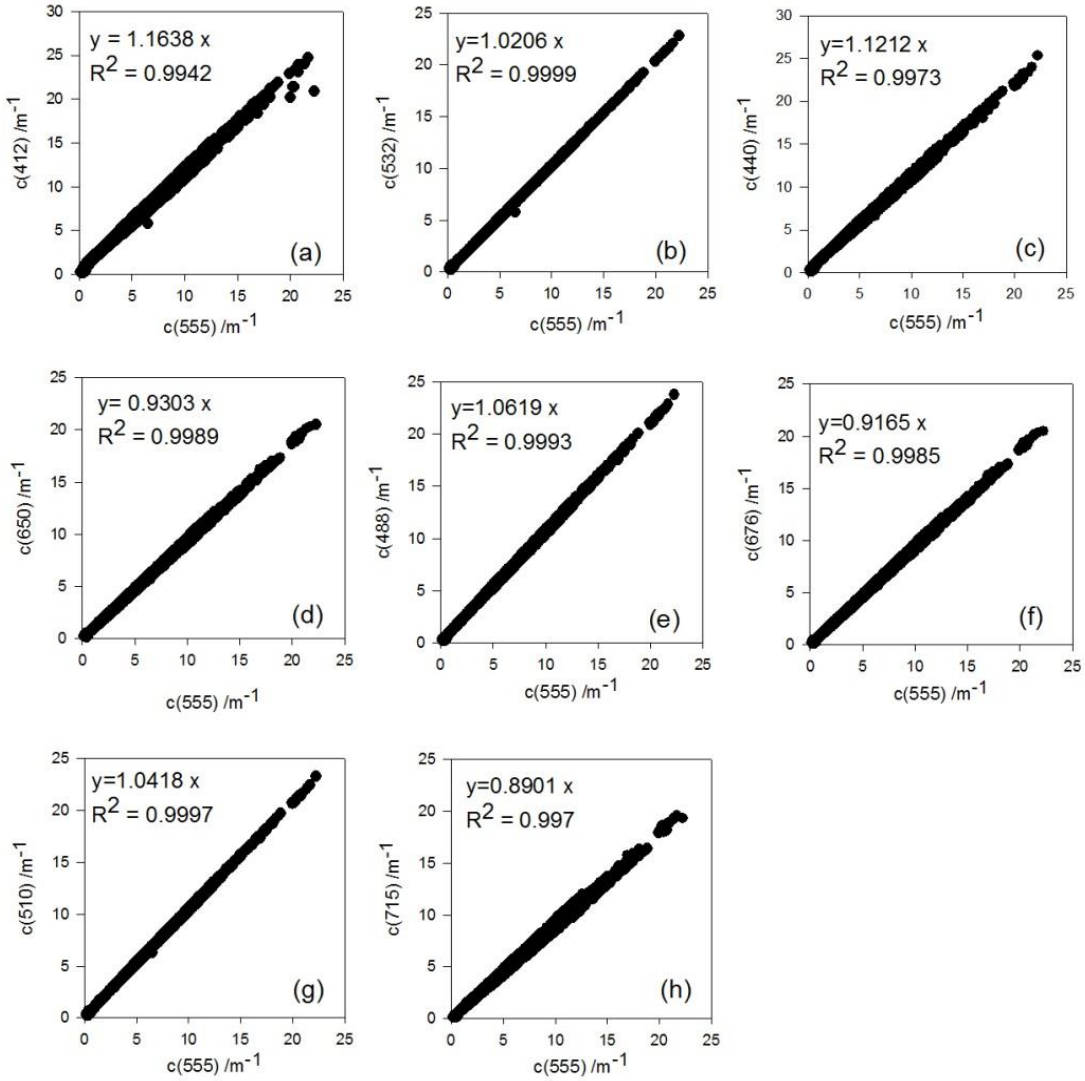

Figure 4.9: Regression of $c_{ac\text{-}9}(555)$ with other *ac-9* wavebands (a) $c_{ac\text{-}9}(412)$, (b) $c_{ac\text{-}9}(440)$, (c) $c_{ac\text{-}9}(488)$, (d) $c_{ac\text{-}9}(510)$, (e) $c_{ac\text{-}9}(532)$, (f) $c_{ac\text{-}9}(650)$, (g) $c_{ac\text{-}9}(676)$ and (h) $c_{ac\text{-}9}(715)$.

a Effect of Chlorophyll-a on the 555 nm Attenuation Channel

In order to estimate the effect of chlorophyll-a (*CHL*) on the 555 nm attenuation channel, the data from the fluorometer were utilised. An estimation of the *CHL* concentration was established using the manufacturer's calibration information (details of the calibration procedure can be found in the device manual (WET Labs, 2011) and in Section 3.4.2) and this concentration was multiplied by the specific attenuation coefficient for chlorophyll (Table 4.2; Neil et al. (2011)) to estimate $c_{CHL}(\lambda)$. The percentage of $c_{ac\text{-}9}(555)$ attributable to $c_{CHL}(555)$ was calculated for the whole time series and the results are shown in Figure 4.10.

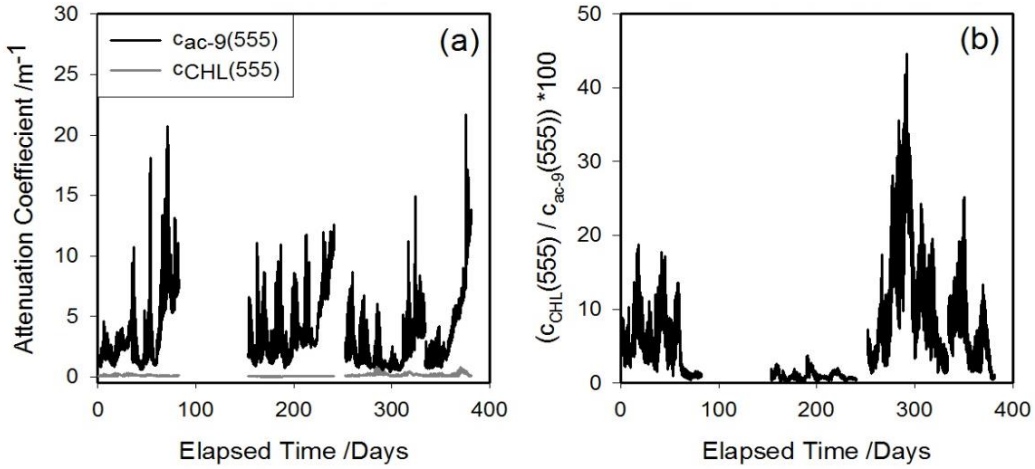

Figure 4.10: Estimated contribution of *CHL* to the attenuation signal of the *ac-s* with (a) showing the time series for both $c_{ac\text{-}9}(555)$ and $c_{CHL}(555)$ on the same plot & (b) showing the percentage contribution of $c_{CHL}(555)$ to $c_{ac\text{-}9}(555)$.

Figure 4.10 shows there is very little contribution by *CHL* to $c_{ac\text{-}9}(555) \approx 10$ - 20%. Sometimes a period of high chlorophyll concentration, such as the spring bloom increased the contribution of chlorophyll to $c_{ac\text{-}9}(555)$ to almost 50%, however when the time series as a whole was considered, the two variables were weakly correlated.

4.5.5 Data Processing

a Processing Introduction

Given the issues described above, standard processing techniques could not be applied to the *COBS* optical data. Therefore custom MATLAB scripts were written to analyse the time series. The processing procedure is shown in Figure 4.11. All of the raw data were pre-processed by the manufacturer's software before the analysis in MATLAB was completed. In Figure 4.11, the solid circles represent the pre-processed raw data from the instruments, the solid rectangles represent a MATLAB function written to process the data for analysis, the dashed circles represent the data output by the program as an Excel spread sheet and the dashed rectangles represent the novel analysis techniques described in above.

Each MATLAB function was written to take into consideration the unique problems of the Liverpool Bay optical data, and attempts to extract information from data that would ordinarily be discarded. The processing steps (solid rectangles) shown in Figure 4.11 are described fully in the remainder of this section.

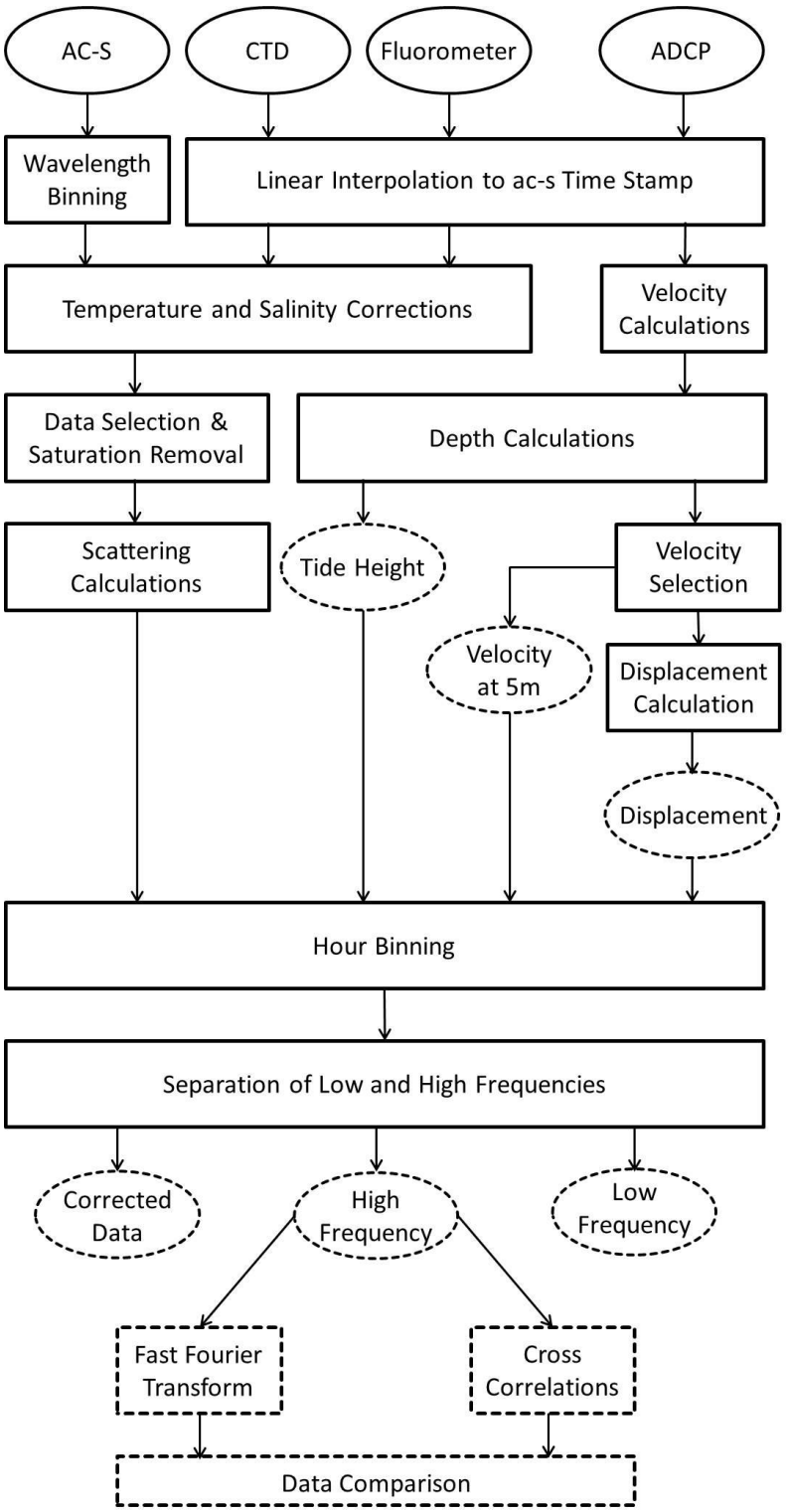

Figure 4.11: Processing steps for data from site A. Solid circles represent raw data processed by their respective software (Section 4.1), solid rectangles are custom MATLAB functions written to process the data for analysis, dashed circles represent outputs by MATLAB and dashed rectangles represent analysis techniques specific to this thesis.

b Data Input

ac-s data were read into MATLAB using a function written for the purpose. The function opened all of the *WAP* processed files for the cruise that was to be analysed. The *MergeACS.m* function required the number of introductory lines at the start of each file to be specified (this was different for each instrument as it was based on the number of wavelengths). As the time scale for the *ac-s* was in milliseconds the files were merged on the time stamp for each file (each file starts at zero). The *ac-s* was setup to sample for 10 seconds every 20 minutes. The MATLAB function located the last 20 minute gap in the previous file and first 20 minute gap in the next file to determine the time step between the files and then assigned either 250 ms or 20 minutes ($1.2x10^6$ ms) to the start of the next file. This process was repeated for all *ac-s* files for each cruise and a matrix of *ac-s* data was created.

The *CTD* and *ECO* Fluorometer data had to be recovered from the post-processed files provided by NOC:Liverpool before being read into MATLAB. All of the header information at the start of the files was removed to enable MATLAB to process the data. The files were read in using the *fopen* function that requires specification of the number of columns and the data type contained in that column. The time stamp from both the *CTD* and *WAP* (Section 3.5.1) software was output as a Julian date and in order to be matched up with the *ac-s* a conversion from Julian date to time (in milliseconds) from the *ac-s* switch on had to be completed. A linear interpolation was then completed to align the instrument time stamps.

The *ADCP* data files were read into MATLAB using the *dlmread* function. As the date within the *ADCP* files were formatted as separate columns, the ACDP time stamp merged the columns into a date vector which could then be manipulated to a serial date number. From this point the method was the same as with the *CTD*.

c Linear Interpolation

Linear Interpolation with respect to time was applied to the *CTD*, fluorometer and *ADCP* data using a standard MATLAB function (*interp1*). To linearly interpolate the temperature (from *CTD* data), for example;

$$y = y_0 + (x - x_0)\frac{y_1 - y_0}{x_1 - x_0} \tag{4.22}$$

In this case *y* was the temperature value at the *ac-s* time stamp (a required value), y_0 and y_1 are the temperature measurements made on either side of the *ac-s* time to be evaluated, *x* is the *ac-s* time value and x_0 and x_1 were the times that the two temperature measurements were made. The linear interpolation was repeated for all *ac-s* time values.

d Wavelength Binning

The *ac-s* measured absorption and attenuation at up to 90 wavelengths between 400 and 800 nm. This is a large amount of data to be processed, but for the intended application the nine wavelengths covered by a multichannel *ac-9* were sufficient. It can be seen from Figure 4.12 that reducing the number of wavelengths does not significantly affect the spectral result (Section 3.1.1).

Reducing the *ac-s* data to *ac-9* compatible wavelengths was accomplished by averaging the values of the *ac-s* channels that were within the band width (± 10 nm/channel) of each *ac-9* channel. The number of channels as well as the wavelength of each channel differed slightly between individual *ac-s* instruments and therefore the channels used were selected manually by examination of the raw data files. A MATLAB program written for the purpose was then used to select only the preselected channels for each *ac-9* wavelength and the mean taken.

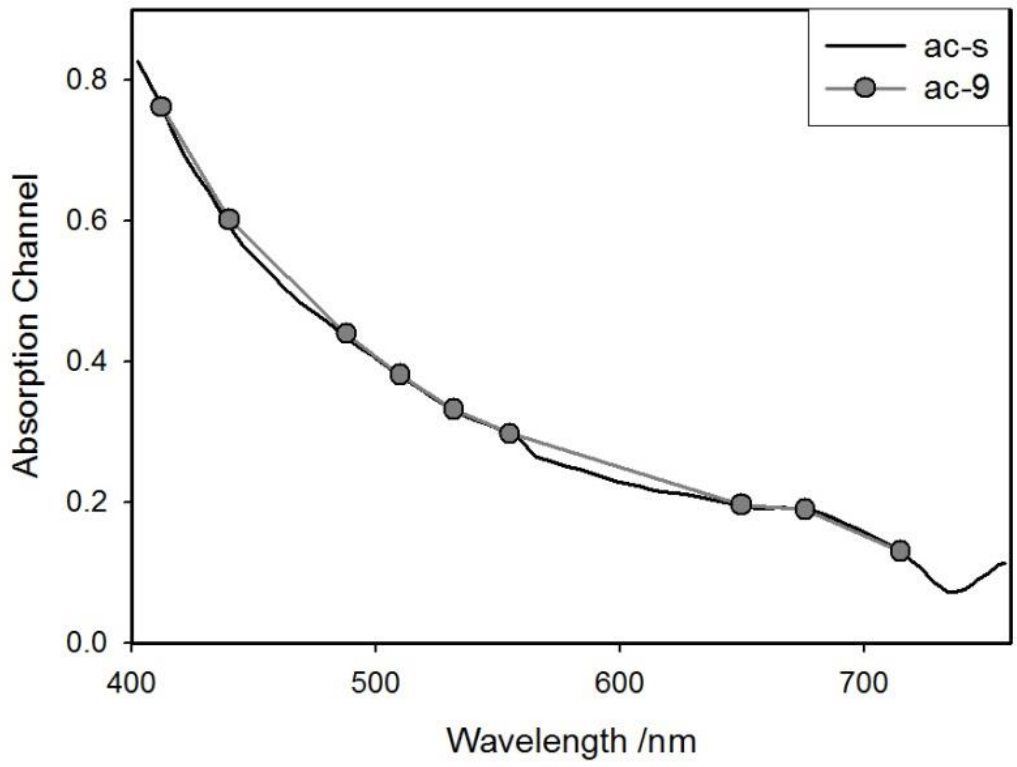

Figure 4.12: Spectrum from *ac-s* before and after wavelength binning.

e Temperature and Salinity Corrections

Temperature and salinity corrections were applied to the *ac-s* data using the method described in Section 3.5.2. The values of the coefficients were taken from Sullivan et al. (2006). The coefficients were selected and averaged using the same selection criteria described for the wavelength binning.

f Data Selection and Saturation Removal

Data selection was required as the *ac-s* was switched on and off on the deck as opposed to under the water. These measurements in air must be removed in order to use the full time series. An example of this is shown in Figure 4.13.

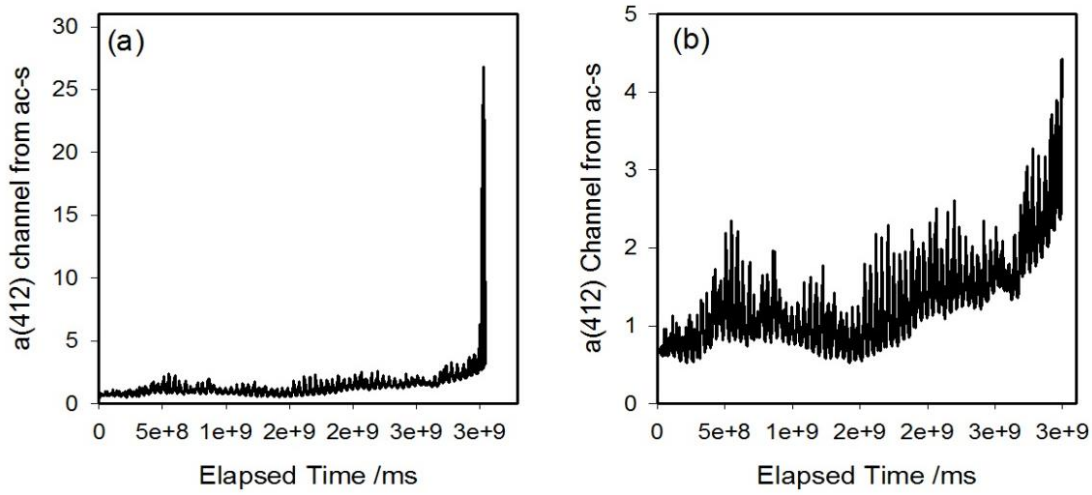

Figure 4.13: (a) Before and (b) after data selection is applied. The large spike at the end of the data is removed as these data were recorded on the deck of the ship.

Sometimes the *ac-s* signals became saturated; this was usually due to fouling or the occurrence of optically dense material in the light path. In the case shown in Figure 4.14 the cause of the intermittent saturation was cleared by the flow in the instrument tubes.

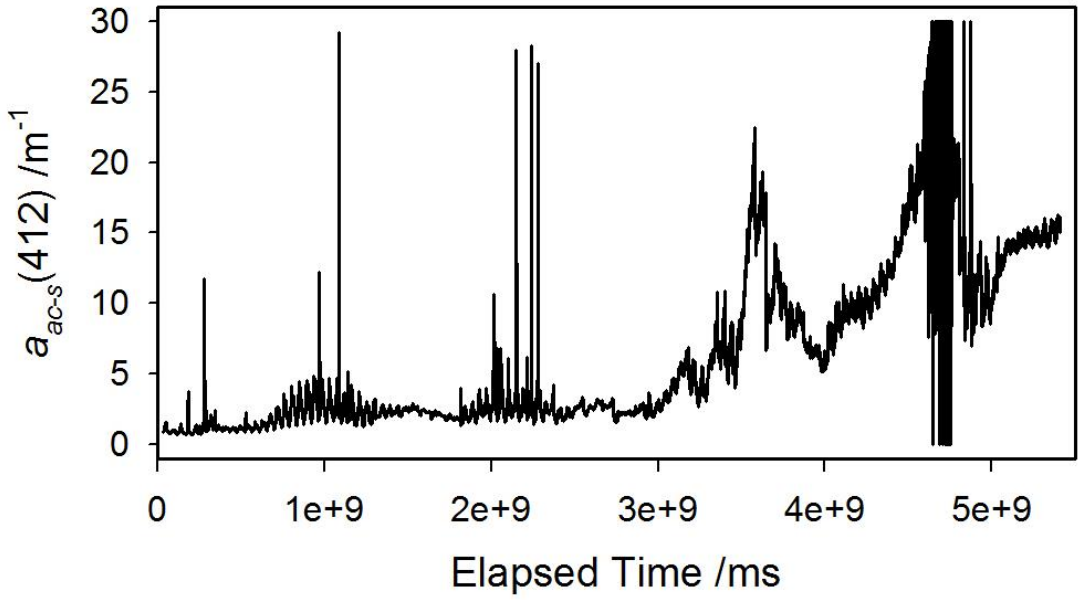

Figure 4.14: Time series demonstrating instrument saturation.

g Hourly Binning

The data were then averaged into one hour bins. In order to utilise this method for the time series data, the upper and lower limits were defined as the maximum and minimum values for the time series. The number of bins was defined as one more than the number of hours for which the instrument was deployed (rounded to the nearest whole hour). The MATLAB function *histc* was used to determine which bin each value was located in. This location information was then used to create a new matrix for each bin, the columns of which were time and the *ac-s* data, each of which were averaged. The average values were then combined to create a new matrix of only the average values.

h Velocity Calculations

The raw *ADCP* data provided the north, east and vertical components of the current velocity at 1 m depth intervals for the water column. The horizontal component vectors were used to calculate the magnitude and direction of the velocity in two dimensions. This was completed using the *cart2pol* function in MATLAB, which outputs a direction and magnitude in radians which was then converted to degrees. If the vertical component was included the current velocity could be expanded to 3 dimensions to complete analysis of local re-suspension. This was not done in this work and but could be considered in future studies.

i Tide Height

The ancillary measurements made by the *ADCP* include the heading, pitch, roll, temperature and pressure of the instrument. The pressure can be used to calculate depth using the Equations (4.23) - (4.25) (Seabird, 2008);

$$depth = \frac{-1.82 \times 10^{-15}p^4 + 2.279 \times 10^{-10}p^3 - 2.2512 \times 10^{-5}p^2 + 9.72659p}{g} \quad (4.23)$$

$$g = 9.780318\left(1 + (5.2788 \times 10^{-3} + 2.36 \times 10^{-5}x^2)\right) + 1.092 \times 10^{-6}p \quad (4.24)$$

$$x = \sin^2\left(\frac{53.79389}{57.29578}\right) \quad (4.25)$$

In Equations (4.23) - (4.25), p is the pressure in decibars, g is the local acceleration due to gravity, x is the position (the value 53.79389 is the latitude of Site A in decimal form). The tide height varies as shown in Figure 4.15. There are 2 main features in the tide height, the semi-diurnal tidal wave and the amplitude modulation caused by the spring-neap cycle.

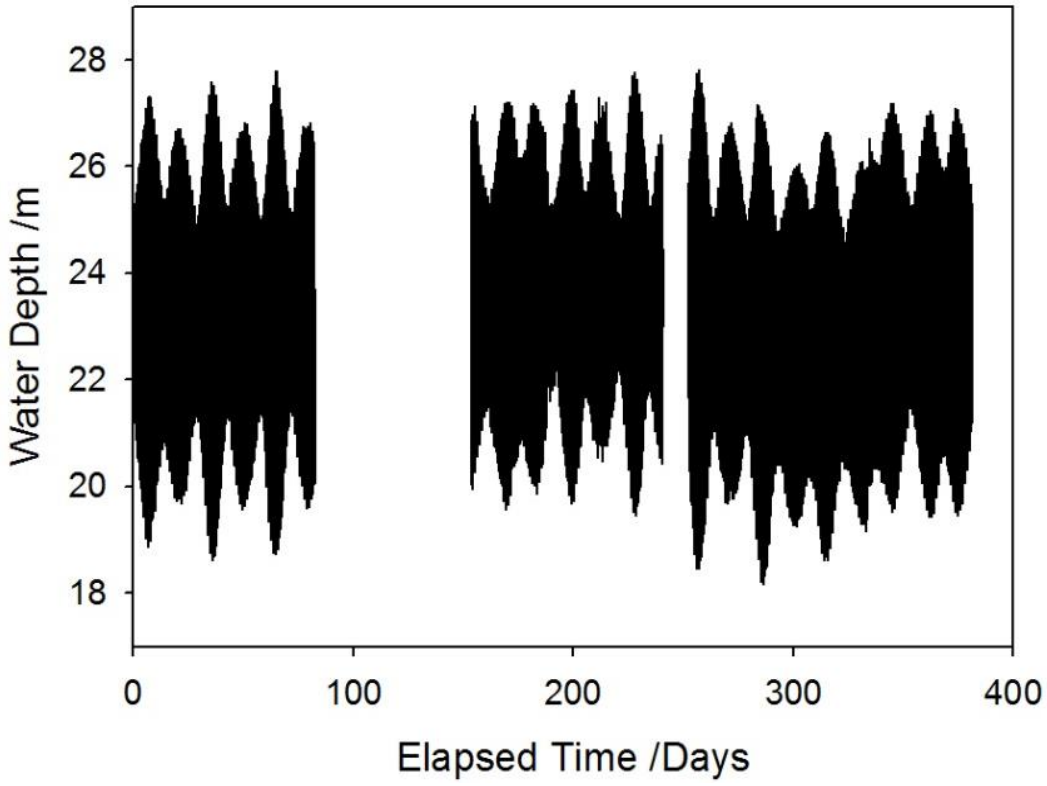

Figure 4.15: Water Depth measured by *ADCP*

j Current Velocity at ac-s Depth

The current velocity was measured by the *ADCP* which was anchored to the sea bed, whereas the *ac-s* was fixed to a buoy and held 5m below the surface. This meant that the *ac-s* position in the water column changed relative to the *ADCP* with the tide. A schematic is shown in Figure 4.16.

In order to calculate the current velocity at the *ac-s* depth correctly the calculated tide height was used with the current velocity at each depth to select the current velocity at 5 m below the surface. The result was a North-West South-East direction of flow as shown in Figure 4.17. This is equivalent to an onshore/offshore tidal current in the Liverpool Bay area.

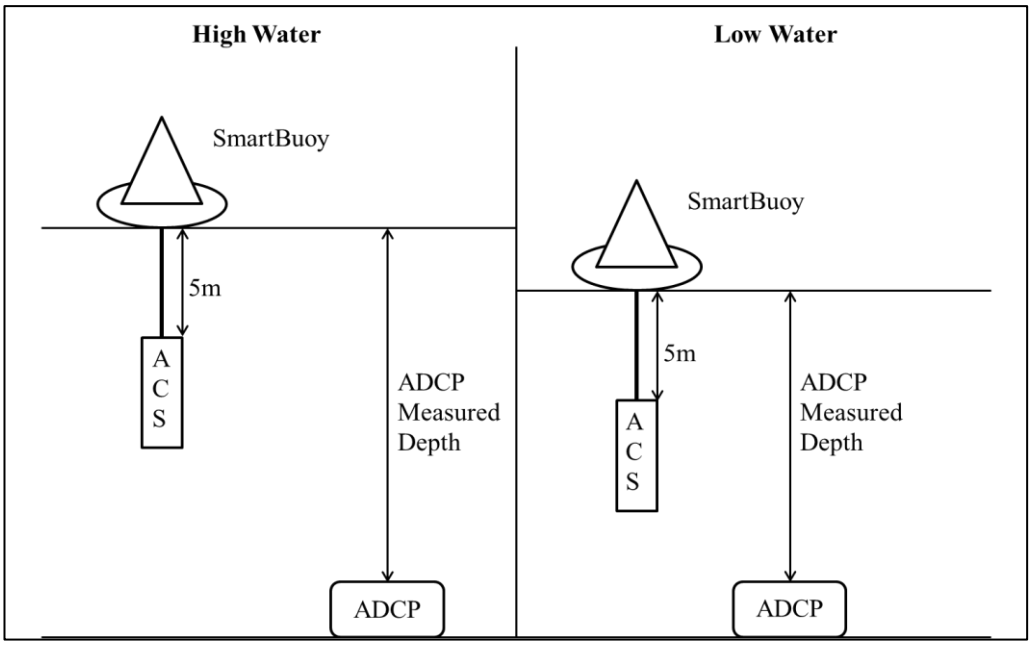

Figure 4.16: Schematic of the instrumentation setup at site A. The *ac-s* is deployed from a mooring 5 m below the surface whereas the *ADCP* is permanently on the sea bed.

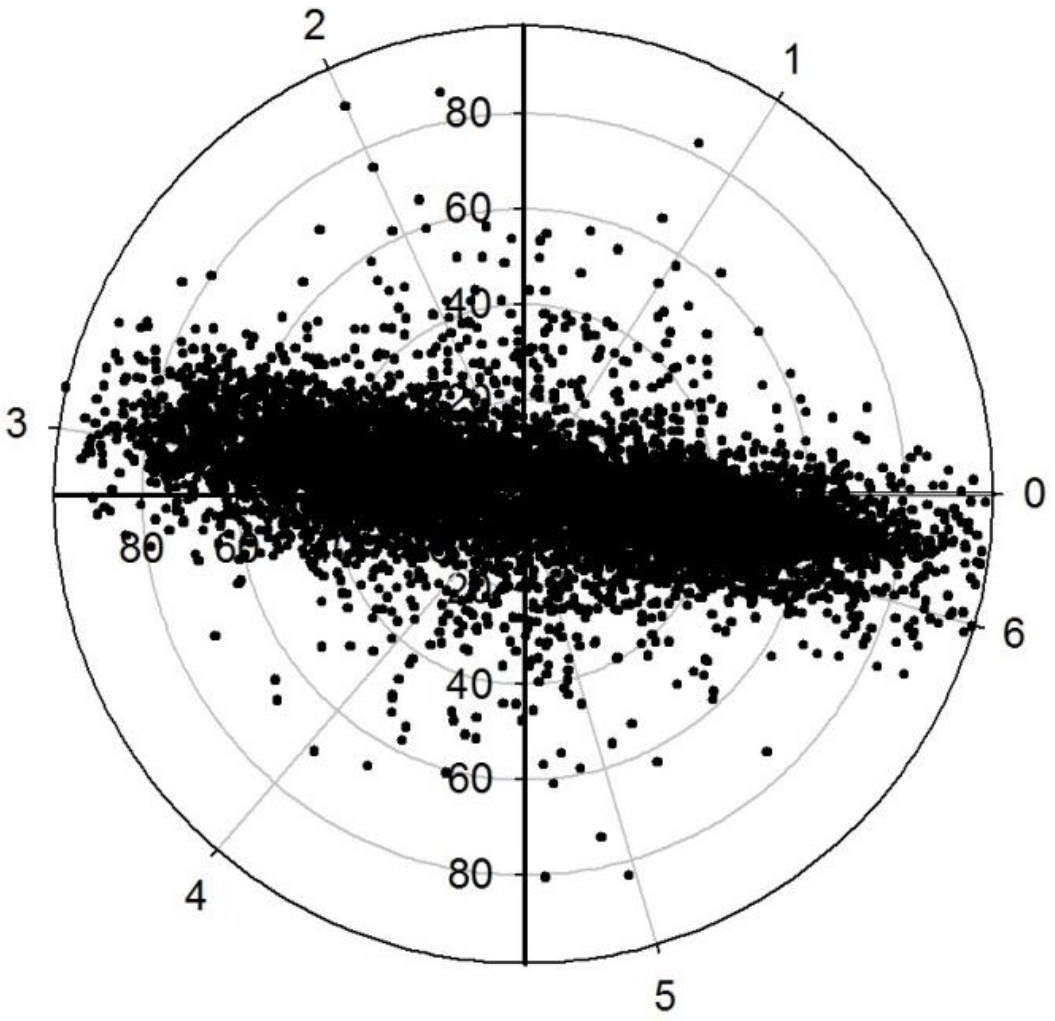

Figure 4.17: Polar plot showing the magnitude and direction of the current velocity 5 m below the surface at the mooring site. The numbers around the circumference show the direction of current velocity in radians and the numbers through the centre indicate the magnitude measured in cm s^{-1}.

k Displacement Calculation

The displacement of a particle along the main tidal directional axis was calculated by first realigning the orientation of the axis to the main tidal direction and adjusting the velocity directions to align along the new axis. This was done by subtracting the tangent of the gradient of the best fit line in the polar plot from each velocity.

The relative velocity was then calculated using Equations (4.26) - (4.28).

$$\theta_{new} = \theta - \tan^{-1}(m) \tag{4.26}$$

$$v_{rel} = v_{mag} \cos \theta_{new} \tag{4.27}$$

$$d_{rel} = \sum v_{rel} \times \Delta t \tag{4.28}$$

where θ_{new} is the relative direction of the current velocity, θ is the original direction of the current velocity, m is the gradient of the best fit line, v_{rel} is the relative current velocity, v_{mag} is the magnitude of the current velocity, d_{rel} is the relative displacement and Δt is the time increment between measurements, in this case Δt is always equal to 1 hour.

l Data Output

All data and analysis results from the above analysis were output from MATLAB as separate Microsoft Excel spread sheets for archiving. Data were grouped by the level of processing which had been applied, for example; original, low frequency and high frequency data (Section 8.1), Fourier transform and cross correlation results. Certain data (such as the original, high and low frequency data of the attenuation channel at 555 nm ($c_{ac\text{-}9}(555)$), temperature, salinity, tide height, current velocity at the *ac-s* depth and displacement) which were more useful for comparison and analysis of the region were copied into an additional spreadsheet for further analysis. As an additional step, the comparison data were normalised to a maximum value equal to 1 so that comparisons across each time series could be completed directly.

4.6 Chapter Summary

1. The main instruments used throughout this thesis are the *ac-9*, or the *ac-s* with spectral binning to produce *ac-9* compatible wavebands. However interpretation of these data required ancillary measurements. An *ADCP* was deployed to measured current velocity at a mooring site by using the Doppler effect to measure the velocity of scatterers in the water. A *CTD* measured

temperature salinity and depth to provide physical information about the area of interest and also to correct the *ac-s/9* for temperature and salinity variations. The *ECO* Fluorometer provided fluorescence measurements which can be approximately converted into chlorophyll concentration. The *HS2* measured backscattering at 470 and 676 nm and chlorophyll-a fluorescence at 676 nm.

2. Laboratory sample analysis is also important as the concentration of *OSCs* must be known to validate *IOP* inversion methodologies and to calculate the *SIOPs* for a given area. Care must be taken when measuring the absorption spectra of phytoplankton and mineral suspended solids that an appropriate β factor correction has been applied.

3. The value adopted for the β factor may be dependent on several factors including particle type, wavelength and the individual filter pad. Since no definitive method for correction of path length amplification has been proposed, a value of $\beta = 1.73$ has been used, derived from the comparison of filter pad and *ac-9* measurements by Neil et al. (2011).

4. *SIOP* values were calculated using the linear regression techniques and end member analysis in the case of specific scattering. Initial values for the *SIOPs* were taken from Neil et al. (2011).

5. The *COBS* temporal data was of poor quality due to fouling over the long deployment periods. Novel data processing techniques were developed to overcome the issues caused by the poor deployment methodology.

Chapter 5 Generation of a Modelled Data Set

In order to test the validity of any proposed inversion technique, a modelled data set was required. This allowed inversion methods to be tested with data whose origins were known, and any uncertainties in the data set were also fully understood and controllable. This chapter outlines how the modelled data set was generated and how uncertainties were added.

5.1 Specifying ranges for optically significant constituent (*OSC*) concentrations

Concentrations of optically significant constituents (*OSCs*) were generated by selecting random values from a specified range. The range for each constituent was chosen to represent typical values for the Irish Sea and adjacent waters and is shown in Table 5.1.

Table 5.1: Ranges of *OSC* Concentrations, representing typical values for the Irish Sea, used to generate the modelled data set.

Constituent	Minimum Concentration	Maximum Concentration
CDOM (m^{-1})	0.01	1.3
CHL (mg m^{-3})	0.1	10
MSS (g m^{-3})	0.3	30

A total of 10,000 combinations of concentrations were created to generate a cuboid of possible concentration values which was equally sampled throughout. No weighting was applied to select combinations of constituents which were representative of particular water types.

5.2 Generating a synthetic data set of inherent optical properties (*IOPs*)

As discussed in Chapter 2, the total inherent optical properties (*IOPs*) of seawater can be obtained by adding the *IOP* contributions of each of the constituents present in the water (Equations (5.1) – (5.3)).

$$a_t(\lambda) = a_w(\lambda) + a_{CDOM}(\lambda) + a_{CHL}(\lambda) + a_{MSS}(\lambda) \tag{5.1}$$

$$b_t(\lambda) = b_w(\lambda) + b_{CDOM}(\lambda) + b_{CHL}(\lambda) + b_{MSS}(\lambda) \tag{5.2}$$

$$c_t(\lambda) = a_t(\lambda) + b_t(\lambda) \tag{5.3}$$

where the subscripts *t*, *w*, *CDOM*, *CHL*, *MSS* indicate total, water, coloured dissolved organic matter, chlorophyll and mineral suspended sediment, *a*, *b*, *c* are the absorption, scattering and attenuation coefficients and λ denotes the wavelength. It should be noted that as the modelled data set represents *ac-9* data, the water component was not included.

The *IOP* contributions for individual constituents can be described as the product of an *OSC* concentration and the relevant *SIOP*. This assumption was discussed in Chapter 2 and it is unclear whether the linearity between the *IOPs* and concentrations is always valid. However, as the purpose of the modelled data set is to test *IOP* inversion methodologies and not to predict *IOP* values from the *OSC* concentrations, the simpler assumption is all that is required. Thus:

$$a_i(\lambda) = a_i^*(\lambda) \cdot X_i \tag{5.4}$$

$$b_i(\lambda) = b_i^*(\lambda) \cdot X_i \tag{5.5}$$

$$a_t(\lambda) = \sum_i [a_i^*(\lambda) \cdot X_i] \tag{5.6}$$

$$b_t(\lambda) = \sum_i [b_i^*(\lambda) \cdot X_i] \tag{5.7}$$

where *i* designates a given *OSC*, the superscript * denotes the relevant *SIOP* and *X* is the *OSC* concentration.

If *SIOP* values are known, the total *IOPs* for each of the combinations of *OSC* concentrations can be calculated using Equations (5.6) and (5.7).

5.3 Modelling measurement uncertainties by adding random noise to the modelled *IOP* data.

Sources of uncertainty in *IOPs* measured using the *ac-9* are outlined in Chapter 3. If the inversion of *IOP* measurements to recover constituent concentrations is to be useful in practice, then it should maintain an acceptable degree of accuracy in the presence of realistically estimated measurement errors. To simulate such errors, random noise was added to the modelled data set in the form of Gaussian distributions, with means equal to the original unperturbed value and standard deviations expressed as fraction of the mean. Perturbed values were calculated using Equation (5.8).

$$IOP_{noise} = IOP + (IOP \cdot \sigma \cdot randn(1)) \tag{5.8}$$

where IOP_{noise} is the perturbed value, *IOP* is the original value, σ is the standard deviation as a fraction of the mean and *randn(1)* represents the output of the MATLAB random number generator function, which selects a random number from a normal distribution with a mean value of zero and a standard deviation of one. Random noise was added to each *IOP* independently.

Table 5.2: Expected and actual mean and standard deviation of $a_{ac\text{-}9}(412)$ with various levels of added random noise.

% σ Added	Expected Mean /m^{-1}	Actual Mean /m^{-1}	Expected σ /m^{-1}	Actual σ /m^{-1}
1	2.6	2.600	0.026	0.0258
5	2.6	2.599	0.13	0.131
10	2.6	2.597	0.26	0.259

This procedure is illustrated for a typical value of $a_{ac\text{-}9}(412)$ = 2.6 m^{-1} (calculated from Equations (5.6) and (5.7) using concentration values of X_{CDOM} = 0.5 m^{-1}, X_{CHL} = 5 mg m^{-3} and X_{MSS} = 20 g m^{-3} and the *SIOP* values from Table 4.2. A histogram of the output was created for 10,000 iterations with input noise standard deviations of 1%, 5% and 10%. The expected and observed standard deviations of the results for each noise level are shown in Table 5.2 and the resulting distributions are plotted in Figure 5.1.

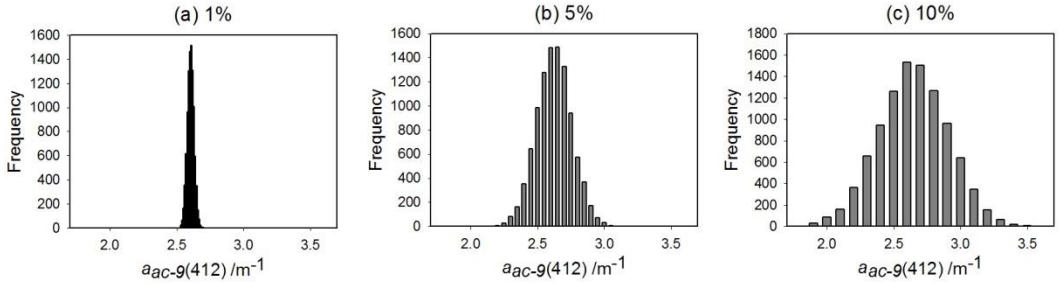

Figure 5.1: Histograms of $a_{ac\text{-}9}(412)$ with added random noise of (a) 1% (b) 5% and (c) 10% of the $a_{ac\text{-}9}(412)$ value added as a standard deviation.

5.4 Modelling Uncertainties in the values of specific inherent optical properties (*SIOPs*).

The *SIOP* values in Table 4.2 were obtained by calculating ratios of *IOPs* and constituent concentrations, and are therefore subject to errors in the measurements of both these quantities. Moreover, the actual values of the *SIOPs* for individual constituents in sea water may exhibit significant seasonal and spatial variability. It is therefore necessary to allow for some form of *SIOP* uncertainty in the data inversion process. Most single-pass inversion procedures involve the selection of a specific set of *SIOP* values which can be systematically incorrect either because of errors in their determination or because they are being used to invert *IOP* data for which they are not applicable. To best understand how uncertainties in the *SIOPs* should be added to the modelled data set, an examination of experimentally measured *SIOPs* for stations in the Irish Sea (Figure 5.2) was carried out.

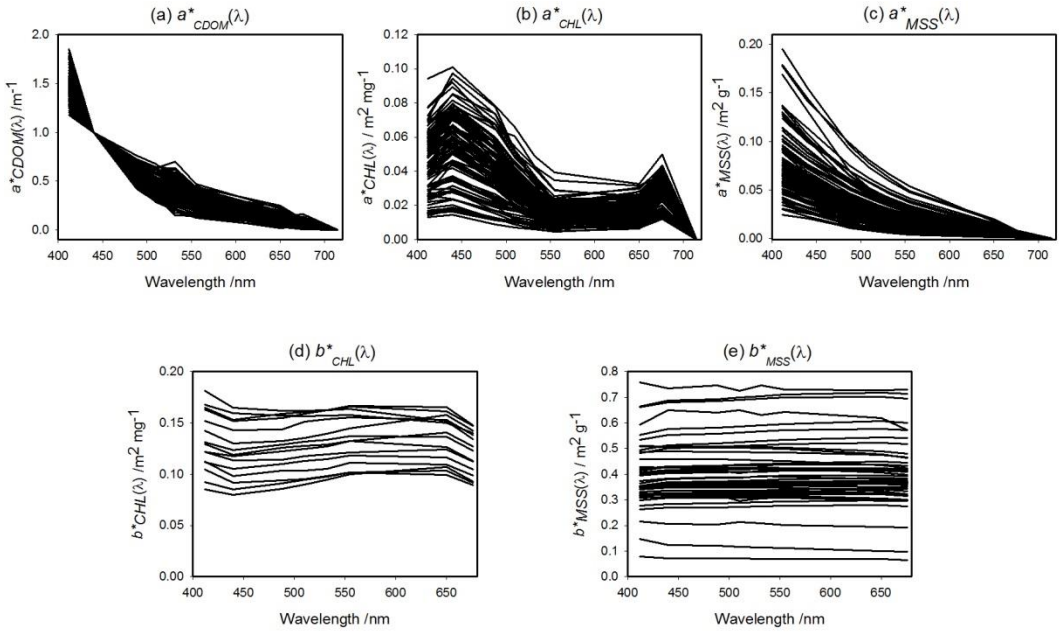

Figure 5.2: Spectral shape of *SIOPs* for (a) $a^*_{CDOM}(\lambda)$, (b) $a^*_{CHL}(\lambda)$, (c) $a^*_{MSS}(\lambda)$, (d) $b^*_{CHL}(\lambda)$ and (e) $b^*_{MSS}(\lambda)$, to demonstrate the observed variability in *SIOP* spectra. Modelled *SIOP* uncertainties attempted to recreate this variability.

5.4.1 Uncertainties in $a^*_{CDOM}(\lambda)$

The spectral slope is the main source of variation in $a^*_{CDOM}(\lambda)$ values. Plot (a) in Figure 5.3 shows the variation in $a^*_{CDOM}(\lambda)$ slope between 400 nm and 550 nm, (the values of $a^*_{CDOM}(\lambda)$ at longer wavelengths are low and therefore difficult to measure). The slope of $a^*_{CDOM}(\lambda)$ was calculated over this wavelength range (Pegau et al., 2002) and $a^*_{CDOM}(\lambda)$ values at red wavelengths were obtained by extrapolation. Figure 5.3 Plot (a) shows the variation in $a^*_{CDOM}(\lambda)$ slopes and Figure 5.3 Plot (b) shows the distribution of slope values. Uncertainties in $a^*_{CDOM}(\lambda)$ were modelled by applying an offset to the $a^*_{CDOM}(\lambda)$ slope, so that

$$S = \tilde{S} + \sigma(\tilde{S}) \times randn(1) \tag{5.9}$$

$$a^*_{CDOM} = \exp\left(-S(\lambda - \lambda_r)\right) \tag{5.10}$$

where S is the altered specific *CDOM* absorption coefficient slope, $\tilde{S}$ is the original specific *CDOM* absorption coefficient slope, $\sigma(\tilde{S})$ is the standard deviation in the original specific *CDOM* absorption coefficient slope (Table 4.2), *randn*(*1*) is the

MATLAB random number generator, $a^*_{CDOM}(\lambda)$ is the altered specific *CDOM* absorption coefficient, λ is the wavelength being examined and λ_r is the reference wavelength (440 nm).

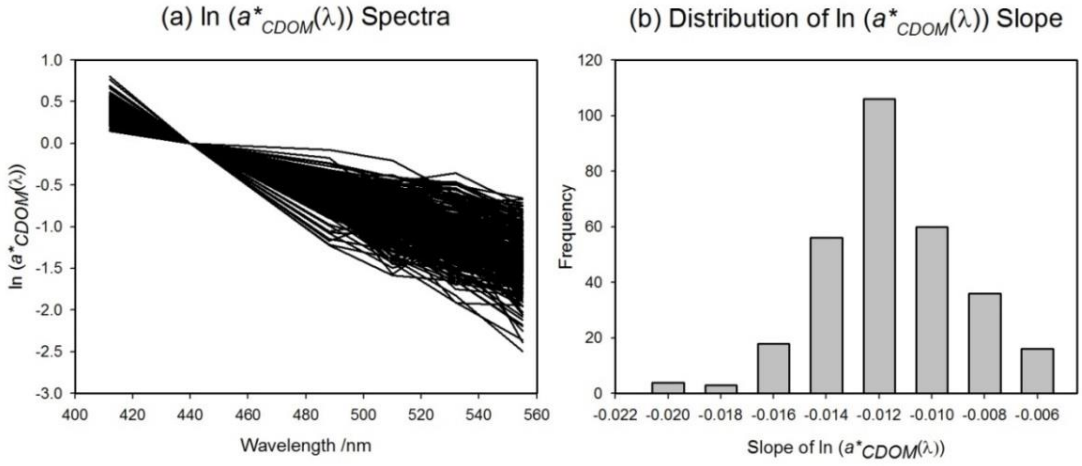

Figure 5.3: (a) Variability in the natural logarithm of $a^*_{CDOM}(\lambda)$ and (b) Histogram of the slopes of the natural logarithm of $a^*_{CDOM}(\lambda)$. By convention $a^*_{CDOM}(440) = 1$ m^{-1}. Data displayed for 300 stations (Neil et al., 2011). The standard deviation of the slopes is 0.003 m^{-1}.

Figure 5.4 shows the natural logarithm of $a^*_{CDOM}(\lambda)$, taken from Neil et al. (2011) with dotted lines indicating the results of changing the slope values by $\pm \sigma(\tilde{S})$.

Comparing Figure 5.3 and Figure 5.4 confirmed that the method of modelling $a^*_{CDOM}(\lambda)$ values using Equations (5.9) – (5.12) is a good representation of the original $a^*_{CDOM}(\lambda)$ spectrum from Neil et al. (2011).

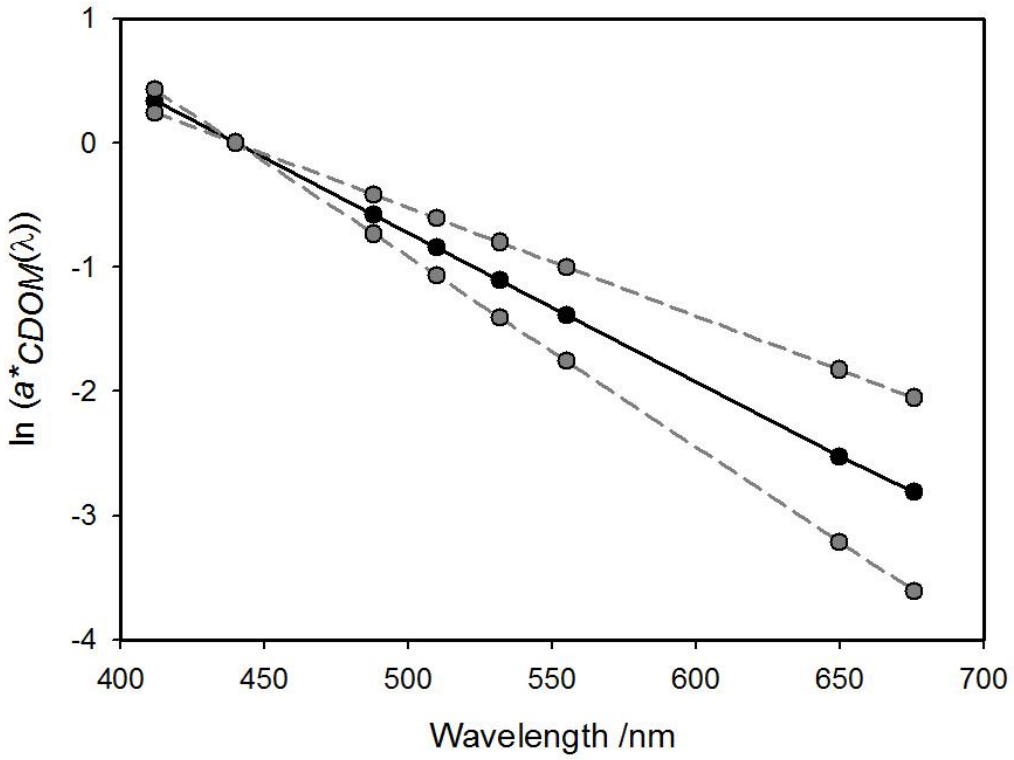

Figure 5.4: Mean modelled spectrum, (Neil et al., 2011), shown as the solid line and the standard deviation of the modelled uncertainties in the *SIOPs* shown as dotted lines.

5.4.2 Uncertainties in $a^*_{CHL}(\lambda)$

There were two possible methods that could have been employed to model the uncertainties in $a^*_{CHL}(\lambda)$. The first was the application of an offset to move the entire $a^*_{CHL}(\lambda)$ spectrum up or down by a constant value. The second method was the application of a multiplier whereby the magnitude of the $a^*_{CHL}(\lambda)$ was altered. The decision as to which method was used was made by plotting the $a^*_{CHL}(676)$ against $a^*_{CHL}(412)$ for a selection of measured $a^*_{CHL}(\lambda)$ spectra (Figure 5.6). If the $a^*_{CHL}(\lambda)$ spectra were best represented by an offset, the plot of $a^*_{CHL}(412)$ against $a^*_{CHL}(676)$ (Figure 5.5, Plot (a)) would show a best fit line with a gradient approximately equal to 1 and a significant intercept. In the case of the variation of $a^*_{CHL}(\lambda)$ spectra being best represented by a multiplier the plot of $a^*_{CHL}(412)$ against $a^*_{CHL}(676)$ (Figure 5.5, Plot (b)) would show a best fit line with a gradient that was not approximately 1 and no significant intercept.

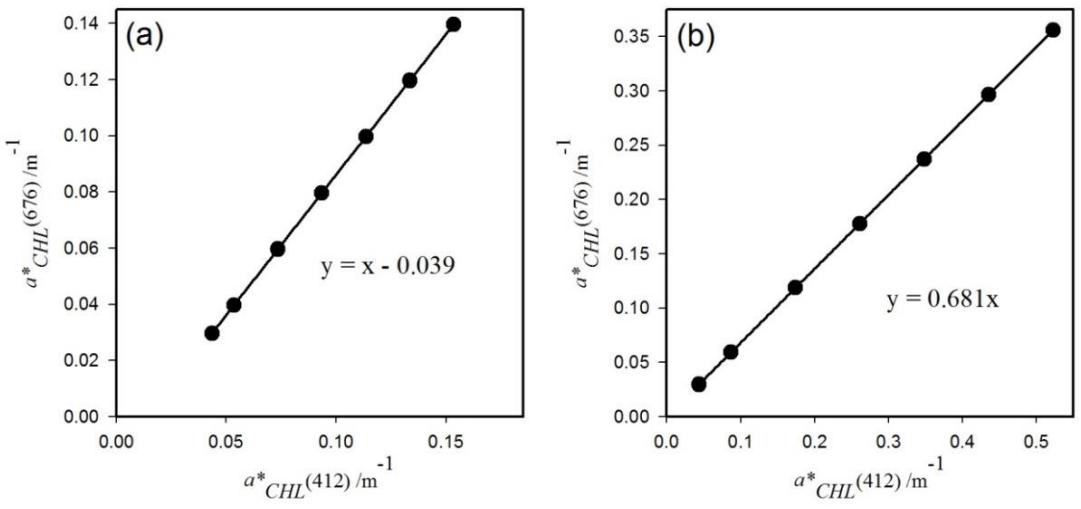

Figure 5.5: Example of a^*_{CHL} (412) against a^*_{CHL} (676) plots when the variation is best represented by (a) an offset and (b) a multiplier. When an offset is applied the gradient of the best fit line is 1 and there is a significant intercept. When the variation is represented by a multiplier the gradient of the best fit line does not equal 1 and there is no intercept.

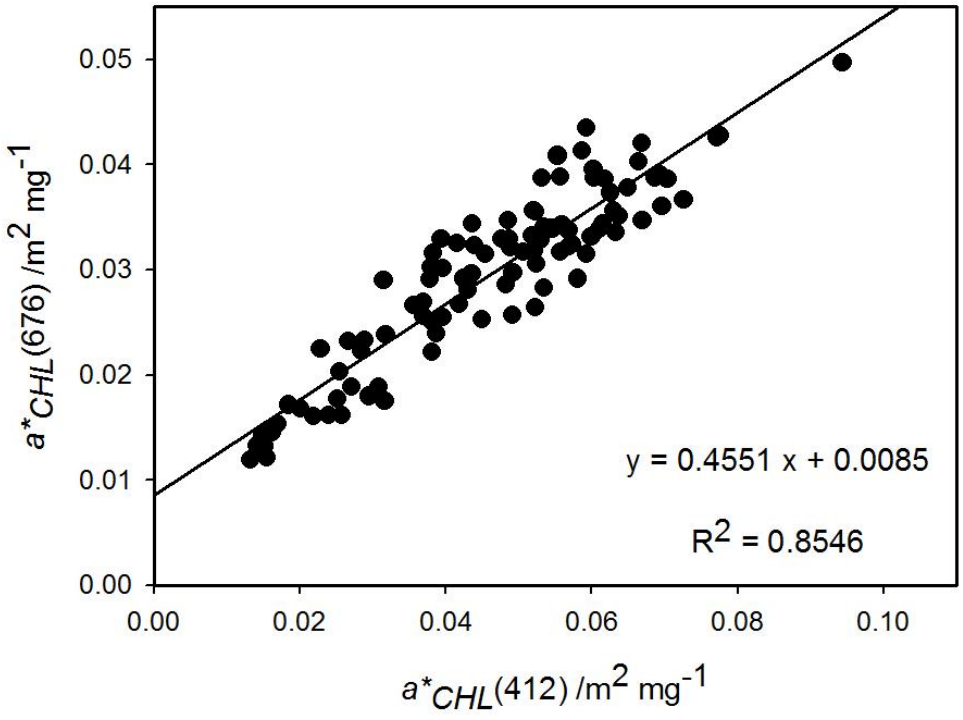

Figure 5.6: a^*_{CHL}(412) against a^*_{CHL}(676) for 100 Irish Sea Stations.

In Figure 5.6, the gradient of the best fit line is not approximately 1 and the intercept is negligible. Therefore, the variation in $a^*_{CHL}(\lambda)$ spectra would be best represented by the application of a multiplier to the mean $a^*_{CHL}(\lambda)$ values. Equations (5.11) and (5.12) show how the multiplier was applied in order to model the variation in $a^*_{CHL}(\lambda)$ spectra.

$$\sigma = \frac{\tilde{a}^*_{CHL}(412) + \sigma\left(\tilde{a}^*_{CHL}(412)\right)}{\tilde{a}^*_{CHL}(\lambda)} - 1 \tag{5.11}$$

$$a^*_{CHL}(\lambda) = \tilde{a}^*_{CHL}(\lambda) \times \left(1 + \left(\sigma \times randn(1)\right)\right) \tag{5.12}$$

where σ is the standard deviation required to account for the variation in Plot (b) in Figure 5.2, $\tilde{a}^*_{CHL}(\lambda)$ is the original specific chlorophyll absorption coefficient, $\sigma(\tilde{a}^*_{CHL}(412))$ is the standard deviation of $\tilde{a}^*_{CHL}(412)$ (Neil et al., 2011), *randn(1)* is the MATLAB random number generator and $a^*_{CHL}(\lambda)$ is the modified specific chlorophyll absorption coefficient.

Figure 5.7 shows the modelled $a^*_{CHL}(\lambda)$ spectrum and the resulting standard deviation using Equations (5.11) and (5.12). A comparison of Figure 5.2 and Figure 5.7 show that applying a multiplier to the mean $a^*_{CHL}(\lambda)$ value accounts for the majority of the variation in $a^*_{CHL}(\lambda)$ spectra.

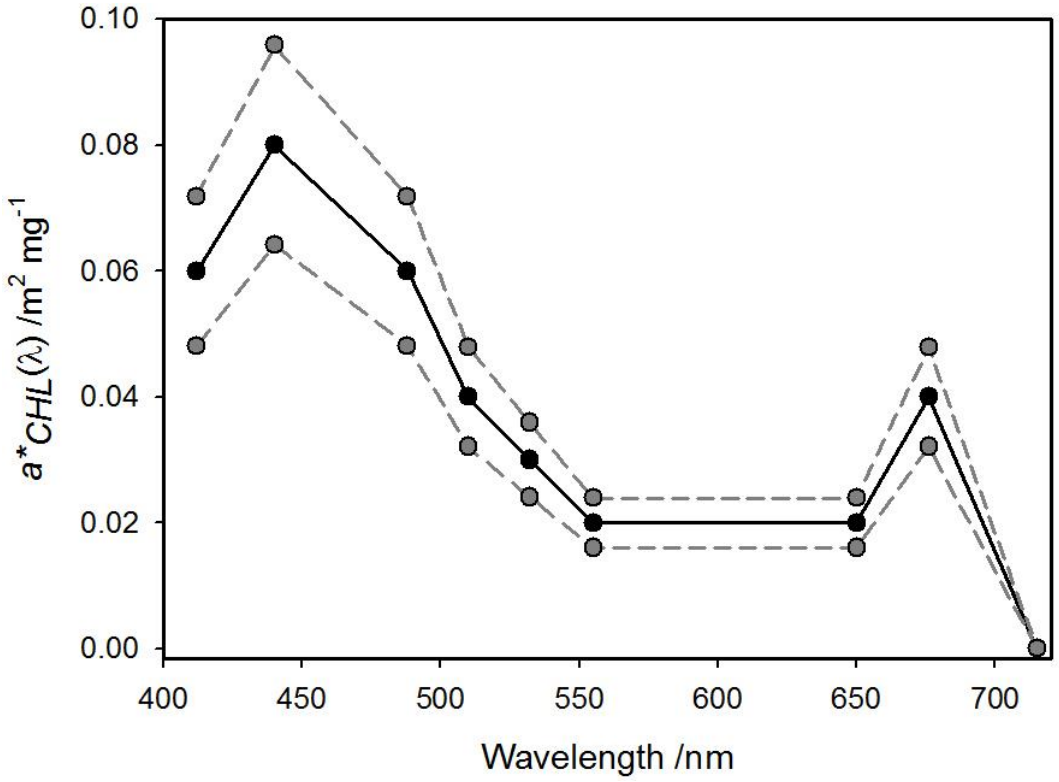

Figure 5.7: Modelled $a^*_{CHL}(\lambda)$ spectrum (Neil et al., 2011) shown as the solid line and the standard deviation of the modelled uncertainties in the *SIOPs* shown as dotted lines.

5.4.3 Uncertainties in $a^*_{MSS}(\lambda)$

In order to model the uncertainties in $a^*_{MSS}(\lambda)$ the spectral slope was examined. Plot (a) in Figure 5.8 visually demonstrates that there is very little significant variation in the slope of $a^*_{MSS}(\lambda)$, while Plot (b) shows the small distribution, with a standard deviation of 0.001 $m^2\ g^{-1}$, in $a^*_{MSS}(\lambda)$ slopes.

Interestingly, this suggests a degree of similarity in the composition of *MSS* throughout the Irish Sea, whereas *CDOM* composition appears to be more variable.

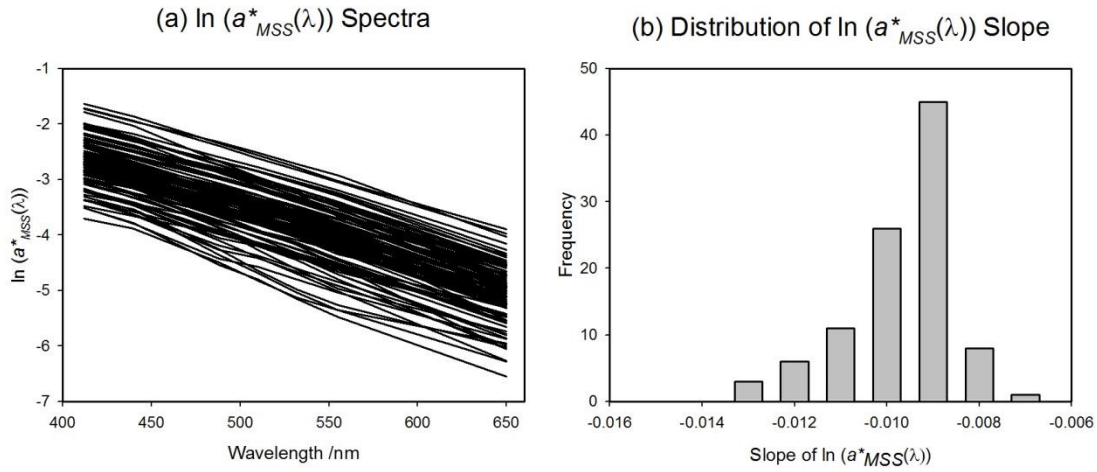

Figure 5.8: (a) Variability in the natural logarithm of $a^*_{MSS}(\lambda)$ and (b) Histogram of the slopes of the natural logarithm of $a^*_{MSS}(\lambda)$. Data displayed for 100 stations (Neil et al., 2011). The standard deviation of the slopes is 0.001 m^2 g^{-1}.

Applying a multiplier to the $a^*_{MSS}(\lambda)$ values represented the variability and also kept the constancy of the $a^*_{MSS}(\lambda)$ slope. Uncertainties in $a^*_{MSS}(\lambda)$ were therefore calculated using Equations (5.13) and (5.14), the modelled $a^*_{MSS}(\lambda)$ spectrum is shown in Figure 5.9.

$$\sigma = \frac{\tilde{a}^*_{MSS}(412) + \sigma\left(\tilde{a}^*_{MSS}(412)\right)}{\tilde{a}^*_{MSS}(\lambda)} - 1 \tag{5.13}$$

$$a^*_{MSS}(\lambda) = \tilde{a}^*_{MSS}(\lambda) \times \left(1 + \left(\sigma \times randn(1)\right)\right) \tag{5.14}$$

Comparing the modelled $a^*_{MSS}(\lambda)$ spectrum in Figure 5.9 and the $a^*_{MSS}(\lambda)$ spectra for Irish Sea data in Plot (c) in Figure 5.2 indicates that applying Equations (5.13) and (5.14) was an appropriate way of modelling $a^*_{MSS}(\lambda)$ values.

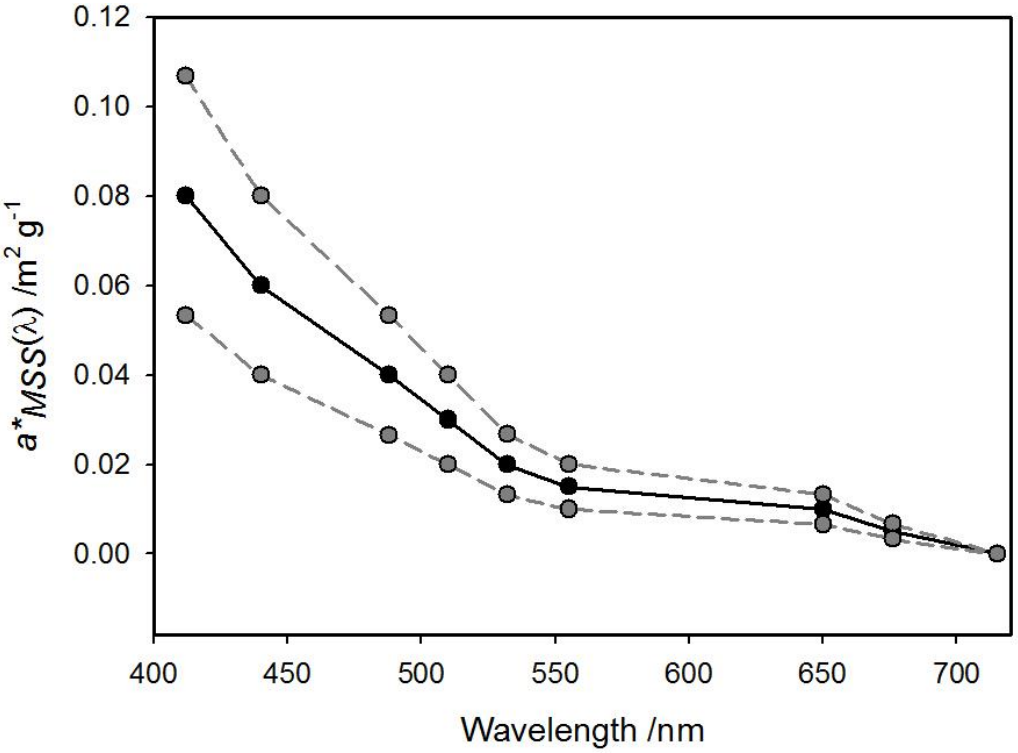

Figure 5.9: Modelled $a^*_{MSS}(\lambda)$ spectrum (Neil et al., 2011) shown as the solid line and the standard deviation of the modelled uncertainties in the *SIOPs* shown as dotted lines.

5.4.4 Uncertainties in Specific Scattering Coefficients

In order to model uncertainties in the specific scattering coefficients, a closer examination of the spectra was required. Neil et al. (2011) presented wavelength-independent values for the specific scattering coefficients as a simplifying step, but the spectra in Plots (d) and (e) in Figure 5.2 show features that are wavelength dependent. However if the $b^*_{CHL}(\lambda)$ and $b^*_{MSS}(\lambda)$ values are normalised (Figure 5.10) then the spectral variability is shown to be less than the uncertainty in the $b^*_{CHL}(\lambda)$ and $b^*_{MSS}(\lambda)$ values. Consequently, the spectral shape of the specific scattering coefficients cannot be confirmed as real spectral features. The specific scattering coefficients were therefore taken to be constant values, and modelled uncertainties were again applied as a multiplier to the mean spectral scattering spectra. Figure 5.11 shows the results of applying the same multiplier as used for $a^*_{CHL}(\lambda)$ and $a^*_{MSS}(\lambda)$ to both the $b^*_{CHL}(\lambda)$ and $b^*_{MSS}(\lambda)$ spectra. As the specific

scattering coefficients have been taken as wavelength independent, the mean and standard deviation of both $b^*_{CHL}(\lambda)$ and $b^*_{MSS}(\lambda)$ have constant values.

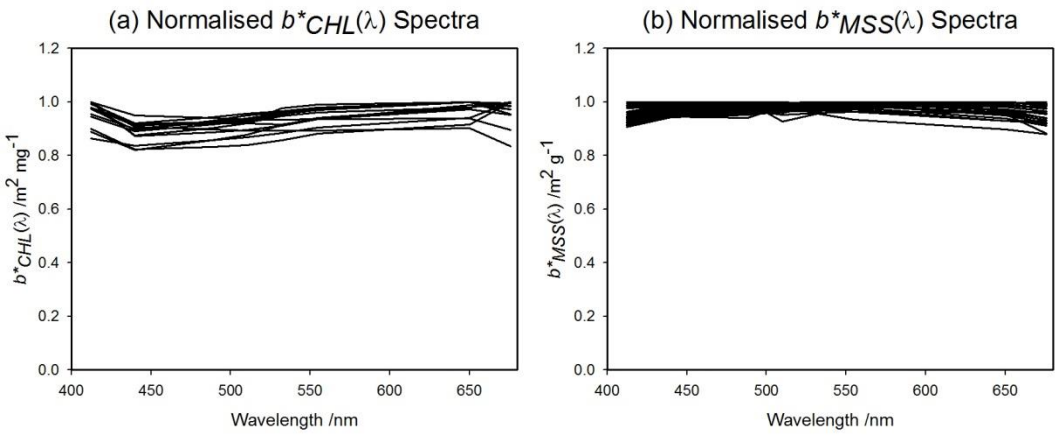

Figure 5.10: Normalised (a) $b^*_{CHL}(\lambda)$ and (b) $b^*_{MSS}(\lambda)$ spectra showing the small level of variability. As the standard deviations given in (Neil et al., 2011) were larger than the variability observed here, any structure within the spectra can be considered negligible.

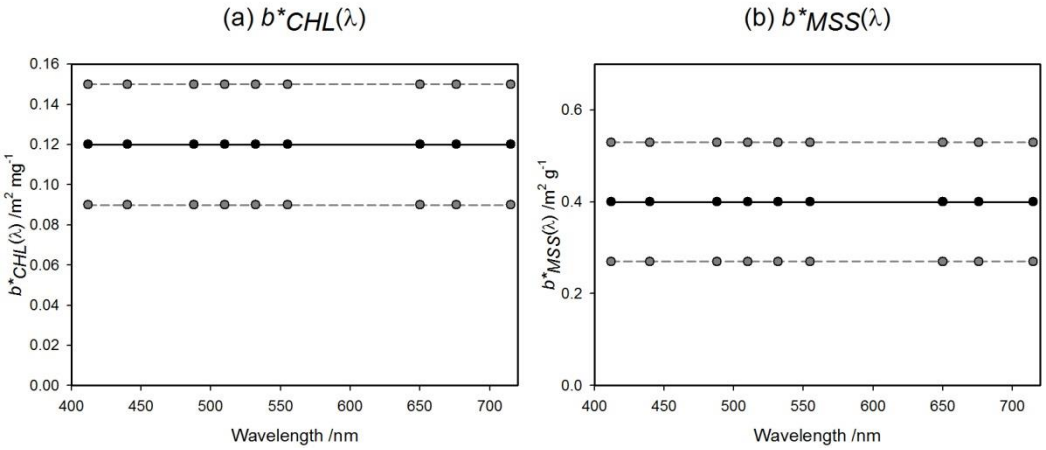

Figure 5.11: Modelled (a) $b^*_{CHL}(\lambda)$ and (b) $b^*_{MSS}(\lambda)$ spectrum (Neil et al., 2011) shown as the solid line and the standard deviation of the modelled uncertainties in the *SIOPs* shown as dotted lines.

Comparing Figure 5.11 to Plots (c) and (d) in Figure 5.2 shows that the standard deviation of the modelled spectral scattering coefficients covers most of the data from the Irish Sea stations.

5.5 Modelling Specific Attenuation Coefficients

In order to calculate the specific attenuation coefficients, the specific absorption and specific scattering coefficients were summed for each *OSC* (Equations (5.15) – (5.17)).

$$c^*_{CHL}(\lambda) = a^*_{CHL}(\lambda) + b^*_{CHL}(\lambda) \tag{5.15}$$

$$c^*_{MSS}(\lambda) = a^*_{MSS}(\lambda) + b^*_{MSS}(\lambda) \tag{5.16}$$

$$c^*_{CDOM}(\lambda) = a^*_{CDOM}(\lambda) \tag{5.17}$$

To calculate the standard deviation to be applied to the specific attenuation coefficients the standard deviations in the specific absorption and specific scattering coefficients were added in quadrature for each *OSC* (Equations (5.18) and (5.19)). As $c^*_{CDOM}(\lambda)$ was equal to $a^*_{CDOM}(\lambda)$, the same offset in the slope was added to both specific absorption and specific attenuation coefficients.

$$\sigma\left(c^*_{CHL}(412)\right) = \sqrt{\left(\sigma\left(a^*_{CHL}(412)\right)\right)^2 + \left(\sigma\left(b^*_{CHL}(412)\right)\right)^2} \tag{5.18}$$

$$\sigma\left(c^*_{MSS}(412)\right) = \sqrt{\left(\sigma\left(a^*_{MSS}(412)\right)\right)^2 + \left(\sigma\left(b^*_{MSS}(412)\right)\right)^2} \tag{5.19}$$

Figure 5.12 shows the results of modelling specific attenuation coefficients using Neil et al. (2011) and the same scaling factor application as for both chlorophyll and *MSS* specific absorption and scattering.

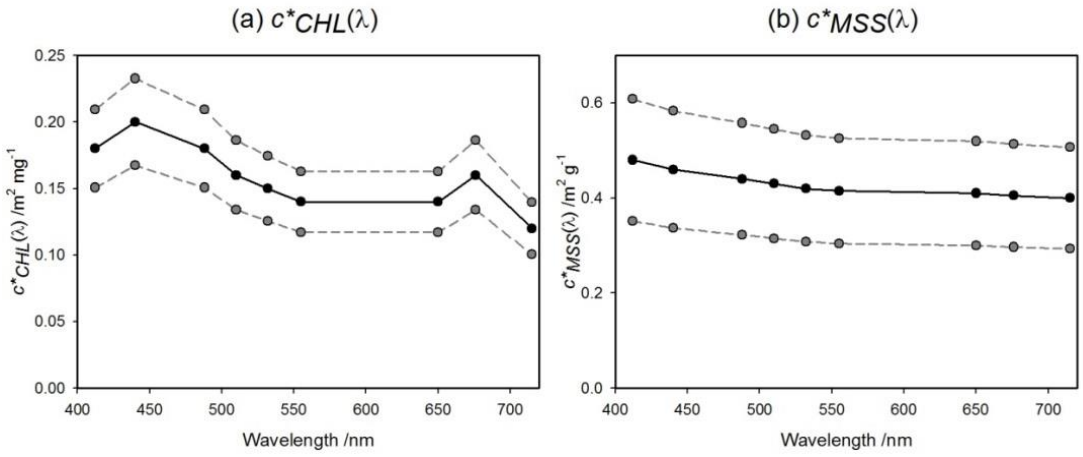

Figure 5.12: Modelled (a) $c^*_{CHL}(\lambda)$ and (b) $c^*_{MSS}(\lambda)$ spectrum (Neil et al., 2011) shown as the solid line and the standard deviation of the modelled uncertainties in the *SIOPs* shown as dotted lines.

5.6 Metrics for evaluating of the quality of *OSC* recoveries.

For the modelled data set, errors in the constituent concentrations recovered by different *IOP* inversion procedures can be calculated exactly. These errors are a function of both the noise introduced to the *IOP* data on which the inversion procedures operate, and of the mismatch between the *SIOPs* used for inversion and those used to create the data set. The overall performance of a given inversion routine can therefore be evaluated by creating *IOP* data sets with different degrees of random noise (Section 5.3), and then using *SIOP* values with known deviations from the true values (Section 5.4) in the inversion process.

5.6.1 Measuring the effect of random errors in *IOP* measurements on *OSC* recoveries.

As the noise in the *IOP* data set was added with a standard deviation equal to a percentage of the mean (Equation (5.8)), a direct comparison between input and output was possible. The standard deviation in the percentage error in the recovered concentrations was therefore used as a measure of performance. This was evaluated using Equations (5.20) and (5.21):

$$x = \left(\frac{X - \tilde{X}}{\tilde{X}}\right) \times 100 \tag{5.20}$$

$$\sigma = \sqrt{\frac{\sum(x - \mu)^2}{(n - 1)}} \tag{5.21}$$

where x is the percentage error in the recovered concentrations, X is the recovered *OSC* concentrations, $\tilde{X}$ are the modelled concentrations, σ is the standard deviation, μ is the mean percentage error and n is the number of each *OSC* concentration recovered.

The gradient of the best fit line in a plot of the percentage standard deviation added against percentage standard deviation in the recovered concentration uncertainties should provide a measurement of the sensitivity of the *IOP* inversion procedure to added measurement uncertainty, with a lower gradient value indicating a greater resistance to added measurement uncertainties.

5.6.2 Measuring the effect of systematic variations in *SIOPs* on *OSC* recoveries.

Calculating the errors in recovered concentrations when the modelled data set is subjected to uncertainties in the *SIOPs* is a little more complicated. The *SIOPs* for each constituent are subject to different uncertainties (Table 4.2), and it is likely that the sensitivity of the *IOP* inversion techniques to *SIOP* uncertainties will be different for each *OSC*. Sensitivity of each *OSC* to *SIOP* uncertainties could also be affected by the relative contribution of that constituent to the total *IOPs*, i.e. the composition of the water may affect how the deconvolution procedures react to *SIOP* uncertainties. This difficulty in proposing a single metric will be discussed further in Chapter 6.

5.7 Chapter summary

1. A modelled data set was generated using randomly selected *OSC* concentrations with ranges which were representative of UK shelf seas. The *OSC* concentrations were multiplied by the relevant *SIOPs* and then summed to give total *IOPs*. The *OSC* concentrations were sampled evenly throughout the ranges and no weighting was applied to favour combinations of *OSC* concentrations that might occur more frequently in a particular body of water.

2. It was proposed that measurement errors could be simulated by adding random noise to each of the *IOPs* individually. Variations in measurement errors were introduced by changing the percentage standard deviation of the Gaussian noise distribution.

3. Uncertainties in the *SIOPs* were modelled by examining each *SIOP* separately. For $a^*_{CDOM}(\lambda)$ uncertainties were modelled by a change in the $a^*_{CDOM}(\lambda)$ slope. For all other specific absorption and scattering coefficients a multiplier was applied to each *SIOP* value. Specific attenuation coefficient uncertainties were modelled by adding the specific absorption and scattering coefficient uncertainties in quadrature.

4. The effect of noise in the *IOP* data on an inversion procedure can be measured by determining the relationship between the standard deviation of the percentage noise added and the percentage standard deviation of the recovered constituent concentrations. For the effect of *SIOP* mismatch (which does not statistically vary during inversion) the mean percentage error in the recovered constituents is proposed as a measure of performance. However due to the complexity of modelling *SIOP* uncertainties, with a different scaling factor applied to each *SIOP* individually, this approach is likely to be over simplistic.

Chapter 6 *IOP* Inversion Methods Applied to the Modelled Data Set

As discussed in Chapter 2, the total value of each *IOP* can be defined as the sum of its component parts, e.g. the absorption coefficient is the sum of the absorption coefficients of each of the optically significant constituents (*OSCs*) in the water (excluding water itself). Furthermore the constituent *IOPs* can be defined as the constituent concentrations multiplied by the corresponding specific inherent optical property (*SIOP*), (Equations (6.1) and (6.2));

$$a_{ac-9}(\lambda) = a_{CDOM}(\lambda) + a_{CHL}(\lambda) + a_{MSS}(\lambda) \tag{6.1}$$

$$a_i(\lambda) = a_i^*(\lambda) \cdot X_i \tag{6.2}$$

where $a_{ac\text{-}9}(\lambda)$, $a_{CDOM}(\lambda)$, $a_{CHL}(\lambda)$ and $a_{MSS}(\lambda)$ are the absorption coefficients associated with the *ac-9*, coloured dissolved organic matter (*CDOM*), phytoplankton pigments (*CHL*) and mineral suspended solids (*MSS*), $a^*_i(\lambda)$ is the specific absorption coefficient for constituent *i*, $a_i(\lambda)$ is the absorption coefficient for constituent *i* and X_i is the concentration of constituent *i*. Combining Equations (6.1) and (6.2) gives an algebraic formula for the total absorption measured by the *ac-9* as a function of the constituent concentrations, Equation (6.3)

$$a_{ac-9}(\lambda) = [a^*_{CDOM}(\lambda) \cdot X_{CDOM}] + [a^*_{CHL}(\lambda) \cdot X_{CHL}] + [a^*_{MSS}(\lambda) \cdot X_{MSS}] \tag{6.3}$$

If the *IOPs* from the *ac-9* and the *SIOPs* for the area of interest are known for an adequate number of different wavelengths, a set of simultaneous equations based on Equation (6.3) can be solved to recover the constituent concentrations. The inversion of *IOPs* to recover constituent concentrations can therefore be formulated as a problem of linear algebra. To recover the three *OSC* concentrations, a set of at least three equations would be required. In principle, this requirement is easily met as the *ac-9* has nine discrete wavelengths which could be used to generate a total of twenty seven equations. Given that there are still three unknowns, this would give an over constrained problem which could be solved using a least squares fit and would resemble a spectral matching problem rather than the linear algebraic one originally

described. This approach to *IOP* inversion generates a number of questions which are addressed in this chapter, including;

1. What is the optimum number of equations required to solve the *IOP* inversion?

2. If the *IOP* inversion procedures perform as expected, i.e. as a set of simultaneous equations, how robust would the optimum method be when subjected to measurement uncertainties in the *IOPs*?

3. How would the procedure behave if the inversion matrix constants were inappropriate for the area of interest, for example if they were averaged over too large a geographical area?

These questions can be answered using a perfectly modelled data set in the first instance and then adding both measurement uncertainties in the form of random noise added to the *IOPs* and systematic uncertainty in the form of alteration in the assumed *SIOP* values (0).

6.1 Previous Work – (Gallegos & Neale, 2002)

6.1.1 The Unconstrained Procedure of Gallegos & Neale (2002)

The Unconstrained Procedure of Gallegos & Neale (2002) used normalised absorption spectra to partition the total absorption coefficient from the *ac-9* into constituent absorption coefficients. Rather than making a scattering correction to the *ac-9* absorption values, a 4^{th} term was added to calculate the percentage of the measured absorption coefficient that was attributable to scattering. This approach avoids the assumptions of the Zaneveld et al. (1994) scattering correction method (Section 3.5.3). Equation (6.4) shows the equation used for applying the correction factor, where the true non-water absorption coefficient ($a_{t\text{-}w}(\lambda)$) is the absorption coefficient measured by the *ac-9* ($a_{ac\text{-}9}(\lambda)$) less the proportion of the scattering coefficient measured by the *ac-9* attributable to the over estimation of the absorption coefficient.

$$a_{t-w}(\lambda) = a_{ac-9}(\lambda) - \varepsilon b_{ac-9}(\lambda) \quad (6.4)$$

Here, $b_{ac\text{-}9}(\lambda)$ is the scattering measured by the *ac-9* and ε is the scattering correction factor, which is dependent on the volume scattering function and optical characteristics of the instrument (e.g. acceptance angle of detector, path length, reflectivity of the tube).

Equation (6.5) was utilised by Gallegos & Neale to calculate the contribution to the absorption by each of the constituents.

$$a_{ac-9}(\lambda) = a_{CDOM}(\lambda) + a_{CHL}(\lambda) + a_{MSS}(\lambda) + \varepsilon b_{ac-9}(\lambda) \quad (6.5)$$

where $a_{CDOM}(\lambda)$ is the contribution of total absorption attributable to *CDOM* etc.

The normalised absorption spectra were defined as;

$$g(\lambda) = \frac{a_{CDOM}(\lambda)}{a_{CDOM}(440)} \quad (6.6)$$

$$\phi(\lambda) = \frac{a_{CHL}(\lambda)}{a_{CHL}(676)} \quad (6.7)$$

$$p(\lambda) = \frac{a_{MSS}(\lambda)}{a_{MSS}(440)} \quad (6.8)$$

where $g(\lambda)$, $\phi(\lambda)$ and $p(\lambda)$ are, respectively, the normalised absorption spectra for *CDOM*, phytoplankton pigment, and non-pigmented particulates. Absorption by *CDOM* and non-pigmented particulates is normalised to a reference wavelength of 440 nm by convention (Kirk, 1994), and 676 nm was chosen to normalise $a_{CHL}(\lambda)$ because it is the absorption peak for phytoplankton chlorophyll.

Assuming that the mean spectral values for the normalised absorption spectra can be defined, the characteristic absorption coefficients at the appropriate reference wavelengths can be determined using Equation (6.9);

$$\begin{bmatrix} a_{CDOM}(440) \\ a_{CHL}(676) \\ a_{MSS}(440) \\ \varepsilon \end{bmatrix} = \begin{bmatrix} g(\lambda_1) & \phi(\lambda_1) & p(\lambda_1) & b_m(\lambda_1) \\ g(\lambda_2) & \phi(\lambda_2) & p(\lambda_2) & b_m(\lambda_2) \\ g(\lambda_3) & \phi(\lambda_3) & p(\lambda_3) & b_m(\lambda_3) \\ g(\lambda_4) & \phi(\lambda_4) & p(\lambda_4) & b_m(\lambda_4) \end{bmatrix}^{-1} \begin{bmatrix} a_{ac-9}(\lambda_1) \\ a_{ac-9}(\lambda_2) \\ a_{ac-9}(\lambda_3) \\ a_{ac-9}(\lambda_4) \end{bmatrix} \quad (6.9)$$

where the transpose, $[a_{CDOM}(440)\ \ a_{CHL}(676)\ \ a_{MSS}(440)\ \ \varepsilon]^T$ are the coefficients to be estimated. The choice of wavelengths ($\lambda_1 - \lambda_4$) is important, due to expected levels of uncertainty. The selection was made to maximise the information about the unknown absorption coefficients.

Gallegos and Neale justified the choice of wavelengths as follows:

- λ_1 = 412 nm because it is a maximum (among the wavelengths available with the *ac*-9) for absorption by *CDOM*.
- λ_2 = 488 nm because it is the wavelength at which $g(\lambda)$, $\phi(\lambda)$ and $p(\lambda)$ have their maximum separation.
- λ_3 = 676 nm because it is an absorption peak for $\phi(\lambda)$.
- λ_4 = 715 nm because $a_{ac\text{-}9}(715)$ is governed largely by ε.

This procedure was called the Unconstrained Procedure because it made no assumptions regarding the negligible absorption by *CDOM* or *MSS* at 715 nm and did not use any supporting measurements.

a Modifications to the Unconstrained Procedure for Comparative Work

The normalised absorption spectra used in Gallegos & Neale (2002) can be calculated from the *SIOPs* (Equations (6.10) – (6.12)).

$$g(\lambda) = \frac{a^*_{CDOM}(\lambda)}{a^*_{CDOM}(440)} \tag{6.10}$$

$$\phi(\lambda) = \frac{a^*_{CHL}(\lambda)}{a^*_{CHL}(676)} \tag{6.11}$$

$$p(\lambda) = \frac{a^*_{MSS}(\lambda)}{a^*_{MSS}(440)} \tag{6.12}$$

Conversely, an additional step can be added to the original method of Gallegos & Neale (2002), to allow the concentrations of constituents to be recovered by dividing the recovered absorption coefficients by the corresponding *SIOPs*. Since the 'alternative simultaneous equations' method presented in this thesis aims to recover constituent concentrations, rather than absorption spectra, Equations (6.13) – (6.15) were used to allow direct comparison between the two approaches.

$$X_{CDOM} = \frac{a_{CDOM}(440)}{a^*_{CDOM}(440)} \tag{6.13}$$

$$X_{CHL} = \frac{a_{CHL}(676)}{a^*_{CHL}(676)} \tag{6.14}$$

$$X_{MSS} = \frac{a_{MSS}(440)}{a^*_{MSS}(440)} \tag{6.15}$$

Note that the *SIOPs* used in this work, derived by Neil et al. (2011), had the $a^*(715)$ value set to zero for all three constituents, as the Zaneveld et al. (1994) scattering corrections were applied to *IOP* data. Consequently the value of ε was always zero and not included in this analysis.

6.2 An Alternative Three Simultaneous Equations Method

Since *IOPs* are additive, their inversion to recover constituent concentrations is a linear problem. As there are three classes of constituents to be recovered, a set of three simultaneous equations is the minimum that can be used to recover the *OSC* concentrations. There are three feasible choices for these equations; three absorption wavelengths (*AAA*), three attenuation wavelengths (*CCC*) and two absorption and one scattering wavelength (*AAC*). These possibilities are outlined in Equations (6.16) – (6.18).

$$\begin{bmatrix} X_{CDOM} \\ X_{CHL} \\ X_{MSS} \end{bmatrix} = \begin{bmatrix} a^*_{CDOM}(\lambda_1) & a^*_{CHL}(\lambda_1) & a^*_{MSS}(\lambda_1) \\ a^*_{CDOM}(\lambda_2) & a^*_{CHL}(\lambda_2) & a^*_{MSS}(\lambda_2) \\ a^*_{CDOM}(\lambda_3) & a^*_{CHL}(\lambda_3) & a^*_{MSS}(\lambda_3) \end{bmatrix}^{-1} \begin{bmatrix} a_{ac-9}(\lambda_1) \\ a_{ac-9}(\lambda_2) \\ a_{ac-9}(\lambda_3) \end{bmatrix} \tag{6.16}$$

$$\begin{bmatrix} X_{CDOM} \\ X_{CHL} \\ X_{MSS} \end{bmatrix} = \begin{bmatrix} c^*_{CDOM}(\lambda_1) & c^*_{CHL}(\lambda_1) & c^*_{MSS}(\lambda_1) \\ c^*_{CDOM}(\lambda_2) & c^*_{CHL}(\lambda_2) & c^*_{MSS}(\lambda_2) \\ c^*_{CDOM}(\lambda_3) & c^*_{CHL}(\lambda_3) & c^*_{MSS}(\lambda_3) \end{bmatrix}^{-1} \begin{bmatrix} c_{ac-9}(\lambda_1) \\ c_{ac-9}(\lambda_2) \\ c_{ac-9}(\lambda_3) \end{bmatrix} \tag{6.17}$$

$$\begin{bmatrix} X_{CDOM} \\ X_{CHL} \\ X_{MSS} \end{bmatrix} = \begin{bmatrix} a^*_{CDOM}(\lambda_1) & a^*_{CHL}(\lambda_1) & a^*_{MSS}(\lambda_1) \\ a^*_{CDOM}(\lambda_2) & a^*_{CHL}(\lambda_2) & a^*_{MSS}(\lambda_2) \\ c^*_{CDOM}(\lambda_3) & c^*_{CHL}(\lambda_3) & c^*_{MSS}(\lambda_3) \end{bmatrix}^{-1} \begin{bmatrix} a_{ac-9}(\lambda_1) \\ a_{ac-9}(\lambda_2) \\ c_{ac-9}(\lambda_3) \end{bmatrix} \tag{6.18}$$

where $a_{ac\text{-}9}(\lambda)$, $b_{ac\text{-}9}(\lambda)$ and $c_{ac\text{-}9}(\lambda)$ are the absorption scattering and attenuation coefficients measured by the *ac-9*, X_{CDOM}, X_{CHL} and X_{MSS} are the concentrations, $a^*_{CDOM}(\lambda)$, $a^*_{CHL}(\lambda)$ and $a^*_{MSS}(\lambda)$ are the specific absorption coefficients and $c^*_{CDOM}(\lambda)$, $c^*_{CHL}(\lambda)$ and $c^*_{MSS}(\lambda)$ are the specific attenuation coefficients at wavelength λ for *CDOM*, *CHL* and *MSS* respectively. Note that the specific attenuation coefficients are taken as the sum of the specific absorption and specific scattering coefficients ($c^*(\lambda) = a^*(\lambda) + b^*(\lambda)$). The possibility of using three scattering wavelengths was ruled out here as, since *CDOM* does not scatter, no *CDOM* concentration recovery would be possible with this format for *IOP* inversion. The *AAA* equations are the equivalent of the method of Gallegos & Neale (2002) with the scattering correction coefficient, ε, removed. The *CCC* equations are proposed as a method of achieving *IOP* inversion for data from the Liverpool Bay Coastal Observatory (Appendix A). The *AAC* equations are proposed as the

absorption spectra of *CDOM* and *MSS* are very similar and inversion of the absorption coefficients has proved troublesome in the past (Schofield et al., 2004; Gallegos & Neale, 2002; Bricaud & Stramski, 1990; Morrow et al., 1989; Roesler et al., 1989) and therefore addition of an attenuation coefficient should enable *CDOM* and *MSS* concentrations to be determined with greater accuracy.

If the data contained no uncertainties, the choice of wavelengths would not matter; however as *ac-9* data does contain uncertainties, the selection of wavelengths is important. A method to select the wavelengths is outlined in Section 6.5.1.

6.3 The Many Equations Method (*MEM*)

As the inversion of *IOPs* into constituent concentrations is a linear problem choosing three simultaneous equations was an obvious choice. However the *ac-9* provides *IOP* data at nine wavelengths and therefore an over constrained procedure which makes use of all of the available data would be possible. In this case, the method would be more akin to a spectral matching problem than linear inversion. When simultaneous equations are converted to matrix form, an over constrained system can be solved using a least squares fit as opposed to matrix inversion and multiplication. The *MEM* is shown in Equation (6.19);

$$\begin{bmatrix} a_{ac-9}(412) \\ a_{ac-9}(440) \\ a_{ac-9}(488) \\ a_{ac-9}(510) \\ a_{ac-9}(532) \\ a_{ac-9}(555) \\ a_{ac-9}(650) \\ a_{ac-9}(676) \\ a_{ac-9}(715) \\ c_{ac-9}(412) \\ c_{ac-9}(440) \\ c_{ac-9}(488) \\ c_{ac-9}(510) \\ c_{ac-9}(532) \\ c_{ac-9}(555) \\ c_{ac-9}(650) \\ c_{ac-9}(676) \\ c_{ac-9}(715) \end{bmatrix} = \begin{bmatrix} a^*_{CDOM}(412) & a^*_{CHL}(412) & a^*_{MSS}(412) \\ a^*_{CDOM}(440) & a^*_{CHL}(440) & a^*_{MSS}(440) \\ a^*_{CDOM}(488) & a^*_{CHL}(488) & a^*_{MSS}(488) \\ a^*_{CDOM}(510) & a^*_{CHL}(510) & a^*_{MSS}(510) \\ a^*_{CDOM}(532) & a^*_{CHL}(532) & a^*_{MSS}(532) \\ a^*_{CDOM}(555) & a^*_{CHL}(555) & a^*_{MSS}(555) \\ a^*_{CDOM}(650) & a^*_{CHL}(650) & a^*_{MSS}(650) \\ a^*_{CDOM}(676) & a^*_{CHL}(676) & a^*_{MSS}(676) \\ a^*_{CDOM}(715) & a^*_{CHL}(715) & a^*_{MSS}(715) \\ c^*_{CDOM}(412) & c^*_{CHL}(412) & c^*_{MSS}(412) \\ c^*_{CDOM}(440) & c^*_{CHL}(440) & c^*_{MSS}(440) \\ c^*_{CDOM}(488) & c^*_{CHL}(488) & c^*_{MSS}(488) \\ c^*_{CDOM}(510) & c^*_{CHL}(510) & c^*_{MSS}(510) \\ c^*_{CDOM}(532) & c^*_{CHL}(532) & c^*_{MSS}(532) \\ c^*_{CDOM}(555) & c^*_{CHL}(555) & c^*_{MSS}(555) \\ c^*_{CDOM}(650) & c^*_{CHL}(650) & c^*_{MSS}(650) \\ c^*_{CDOM}(676) & c^*_{CHL}(676) & c^*_{MSS}(676) \\ c^*_{CDOM}(715) & c^*_{CHL}(715) & c^*_{MSS}(715) \end{bmatrix} \begin{bmatrix} X_{CDOM} \\ X_{CHL} \\ X_{MSS} \end{bmatrix} \quad (6.19)$$

6.4 Deconvolution Methods Results for Perfectly Modelled Data

6.4.1 Gallegos & Neale (2002) Unconstrained Procedure

The altered Unconstrained Procedure of Gallegos & Neale (2002) performs as a set of three simultaneous equations and therefore provides an algebraic solution for all combinations of constituents. It produced perfect constituent recoveries when perfectly modelled data were used (Figure 6.1).

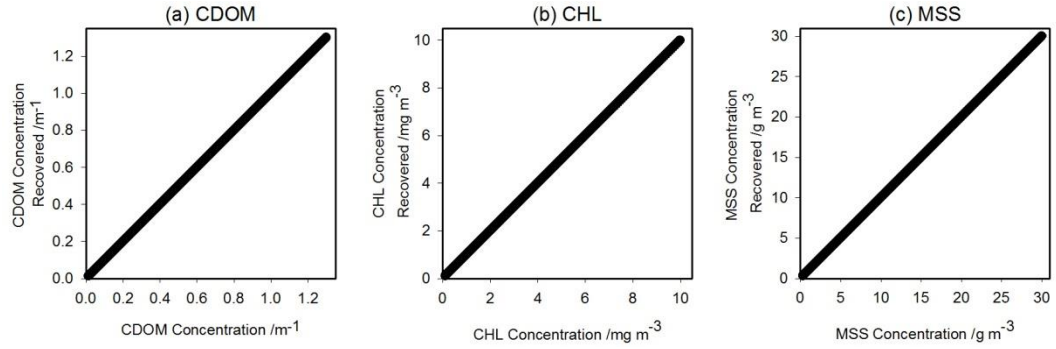

Figure 6.1: Results for (a) *CDOM*, (b) *CHL* and (c) *MSS* concentration recoveries when the altered Unconstrained Procedure of Gallegos & Neale (2002) was tested with perfectly modelled data.

6.4.2 Simultaneous Equations Method (*SEM*)

The *SEM* (Equations (6.16) - (6.18)) also produced perfect constituent recoveries when perfectly modelled data were used (Figure 6.2).

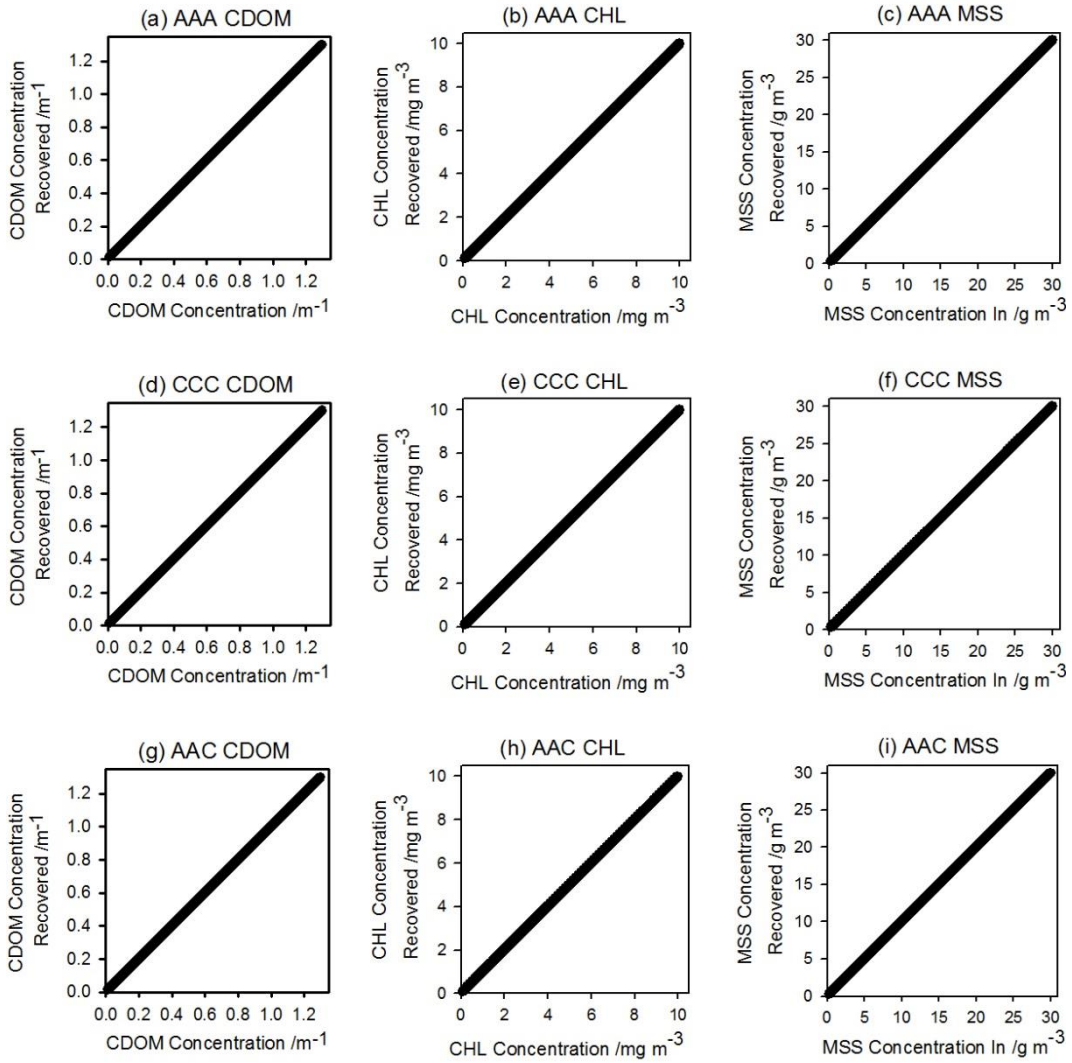

Figure 6.2: Results for three *OSC* concentration recoveries when the each of the *SEM* combinations was tested with perfectly modelled data. With (a) *CDOM*, (b) *CHL* and (c) *MSS* concentrations recovered using the *AAA* method; (d) *CDOM*, (e) *CHL* and (f) *MSS* concentrations recovered using the *CCC* method and (g) *CDOM*, (h) *CHL* and (i) *MSS* concentrations recovered using the *AAC* method.

6.4.3 The Many Equations Method (*MEM*)

Perfect constituent recoveries were also obtained when the Many-Equations Method (*MEM*), which uses a least square fitting method, was applied to perfectly modelled data. The results are shown in Figure 6.3.

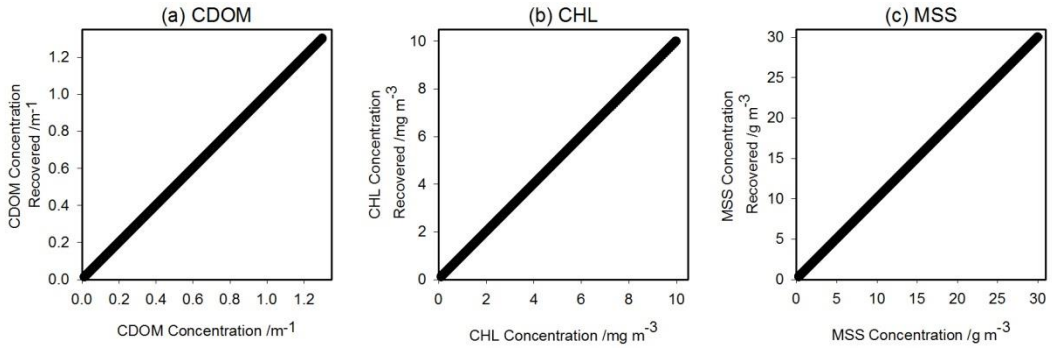

Figure 6.3: Results for (a) *CDOM*, (b) *CHL* and (c) *MSS* concentration recoveries when the *MEM* was tested with perfectly modelled data.

6.5 The Effect of Adding Measurement Uncertainties (as noise in the *IOPs*) to the Modelled Data Set

6.5.1 Simultaneous Equation Methods (*SEM*)

a The Effect of Random Noise on Wavelength Selection

First, the combination of wavelengths that produced the lowest standard deviation in the percentage error in the recoveries had to be determined. All possible combinations of wavelengths were tested, with no bias for wavelength order, for a 1% measurement uncertainty (1% measurement uncertainty is defined in 0 as 1% of the mean value added as a standard deviation). Table 6.1 shows the combination of wavelengths that proved to be the most noise resistant for each set of equations.

Table 6.1: Wavelengths used to optimise each set of equations.

SEM	λ_1 /nm	λ_2 /nm	λ_3 /nm
AAA	412	676	650
CCC	412	555	440
AAC	412	676	676

Notice, in Table 6.1, that the order of the wavelengths is important, with λ_3 less than λ_2 in both the *AAA* and *CCC* set of equations. This is because λ_1 acts largely on the *CDOM* concentration recovery, λ_2 on the *CHL* concentration recovery and λ_3 on the *MSS* concentration recovery and as such the order of the wavelengths is very important to the effectiveness of the inversion method.

Looking closer at the optimum wavelengths, it can be assumed that λ_1 = 412 nm is the best choice of first wavelength as it is the maximum (of the wavelengths available) for *CDOM* absorption. In the second column, λ_2 = 676 nm for the two sets of equations containing absorption coefficients as *CHL* absorption is clearly distinguishable at 676nm. Finally, λ_3 = 676 nm for the *AAC* set of equations as the *CHL* is mainly an absorber at 676 nm and therefore *MSS* scattering is most distinguishable from *CHL* scattering at 676 nm.

b Results of Three Simultaneous Equations with Simulated Measurement Uncertainties

Using the wavelengths shown in Table 6.1, each set of equations was tested with measurement uncertainties in the *IOPs* (simulated by adding random noise to the modelled data). Figure 6.4 shows the percentage standard deviation in the recovered values plotted against the percentage standard deviation added, with Plot (d) showing the *CHL* recovery for the *AAA* and the *AAC* set of equations as the scale required to see all three cases could not distinguish both results. The gradient of the recovered data provided a measure of the sensitivity; the lower the gradient, the higher the resistance.

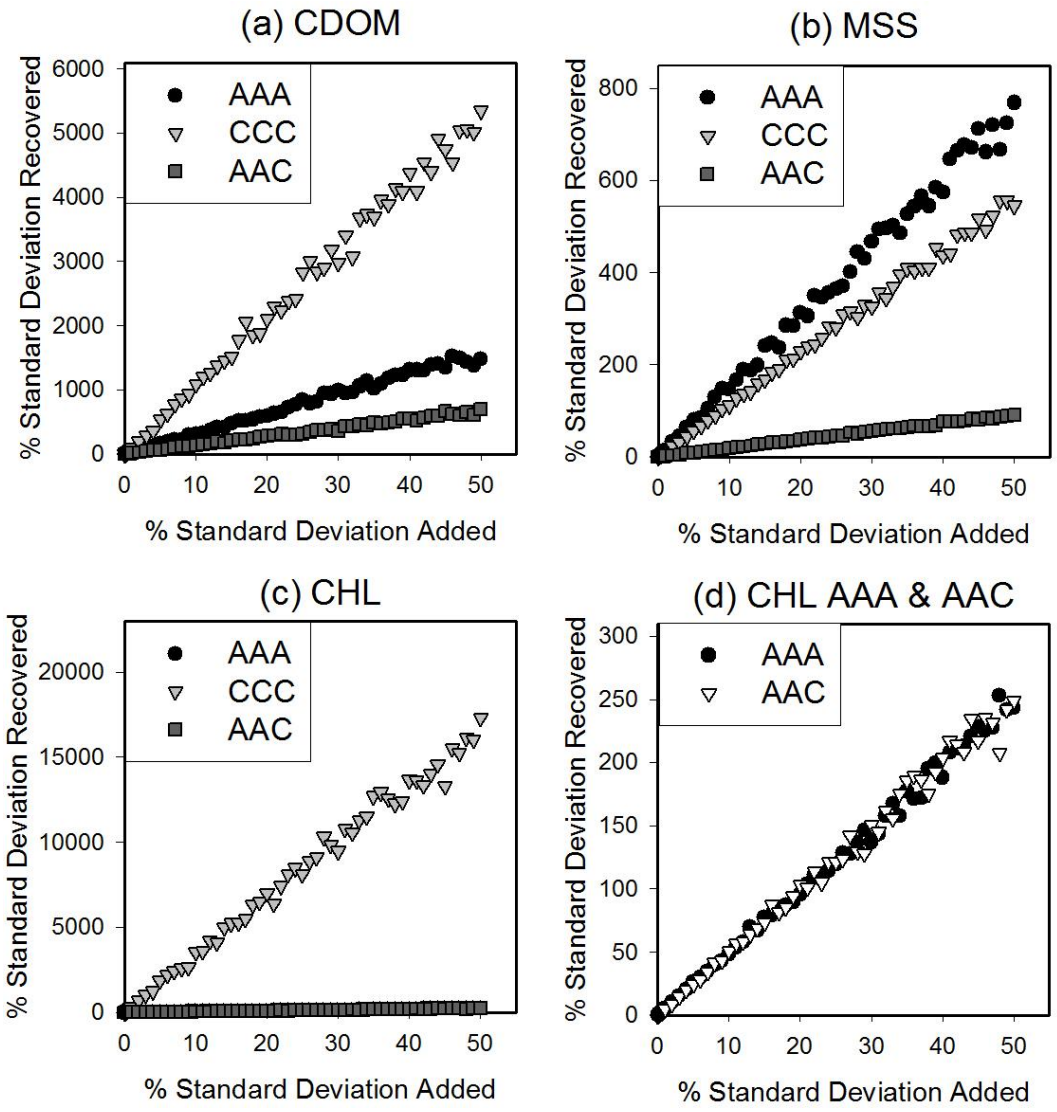

Figure 6.4: Comparison of compositions showing the average percentage standard deviation for (a) *CDOM*, (b) *CHL* and (c) *MSS* concentration recovered when subjected to increasing measurement uncertainties added. The equation set with the smallest gradient is the most resistant to measurement uncertainty. Plot (d) is an enlargement of the *AAA* and *AAC* methods for *CHL* concentration recovery as the results in Plot (c) are unclear, it is clear from (d) that the two methods are indistinguishable for *CHL* concentration recovery.

c The Optimum Combination

The results in Figure 6.4 show that the *AAC* set of equations was the most resistant to measurement uncertainty. The *AAA* set of equations were equally resistant for *CHL* concentration recoveries, but since *AAC* performed best for all three constituents it was considered to be the optimum combination.

6.5.2 Results of Gallegos & Neale (2002) with Measurement Uncertainties

The Gallegos & Neale (2002) Unconstrained Procedure and the *AAC* set of equations are compared in Figure 6.5. The *AAC* equations have smaller gradients in these plots, and are therefore more resistant to measurement uncertainties.

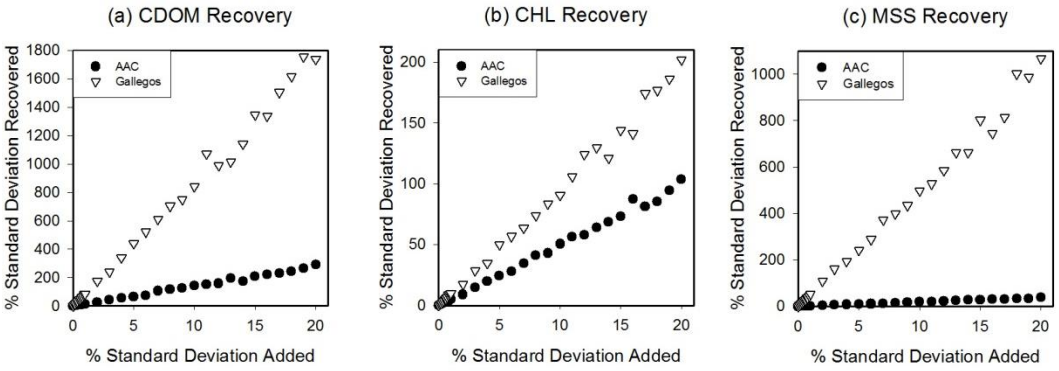

Figure 6.5: Comparison between *AAC* set of equations and the Gallegos & Neale (2002) Unconstrained Procedure for added measurement uncertainties.

One significant difference between the Unconstrained Procedure of Gallegos & Neale (2002) and the *AAC* set of equations was the inclusion of the scattering correction factor by Gallegos & Neale (2002). If future analysis included the use of *SIOPs* that were non-zero at 715 nm then the addition of ε could be tested. The recommendation would be to use either the *AAC* set of equations in two stages with a second iteration once the correct $a_{ac\text{-}9}(\lambda)$ and $c_{ac\text{-}9}(\lambda)$ values have been calculated or to use the Gallegos & Neale (2002) Unconstrained Procedure with the wavelengths outlined in Table 6.1.

Figure 6.6 compares the Gallegos & Neale (2002) Unconstrained Procedure to the *AAA* set of equations to demonstrate that the optimum choice of wavelengths are those found using the iterative approach from Table 6.1, rather than the ones selected by Gallegos & Neale (2002).

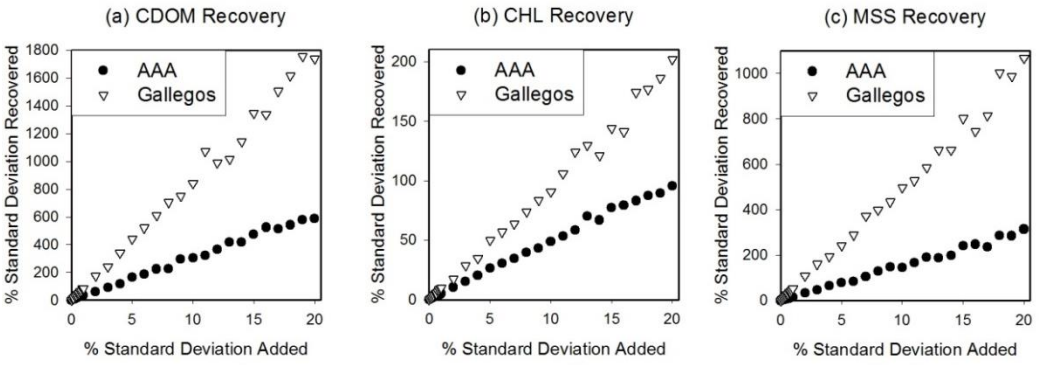

Figure 6.6: Comparison of *AAA* and Gallegos to justify the wavelength selection method used in Section 6.6.1

6.5.3 Results of the *MEM* with Measurement Uncertainties

Comparing the sensitivity of the *MEM* and the *AAC* set of equations to measurement uncertainty shows that the addition of more wavelengths has a detrimental effect on the recovery of constituent concentrations (Figure 6.7).

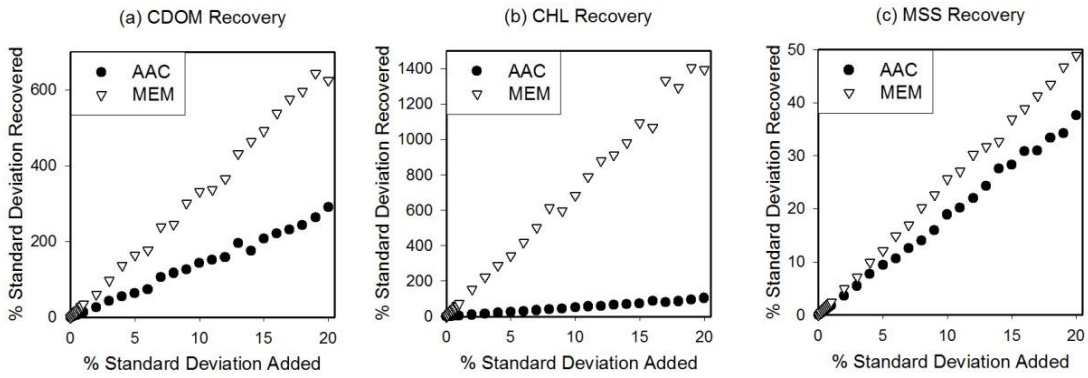

Figure 6.7: Comparison of constituent concentration recoveries between *AAC* and the *MEM* for noise added to the *IOP* data only.

It might have been expected that as the *MEM* was making use of more data, the resulting constituent concentration retrievals would be less sensitive to measurement

uncertainties. Figure 6.7 demonstrates that this was not the case, and the apparently counter-intuitive result is discussed in further detail in Section 6.5.4.

6.5.4 A Closer Examination of the *MEM*

Given that the *MEM* uses all of the available spectral information, it was expected that it would be the optimum method of *IOP* inversion. However, much of this information could be redundant as the *AAC* method has selected wavelengths that contain the main spectral features for each of the *OSCs*. A linear algebra technique called Singular Value Decomposition (*SVD*) can determine if the information contained in the *SIOP* matrix of the *MEM* is redundant and also can determine if the matrix is close to singular, which would cause instability in the solution when the *MEM* is completed. *SVD* is regularly used alongside linear least squares regression to reduce redundancy in the least squares fitting (Lawson & Hanson, 1995; Golub & Reinsch, 1970; Golub, 1968). A brief explanation of *SVD* is given below;

A rectangular matrix *A* can be broken down into the product of three matrices – an orthogonal matrix *U*, a diagonal matrix *S* and the transpose of an orthogonal matrix *V* (Equation (6.20));

$$A_{mn} = U_{mm} S_{mn} V_{nn}^{T} \tag{6.20}$$

where; $U^T U = I$, $V^T V = I$; the columns of *U* are orthonormal eigenvectors of AA^T, the columns of *V* are orthonormal eigenvectors of $A^T A$ and *S* is a diagonal matrix containing the square roots of eigenvalues of AA^T in descending order. If the values of *S* are close to 0, then the results of *IOP* inversion by linear least squares fitting (the *MEM*) will be unstable (Lawson & Hanson, 1995; Golub & Reinsch, 1970; Golub, 1968).

In the case of the *MEM*, the *SVD* results are shown in Equations (6.21) – (6.24). The singular matrix *S* shows that the third column is close to 0, this makes the results of the *MEM* unstable, resulting in large uncertainties in the recovered concentrations.

$$SIOPs = \begin{bmatrix} 1.4 & 0.06 & 0.08 \\ 1 & 0.08 & 0.06 \\ 0.56 & 0.06 & 0.04 \\ 0.43 & 0.04 & 0.03 \\ 0.33 & 0.03 & 0.02 \\ 0.25 & 0.02 & 0.015 \\ 0.08 & 0.02 & 0.01 \\ 0.06 & 0.04 & 0.005 \\ 1.4 & 0.18 & 0.48 \\ 1 & 0.20 & 0.46 \\ 0.56 & 0.18 & 0.44 \\ 0.43 & 0.16 & 0.43 \\ 0.33 & 0.15 & 0.42 \\ 0.25 & 0.14 & 0.415 \\ 0.08 & 0.14 & 0.41 \\ 0.06 & 0.16 & 0.405 \\ 0 & 0.12 & 0.40 \end{bmatrix} \quad (6.21)$$

$$U = \begin{bmatrix} -0.47235 & 0.379991 & 0.24604 \\ -0.33953 & 0.258799 & -0.31829 \\ -0.1916 & 0.135257 & -0.35672 \\ -0.14674 & 0.106135 & -0.19427 \\ -0.11336 & 0.075636 & -0.10796 \\ -0.08488 & 0.0647 & -0.07957 \\ -0.02841 & 0.012505 & -0.18753 \\ -0.02225 & 0.004691 & -0.49321 \\ -0.52278 & 0.002726 & 0.420473 \\ -0.38996 & -0.11847 & -0.14386 \\ -0.24203 & -0.24201 & -0.18228 \\ -0.19717 & -0.27113 & -0.01984 \\ -0.16379 & -0.30163 & 0.066475 \\ -0.13532 & -0.31256 & 0.094861 \\ -0.07884 & -0.36476 & -0.0131 \\ -0.07269 & -0.37257 & -0.31878 \\ -0.05043 & -0.37726 & 0.174433 \end{bmatrix} \quad (6.22)$$

$$S = \begin{bmatrix} 2.851326 & 0 & 0 \\ 0 & 1.038753 & 0 \\ 0 & 0 & 0.06949 \end{bmatrix} \quad (6.23)$$

$$V = \begin{bmatrix} -0.93787 & 0.345232 & 0.034871 \\ -0.13989 & -0.28422 & -0.9485 \\ -0.31754 & -0.89445 & -0.314853 \end{bmatrix} \quad (6.24)$$

6.5.5 Selection of the *IOP* inversion method most resistant to measurement uncertainties

Summarising the results in Section 6.5, the *AAC* set of equations was the most resistant of the *SEM* sets to simulated measurement uncertainty, and also produced more robust retrievals than the Gallegos & Neale (2002) Unconstrained Procedure and the *MEM* (Figure 6.8). The Gallegos & Neale (2002) results were the least resistant to measurement uncertainty for both *CDOM* and *MSS* concentration recoveries. The *MEM* and *AAC* methods were indistinguishable for the recovery of *MSS* concentration; however the *MEM* exhibited the most sensitivity to random noise for *CHL* concentration recoveries. In view of these results, the *AAC* inversion technique was adopted for the remainder of this work. The next problem is to establish how it performs if the *SIOPs* assumed for the inversion process are not an exact match for those used in creating the *IOP* data.

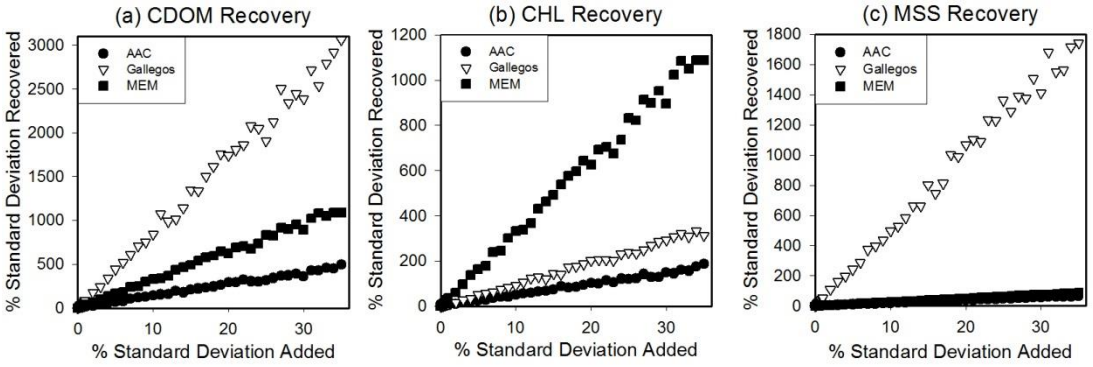

Figure 6.8: Comparison of all *IOP* inversion techniques for (a) *CDOM* concentration recovery, (b) *CHL* concentration Recovery and (c) *MSS* concentration recovery.

6.6 Recoveries using the *AAC* method with measurement uncertainties in the *IOPs*

Plot (a) in Figure 6.9 shows that there is a linear relationship between the percentage standard deviation added as measurement uncertainty and the percentage standard deviation in the recovered constituent concentrations.

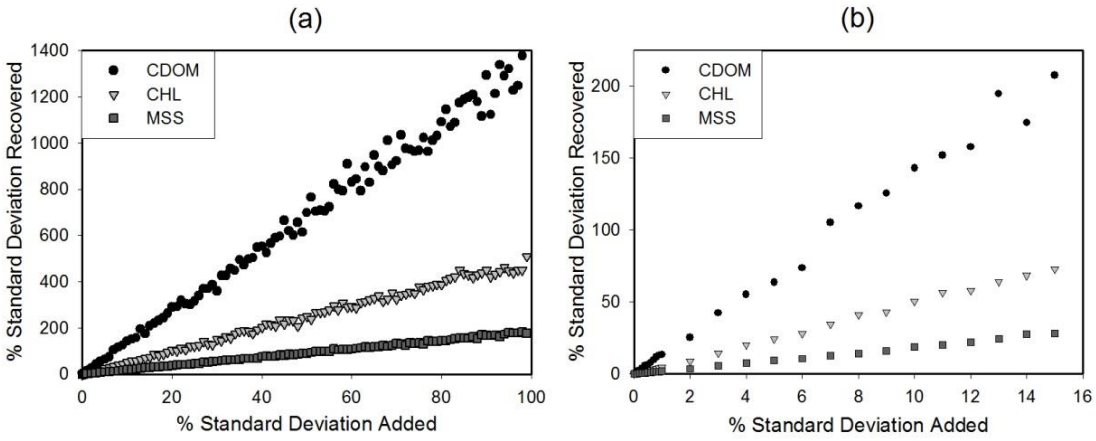

Figure 6.9: Standard deviation in the percentage error of the recovered concentrations for increasing amounts of measurement uncertainty added to the *IOPs* using the *AAC* inversion technique with (a) showing the full range of added measurement uncertainty and (b) showing the limited range associated with likely measurement uncertainties.

For a reasonable value of measurement uncertainty, i.e. up to about 15% standard deviation, Plot (b) in Figure 6.9 shows very large percentage standard deviations in the recoveries. According to the manufacturer's specifications, the *ac-9* has an absolute error of ± 0.003 m^{-1} (WET Labs, 2006). This translates to percentage errors of between 0.4% and 15% for the range of *IOPs* in the modelled data set. These results show that the uncertainties caused by instrument limitations can cause percentage uncertainties in *OSC* concentrations of up to 208% for *CDOM*, 74% for *CHL* and 29% for *MSS*. This is discussed in greater detail in Section 6.7.

6.6.1 Model Performance Check

To ensure that the modelled data set was recovering the constituent concentrations as expected, it was necessary to check that the *OSC* concentrations recovered had a Gaussian distribution with a standard deviation equal to the one shown in Plot (b) in Figure 6.9 for the same level of added measurement uncertainty. The histograms in Figure 6.10 show the percentage uncertainty in the recoveries for input *IOP* noise of 1%, 5% and 10% where the original concentration values of X_{CDOM} = 0.5 m^{-1}, X_{CHL} = 5 mg m^{-3} and X_{MSS} = 20 g m^{-3} for 10,000 iterations.

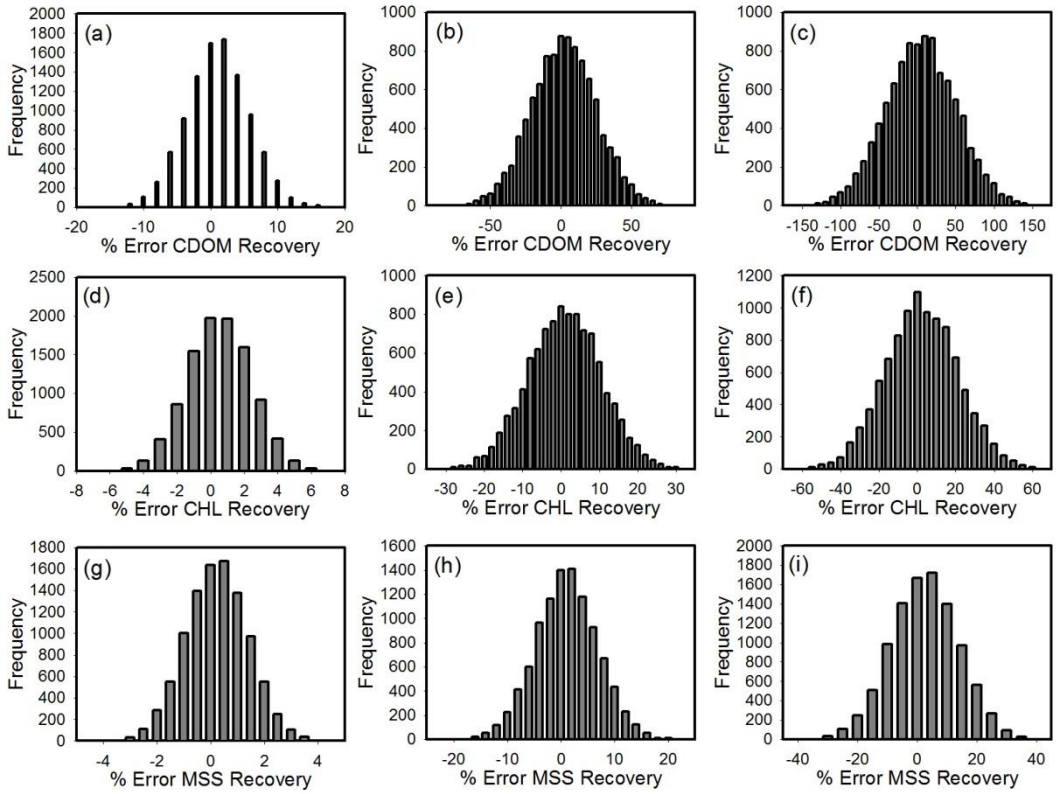

Figure 6.10: Histograms of percentage error in recovered *OSC* concentrations for (a) *CDOM* with σ = 1% (b) *CDOM* with σ = 5% (c) *CDOM* with σ = 10% (d) *CHL* with σ = 1% (e) *CHL* with σ = 5% (f) *CHL* with σ = 10% (g) *MSS* σ = 1% (h) *MSS* with σ = 5% & (i) *MSS* with σ = 10%

Table 6.2 shows that the mean value of the percentage error in the recovered concentrations is close to zero which is what would be expected when the *IOP* inversion procedure was performing correctly.

Table 6.2: Expected and actual mean and standard deviation values for the *OSC* concentration recoveries when tested on one set of concentrations. The expected mean is zero in all cases.

% σ	***CDOM***			***CHL***			***MSS***		
	$\bar{x}$	**σ**		$\bar{x}$	**σ**		$\bar{x}$	**σ**	
		Exp	**Act**		**Exp**	**Act**		**Exp**	**Act**
1%	0.05	13.4	4.66	0.02	4.82	1.89	-0.01	1.83	1.16
5%	-0.4	63.8	23.0	-0.005	24.3	9.52	0.05	9.41	5.80
10%	0.3	143	46.0	-0.1	50.6	19.02	0.07	18.9	11.4

Notice however that the actual standard deviations are considerably lower than those expected from Plot (b) in Figure 6.9. This is due to the use of only one set of *OSC*

concentrations as opposed to sampling across the full range of available concentrations. This result demonstrates that the uncertainties in the recovered concentrations are dependent on the relative contribution of each constituent to the total *IOP*. This point will be discussed in detail in Section 6.7.

6.7 The Effect of Water Type on the Recovery of Constituent Concentrations

The apparently large effect of measurement uncertainty on constituent concentrations (Figure 6.9) could be related to the way the modelled data set was constructed, since all possible combinations of constituents were considered equally and no weighting was given to those combinations which were most likely to occur in practice. It is possible that unrealistically small constituent concentrations have the effect of making the percentage standard deviation in the recoveries artificially large.

In order to examine this, values of the concentrations in the modelled data were converted into their contributions to the total absorption coefficient by means of Equation (6.25) (i is any constituent).

$$Z_i = \left(\frac{a_i(\lambda)}{a_{ac-9}(\lambda)} \right) \times 100 \tag{6.25}$$

Figure 6.11 shows the percentage of the constituent absorption contribution to the total absorption against the percentage error in the constituent recovery for measurement uncertainties of 1% standard deviation.

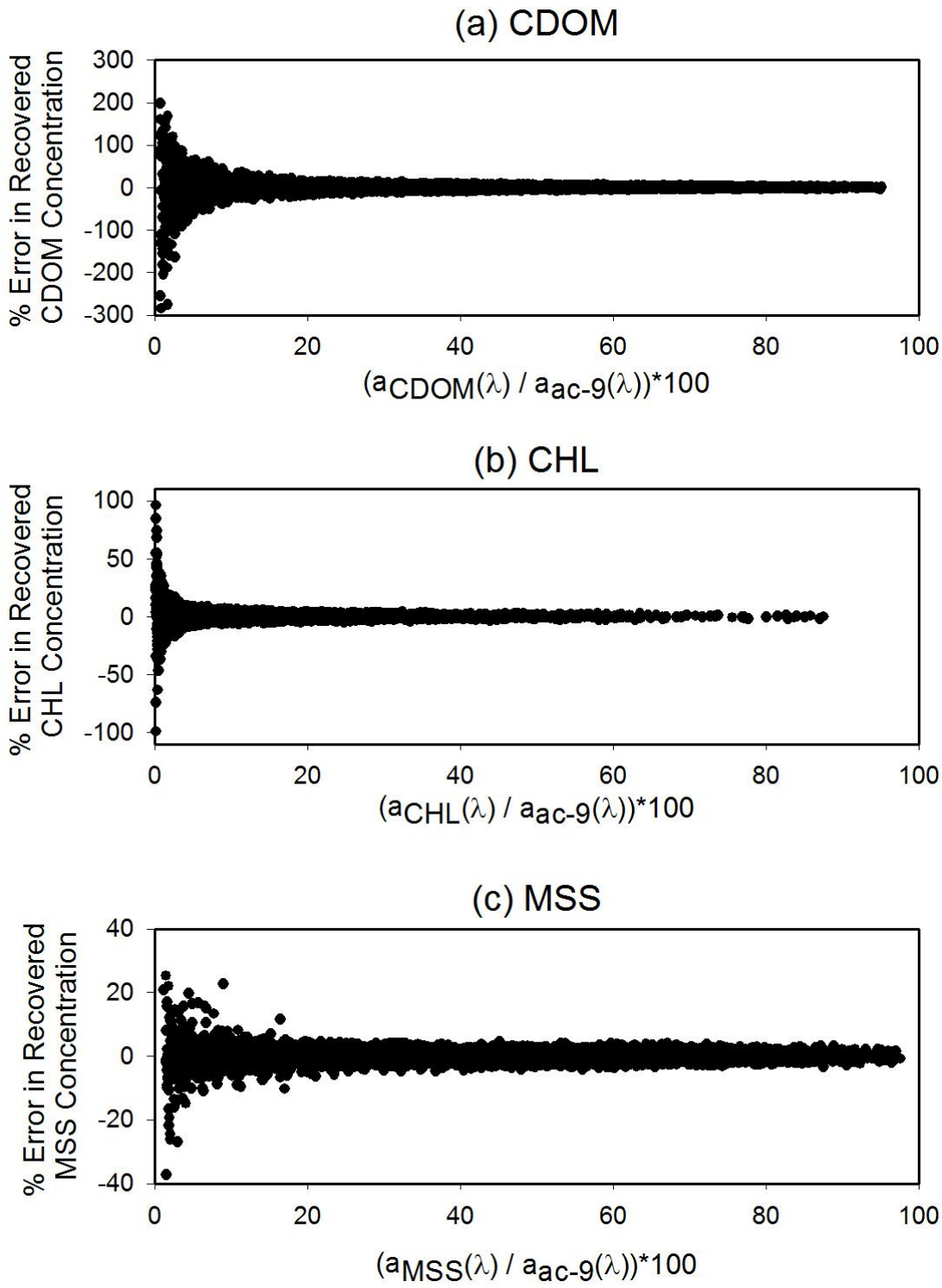

Figure 6.11: Percentage error in constituent recovery with percentage contribution of each constituent for measurement uncertainties of 1% standard deviation for (a) *CDOM*, (b) *CHL* and (c) *MSS*.

When the contribution of each constituent to the total absorption coefficient was low, the effects of measurement uncertainties were very large and that as the contribution increased there was a significant decrease in the percentage error of the constituent recovery. This indicates that the quality of the recoveries obtained from the *IOP* inversion process depends on the composition of the water to which it is applied.

For the Irish Sea and adjacent waters, four conceptual water types could be defined. *Offshore* water has low concentrations of each constituent and can be found in the middle of the Irish Sea away from the coasts, *muddy* water has a large concentration of *MSS* and low concentrations of *CDOM* and *CHL* and is found, for example, in the Bristol Channel. *Fjord* water has high concentrations of *CDOM* and low concentrations of *CHL* and *MSS* and is found in the Scottish Sea Lochs and *bloom* water has a high concentration of *CHL* and low concentrations of *CDOM* and *MSS* and occurs in some parts of the Irish Sea in the spring and summer months. These four distinct water types were defined by assigning appropriate concentrations for each constituent and the contribution of each constituent to the total absorption was calculated. This allowed the expected uncertainty in the recovered concentration for each constituent to be determined for each water type by averaging the absolute values of the results shown in Figure 6.11. The definition of each water type and the relative contribution to the absorption coefficient and the expected percentage error are shown in Table 6.3. These results show that the uncertainties in recovered *OSC* concentrations are heavily dependent on the water type being examined. In the case of real *IOP* data (Chapter 7) the change in water type might also result in a change in the *SIOP* values. This would increase the uncertainties in the recovered *OSC* concentrations with changing water types.

Table 6.3: Contributions to the total absorption from each constituent for 4 water types and the absolute value of the percentage error in the recoveries (predicted from Figure 6.11) for measurement uncertainties of 1% standard deviation.

Water Type	**Concentrations**			**% of Total Absorption**			**% Error in Recoveries**		
	CDOM **/m^{-1}**	***CHL*** **/mg m^{-3}**	***MSS*** **/g m^{-3}**	***CDOM***	***CHL***	***MSS***	***CDOM***	***CHL***	***MSS***
Offshore	0.21	2.1	2	42	34	24	2.64	0.75	0.95
Muddy	0.21	2.1	15	16	13	71	4.14	1.82	0.04
Fjord	0.51	2.1	2	64	21	15	1.35	1.79	2.05
Bloom	0.21	9.6	2	19	70	11	4.07	0.66	2.37

6.8 The Problem with *SIOP* uncertainties

The results obtained by using the *AAC* method to recover constituent concentrations indicated a large sensitivity to the relative contribution of the individual constituents to the total *IOPs*, and a similar sensitivity is likely to arise in response to uncertainties in the *SIOPs*. Preliminary tests (not presented here) showed that the standard deviations in the *SIOPs* tabulated by Neil et al. (2011) were too large for sensible constituent concentration recoveries to be made. The values used in the tests carried out in the following section were therefore significantly reduced.

Four sets of *OSC* concentrations (and hence *IOP* values) were selected to represent each of the water types described in Section 6.7. For each set of concentrations, 10,000 attempts were made to recover individual values using different assumptions regarding the *SIOPs*. The *SIOP* uncertainties were modelled as a fraction of the 412 nm values for *CHL* and *MSS*, and of the log slope for *CDOM* For example if 1% *SIOP* uncertainty is added, the standard deviation of the uncertainty added is 1% of the $a^*_{CDOM}(\lambda)$ slope in the case of $a^*_{CDOM}(\lambda)$, 1% of $a^*_{CHL}(412)$ in the case of $a^*_{CHL}(\lambda)$, 1% of $a^*_{MSS}(412)$ in the case of $a^*_{MSS}(\lambda)$, 1% of $c^*_{CHL}(412)$ in the case of $c^*_{CHL}(\lambda)$ and 1% of $c^*_{MSS}(412)$ in the case of $c^*_{MSS}(\lambda)$.

6.8.1 Recoveries using the *AAC* method with *SIOP* uncertainties.

The coefficient of variance (*CV*) is defined for each *OSC* concentration recovery against the percentage of $a^*_i(412)$ added as *SIOP* uncertainty for each of the water types defined in Table 6.4.

$$CV_i = \frac{\sigma(X_i)}{\bar{X}_i} \tag{6.26}$$

where CV_i, is the coefficient of variance in constituent i, $\sigma(X_i)$ is the standard deviation in the recovered concentration and $\bar{X}_i$ is the mean recovered concentration. Figure 6.12 shows the *CV* for each *OSC* concentration recovery against the percentage of $a^*_i(412)$ added as *SIOP* uncertainty for each of the water types defined in Table 6.4.

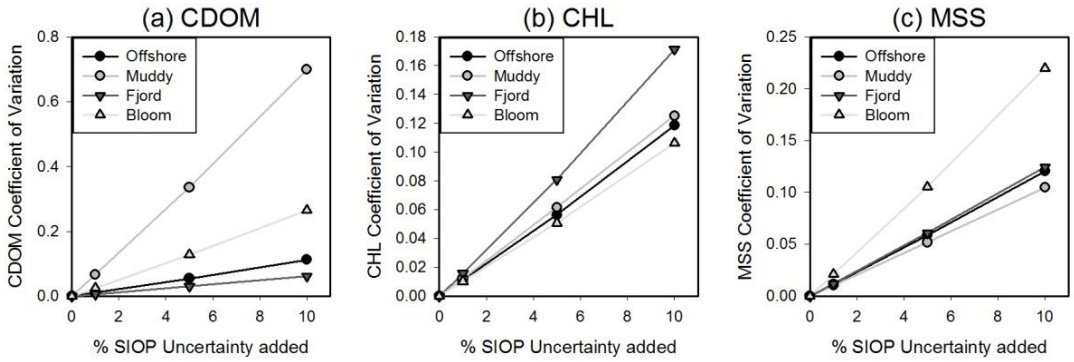

Figure 6.12: Coefficient of variation for recovered (a) *CDOM*, (b) *CHL* and (c) *MSS* concentrations with increasing *SIOP* uncertainties added for each of the defined water types.

For each *OSC* the least sensitivity occurred for the water type where the *OSC* was dominant. Thus the maximum sensitivity of *CDOM* concentration recovery occurred in *muddy* water, for *CHL* concentration recoveries the highest sensitivity occurred in *fjord* water, and for *MSS* concentration recoveries greatest sensitivity occurred in *bloom* water.

The concentrations input into the system and the mean values recovered are shown in Table 6.4, where it can be seen that *CDOM* was underestimated for each water type and *MSS* was overestimated.

Table 6.4: *OSC* concentration recoveries using the *AAC* inversion method subjected to *SIOP* uncertainties. The recovered mean value shown is the average across all noise levels examined.

OSC	**Offshore**		**Fjord**		**Bloom**		**Muddy**	
	In	**Out**	**In**	**Out**	**In**	**Out**	**In**	**Out**
CDOM	0.21	0.197	0.51	0.498	0.21	0.155	0.21	0.185
CHL	2.1	2.094	2.1	2.087	9.6	9.593	2.1	2.086
MSS	2	2.246	2	2.248	2	2.999	15	15.471

The spread of results for each water type is shown in Figure 6.13 – Figure 6.16, where the histograms show the spread for *CDOM*, *CHL* and *MSS* concentrations with 1%, 5% and 10% *SIOP* uncertainties added to the modelled data set. These figures demonstrate that a relatively small amount of uncertainty in the *SIOPs* can produce a large spread in values for the recovered constituent concentrations.

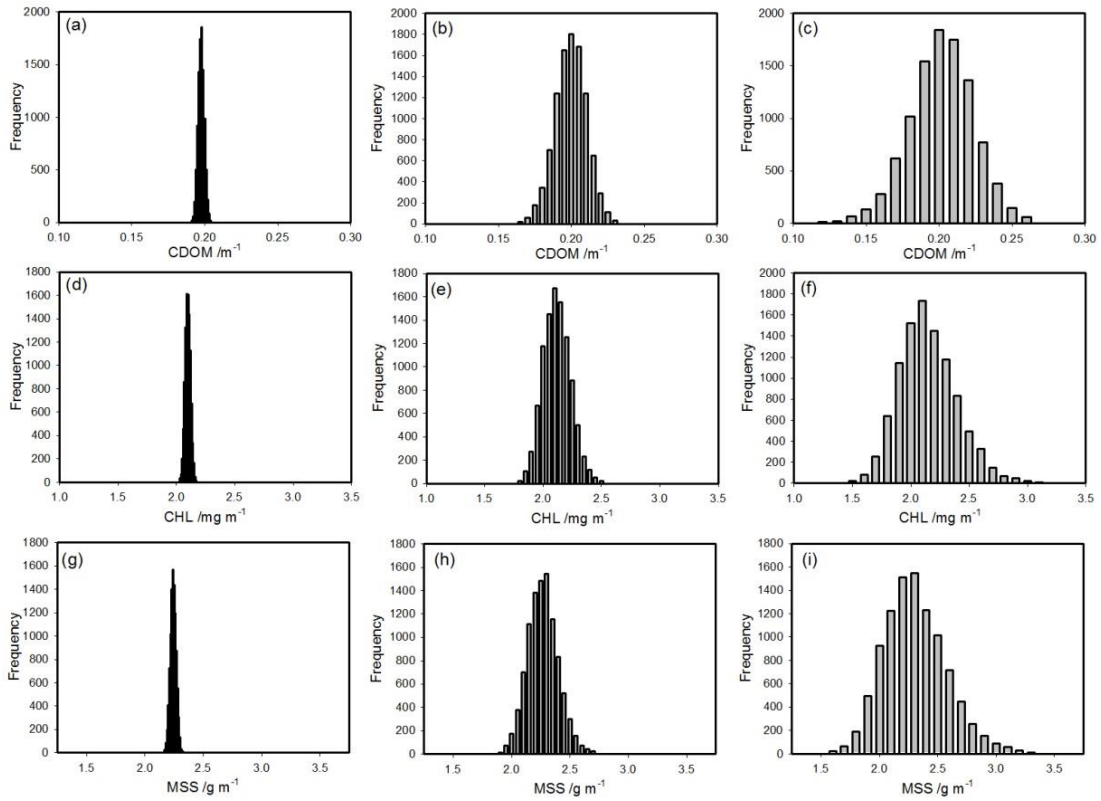

Figure 6.13: Histograms showing the range of *OSC* concentration recoveries with added *SIOP* uncertainties for *offshore* water. (a) - (c) *CDOM* concentration recovery for 1%, 5% and 10% respectively, (d) - (f) *CHL* concentration recovery for 1%, 5% and 10% respectively and (g) - (i) *MSS* concentration recovery for 1%, 5% and 10% respectively.

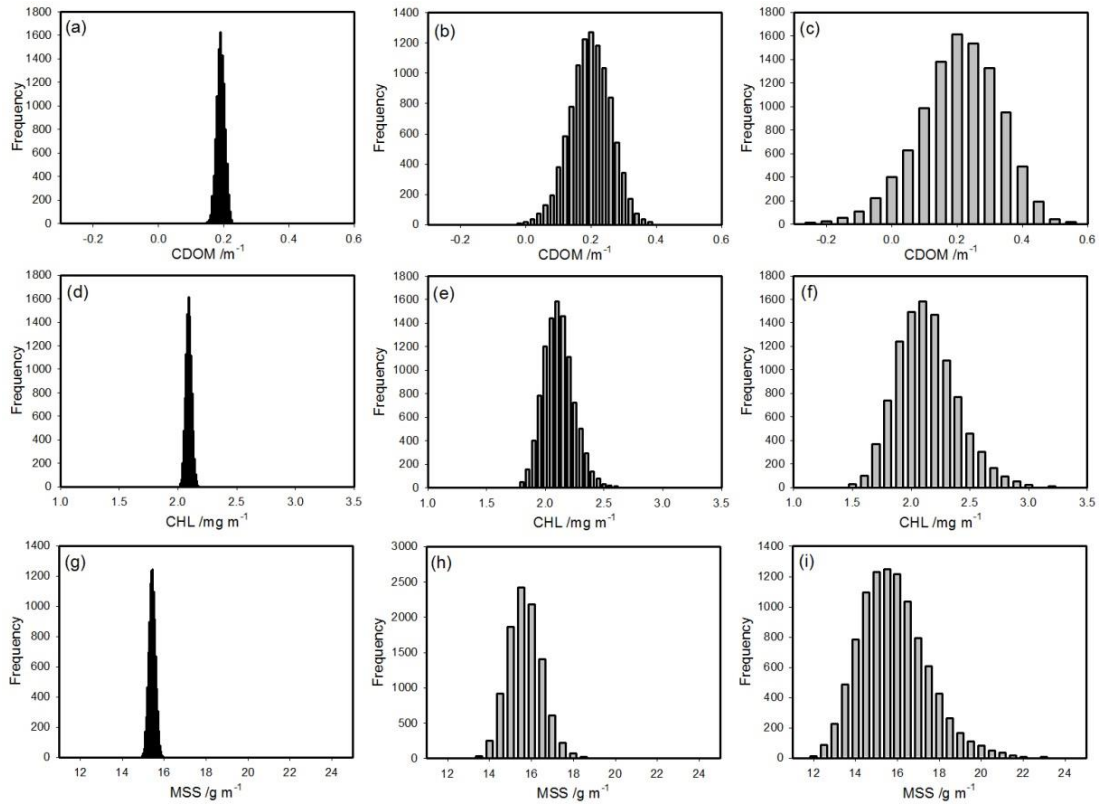

Figure 6.14: Histograms showing the range of *OSC* concentration recoveries with added *SIOP* uncertainties for *muddy* water. (a) - (c) *CDOM* concentration recovery for 1%, 5% and 10% respectively, (d) - (f) *CHL* concentration recovery for 1%, 5% and 10% respectively and (g) - (i) *MSS* concentration recovery for 1%, 5% and 10% respectively.

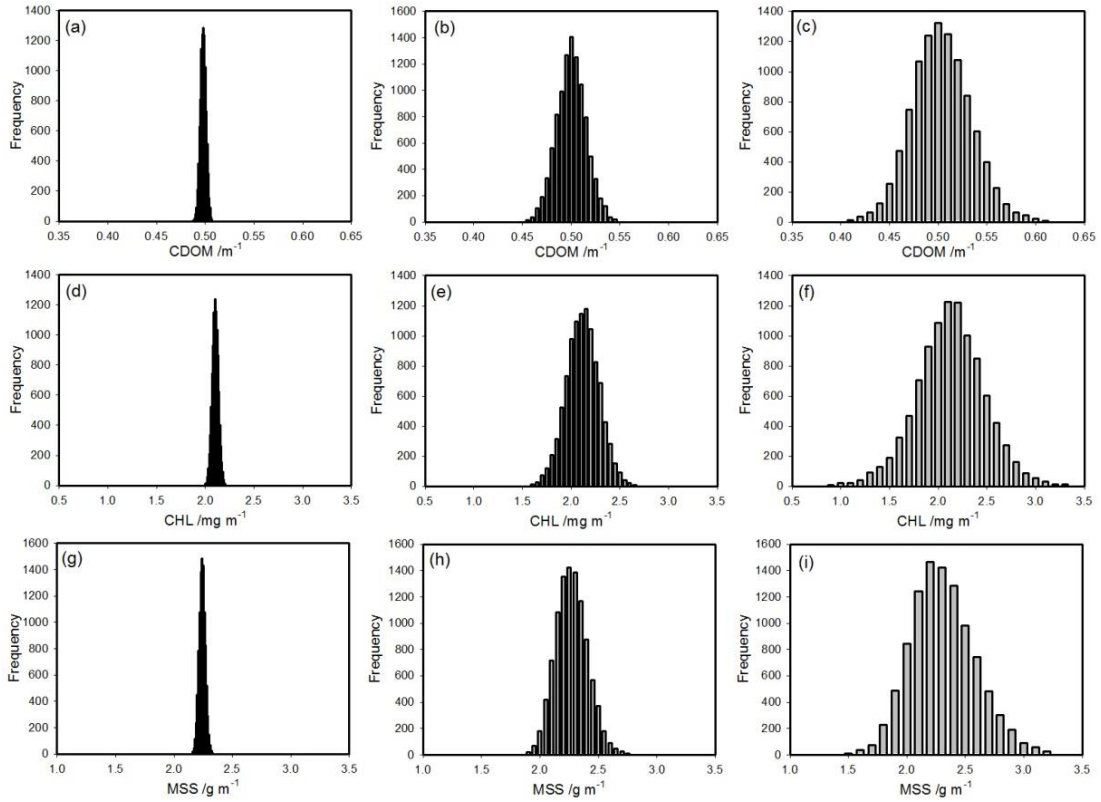

Figure 6.15: Histograms showing the range of *OSC* concentration recoveries with added *SIOP* uncertainties for *fjord* water. (a) - (c) *CDOM* concentration recovery for 1%, 5% and 10% respectively, (d) - (f) *CHL* concentration recovery for 1%, 5% and 10% respectively and (g) - (i) *MSS* concentration recovery for 1%, 5% and 10% respectively.

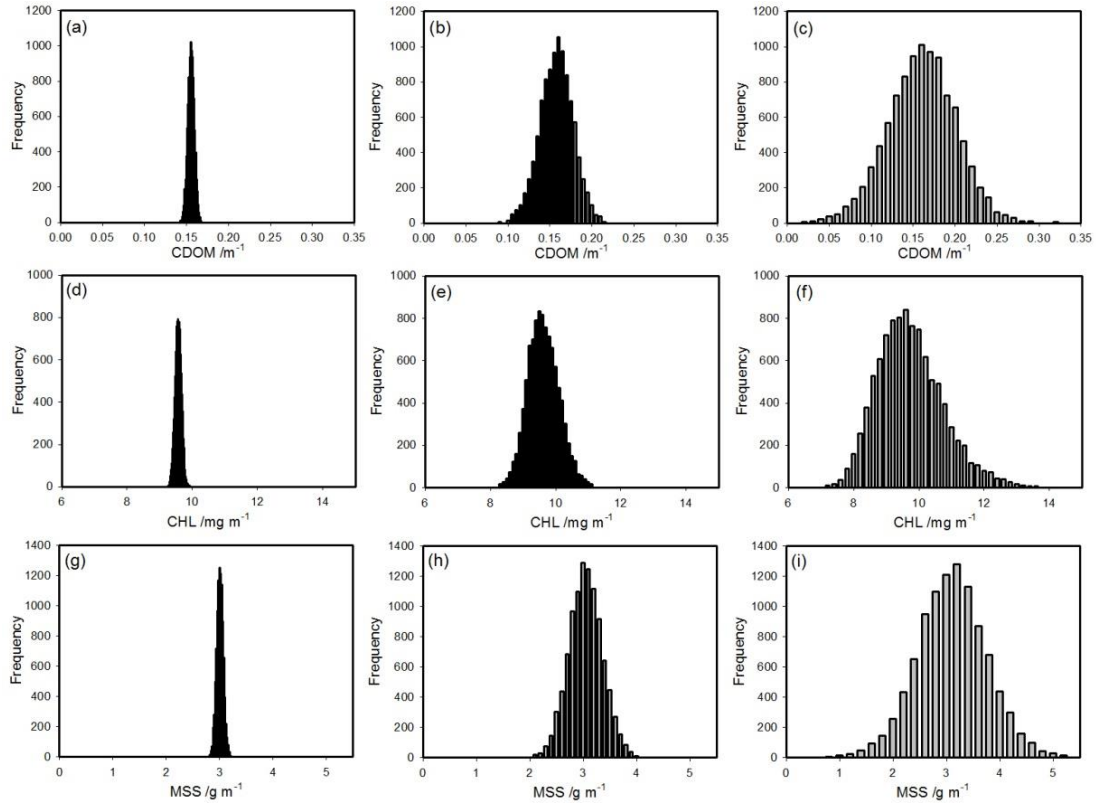

Figure 6.16: Histograms showing the range of *OSC* concentration recoveries with added *SIOP* uncertainties for *bloom* water. (a) - (c) *CDOM* concentration recovery for 1%, 5% and 10% respectively, (d) - (f) *CHL* concentration recovery for 1%, 5% and 10% respectively and (g) - (i) *MSS* concentration recovery for 1%, 5% and 10% respectively.

It appears, therefore, that inversion of *ac-9* data using the optimum (*AAC*) method is more sensitive to uncertainties in the assumed values of the *SIOPs* than to measurement uncertainties in the *IOPs*.

6.9 *OSC* Recoveries when both measurement uncertainties and *SIOP* uncertainties are considered.

In order to demonstrate the recovery errors that could be expected for field data, a test was conducted with uncertainties added to both the *IOPs* and the *SIOPs* using the *offshore OSC* concentrations. From the analysis of *ac-s* signals (Chapter 3), uncertainties are expected to be of the order of 8% in the *IOPs* just from instrument noise. The standard deviation in the percentage error for the recovered

concentrations would be very large for this amount of input *IOP* noise. The standard deviations on the *SIOP* values derived by Neil et al. (2011) (~ 30% of the mean values) were also too large to recover constituent concentrations. For demonstration purposes, the uncertainties were halved; Figure 6.17 shows histograms of the *OSC* concentration recoveries for 4% measurement uncertainties in the *IOPs*, 15% uncertainty in the *SIOPs* and both 4% uncertainty in the *IOPs* and 15% uncertainty in the *SIOPs* together.

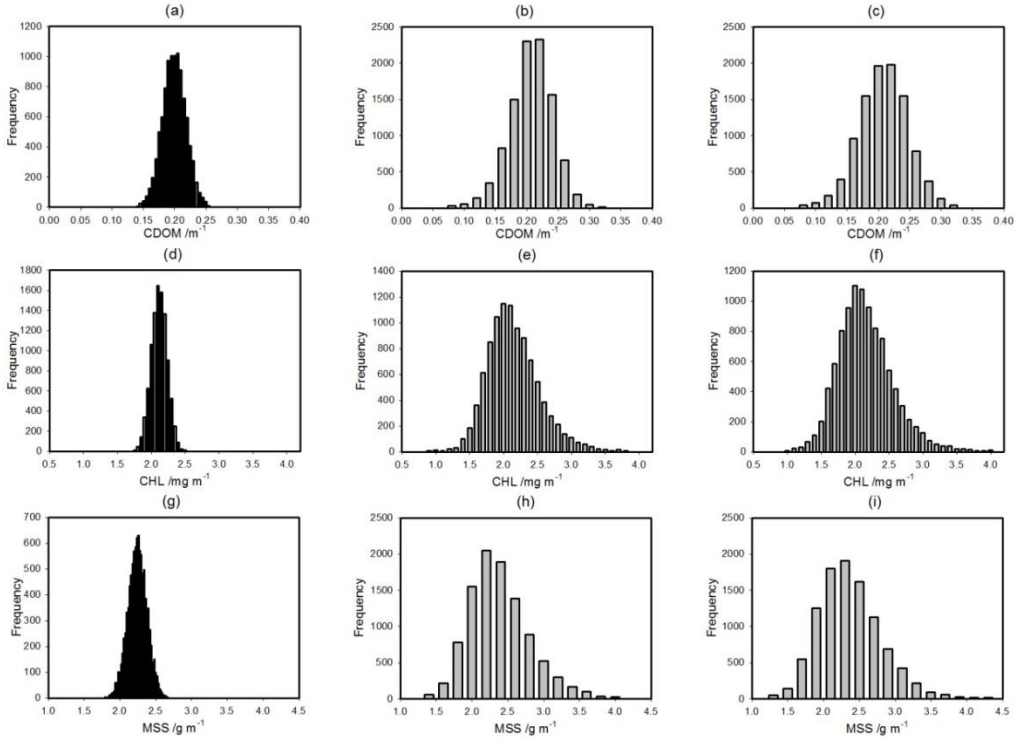

Figure 6.17: Histograms showing the range of *OSC* concentration recoveries with added uncertainties for *offshore* water. (a) - (c) *CDOM* concentration recovery for 4% *IOP* uncertainty, 15% *SIOP* uncertainty and both uncertainties combined. (d) - (f) *CHL* concentration recovery for 4% *IOP* uncertainty, 15% *SIOP* uncertainty and both uncertainties combined. (g) - (i) *MSS* concentration recovery for 4% *IOP* uncertainty, 15% *SIOP* uncertainty and both uncertainties combined.

Clearly, uncertainties in the *SIOPs* have a larger impact on the errors in the recovered *OSC* concentration than the *IOPs*. When the uncertainties in *IOPs* and *SIOPs* are applied together the uncertainty in the recovered *OSC* concentrations is the result of the *IOP* and *SIOP* uncertainties adding in quadrature. The mean and standard deviation for each *OSC* recovery is shown in Table 6.5.

Table 6.5: Mean ($\bar{x}$), standard deviation (σ), and σ as a percentage of $\bar{x}$ of *OSC* concentrations recovered for *offshore* water with measurement uncertainty in the *IOPs* only, *SIOPs* only and both *IOP* and *SIOP* uncertainties in the measureable range and then realistic uncertainty levels Neil et al. (2011).

Errors In	***CDOM***			***CHL***			***MSS***		
	$\bar{x}$	**σ**	**%**	$\bar{x}$	**σ**	**%**	$\bar{x}$	**σ**	**%**
4% *IOPs*	0.197	0.019	9.68	2.092	0.118	5.63	2.237	0.134	5.97
15% *SIOPs*	0.197	0.035	17.7	2.097	0.400	19.1	2.289	0.440	19.2
4% *IOPs* & 15% *SIOPs*	0.197	0.040	20.2	2.106	0.425	20.2	2.272	0.454	20.0
8% *IOPs* & ~30% *SIOPs*	0.193	0.164	85.1	1.973	1.701	86.2	2.497	2.555	102

When the tests in Figure 6.17 were completed for higher, but realistic, levels of uncertainty in both the *IOPs* and *SIOPs*, the standard deviations in the recovered concentrations were more than four times larger than for the previous test. Consequently, the inversion of real *ac-s* field data might be expected to pose a significant challenge.

When these results are coupled to the results from the change in water type analysis in Section 6.7, it can be assumed that the appropriateness of the *SIOP* values for a given water type (Section 2.6) will need to be considered before an attempt at *IOP* inversion is made.

6.10 Chapter Summary

1. Three methods were considered for recovering constituent concentrations from total *IOP* measurements. The first was the Unconstrained Procedure of Gallegos & Neale (2002), the second was a set of three simultaneous equations consisting of any combination of absorption and attenuation wavelengths and the third (*MEM*) used all available *ac-9* data and recovered constituent concentrations using spectral least squares fitting.

2. All of the methods were tested with modelled *ac-9* data (0) and recovered perfect *OSC* concentrations when no measurement uncertainties were added. When measurement uncertainties were added to the modelled data set, the three methods showed differing sensitivity to the added uncertainties. The

most resistant to uncertainties was the *AAC* method, where two absorption wavelengths and one attenuation wavelength were used in simultaneous equations to recover *OSC* concentrations.

3. Further testing of the AAC method showed that the recovery of *CDOM* concentration was most sensitive to measurement uncertainties in the *IOP* data. When the percentage standard deviation added to the *IOPs* was compared to the standard deviation in the percentage error of the recovered constituent concentrations, all three *OSC* recoveries displayed a linear response. This meant that the uncertainty in recovered constituent concentrations could be easily predicted when uncertainty in the *IOPs* was known.

4. The relative contribution of the *OSC* concentration to the total *IOPs* played a major role in determining the uncertainties in the constituent recoveries. An examination of different conceptual water types showed that for 1% standard deviation in the *IOPs*, standard deviations in *MSS* concentration recovery (for example) varied from 0.04% in *muddy* water to 2.37% in *bloom* conditions.

5. The effect of *SIOP* uncertainties was also tested for the four distinct water types, but for a smaller range than the standard deviations given in Neil et al. (2011). *CDOM* concentration recovery was most sensitive in *muddy* water, *CHL* concentration recovery in *fjord* water and *MSS* concentration recovery in *bloom* water. In addition, a general tendency to underestimate *CDOM* and an overestimate *MSS* was observed.

When a realistic combination of expected uncertainties was applied, the uncertainty in the recoveries increased to 85% for *CDOM* and *CHL* and 102% for *MSS* concentration recoveries. These values suggest that recovering *OSC* concentrations for field data using the inversion methods considered in this chapter is likely to pose considerable challenges.

Chapter 7 *IOP* inversion applied to field *ac-9* measurements

The results from testing linear *IOP* inversion procedures using modelled *ac-9* data with added noise and *SIOPs* uncertainties suggested that unacceptably high errors might occur in the recovery of *OSC* concentrations. In order to determine how this applied to *IOP* measurements made using an *ac-9* in the field; the three-equation inversion procedure was applied to an archived data set from the UK shelf sea. This chapter reviews attempts to recover *OSC* concentrations from *ac-9* measurements made in situ, and considers whether any discrepancies occur at random or if some structure is discernable that might hint at underlying mechanisms. It also considers whether *IOP* inversion results (on their own or in combination with data from other optical instruments) might be used as an indicator of links between the physical and biological structure of the water column. This would allow the *ac-9* optical signal to be usefully used in conjunction with other optical and physical data even if there were systematic errors in the recovered *OSC* concentrations.

7.1 *IOP* Inversion method applied to West Shelf data set

7.1.1 West Shelf Data Selection

Data were taken from an archived data set for the UK shelf sea which included stations in the Bristol Channel, Clyde Sea, Irish Sea, Loch Etive, Oban and the Sound of Jura. The UK shelf map, Figure 7.1 (more detail in Appendix B) shows data collection areas and the number of stations in each. *ac-9* data from the archive were selected only where concurrent *OSC* concentration measurements were available. From this selected data set, obvious outliers in recovered *OSC* concentrations and low values that could not have been accurately recovered using the techniques outlined in Chapter 4 were removed. The acceptable ranges of *OSC* concentrations are given in Table 7.1.

.

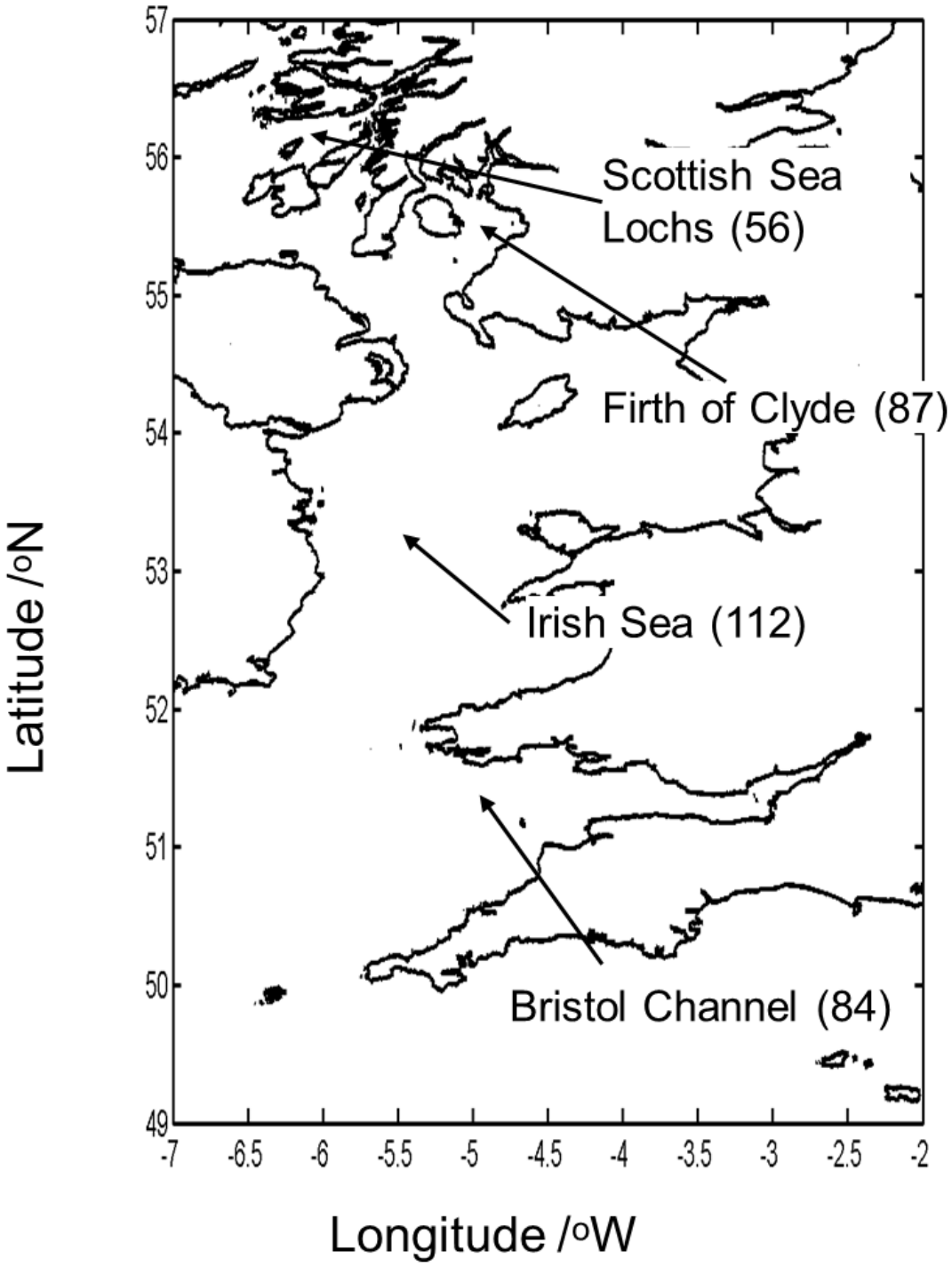

Figure 7.1: Map of UK shelf sea with the cruise areas indicated and the number of suitable stations in each area indicated in brackets.

Table 7.1: Ranges of *OSC* Concentrations within the archive data set selected to test the *AAC* inversion method for field *ac-9* measurements.

OSC	**Minimum Concentration**	**Maximum Concentration**
CDOM	0.015 m^{-1}	1.5 m^{-1}
CHL	0.2 mg m^{-3}	20 mg m^{-3}
MSS	0.3 g m^{-3}	30 g m^{-3}

Quality-controlling the data in this way allowed the *IOP* inversion method to be tested without adding additional uncertainty by including extremes in the measured *OSC* concentrations. It provided a total of 339 *OSC* concentration measurements for testing the *IOP* inversion procedure.

7.2 Results from inverting West Shelf *ac-9* data

Figure 7.2 shows the recovered *OSC* concentrations plotted against the measured values for the selected shelf sea data set, together with histograms showing the distributions of percentage errors in recovered concentrations for each case. It can be seen that a significant proportion of all three *OSC* concentration recoveries were underestimated. This underestimation was not observed when the same inversion method was applied to the modelled data, and appears to indicate that the *SIOP* values used in the inversion were not a perfect match for the field data.

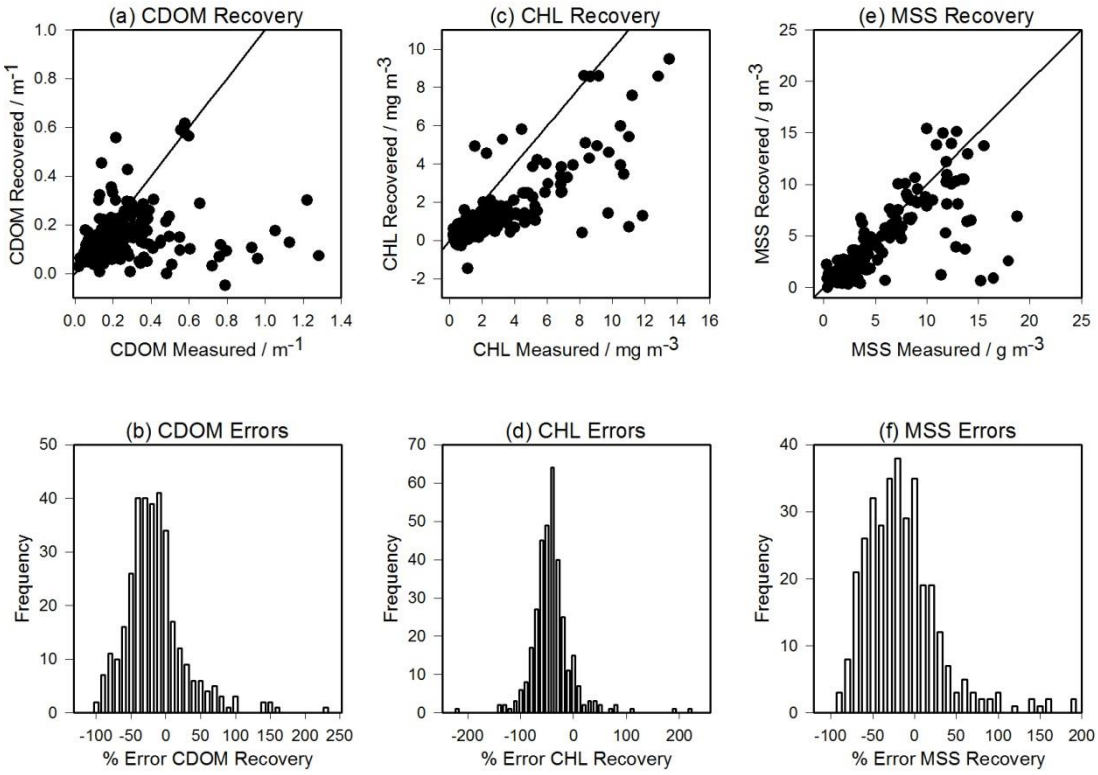

Figure 7.2: The recovered concentration against the measured concentration for each *OSC* for the UK Shelf data set with histograms of the percentage error in each case, (a) *CDOM* recovered against measured concentration, (b) histogram of the percentage error in the recovered *CDOM* concentration, (c) *CHL* recovered against measured concentration, (d) histogram of the percentage error in the recovered *CHL* concentration, (e) *MSS* recovered against measured concentration, (f) histogram of the percentage error in the recovered *MSS* concentration. 1:1 lines are drawn on Plots a, c and e.

At first glance, the results in Figure 7.2 appear to be somewhat better than might have been predicted from (Chapter 6). However closer examination (Table 7.2) shows that less than half of the stations exhibit recoveries that fall within ± 20% of the measured values, which was considered to be a reasonable level of uncertainty for ecological studies. Moreover, none of the 339 stations investigated had recovery errors below 30% when all three *OSCs* were considered.

These results indicate that a simple, globally applicable procedure for inverting *IOP* data acquired in shelf seas based on the simultaneous equation approach with fixed *SIOP* assumptions is not likely to provide *OSC* concentrations that match those

measured *in situ*, in spite of the promising performance obtained for a noise-free synthetic data set.

Table 7.2: Table showing the number of stations with uncertainties within the predicted range of 20%

***OSC* Concentration Recovered**	**Number of stations with uncertainty ± 20%**	**Percentage of stations with uncertainty ± 20%**
CDOM	143	42%
CHL	60	18%
MSS	140	41%

7.3 Feature mapping and water classifications in the Scottish Sea Lochs

In order to better understand the operation of the inversion procedure, four stations in Scottish sea lochs were examined in detail. Sea lochs (Scottish fjords) were particularly suited for this work because they usually exhibit marked stratification generated by repeated inflows of low salinity, high nutrient water which floats on top of a dense, relatively stagnant deeper layer. This stratification allowed the possibility of changes in the proportions of the optically significant constituents (effectively changes in water type) within each profile to be investigated, and it was hoped that it would provide some insight into the origins of errors in the *IOP* inversion process. Figure 7.3 shows the location of the four stations analysed in this section: Inchmarnock Water (CL01-09), Loch Striven (CL01-18), Rothesay Bay (CL01-19) and Loch Creran (SJ04-15).

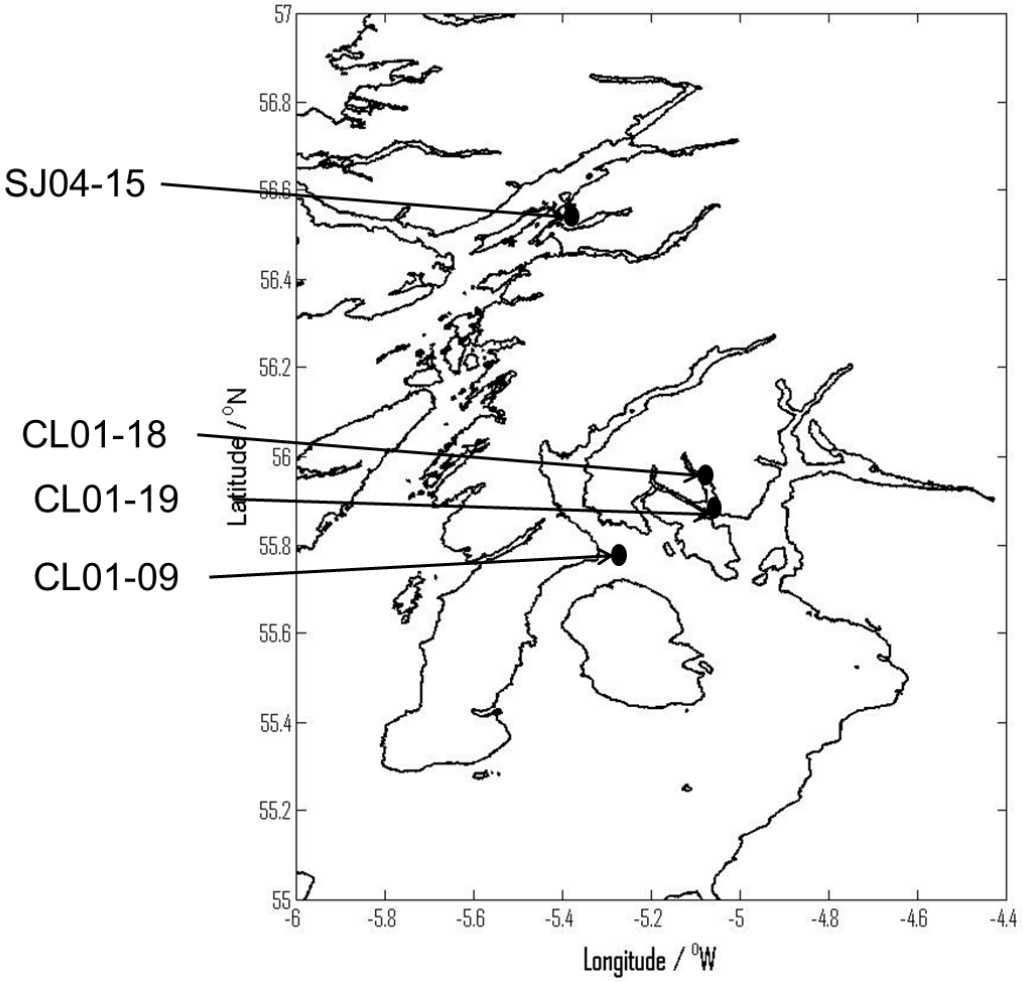

Figure 7.3: Map of Scottish Sea Lochs with black dots indicating the location of each of the four stations to be analysed further. CL01-09 is located in Inchmarnock Water, north of Arran at the mouth of Loch Fyne. CL01-18 is located in Loch Striven. CL01-19 is Rothesay Bay and SJ04-15 is further north in Loch Creran.

7.3.1 Recoveries of *OSC* concentrations for the selected Scottish Sea Loch Stations

Table 7.3 shows the measured and recovered *OSC* concentrations for each of the four stations. The recovered *OSC* concentrations are generally underestimated when compared to the measured values, which is consistent with the result obtained for the shelf sea data set.

Table 7.3: Measured and recovered *OSC* concentrations for the four stations to be analysed in closer detail.

Station Code	Depth /m	*CDOM* /m^{-1}		*CHL* /mg m^{-3}		*MSS* /g m^{-3}	
		Actual	**Recovered**	**Actual**	**Recovered**	**Actual**	**Recovered**
CL01-09	0	0.5503	0.1486	3.8913	1.3614	2.2333	1.3119
	5	0.3085	0.1423	2.7132	1.3813	2.0000	1.3131
	40	0.1957	0.1491	0.9942	0.2164	2.3667	1.2553
CL01-18	0	0.2533	0.217	6.8544	2.506	0.9333	0.832
	10	0.3039	0.271	11.0313	0.713	1.1667	0.823
	50	0.2924	0.245	1.5478	4.925	2.300	0583
CL01-19	0	0.1980	0.155	8.1396	0.383	1.567	1.719
	7	0.3039	0.266	10.7100	3.467	1.667	0.861
	20	0.3477	0.242	5.3907	4.206	1.900	0.791
SJ04-15	0	0.1993	0.334	3.1331	1.796	1.1778	1.551
	40	0.3384	0.251	1.2241	0.417	1.8222	1.167

7.3.2 Results from Inchmarnock Water (CL01-09)

The first station to be examined was CL01-09 (Figure 7.3), located in Inchmarnock Water, north of Arran at the mouth of Loch Fyne. This station, which is located at the meeting point of several arms of the Firth of Clyde, was selected as the backscattering peak occurred at mid-depth rather than at the bottom, which makes the station interesting from the point of view of the distribution of suspended mineral particles. *OSC* concentration measurements were made at three different depths at the station, and both the measured and recovered concentrations are shown in Table 7.3.

a An examination of water column structure.

In order determine whether the apparent failure of the inversion procedure occurred randomly or in a structured manner, additional information available for the station was used. This included fluorescence and backscattering profiles acquired using a HOBILabs Hydroscat 2 (*HS2*) as well as *CTD* measurements of temperature and salinity. To start with, two scatterplots were made. In the first, fluorescence was plotted against backscattering at 676 nm (b_b(676)). Only phytoplankton cells fluorescence in this waveband and these cells have relatively low backscattering

efficiencies. In contrast, suspended mineral particles do not exhibit red fluorescence and are strong sources of optical backscattering. Therefore a plot of fluorescence against $b_b(676)$ should separate the *CHL* and *MSS* dominated regions within the profile. The second scatterplot displayed $b_b(676)$ against total scattering at 676 nm ($b_{ac\text{-}9}(676)$). The ratio of $b_b(676)$ and $b_{ac\text{-}9}(676)$ is closely related to the scattering phase function (Chapter 2) and can therefore be used to distinguish between different particle assemblages (Boss et al., 2009a). These two plots, when examined concurrently should provide useful insights into the dominant particle types and their location within a water column. Figure 7.4 shows these plots for CL01-09.

Figure 7.4 (a) suggests that the fluorescence/backscattering data can be split into three distinct Clusters, labelled A, B and C. Figure 7.5 shows that these Clusters occupy different depths in the water column, with Cluster A corresponding to the surface, Cluster B to mid depth and Cluster C to the bottom of the profile. The high fluorescence and low backscattering (Figure 7.4 (a)) in Cluster A suggests that the particle population in the upper layer was dominated by phytoplankton cells. Cluster C, with high backscattering and low fluorescence, appears to consist of a high proportion of mineral particles. Cluster B, which exhibited higher fluorescence for a given backscattering coefficient than Cluster C, is more difficult to interpret but might consist of a mixture of the two particle types. Some support for this interpretation is provided by Figure 7.4 (b), which shows Hydroscat backscattering plotted against *ac-9* total scattering with the position of the Plot (a) Clusters indicated. Data points for Clusters B and C follow a single line. The fact that these two Clusters are collinear suggests that they have the same phase functions, and by implication may have similar particle size distributions. Cluster A, tentatively identified as phytoplankton cells, follows a line in Plot (b) that is clearly divergent from Clusters B and C. The particles in A therefore, have a quantifiably different scattering phase function, suggesting that the scattering originates from a different particle type. Cluster B has a small fluorescence component which suggests the inclusion of some (possibly senescent) phytoplankton cells in the mixture.

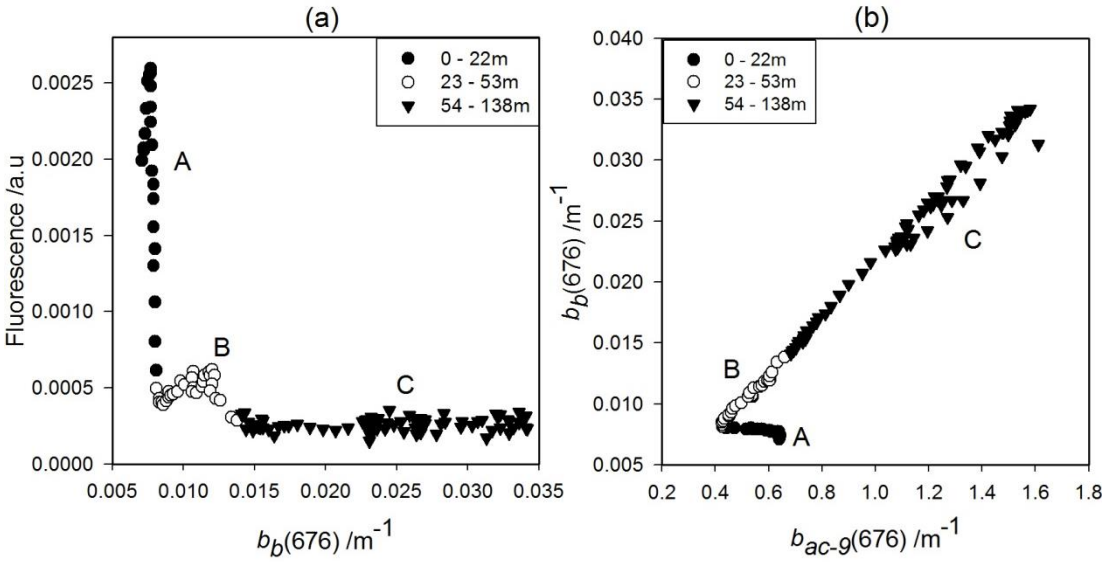

Figure 7.4: Examination of optics measurements for CL01-09 to determine sections of the profile with similar optical characteristics with (a) Fluorescence and backscattering to determine areas of *CHL* and *MSS* and (b) backscattering and scattering to examine areas with different characteristics, labelled A, B and C.

When the positions of the Clusters identified in Figure 7.4, Plot (a), are indicated on measured profiles of temperature, salinity, fluorescence and backscattering (Figure 7.5), it becomes obvious that the optical properties of the water column are vertically structured, and that this structure corresponds to some extent to identifiable hydrographic features. Cluster A, which has high fluorescence and low backscattering, occupies a surface layer with relatively high temperature and low salinity. Cluster B, with the decreasing fluorescence and increasing backscattering, occupies an intermediate layer which has the lowest temperature of the profile and higher salinity than the surface layer. Cluster C has very low fluorescence, elevated backscattering, and occupies the lowest 85 m of the water column. The $b_b(676)$ / $b(676)$ plot suggests that the particle population is homogeneous throughout this lowest layer, but there is an interesting feature at around 90 m where particle abundance appears to increase (Figure 7.5 Plot (d)) just above a marked step in the temperature profile (Figure 7.5 Plot (a)).

The water column at station CL01-09 is therefore vertically structured, with optical properties reflecting the presence of a phytoplankton-dominated upper layer, a

mineral particle-dominated lower layer, and a middle layer which appears to indicate the presence of mixed particle types.

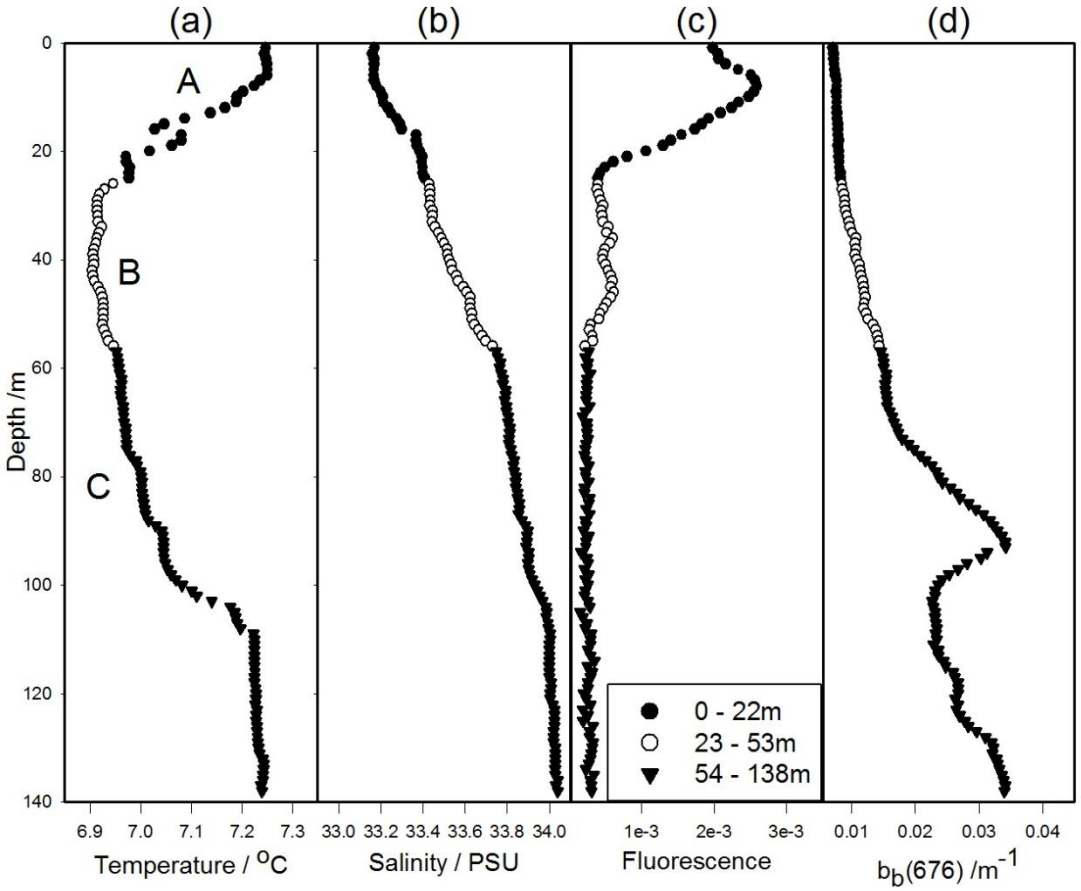

Figure 7.5: Depth profiles of (a) temperature, (b) salinity, (c) fluorescence and (d) backscattering for station CL01-09. The areas labelled A, B and C in Figure 7.4 are shown with the same markers to outline where each of the clusters is located on the depth profiles.

b Inversion of ac-9 signals in a structured water column.

Since constituent concentration measurements were only available at three depths for station CL01-09, an alternative means of assessing the performance of the inversion procedure outlined in Section 6.5.1 throughout the profile was required. This was achieved by using other available observations as proxies: fluorescence for *CHL*, salinity for *CDOM*, and backscatter for *MSS* (Section 4.4). Figure 7.6 shows that for *CHL* and *MSS*, the comparison of inversion products with proxy variables appeared to be very good with approximately linear relationships being observed. Cluster A data from just below the surface deviated somewhat from these linear relationships and further work is required to determine whether this deviation was due to physiological differences in the phytoplankton population in a shallow surface layer. The relationship between *CDOM* and salinity was more complex (possibly due to multiple *CDOM* sources, Section 4.4) but there was a tendency for high recovered *CDOM* to be correlated with low salinity.

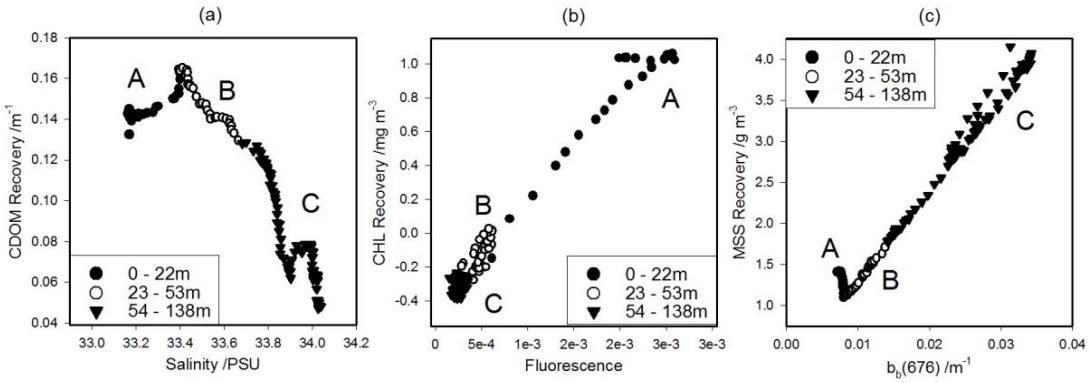

Figure 7.6: Recoveries of *OSC* concentrations with ancillary measurements to determine the ability of *IOP* inversion to recover general patterns in the water column. *OSCs* are compared to proxy variables (a) *CDOM* against salinity, (b) *CHL* against fluorescence and (c) *MSS* against backscattering at 676 nm.

The conclusion appears to be that, for this station, the *ac-9* inversion procedure is producing profiles of *CHL* and *MSS* (and to some extent *CDOM*) which are roughly correlated with proxy measurements of these quantities and give a coherent picture of the optical and hydrographic structure of the water column. The discrepancy between the *OSC* concentrations generated by the inversion procedure and those derived from water sample analysis could be due to two factors: one is the use of

SIOP values which were not locally determined, and the other is the possibility that the water samples were not representative of the composition of the water column in which the profile was acquired.

7.3.3 Results from Loch Striven (CL01-18)

The method devised for station CL01-09 was repeated for another station from the Clyde Sea, this time at the head of Loch Striven (CL01-18, Figure 7.3). This station is located at the head of a fjord basin whose waters are somewhat isolated from the Firth of Clyde, and potentially provided a different type of hydrography with which to test the analysis technique.

Figure 7.7 shows the fluorescence plotted against backscattering (Plot (a)) and backscattering plotted against scattering (Plot (b)) for CL01-18. In this instance, four data clusters were tentatively identified. Cluster A consisted of data from the surface, Cluster B from the upper mid depth, Cluster C from the lower mid depth and Cluster D from the bottom of the profile (see Figure 7.8). Cluster A had a relatively high fluorescence to backscattering ratio, which suggests a significant phytoplankton contribution, while Cluster D with the highest backscattering and lowest fluorescence probably consisted of mineral particles. Clusters B and C are more difficult to interpret using just the information shown in Plot (a). However Plot (b) shows two linear groups of points (indicating constant backscattering to scattering ratios), one for Cluster A and the other for Cluster C and D. This suggests that there are two basic particle types with different scattering phase functions. Cluster B forms a bridge between these two lines, and probably indicates a mixture of the two basic types. This is consistent with the position of the Cluster B data in the water column Figure 7.8.

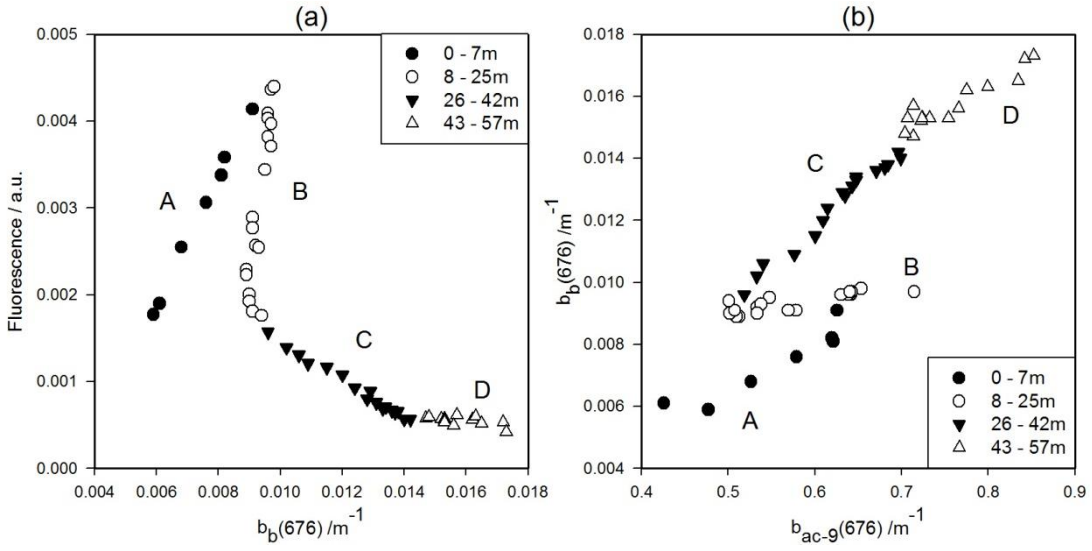

Figure 7.7: Examination of optics measurements for CL01-18 to determine sections of the profile with similar optical characteristics with (a) Fluorescence and backscattering to determine areas of *CHL* and *MSS* and (b) backscattering and scattering to examine areas with different characteristics, labelled A, B, C and D.

CTD profile measurements (Figure 7.8) show a relatively high temperature, low salinity surface layer above 8 m, which is occupied by Cluster A, and a low temperature, high salinity layer below 25 m which is occupied by Clusters C and D. Cluster B which occupies the intermediate layer (8 - 25 m) which forms a gradient in these physical properties which supports the mixing hypothesis derived from the optics. Interestingly, the fluorescence profile for this station suggests that the maximum chlorophyll concentration may occur at the bottom of the surface layer.

The *OSC* concentrations recovered from the *IOP* inversion procedure were again compared to the proxy variables (Figure 7.9). A good linear relationship was found between recovered *CHL* and fluorescence, and a negative correlation (with multiple gradients) between recovered *CDOM* and salinity. The relationship between recovered *MSS* and backscattering was linear for the low-chlorophyll, deep water Clusters (C and D) but this relationship was more complex for Clusters A and B, which may indicate a failure of the inversion process due to inappropriate *SIOP* values.

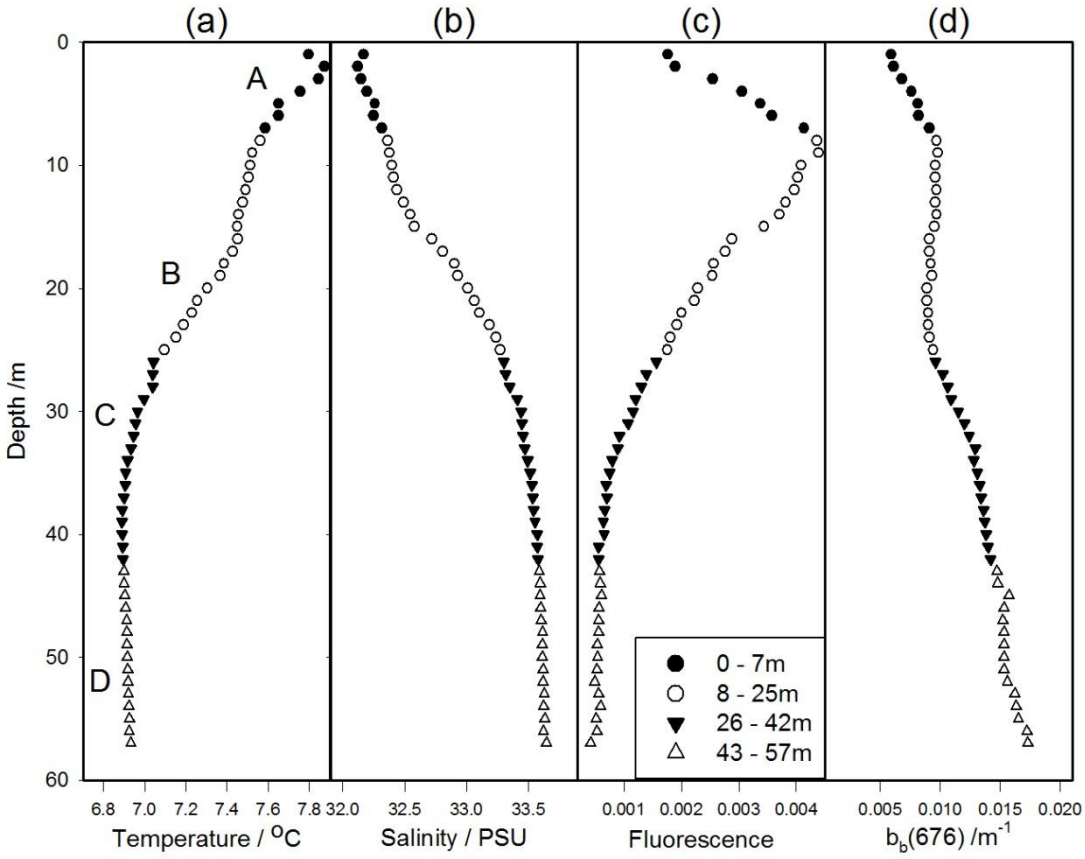

Figure 7.8: Depth profiles of (a) temperature, (b) salinity, (c) fluorescence and (d) backscattering for station CL01-18. The areas labelled A, B and C in Figure 7.7 are shown with the same markers to outline where each of the clusters is located on the depth profiles.

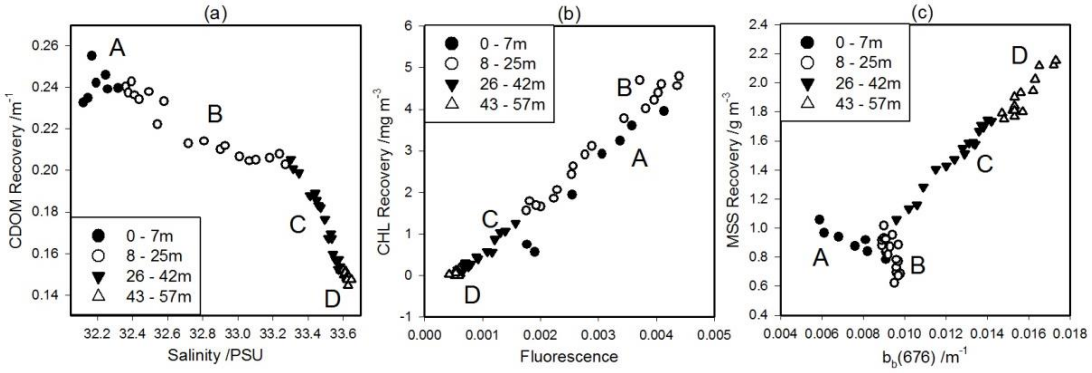

Figure 7.9: Recoveries of *OSC* concentrations with ancillary measurements to determine the ability of *IOP* inversion to recover general patterns in the water column. *OSCs* are compared to the usual proxy variables for each (a) *CDOM* against salinity, (b) *CHL* against fluorescence and (c) *MSS* against backscattering at 676 nm.

7.3.4 Results from Rothesay Bay (CL01-19)

The method was repeated for another station from the Clyde Sea, Rothesay Bay (CL01-19, Figure 7.3). This station was chosen as the water sample analysis indicated that *CDOM* concentration increased with depth, which is unusual in these waters. Again, the measured and recovered *OSC* concentrations for this station are shown in Table 7.3.

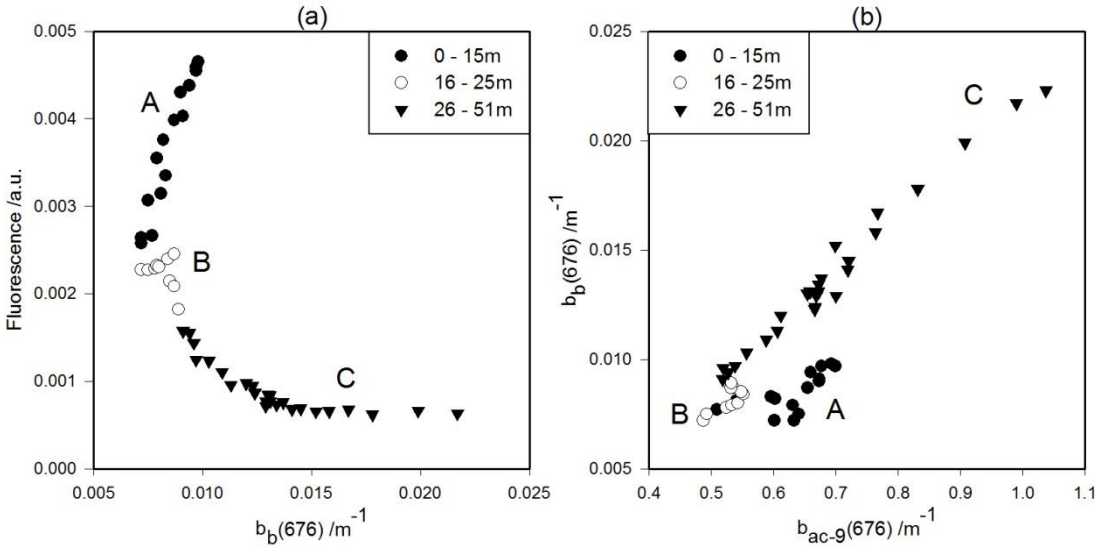

Figure 7.10: Examination of optics measurements for CL01-19 to determine sections of the profile with similar optical characteristics with (a) Fluorescence and backscattering to determine areas of *CHL* and *MSS* and (b) backscattering and scattering to examine areas with different characteristics, labelled A, B and C.

Figure 7.10 shows the fluorescence against backscattering (Plot (a)) and the backscattering against scattering (Plot (b)) for CL01-19. Three data Clusters were tentatively identified. Cluster A consisted of data from the surface, Cluster B from the mid depth and Cluster C from the bottom of the profile. Cluster A had relatively high fluorescence and low backscattering with a positive fluorescence to backscattering gradient which suggests a significant phytoplankton contribution, while Cluster C with the highest backscattering and lowest fluorescence probably consisted of mineral particles. Plot (b) shows two lines (indicating constant backscattering to scattering ratios), one for Cluster A and the other for Cluster C.

CTD profile measurements (Figure 7.11) show a relatively high temperature, low salinity surface layer above 15 m, which is occupied by Cluster A, and a low

temperature, high salinity layer below 25 m which is occupied by Cluster C. The intermediate layer (15 - 25 m) forms a gradient in these physical properties which supports the mixing hypothesis derived from the optics. Interestingly, the fluorescence profile for this station suggests that the maximum chlorophyll concentration may occur in the middle of the surface layer. This was confirmed by examining the profile of $a_{ac\text{-}9}(676)$, which showed the same sub-surface peak.

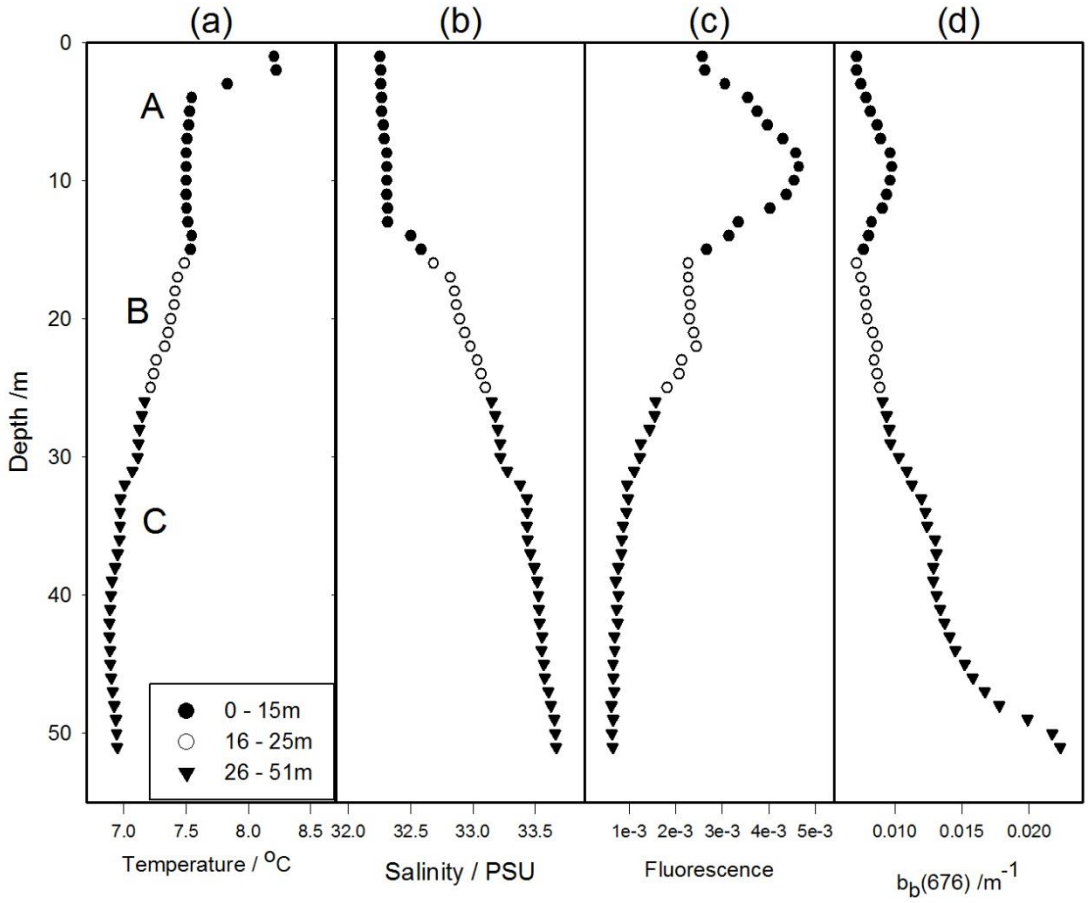

Figure 7.11: Depth profiles of (a) temperature, (b) salinity, (c) fluorescence and (d) backscattering for station CL01-19. The areas labelled A, B and C in Figure 7.10 are shown with the same markers to outline where each of the clusters is located on the depth profiles.

The *OSC* concentrations recovered from the *IOP* inversion procedure were again compared to the proxy variables (Figure 7.12). A good linear relationship was found between recovered *CHL* and fluorescence. A negative correlation (with slightly different gradients) between recovered *CDOM* and salinity was found for each of the

Clusters. The relationship between recovered *MSS* and backscattering was linear for the deeper Clusters B and C but this relationship was more complex again for Cluster A, with slight deviation from the linear relationship.

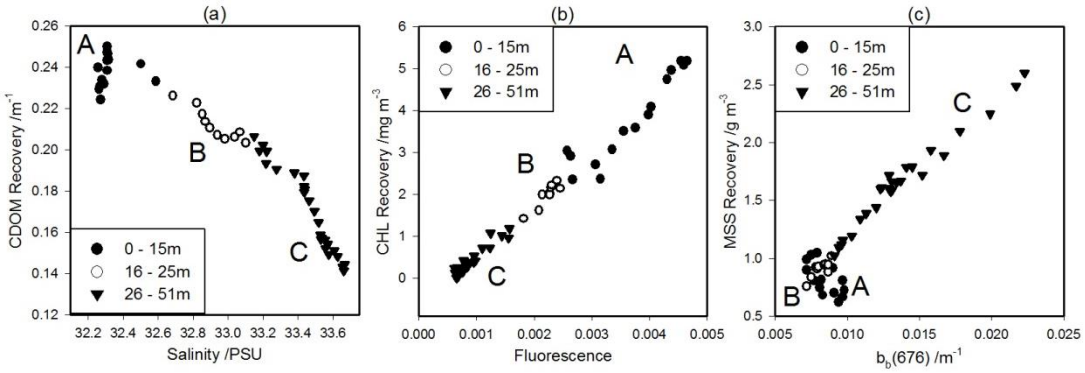

Figure 7.12: Recoveries of *OSC* concentrations with ancillary measurements to determine the ability of *IOP* inversion to recover general patterns in the water column. *OSCs* are compared to the usual proxy variables for each (a) *CDOM* against salinity, (b) *CHL* against fluorescence and (c) *MSS* against backscattering at 676 nm.

7.3.5 Results from Loch Creran (SJ04-15)

For the Loch Crerean station (SJ04-15, Figure 7.3), the measured and recovered *OSC* concentrations are given in Table 7.3. This station was chosen as it is well separated geographically from the Clyde area. In addition, the proposed method of analysis produced unexpected results and appeared to demonstrate the limitations of the method.

Figure 7.13 shows the fluorescence against backscattering (Plot (a)) and the backscattering against scattering (Plot (b)) for SJ04-15. In this case, two data clusters were tentatively identified. Cluster A consisted of data from the surface and Cluster B from the bottom of the profile. Cluster A had relatively high fluorescence and low backscattering with a positive fluorescence to backscattering gradient which suggests a significant phytoplankton contribution, while Cluster B had high backscattering and low fluorescence, and probably consisted of mineral particles. Plot (b) shows a linear backscattering to scattering ratio within Cluster B, while

Cluster A has a non-linear backscattering to scattering ratio which could suggest a mixture of particle types with different scattering phase functions.

CTD profile measurements (Figure 7.14) show a relatively high temperature, low salinity surface layer above 10 m, which is occupied by Cluster A, and a low temperature, high salinity layer below 10 m which is occupied by Cluster B.

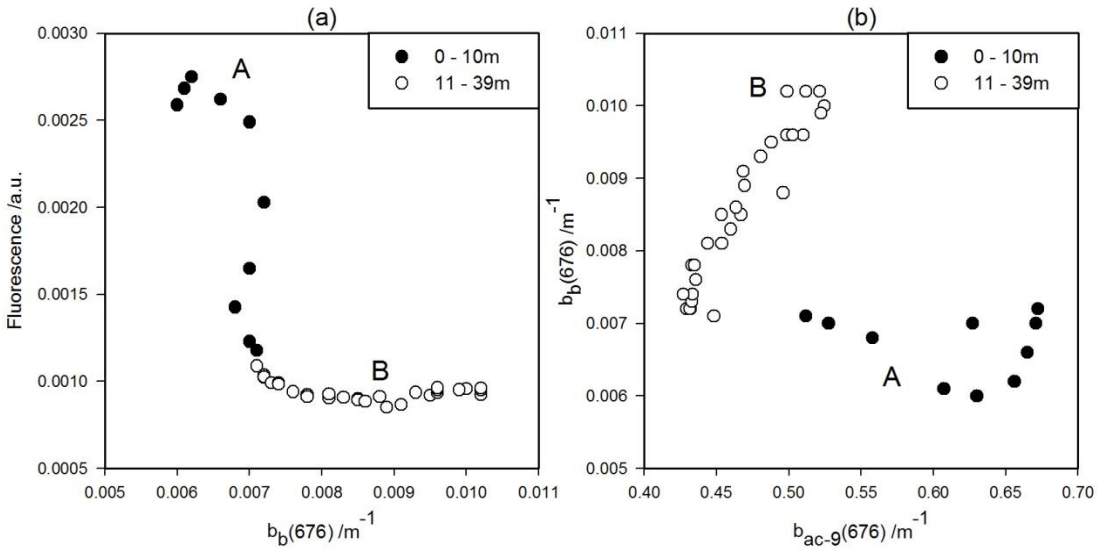

Figure 7.13: Examination of optics measurements for SJ04-15 to determine sections of the profile with similar optical characteristics with (a) Fluorescence and backscattering to determine areas of *CHL* and *MSS* and (b) backscattering and scattering to examine areas with different characteristics, labelled A and B.

The *OSC* concentrations recovered from the *IOP* inversion procedure were again compared to the proxy variables (Figure 7.15). A generally negative relationship between recovered *CDOM* and salinity was found for both Clusters A and B. The relationship between recovered *MSS* and backscattering was linear for the deeper Cluster B but this relationship was more complex for Cluster A, as was already observed in the backscattering to scattering ratio for both Clusters. The relationship between *CHL* and fluorescence was also less simple, with an obvious flattening of the recoveries at higher fluorescence measurements in Cluster A and mismatches at the lower fluorescence measurements in Cluster B.

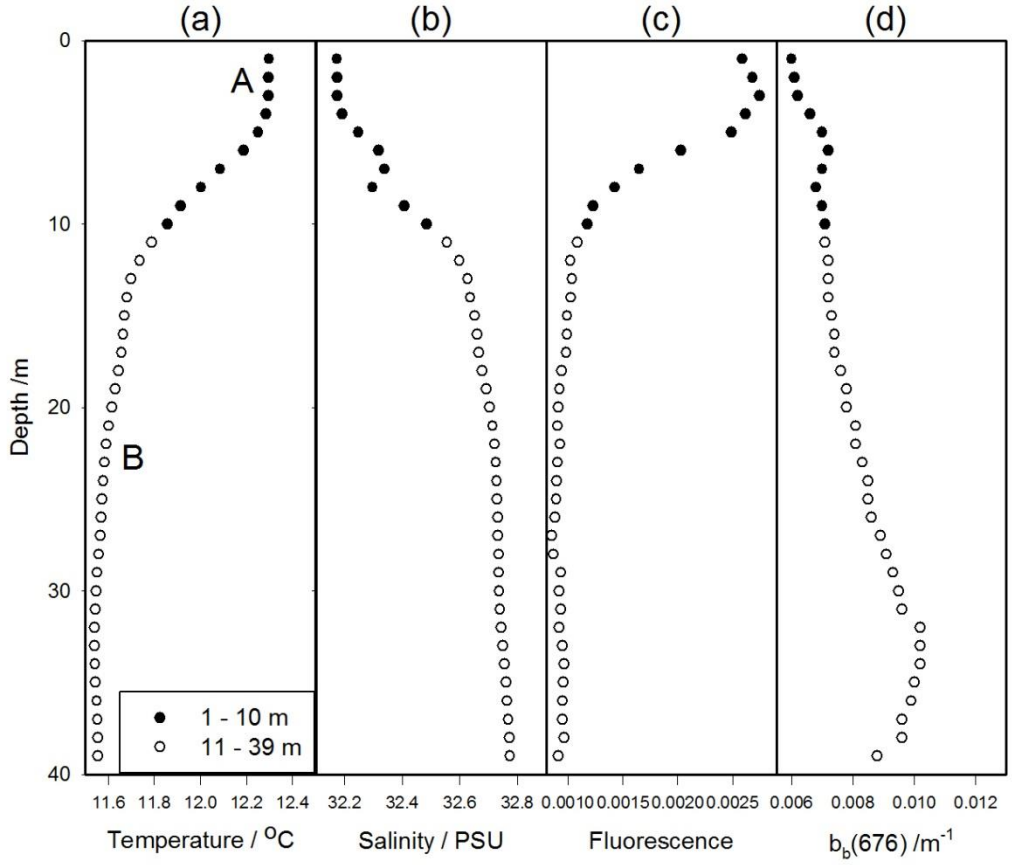

Figure 7.14: Depth profiles of (a) temperature, (b) salinity, (c) fluorescence and (d) backscattering for station SJ04-15. The areas labelled A, B and C in Figure 7.13 are shown with the same markers to outline where each of the clusters is located on the depth profiles.

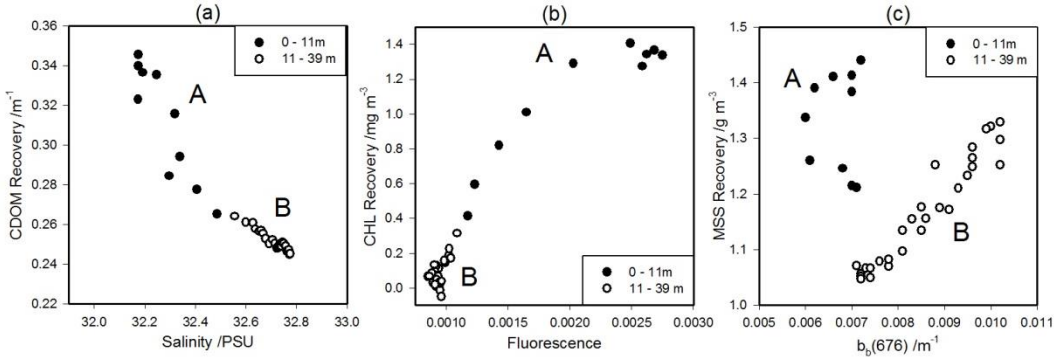

Figure 7.15: Recoveries of *OSC* concentrations with ancillary measurements to determine the ability of *IOP* inversion to recover general patterns in the water column. *OSCs* are compared to the usual proxy variables for each (a) *CDOM* against salinity, (b) *CHL* against fluorescence and (c) *MSS* against backscattering at 676 nm.

7.3.6 Conclusions drawn from the examination of individual station profiles.

The analysis of individual station profiles allows some conclusions to be drawn regarding the interpretation of optical measurements in a sea loch environment:

1. The optical properties of a water column can vary significantly over a few meters in response to changes in the types of particles present as well as the concentration of *CDOM*.

2. The proportion of phytoplankton and minerals in the Scottish sea lochs varies, with phytoplankton occurring in the surface layer and minerals dominating the optical properties near the bottom. Mixed particle assemblages may be found in intermediate layers.

3. The different proportion of particles between the surface and the bottom at each station suggest that the *SIOP* values for each station may vary with depth. This implies that *SIOP* values may need to be determined on a much finer scale if *IOP* inversion methodologies are to be carried out effectively.

4. The ratio of backscattering to total scattering, which is related to the scattering phase function, appears to be a sensitive indicator of particle type.

5. The constituent concentrations recovered by the *ac-9* inversion procedure may not give an absolute match with those found by sample analysis in the laboratory, due to uncertainties in the location of water samples and measurement uncertainties in the laboratory measurements of *OSC* concentrations. These uncertainties are carried through to *SIOP* calculations and cause inappropriate *SIOP* values to be used. The *OSC* concentrations used for comparison could account for the underestimation as they themselves are not error free.

6. Comparison between recovered *OSC* concentrations and proxy variables (fluorescence, backscattering and salinity) indicates that the inversion of *ac-9* data can give useful information on the relative distribution of constituents in the water column. Significantly, however, there are specific instances (e.g.

Cluster A in Figure 7.9 Plot (b) & Figure 7.15 Plot (c)) where the inversion appears to give poor results.

It can be concluded that combining the *ac-9* with the other optical and physical measurements has the potential for giving insights into the spatial distributions of materials and processes in the water column. This technique could be used to provide information on water column structure and associated ecological processes even in cases where quantitatively exact inversions were not obtained.

7.4 Combined analysis of the four station profiles

The previous section suggested that the *IOP* inversion appeared to be failing as a result of the systematic uncertainties associated with the laboratory measurements of *OSC* concentrations and *SIOP* values, rather than in a random manner. To further this analysis the following section combines the four sea loch stations to determine if this procedure can only be completed station-by-station or if the analysis can be applied to a whole data set to gain useful insights on an area of interest.

7.4.1 Optical data analysis applied to combined stations

Figure 7.16 shows the results of plotting the fluorescence against backscattering and backscattering against total scattering for all of the four stations described above.

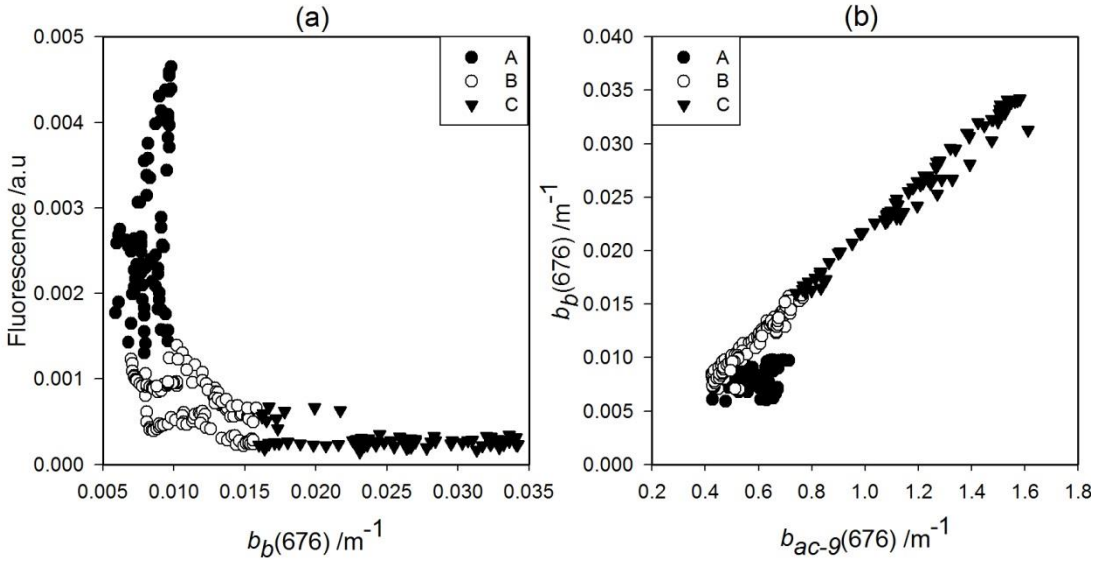

Figure 7.16: Examination of ancillary optical measurements for each of the four previously analysed stations to determine if the areas with similar optical characteristics are related to each other (a) fluorescence and backscattering to determine areas of *CHL* and *MSS* and (b) backscattering and scattering to examine areas with different characteristics, labelled A, B and C (legends).

The data have been grouped into three clusters (A, B and C). Cluster A contains surface layer observations from all of the profiles it has a high fluorescence to backscattering ratio and is therefore composed mostly of phytoplankton cells. Cluster C has high backscattering and low fluorescence, suggesting a large *MSS* content, and occupies the bottom of each profile. Cluster B, which exhibits low values of both fluorescence and backscattering, could be a mixture of particles and occupies the mid-depth of each profile. Clusters B and C have the same $b_b(676)/b_{ac\text{-}9}(676)$ ratio (Plot (b)) and therefore the same scattering phase function. The slope of the combined B/C cluster has a value of 0.023, which is close to the average backscattering ratio of 0.0183 for marine particles determined in the classic measurements by Petzold (Mobley, 1994). The fact that the suspended particles in the deeper layers of four separate stations have similar backscattering ratios suggests a similarity in size distribution and refractive index. Cluster A, on the other hand,

has a distinctly lower backscattering ratio which indicates particles with significantly different physical characteristics. This is consistent with phytoplankton cells being the main constituent of the particle population in the surface layer.

7.4.2 Comparison of inversion products to proxy variables for all four stations

Comparing the recovered *OSC* concentrations to their proxy variables (Figure 7.17), it can be seen that the correlations are consistent across all of the stations that were analysed. This is particularly remarkable since the scale of the axes in Figure 7.17 is small compared to the range in the UK Shelf data set, and therefore fine scale deviations from the trend are emphasised.

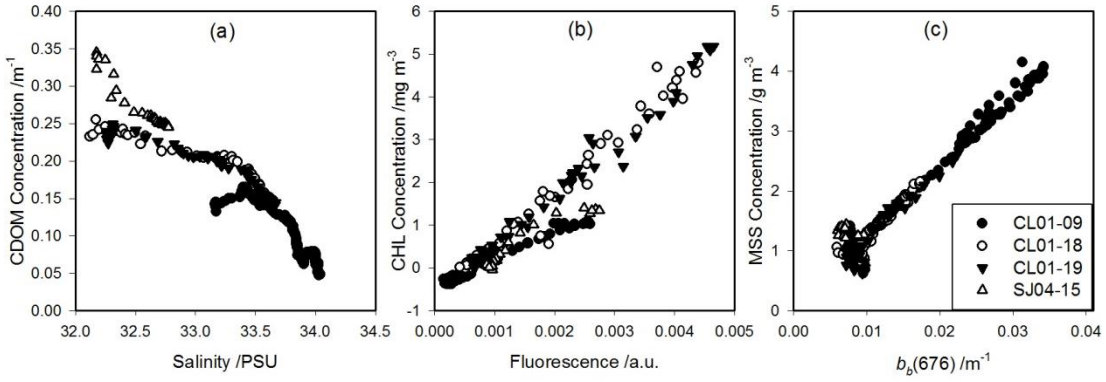

Figure 7.17: Recoveries of *OSC* concentrations with ancillary measurements to determine the ability of *IOP* inversion to recover general patterns in the water column. *OSCs* are compared to the usual proxy variables for each (a) *CDOM* against salinity, (b) *CHL* against fluorescence and (c) *MSS* against backscattering at 676 nm.

These results show that despite probable measurement errors in *IOP* values and uncertainty concerning the use of UK shelf mean *SIOP* values in the inversion process, the proposed *IOP* inversion procedure recovers *OSC* concentration values that bear consistent relationships to relevant proxy variables. The robustness of these relationships can partly be attributed to the fact that the *IOP* and other measurements are closely co-located (unlike water sample analyses). However it should also be pointed out that two of the traditionally defined measures of *OSCs* (*CHL* and *MSS*) are not necessarily good representations of the optical properties of these substances

in the water column: they do not, for example, reflect the widely different morphology of phytoplankton cells and the existence of minerals in a range of flocculated states.

7.5 Chapter Summary

1. The *IOP* inversion procedure outlined in Chapter 6 was applied to selected *ac-9* archive data for the UK shelf sea. In general *OSC* concentration recoveries were underestimated using UK shelf average *SIOPs*, and none of the 339 stations examined had errors below 30% for all three *OSC* concentrations. This indicates a systematic bias in the *SIOP* values used in the deconvolution, possibly resulting from the assumption of zero infra-red absorption in both the *SIOPs* and the *IOP* measurements.

2. In addition to the systematic biases in the *IOP* inversion results, significant random uncertainties were also observed. It is possible that these could be reduced by using regionally determined *SIOP* values rather than averages for the whole UK Shelf data set.

3. In order to examine how the discrepancies between *IOP* inversion results and *OSC* measurements originated, four stations from the Scottish sea lochs were examined in detail using additional optical and physical measurements to supplement the information available from the *ac-9* profiles. Fluorescence versus backscattering and backscattering versus scattering plots were created to identify particle populations with distinct optical characteristics, and the location of these populations was mapped onto profiles of water column structure obtained using *CTD* data. Finally the *OSC* concentrations obtained by inverting the *ac-9* signals were plotted against proxy variables (salinity, fluorescence and backscattering for *CDOM*, *CHL* and *MSS* respectively) to determine whether a coherent picture of the distribution of these materials in the water column was obtained even if there were systematic errors in the recovered concentrations.

4. Combining the results obtained for these stations showed that the *IOP* inversion was providing coherent information on particle populations across the whole region of interest, even when it did not accurately match measured constituent concentrations. It also became clear that validation of *IOP* inversion techniques using currently available data was limited due to measurement uncertainties and assumptions, and that a more targeted measurement campaign was required.

5. By combining the *ac-9* data with other optical measurements, encouraging results were obtained which suggested that *in situ* monitoring of changes in the spatial and temporal distributions of materials and processes in the water column was feasible using optical means even where implementation of a rigorous *IOP* inversion strategy has proved to pose significant challenges.

6. In this chapter the results from the spatial analysis of four discrete locations demonstrate that is possible to recover information from *IOP* inversion results despite the large uncertainties in the recovered *OSC* concentrations. This original analysis technique is a powerful tool for the analysis of station profiles. In order to extend the analysis beyond archive data towards new *in situ* methods of optical data collection (moorings, autonomous underwater vehicles (*AUVs*), Argo floats and the Global Ocean Observing System (*GOOS*)) additional data processing and analysis methods for temporal data that could be subjected to fouling is also required. Coupling the spatial analysis technique with one for temporal data would provide a more effective analysis method to overcome problems associated with these new data collection methods, such as fouling of the optical instruments. A temporal analysis technique is presented for mooring data collected in Liverpool Bay in the following chapter.

Chapter 8 Analysis of Temporal Optical Data Subjected to Fouling – Liverpool Bay

While predictive, the spatial analysis technique developed in the previous chapter may not be enough for the analysis of data from long term deployments. Time series data suffers from unique problems with fouling and instrument drift which cannot be corrected mid-deployment. In some cases the quality of the data is such that standard data processing techniques (Chapter 3 & Chapter 4) cannot be applied to the data, in these instances the data would normally be discarded. Presented in this chapter is a series of standard signal processing techniques that when applied in the new ways outlined, prove effective tools for the analysis of heavily fouled temporal data. Coupled with the spatial analysis in Chapter 7 the analysis of less than optimum data is straightforward and results can still be attained.

The optical data from an *ac-s* deployed as part of the Liverpool Bay Coastal Observatory (Appendix A) a heavily fouled temporal data set and as consequence a set of unique MATLAB processing scripts had to be written to recover and match the optical and physical data taken from the mooring (Section 4.5). After the data analysis was applied, the series of standard signal analysis techniques presented below were applied to try to gain insight about the turbidity signal in Liverpool Bay. For each technique described below a small example to test the method from previously published results from Liverpool Bay is also completed. Each example makes use of known dynamics of Liverpool Bay which are outlined in detail in Appendix A for reference.

8.1 Separation of Low and High Frequency Signals

It was assumed that instrument fouling resulting from the long deployment period generated a low frequency component of the *ac*-*s* signal corresponding to a general increase in both absorption and attenuation. Therefore a moving average was applied to each wavelength channel and then subtracted from the data. The result of the moving average was taken to represent the low frequency component and the data remaining after the moving average was subtracted the high frequency component.

The moving average was applied using the *smooth* function in MATLAB: this was repeated 15 times as testing confirmed that there was no significant difference in the low frequency signal after this point. The "smoothed" data were then subtracted from the original to obtain the high frequency data. The original, low and high frequency data obtained from smoothing method are shown in Figure 8.1.

The MATLAB function *smooth* applies a moving average filter to a column vector *x*, and results are returned in a second column vector *y*, as Equation (8.1). The default span, applied in this work, for the moving average is five. The smoothed data is calculated by Equation (8.2).

$$y_s = smooth(y) \tag{8.1}$$

$$y_s(i) = \frac{1}{2N+1}\big(y(i+N) + y(i+N-1) + \cdots + y(i-N)\big) \tag{8.2}$$

where $y_s(i)$ is the smoothed value for the ith data point, N is the number of neighbouring data points on either side of $y_s(i)$, and $2N+1$ is the span (in this work $N = 2 \rightarrow span = 5$).

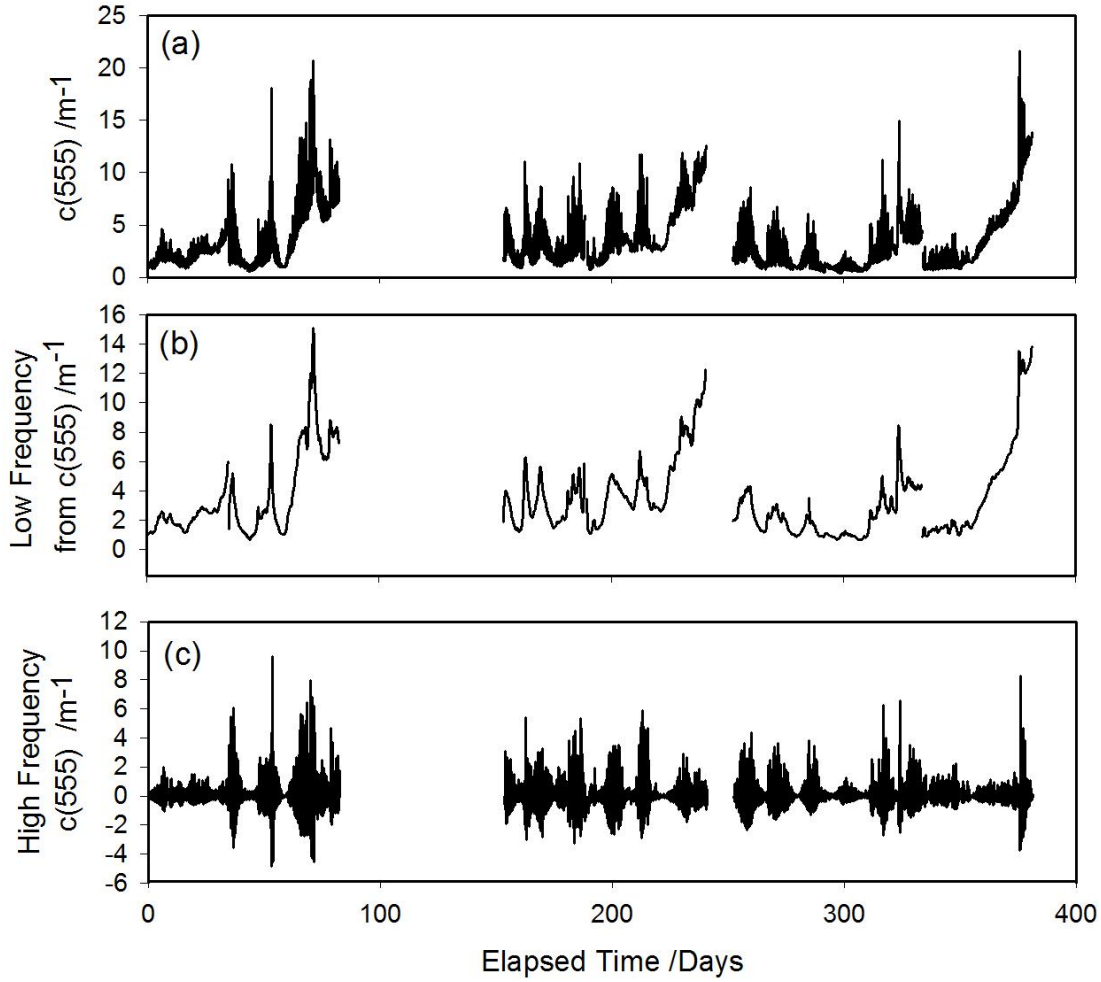

Figure 8.1: Plots showing removal of long term trends (a) shows the raw data, (b) shows the low frequency signal subtracted from the original & (c) shows the high frequency signal.

An alternative method for separating the frequency components using a high-pass filter was also attempted using a fast Fourier transform (*FFT*) of the data and removing all frequencies below 0.52 day^{-1}, the same cut off as that resulting from the smoothing method. Applying the *FFT* was as effective as the smoothing method for separating the low and high frequency signals, but since the Liverpool Bay time series was not continuous the *FFT* resulted in artefacts at the start and end of each deployment. These effects can be seen in Figure 8.2 which clearly demonstrates that other than the "edge effects" of the *FFT* the two methods are equivalent. In practice, the smoothing method was adopted to minimise the number of processing steps required.

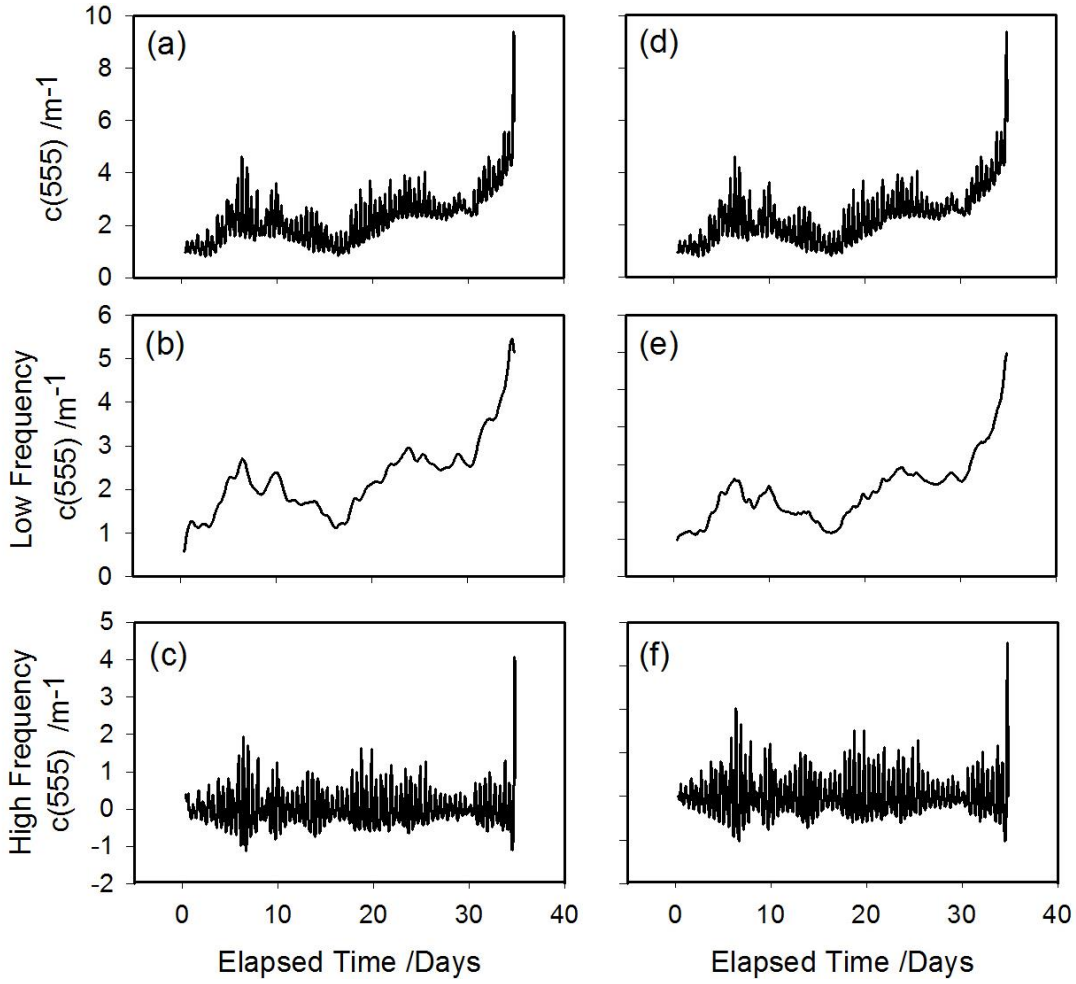

Figure 8.2: Plots showing removal of long term trends by two different methods (a)-(c) show the results of applying an *FFT* and (d)-(f) show the results of applying repeated smoothing for one deployment (*COBS* 71 7th July 2010 – 11th August 2010).

8.1.1 Method Testing: Residual Current Velocity

The method of separating the low and high frequency data described above was tested by applying it to current velocity data for Liverpool Bay. the low frequency data from the current velocity was examined to confirm the previously published results for the residual current velocity in Liverpool Bay. The polar plot in Figure 4.17 showed the magnitude and direction of the current velocity 5 m below the surface (the depth of the *ac*-s), which demonstrated the onshore-offshore direction of the current velocity. When the current velocity was averaged over a 25 hour time

period the tidal component was removed to reveal the direction of the residual current flow at the site (Figure 8.3).

It can be seen in Figure 8.3 that the trend of the current velocity was in the northeast direction, which implied that the residual current flows up the coast of England towards Scotland. This strongly agreed with the literature where more extensive studies of the current flow have been conducted (Polton et al., 2011; Palmer, 2010; Verspecht et al., 2009; Howarth et al., 2008).

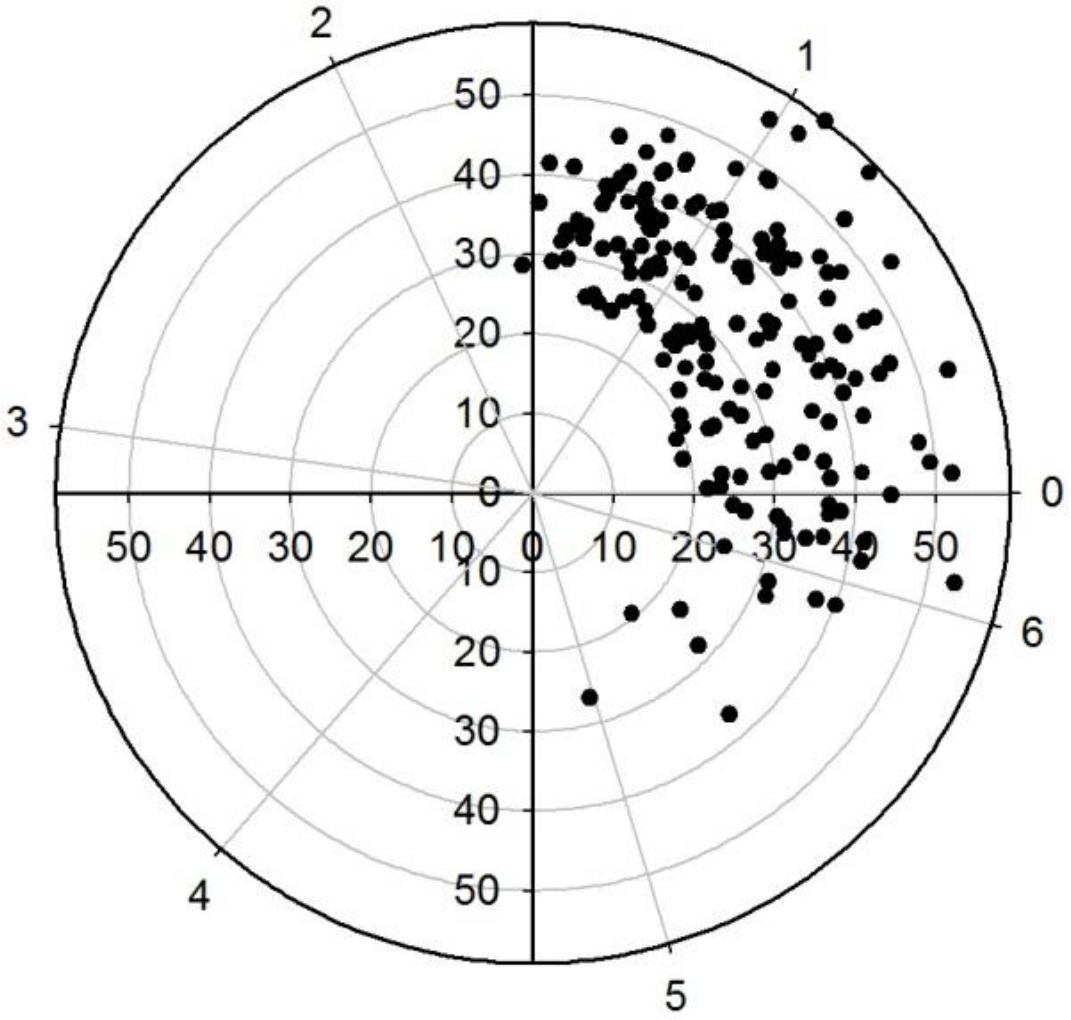

Figure 8.3: Polar plot demonstrating the direction of the residual current flow at Site A. Notice the general trend towards the Lancashire coast which agrees with the literature

8.2 Fast Fourier Transform Analysis

The high frequency component of the main indicators of variability in Liverpool Bay ($c_{ac\text{-}9}$(555), fluorescence, salinity, magnitude of velocity, displacement and depth) were normalised and a fast Fourier transform (*FFT*) applied. The frequency analysis gave an indication of the main driver of the high frequency turbidity signal. Each variable showed a clear tidal dependence with peaks at the main tidal frequencies (Table 8.1, Apel (1987)).

Table 8.1: Tidal Components

Label	Tidal Mode	Period /hour	Frequency /Days
Semi-Diurnal			
M_2	Principal Lunar	12.421	1.932
S_2	Principal Solar	12	2
N_2	Elliptical Lunar	12.658	1.896
K_2	Declination Luni-Solar	11.967	2.006
Diurnal			
K_1	Declination Luni-Solar	23.935	1.003
O_1	Principal Lunar	25.819	0.930
P_1	Principal Solar	24.066	0.997
Q_1	Elliptical Lunar	26.868	0.893
Long-Period Tides			
M_f	Fortnightly Lunar	327.86	0.073
M_m	Monthly Lunar	661.31	0.036

Figure 8.4 shows the result of applying an *FFT* to $c_{ac\text{-}9}$(555). The largest peak occurred at 1.933 day^{-1} and using Table 8.1 this peak was identified as the M_2 tidal mode. This confirmed that $c_{ac\text{-}9}$(555) was driven by the tidal height. All of the properties displayed this semi-diurnal dependence (Figure 8.5) with the exception of the current velocity, which had the largest peak at 3.866 day^{-1}. This result was consistent with a semi-diurnal tide which would have two maxima in velocity magnitude for every complete tide; the direction of the current velocity alternated with the tide. However $c_{ac\text{-}9}$(555) also showed clear peaks at 3.866 day^{-1}. This suggested that $c_{ac\text{-}9}$(555) also had a component driven by the current velocity, not just the tidal height. Reconstruction of the $c_{ac\text{-}9}$(555) signal by addition of sine waves with the main Fourier frequencies showed that the peaks at 3.866 day^{-1} and 4 day^{-1} were the source of secondary or "subsidiary peak" that appeared in the $c_{ac\text{-}9}$(555) signal. The subsidiary peaks were always observed in the time series corresponding

to the flood phase of the tide. Given that the subsidiary peaks are related to the Fourier frequencies at 3.866 day^{-1}, it can be assumed that the current velocity was the driver of this peak. The source of the subsidiary peaks is discussed in further detail in Section 8.4.3.

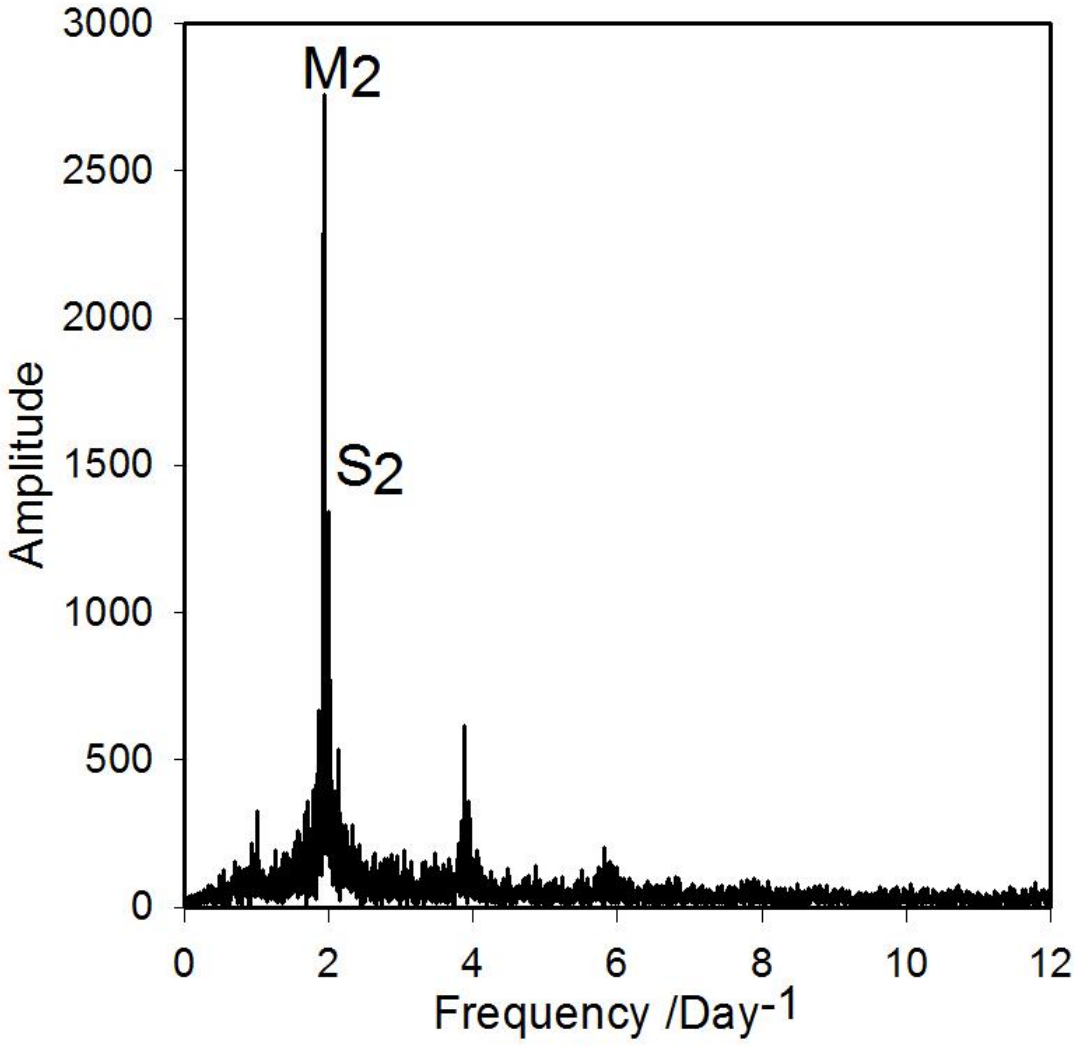

Figure 8.4: Fourier Transform of the attenuation signal at 555nm. Frequencies around 2 day^{-1} correspond to the semi-diurnal tidal frequencies, while those around 3.7 day^{-1} are responsible for subsidiary peaks in attenuation observed at high tide.

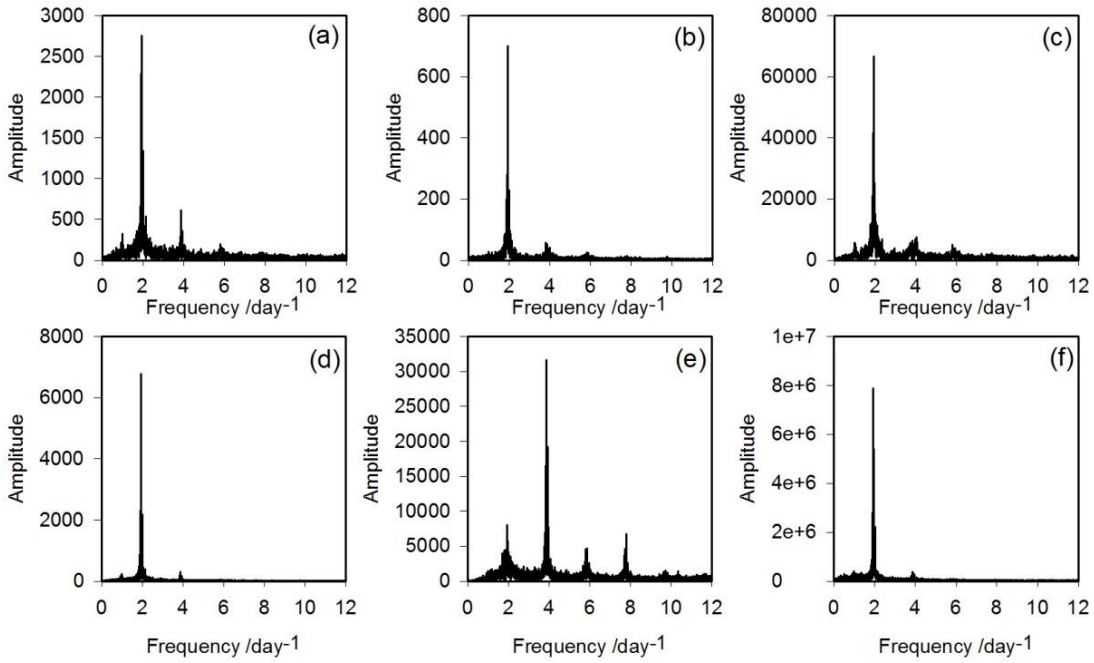

Figure 8.5: Fourier Transform analysis of physical properties of Site A with (a) $c_{ac\text{-}9}(555)$ (b) Salinity (c) Fluorescence (d) Tidal Amplitude (e) Current Velocity (f) Displacement. The other peaks at higher frequencies that can be seen on these graphs are harmonics of the two main peaks.

8.3 Cross Correlation Analysis

An initial attempt was made to use the *FFT* result to determine the phase relationship between the optical signals. However the combination of noise in the data and the occurrence of phase changes throughout the year meant that the *FFT* phase was too sensitive to produce conclusive results. In particular, the subsidiary peak did not bear a constant phase relationship to the main signal; therefore it was not possible to retrieve meaningful phase information from the *FFT*.

In view of these difficulties, an alternative method to determine the phase relationship by cross correlation analysis was devised. As an example, the phase relationship between $c_{ac\text{-}9}(555)$ and tidal amplitude will be examined. Figure 8.6 shows the time series of both tidal amplitude (Plot (a)) and $c_{ac\text{-}9}(555)$ (Plot (b)), where it can be seen from the dashed line that the two components are out of phase, with the minimum in tidal amplitude coinciding with the maximum in $c_{ac\text{-}9}(555)$.

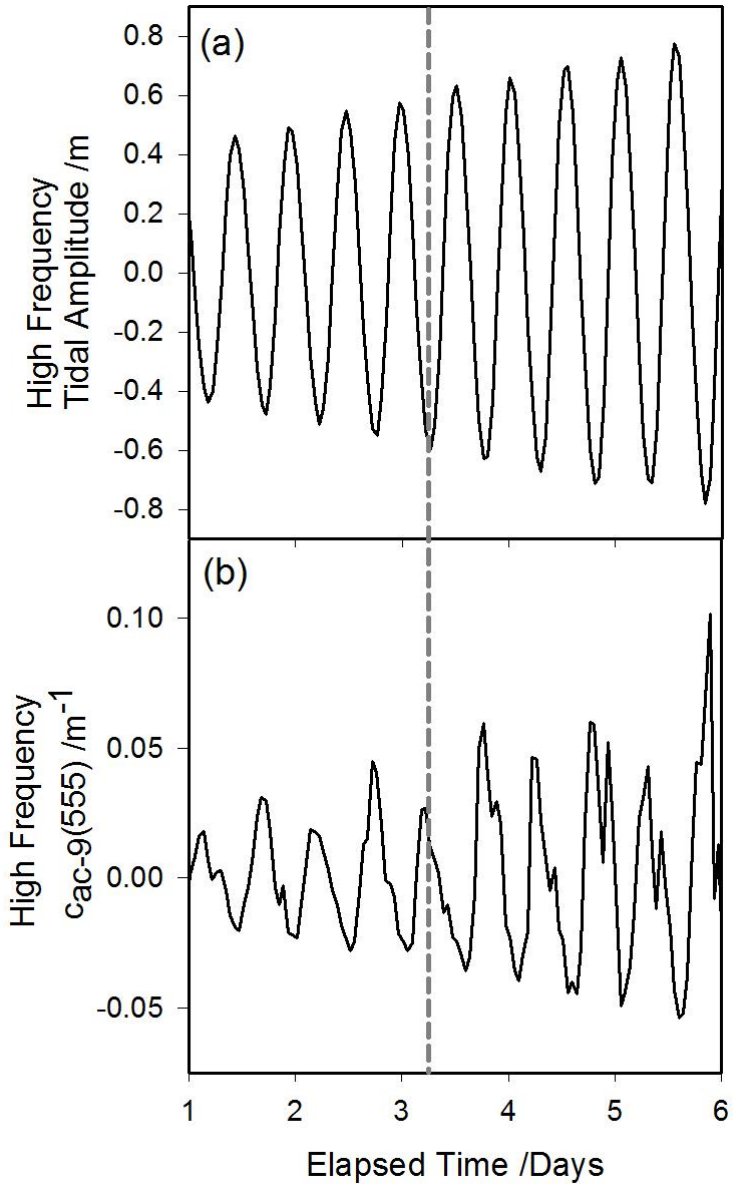

Figure 8.6: Section of time series data for (a) the high frequency signal of tidal amplitude and (b) high frequency signal of $c_{ac\text{-}9}(555)$, to demonstrate the phase relationship between the two components. The dashed line emphasises that the minimum in tidal amplitude coincides with the maximum in $c_{ac\text{-}9}(555)$.

When the cross correlation results are examined (Figure 8.7), it can be seen that the minimum correlation coefficient is at +1 lag which confirms that the two are out of phase. The shift in the cross correlation analysis is related to the subsidiary peak in the $c_{ac\text{-}9}(555)$ time series, which are discussed in more detail in Section 8.4.3. If the main peak in $c_{ac\text{-}9}(555)$ was compared with the tidal amplitude then the two would be perfectly out of phase.

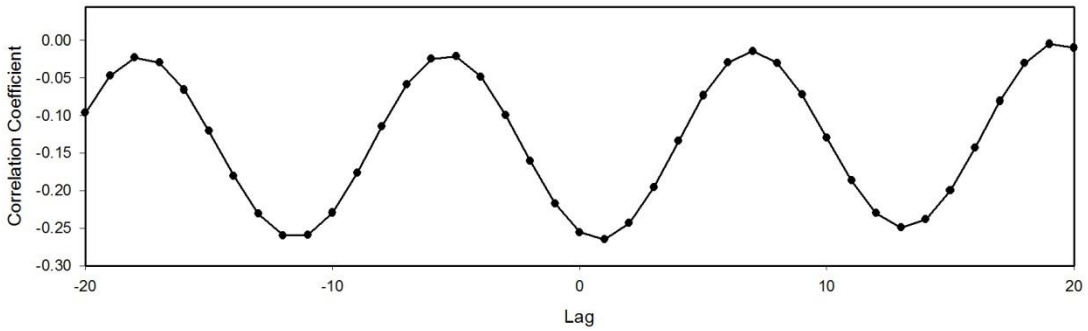

Figure 8.7: Cross correlation result for $c_{ac\text{-}9}(555)$ and tidal amplitude. The minimum in the correlation coefficient is at +1 lag which confirms that the two are out of phase as demonstrated by the time series analysis.

8.3.1 Method Testing: Phase Relationship between Tidal Height and Temperature

In order to test the use of cross correlation analysis as an indicator of the phase relationship, the idea was tested with a previously investigated and published phenomenon occurring in Liverpool Bay.

It was asserted by Polton et al. (2011) that there was a strong annual cycle in which the east-west temperature gradient, i.e. between the coast and the Irish Sea, switched direction seasonally. In the summer months the river outflow was warmer than the ambient sea temperature and in the winter the opposite was true. This reversal occurred because the river temperatures were more tightly coupled to the atmospheric temperature than the sea temperature, which had a greater thermal inertia.

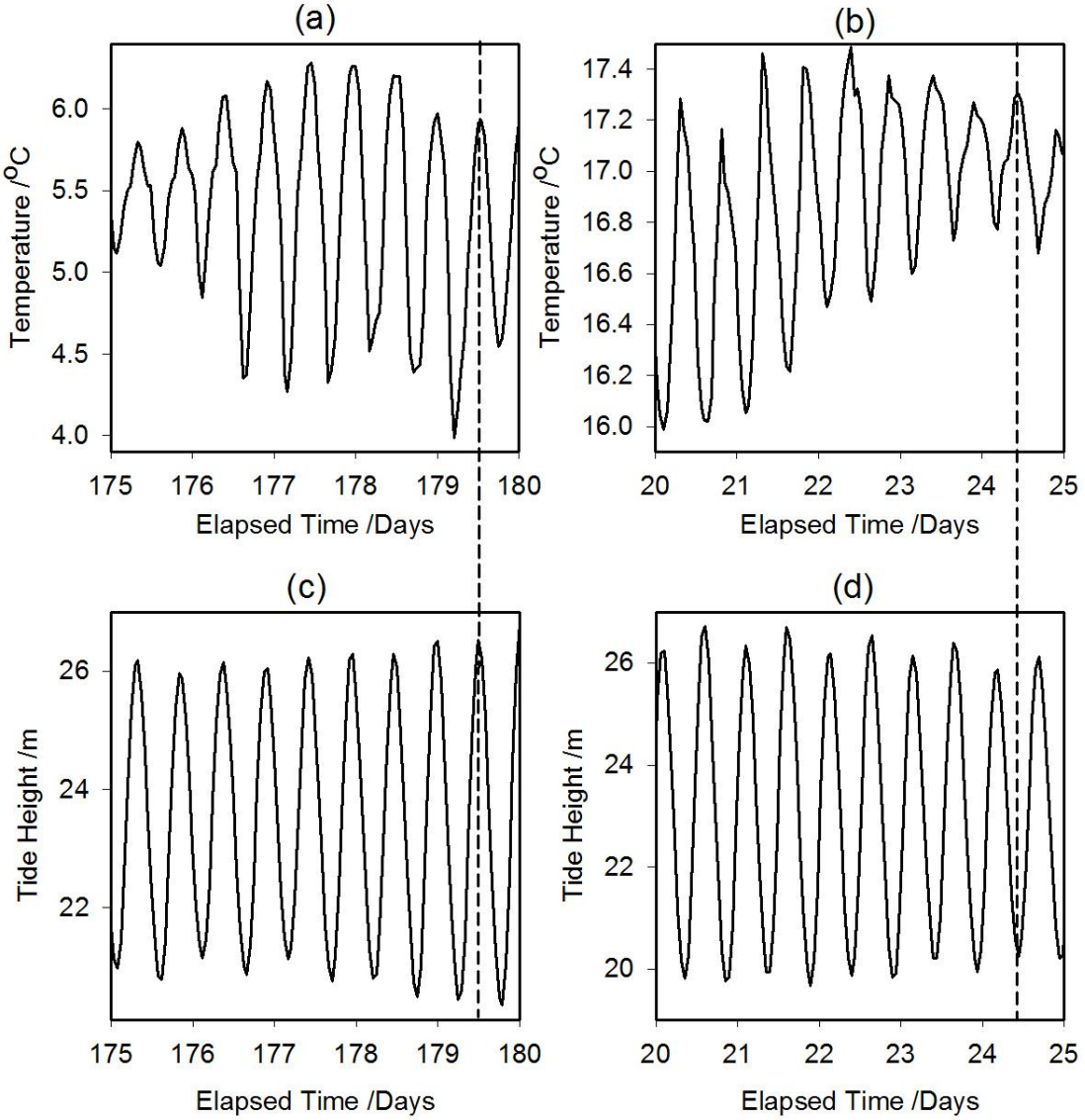

Figure 8.8: Small sections of the temperature time series data for (a) winter (29th December 2010 – 3rd January 2011) and (b) summer (27th July 2010 – 1st August 2010) as well as tidal height time series data for (c) winter (29th December 2010 – 3rd January 2011) and (d) summer (27th July 2010 – 1st August 2010). Comparing the phase relationship of the two sets of seasonal data (e.g. temperature in (a) and tide height in (c)) using the vertical dashed lines, demonstrates the relative change in phase in temperature between summer and winter.

An examination of the temperature and tidal height time series, Figure 8.8, showed a change of phase between the temperature and the tidal height. The phase change between the summer and the winter temperature gradient occurred on the 28th August 2010 and from the winter to the summer temperature gradient on the 23rd March 2011.

This phenomenon was also observed using the cross correlation analysis described in Section 8.3. Figure 8.9 shows the results of the analysis. When the cross correlation was calculated for the whole year the results were skewed as both summer and winter phases were present. However when the annual time series was broken down into summer and winter the clear result was that the tidal height was in phase in the winter and out of phase in the summer. This result confirmed that of Polton et al. (2011) as in winter the temperature decreased as the tide height decreased, i.e. the temperature decreased with the ebb tide, so the lower temperature water was from the coast. In summer the opposite was true with the temperature decreasing with increasing tidal height (flood tide), so the lower temperature water was from the Irish Sea.

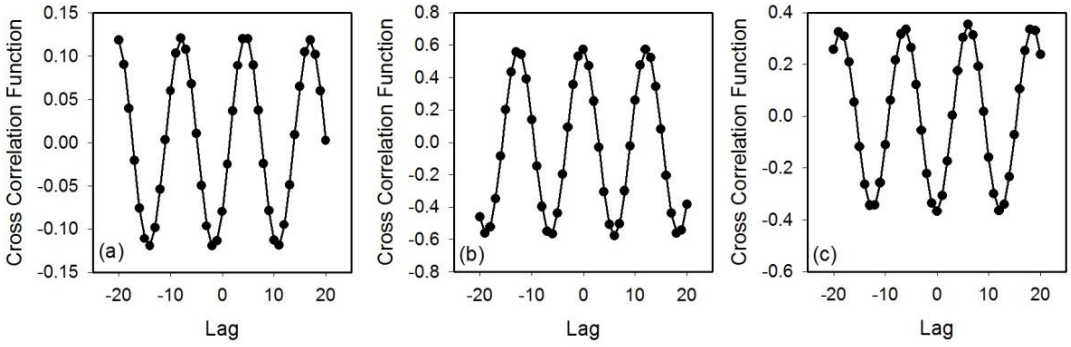

Figure 8.9: Cross correlation analysis between temperature and tidal height for (a) the whole year, (b) summer and (c) winter data to demonstrate the switch in phase relationship with season

8.3.2 Cross Correlation Analysis applied to optical data for Liverpool Bay

Cross correlation analysis for $c_{ac\text{-}9}(555)$ against fluorescence, salinity, current displacement and current velocity (Figure 8.10) provided an insight into the dynamics of the turbidity signal at Site A. Figure 8.10 shows that $c_{ac\text{-}9}(555)$ was in phase with fluorescence and out of phase with salinity and displacement (as well as tidal amplitude as previously established). It also shows that the maximum current velocity occurred at mid-tide (3 hours after the turn) and that slack water was at the tide turn.

These results indicate that $c_{ac\text{-}9}(555)$ had a maximum when the salinity, depth and displacement were at a minimum.

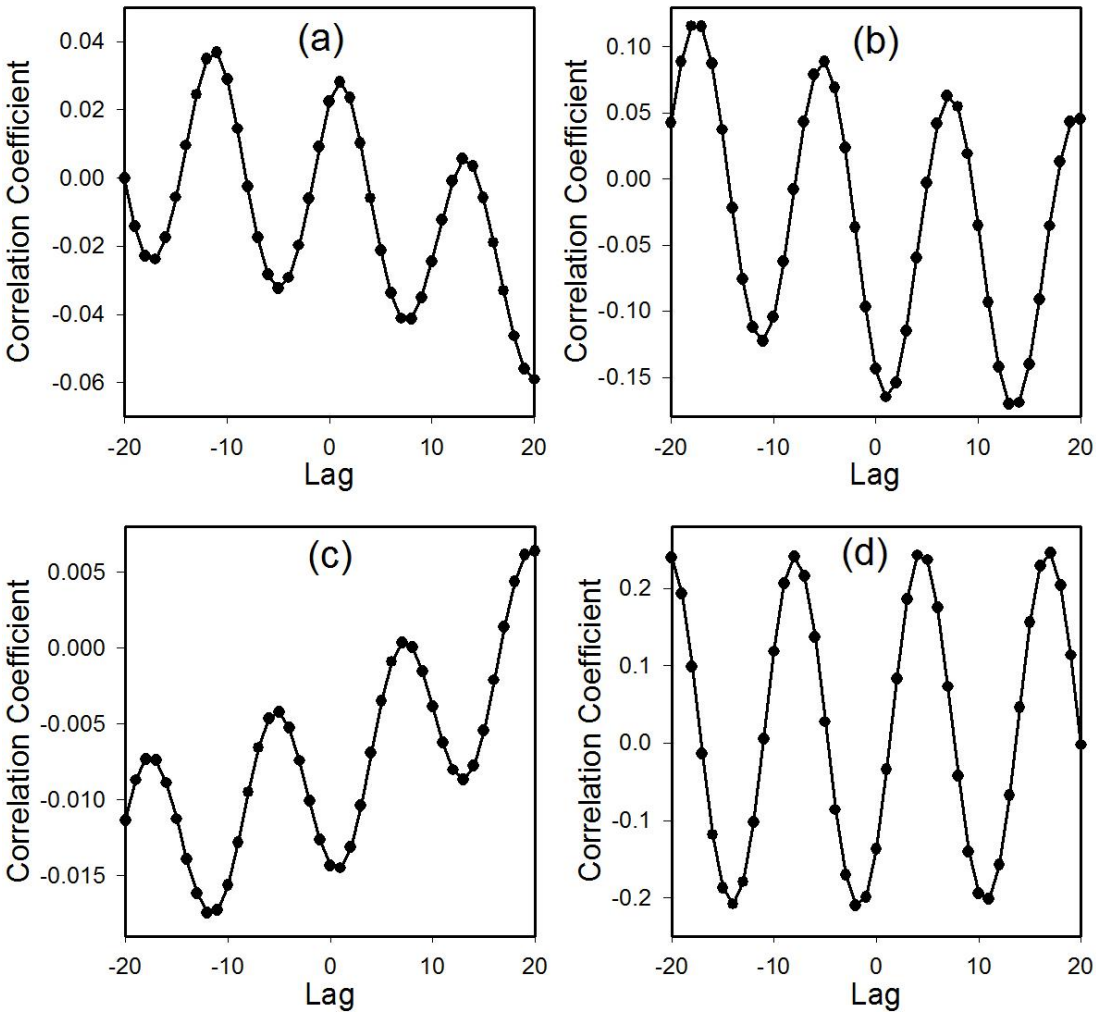

Figure 8.10: Cross Correlation analysis of $c_{ac\text{-}9}(555)$ with (a) Fluorescence (b) Salinity (c) Displacement (d) Current Velocity.

8.4 Source of High Frequency Signal

A closer look at the high frequency signal from the $c_{ac\text{-}9}(555)$ data in Figure 8.11 indicates that the amplitude modulation was related to the spring/neap cycle of the tides, with periods of larger amplitude modulation related to the spring tide and lower amplitude modulation related to the neap tide. This suggests that there was a

greater variation in turbidity at the spring tide. There were three possible mechanisms that could produce such a turbidity signal. The first was local re-suspension at the site, the second was advection of higher turbidity water over the site and the last was the *ac-s* penetrating a benthic layer as its position relative to the sea bed changed with the tidal height.

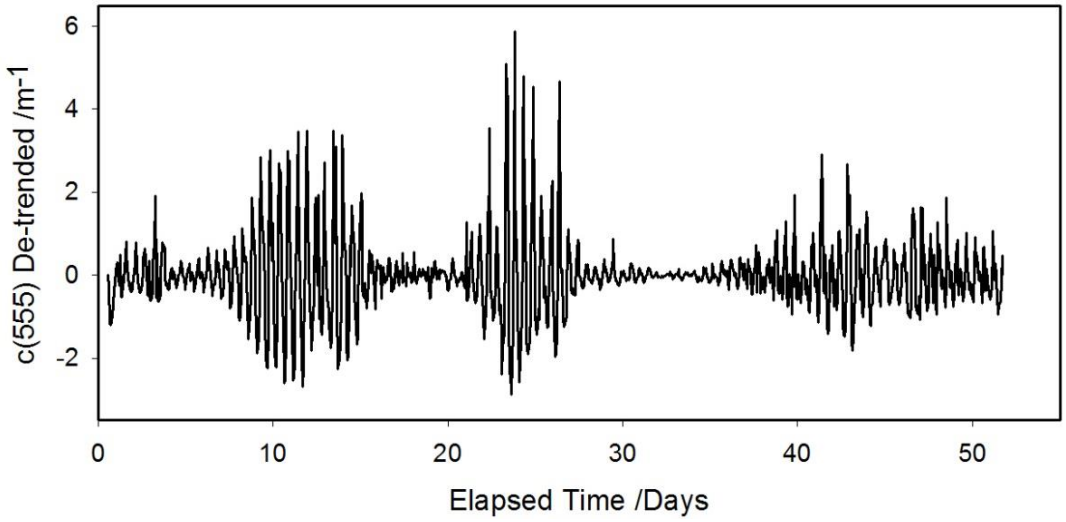

Figure 8.11: High frequency signal result from de-trending procedure applied to $c_{ac\text{-}9}(555)$. Shown is the section of data for *COBS* Cruise Number 75; 12th January 2011 - 16th March 2011.

The *FFT* analysis of the $c_{ac\text{-}9}(555)$ turbidity signal showed that the main turbidity signal had a frequency of 1.933 day^{-1} which was the M_2 tidal mode and that the subsidiary peak at 3.7 day^{-1} was aligned with the current velocity. This showed that the main turbidity signal was driven by the tidal amplitude rather than the current velocity and confirmed that local re-suspension was not the source of the high frequency signal (in the latter case, the current velocity would be the main driver of turbidity).

The cross correlation analysis confirmed that maximum $c_{ac\text{-}9}(555)$ occurred at minimum salinity. This makes it unlikely that the source of the turbidity signal is a particle-laden benthic layer since reduced salinity at this location is associated with surface (more buoyant) waters.

8.4.1 Advection

The remaining possible source for the high turbidity water was advection. The low salinity high turbidity water had a maximum at the low tide, which suggested that it originated from the Lancashire coast. The polar plot demonstrating the direction of current flow in Figure 4.17 and the map showing the location of Site A (Figure A.1) support the conclusion that the high turbidity water originated from the Mersey and Dee Rivers.

This conclusion is consistent with *SPM* analysis completed at the site over a tidal cycle during *COBS* cruise 76. The surface concentration of *MSS* measured hourly for a full tidal cycle is shown in Figure 8.12, with the dark grey dashed lines indicating low tide and the light grey dashed lines indicating high tide. The maxima in *MSS* concentration were coincident with the two low tides.

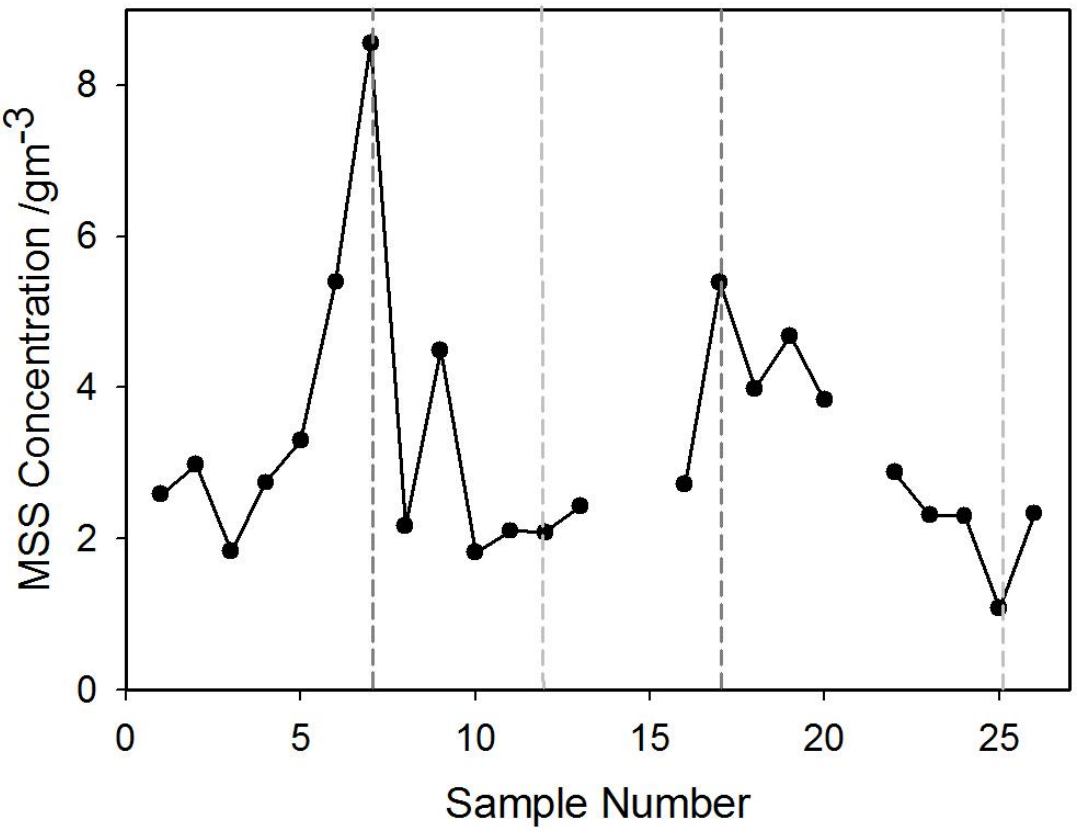

Figure 8.12: Hourly *MSS* concentration measurements taken between 1pm 18th April 2011 and 2pm 19th April 2011, with the dark grey dotted lines representing low tide and the light grey dotted lines representing high tide.

Remote sensing reflectance (R_{rs}(667)) from satellites can be used as an indicator of suspended sediment concentration. An image supplied by Catherine Mitchell at the University of Strathclyde (Figure 8.13) indicated that the concentration of suspended sediments was highest at the mouths of the Mersey and Dee Rivers, lending support to the idea that advection from these sources caused the high frequency signal observed in $c_{ac\text{-}9}$(555).

Krivstov et al. (2008) produced surface *SPM* maps of Liverpool Bay using MATLAB stepwise regression models. These maps also indicate that *SPM* concentrations are higher at the mouths of the Mersey and Dee and that the *SPM* was carried out by the freshwater plume from both rivers to Site A with the ebb tide. These authors also presented LISST measurements taken in Liverpool Bay which supported this conclusion.

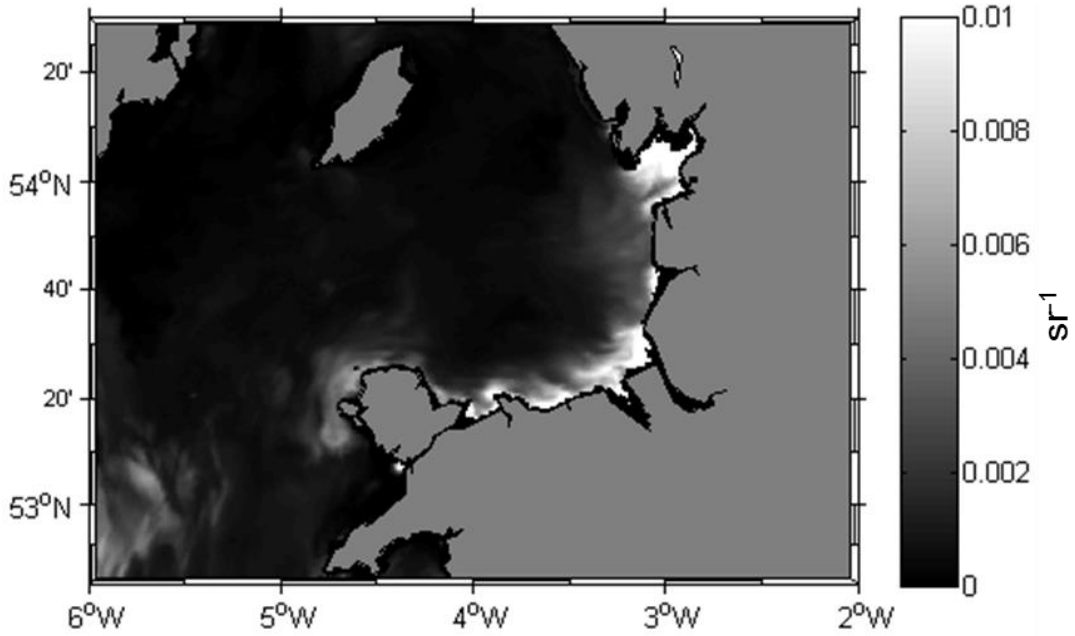

Figure 8.13: R_{rs}(667) image of Liverpool Bay processed by Catherine Mitchell at the University of Strathclyde. The image is derived from MODIS Aqua image captured on 25th May 2013.

8.4.2 Estimates of the contributions of individual Optically Significant Materials to light attenuation at Site A.

The chlorophyll contribution to $c_{ac\text{-}9}(\lambda)$ was estimated using the fluorometer data. The fluorescence counts were converted to chlorophyll concentration using the equation provided by the manufacturer and the chlorophyll concentration was then multiplied by the relevant *SIOP* to estimate $c_{CHL}(\lambda)$ (Section 4.5.4).

The *CDOM* contribution was estimated using in situ *CDOM* measurements completed at NOC: Liverpool. The measurements were made hourly for a period of 25 hours at both the sea surface and bottom. These values were plotted against salinity measured by the *CTD* mounted on the sample frame.

The equation of the best fit line was then used to convert the salinity time series to *CDOM* concentration ($a_{CDOM}(440)$). The absorption spectrum of *CDOM* is an exponential of the form of Equation (8.3). The average spectral slope was calculated from all of the samples and used to estimate the value of $a_{CDOM}(\lambda)$. As *CDOM* does not scatter, the value of $a_{CDOM}(\lambda)$ is equal to $c_{CDOM}(\lambda)$.

$$a_{CDOM}(\lambda) = a_{CDOM}(\lambda_r) \cdot \exp[-S(\lambda - \lambda_r)] \tag{8.3}$$

where $a_{CDOM}(\lambda)$ is the absorption coefficient of *CDOM* at a given wavelength λ and S is the spectral slope of the *CDOM* absorption spectrum normalised at 440 nm.

As the only other optically significant material is mineral suspended solids (*MSS*), the remainder of the $c_{ac\text{-}s}(\lambda)$ must come from the *MSS*. The breakdown of constituent contributions at 555 nm is shown in Figure 8.15.

Figure 8.15 shows that the main contributor to $c_{ac\text{-}9}(555)$ was *MSS* and this was consistent for all wavebands. Thus, even with the large sources of uncertainty in the estimations of constituent concentrations, the optically dominant constituent in Liverpool Bay could be identified as *MSS*.

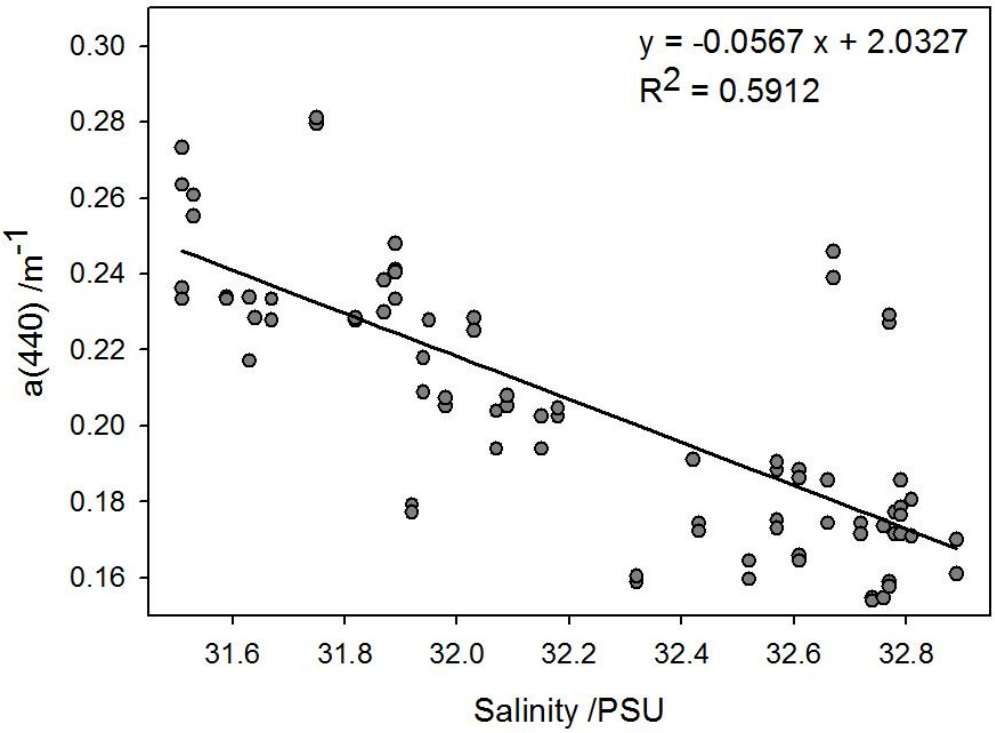

Figure 8.14: *CDOM* concentration (equal to $a_{CDOM}(440)$) plotted against salinity in order to use the salinity measurements at Site A as a proxy variable for *CDOM* concentration.

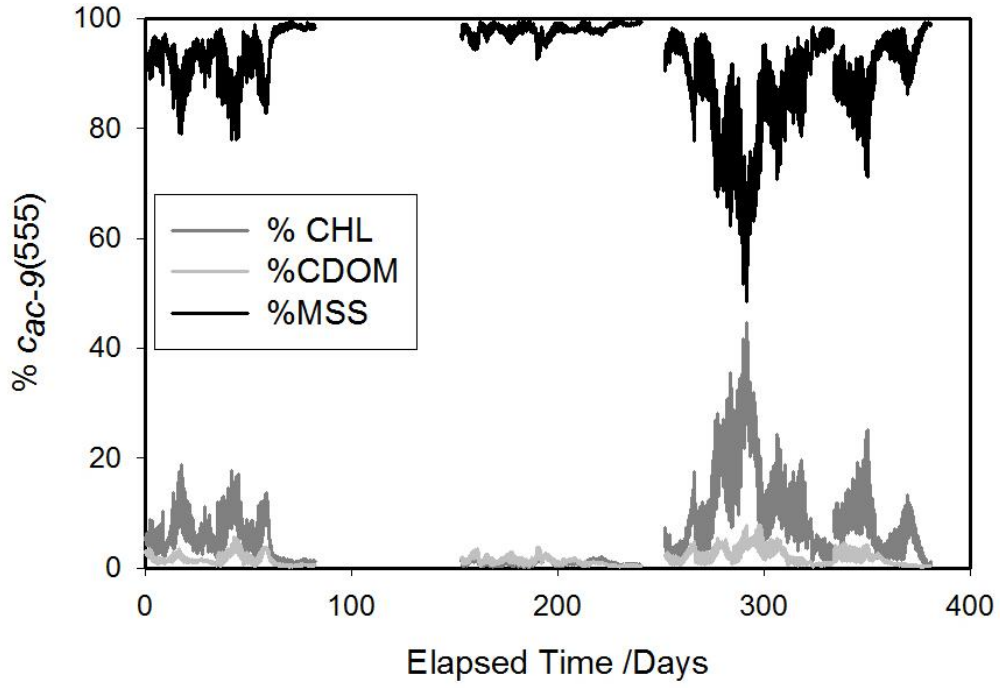

Figure 8.15: Percentage contribution of each constituent to $c_{ac\text{-}9}(555)$

8.4.3 The "Subsidiary Peak"

The subsidiary peak, observed in the *FFT* results at 3.7 day^{-1} (Figure 8.16) must have a different source than the main advection signal. *FFT* analysis suggested that the current velocity was the driver due to the frequency match. The subsidiary peak always appeared during the decreasing phase of the main turbidity signal, corresponding to the flood tide, and also at the maximum current velocity. This suggested that re-suspension was the source of the subsidiary peak.

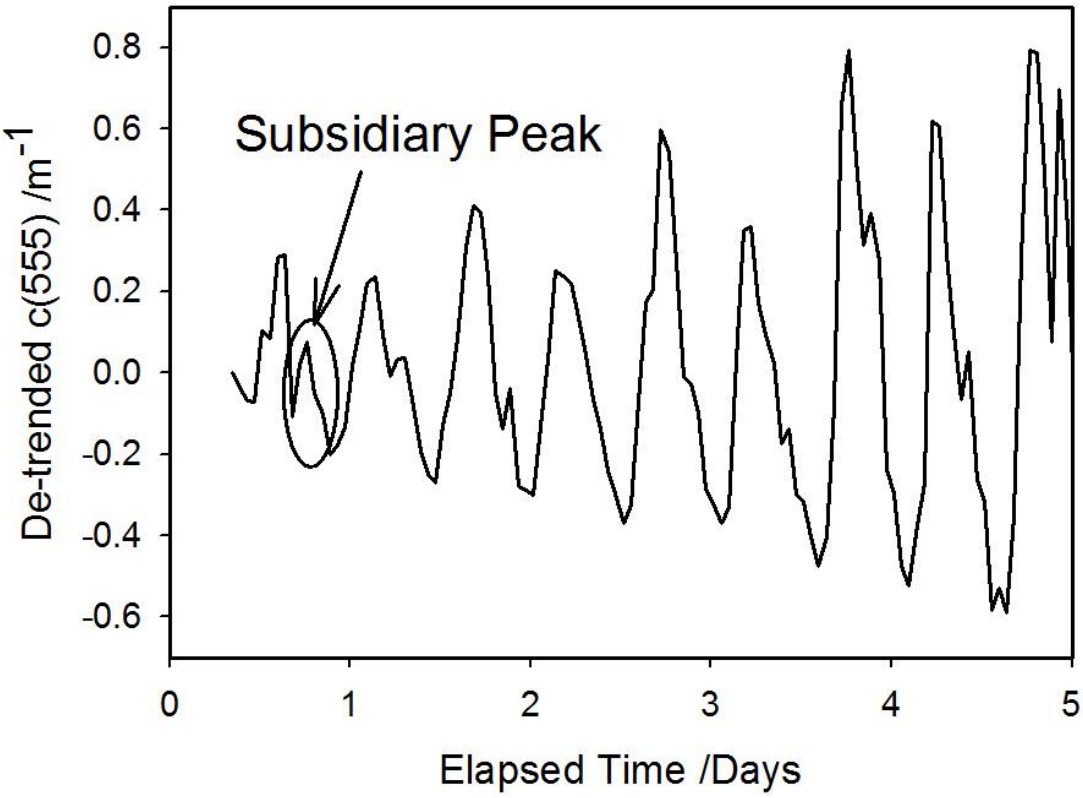

Figure 8.16: Subsection of de-trended c(555) time series to show subsidiary peak on the flood tide. Elapsed Time = 0 is the 7th July 2010.

As previously discussed, Site A experienced semi-diurnal periodic stratification (*SIPS*) caused by tidal straining. Palmer & Polton (2011) estimated that *SIPS* was present for 78.2% of the year, with enduring stratification occurring 21% of the time and enduring mixing < 1% (with enduring defined as lasting longer than one tidal cycle).

In a mixed system, benthic sediment undergoing re-suspension would be able to traverse the entire water column, but in a stratified system it would only rise to the pycnocline. In Liverpool Bay at Site A the *SIPS* mechanism would only allow the re-suspended sediment to be detected by the *ac-s* on its mooring on the flood tide when the water column was fully mixed. The implication is that mixing of the water column offshore from Site A would create a peak in the turbidity signal as the re-suspended sediment was advected over the site on the incoming tide. It may be relevant that Foster et al. (1983) demonstrated that the *Phaeocystis pouchetii* bloom in the summer of 1977 was present throughout the water column in offshore waters, but only present in the subsurface layer in coastal water. They suggested that the decreased vertical stability (and consequently increased mixing) of the offshore water had allowed the cooler more saline phytoplankton rich, *Phaeocystis* dominated bottom waters to reach the surface. The results of the analysis of the optical data from Site A suggested a similar process is causing the subsidiary peak in turbidity, with re-suspended sediments reaching the surface in the offshore water when stratification is broken down and causing a secondary peak in the optical signal when the mixed water is detected by the instruments at Site A.

8.5 Chapter Summary

1. Data from the Liverpool Bay Coastal Observatory was subjected to large amounts of fouling which prevented standard data analysis techniques being applied (Chapter 4 & Appendix A).

2. Repeated data smoothing was used to separate the low and high frequency signal from the turbidity data. This removed the fouling from the data set. The method was tested using current velocity data from the *ADCP* which confirmed the residual current in a north east direction (Polton et al., 2011; Palmer, 2010; Verspecht et al., 2009; Howarth et al., 2008).

3. An *FFT* was applied to the high frequency data to determine the main driver of the turbidity signal. Frequency matching between the turbidity ($c_{ac\text{-}9}(555)$) and the tidal height, salinity, fluorescence, particle displacement, and current velocity determined that the turbidity was driven by the tidal height rather than current velocity.

4. Cross correlation analysis to determine phase relationships was also applied to the turbidity signal. This method was tested by using the known phenomenon of seasonal phase switching between tidal height and temperature, originally described by Polton et al. (2011), the cross correlation analysis matched the published results confirming the validity of the method. The results of cross correlation analysis applied to the turbidity signal showed that turbidity was in phase with fluorescence, out of phase with tidal height and salinity, and 45º out of phase with current velocity.

5. Combining the results of the three novel analysis techniques presented in this chapter showed that the main turbidity signal was caused by advection from the coast. Higher turbidity water with reduced salinity was brought out to the mooring site on the ebb tide causing a turbidity peak at low tide and a turbidity minimum at high tide.

6. A second turbidity signal of lower amplitude, described as the subsidiary peak, was attributed to the re-suspension of particles due to the breakdown of the semi-diurnal stratification in the bay. The re-suspension occurred offshore away from the mooring site and was observed in the turbidity signal during the flood tide when the stratification was broken down and the water column became mixed.

Chapter 9 Discussion and Conclusions

9.1 General Discussion: Summary of Work

The original objective of the work presented in this thesis was to accurately recover optically significant constituent (*OSC*) concentrations from total inherent optical properties (*IOPs*) measured using a WET Labs absorption/attenuation meter (*ac-9*/*ac-s*), utilising specific *IOPs* (*SIOPs*) averaged across the archive UK Shelf data set.

In order to determine an optimum method of *IOP* Inversion, a data set of modelled *IOPs* was generated by randomly selecting *OSC* concentrations from within a predetermined range, multiplying each by the relevant *SIOP*, and summing the results to calculate the total *IOPs* for each combination of concentrations. This procedure was completed for 10,000 sets of *OSC* concentrations. Random noise was then added to the modelled *IOPs* in order to test the sensitivity of inversion methods to measurement uncertainty, and a method was also proposed to examine the likely effect of inappropriate assumptions regarding *SIOP* characteristics.

The simplest approach to recover *OSC* concentrations from *ac-9* data was to solve a set of three simultaneous equations, but it was possible to over constrain the problem since the *ac-9* measures both $a(\lambda)$ and $c(\lambda)$ in 9 wavebands. Several different three-equation methods, including that of Gallegos & Neale (2002), and the fully over constrained method, were tested using the modelled *IOP* data set with and without added measurement uncertainties. When no measurement uncertainties were added all of the methods tested recovered the *OSC* concentrations perfectly, which suggested that any method of *IOP* inversion using an adequate number of simultaneous equations was valid. However with increasing measurement uncertainties, the errors in the recovered *OSC* concentrations became very significant for all of the methods tested. The most robust method was found to be a combination of two absorption wavelengths (412 and 676 nm) and one attenuation wavelength (676 nm), and this '*AAC'* method was used for the remainder of the thesis.

However even the *AAC* procedure proved to be very sensitive to measurement errors in the *IOPs* used as inputs and erroneous assumptions regarding the *SIOPs* used as coefficients in the inversion matrix. In practice, as the *SIOP* uncertainties are usually larger in magnitude than the *IOP* measurement errors therefore it was the *SIOP* uncertainties which had a larger impact on the recovered *OSC* concentrations when realistic levels of uncertainties were considered.

The *AAC* method was then tested on field *ac-9* data from the UK shelf sea archive. Examining each *OSC* individually, there appeared to be a good correlation between measured and recovered *OSC* concentrations (*CDOM* $R^2 = 0.57$, *CHL* $R^2 = 0.63$ and *MSS* $R^2 = 0.63$), however the percentage of stations recovered with errors of less than ± 20% was less impressive, with 42% of stations for *CDOM*, 18% for *CHL* and 41% for *MSS*. No single station demonstrated recovery errors of less than 30% for all three *OSC* concentrations. There was also a systematic underestimation in all three *OSC* concentration recoveries.

In order to better understand the results of the inversion procedure, four stations within the Scottish sea lochs were examined in detail. This allowed the possibility of fine-scale changes in water type within each profile to be investigated, and it was hoped that it would provide some insight into the origins of the apparent errors in the *IOP* inversion procedure. For each of the four stations, it was possible to combine the *IOP* inversion results with other physical and optical data (temperature, salinity, fluorescence and backscattering) to identify areas within each profile that displayed different optical characteristics and gain an estimation of the proportions of *OSC* concentrations in each area. This showed that the optical properties can vary significantly over a few metres in response to changes in both particle type and *CDOM* concentration, and that these changes are linked to layers in the water column with differing hydrographic characteristics. It was also found that the ratio of backscattering to total scattering, which is related to phase function, was a sensitive indicator of particle type. When data from the four stations were combined, the results confirmed those drawn from the individual stations and also that the proposed analysis technique functioned across a large area with different water characteristics. On the whole the analysis showed that the constituent concentrations recovered by

the *ac-9* inversion procedure may not give an absolute match with those found by sample analysis in the laboratory, but comparison with proxy variables (fluorescence, backscattering and salinity) indicated that the inversion of *ac-9* data can give useful information on the relative distribution of constituents in the water column. Combining the *ac-9* with the other optical and physical measurements has considerable potential for giving insights into the spatial distributions of materials and processes, and also their temporal evolution wherever time series data are available.

Temporal data were obtained from the Liverpool Bay Coastal Observatory. In addition to the physical properties monitored at the site, an *ac-s* and an *ECO* fluorometer were deployed 5 m below the surface to monitor the optical properties. Due to long deployment times and less than optimum maintenance, the data recovered from the *ac-s* was of poor quality. However the attenuation channel of the *ac-s* provided an optical signal, which, when coupled to physical measurements, could be analysed to determine temporal changes in water composition and locate the source of the most turbid waters. Signal analysis techniques were employed to analyse the attenuation, current velocity, tidal height, temperature and salinity and to determine that the attenuation signal was largely driven by the advection of *MSS* originating from the Mersey and Dee estuaries. This caused maxima in the attenuation signal to coincide with minima in tidal height and salinity and maxima in temperature. This conclusion was supported by results previously published by Polton et al. (2011). In addition to the main tidal signal, a smaller attenuation maximum was observed, which occurred shortly after the maximum current velocity on the flood tide. This "subsidiary peak" coincided with the breakdown of strain induced periodic stratification (*SIPS*), which has a semi-diurnal frequency in Liverpool Bay. It provided evidence for the occurrence of re-suspension in the bay away from the site which was then observed due to advection by the tidal current.

9.2 Conclusions

This section provides conclusions for the key issues identified in Chapter 1. These issues are summarised (in italics) before each conclusion.

- *Development of a modelled IOP data set to represent realistic UK Shelf values in order to fully characterise IOP Inversion methodologies.*

A modelled data set was devised by randomly sampling *OSC* concentrations from a defined range that covered the UK Shelf data set. No weighting was added to the concentrations to give preference to the most likely combination of constituent concentrations. Using the *SIOPs* of Neil et al. (2011) the modelled *OSC* concentrations were multiplied by the relevant *SIOP* and summed to give perfectly modelled total *IOPs*. In order to determine the optimum method of *IOP* inversion methodology, measurement uncertainties in the *IOPs* were simulated by adding random noise, in the form of a Gaussian distribution, to the modelled *IOP* data set. The uncertainties in *SIOPs* were modelled in order to match the observed variability in the *SIOPs* within UK Shelf data set. The uncertainties were modelled to represent the inappropriateness of the *SIOPs* for a given area, rather than as random uncertainties, which do not fit *SIOP* uncertainties. The developed model along with modelled uncertainties fully characterise the UK Shelf data set and therefore can be used to effectively test the *IOP* inversion methodologies on realistic modelled data.

- *Selection of the optimum method of IOP inversion, by rigorous testing and comparison.*

Several methods of *IOP* inversion were tested including the previously published method of Gallegos & Neale (2002) and the original methods proposed in this thesis: the three simultaneous equations method (many combinations proposed: three absorption wavelengths; three attenuation wavelengths; and two absorption wavelengths and one attenuation wavelength) and the over constrained system utilising all possible absorption and attenuation wavelengths from the *ac-9* (18 in total). All methods tested had perfect recoveries when the perfectly modelled data

set was used. When measurement uncertainties were added to the modelled *IOP* data set, the results showed an increasing sensitivity when the size of the measurement uncertainties were increased. The sensitivity was measured as the gradient of the percentage standard deviation added to the *IOP* data against the percentage standard deviation in the recovered *OSC* concentrations. The optimum method was considered to be the method which had the lowest sensitivity to added measurement uncertainties. When all of the methods were compared, the optimum method was found to be one of the methods proposed during this work: three simultaneous equations using two absorption wavelengths and one attenuation wavelength (*AAC*).

- *Further characterisation of the optimum method of IOP inversion using the modelled data set with added measurement uncertainties.*

Having selected the *AAC* method as the optimum method of *IOP* inversion, further characterisation was required to understand how the method would perform with field *ac-9* measurements and inappropriate *SIOP* values, such as the UK Shelf data set. Testing showed that despite being the optimum method, the *AAC* was still very sensitive to *IOP* measurement uncertainties. When uncertainties of the order of 8% (the estimate of reasonable *IOP* measurement uncertainties found through testing data from the Oban 2004 cruise Section 3.7) were added to the *IOP* data resulting *OSC* concentration recoveries were of the order of 117% for *CDOM*, 42% for *CHL*, and 14% for *MSS* concentration recoveries. These uncertainties in *OSC* concentration recoveries show that only *MSS* has reasonable uncertainties however these results are for uncertainties in the *IOPs* only with no uncertainties in the *SIOPs*. Further testing shows that water type has a large impact on the results, different types of water (offshore, fjord, muddy or bloom) can dramatically change the sensitivity of each *OSC* concentration to the *IOP* inversion process. Recoveries in *CDOM* concentration vary between 1.4% in fjord waters and 4.1% in bloom waters, *CHL* concentration recoveries vary between 0.7% in bloom waters and 1.8% in both muddy and fjord waters and *MSS* concentration varies between 0.04% in muddy waters and 2.4% in bloom waters; with 1% standard deviation added to the *IOPs* as measurement uncertainties, these numbers are significantly increased with more

realistic measurement uncertainties added to the *IOPs* and again assume no *SIOP* uncertainty. The effect of adding uncertainties to the *SIOPs* was tested and found that realistic values for *SIOP* uncertainty could not be added and still gain meaningful *OSC* concentration results, therefore significantly reduced values of *SIOP* uncertainty had to be added to the modelled data set. *SIOP* uncertainties were added to four distinct water types to test the effect of using inappropriate *SIOP* values on the *IOP* inversion method. The results again showed that the water type played a major role in the level of uncertainties in the recovered *OSC* concentrations. Adding both uncertainties in the *IOPs* and *SIOPs* showed that due to the much larger uncertainties in the *SIOPs* the major contributor to the uncertainties in recovered *OSC* concentrations is the appropriateness of the *SIOPs* for the area of interest. The use of averaged *SIOPs* may not be appropriate if the *IOP* inversion recoveries are to be accurate.

- *Development of a novel method of spatial analysis to test the results of IOP inversion method limitations and to determine particle populations within a water column.*

Given the sensitivity of the *IOP* inversion method to added measurement uncertainties the *IOPs* and inappropriateness in the *SIOPs* it was important to develop a new method of data analysis to recover information on particle populations within a water column using the *IOP* inversion results and other physical and optical measurements made at the station. Four stations from the Scottish sea lochs were examined in detail by plotting the fluorescence against backscattering to determine populations of particulates that had high fluorescence and low backscattering (general characteristics of *CHL*) and low fluorescence and high backscattering (generally classified as *MSS*). A plot of backscattering against total scattering was then used to determine regions of similar scattering phase function, used to determine different particle types. When combined clusters of different particle populations could be identified as either *CHL*, *MSS*, or a combination of the two (mixed). When the clusters were projected onto profiles of temperature, salinity, fluorescence and backscattering, the location of each cluster within the profile could be identified. In

every station examined, particle clusters with the same properties were located together within a profile and those particles identified as *CHL* were located closer to the surface, populations identified as *MSS* were located at the bottom of the profile and clusters identified as mixed were located in between the *CHL* and *MSS* populations, suggesting that the spatial analysis technique was working as expected. Further development to include the recovered *OSC* concentrations from the *IOP* inversion method for each station was also completed, where the *OSC* concentration was plotted against the relevant proxy variable (salinity for *CDOM*, fluorescence for *CHL* and backscattering for *MSS*) and good correlation between each was observed. This suggested that the failure of the *IOP* inversion was not random and a systematic uncertainty was the cause of inversion failure, suggesting that the *SIOPs* were inappropriate for the area under investigation. Expansion of the proposed spatial analysis demonstrated that the technique could be employed on a wide area and that the results would still be valid. Expansion of the method for a large spatial area increased the application of the method to include the analysis of large spatial data sets where standard analysis techniques have previously failed and also improved the functionality of the *IOP* inversion technique, which was too sensitive to measurement uncertainties to be a useful tool in its own right.

- *Development of temporal analysis techniques for the analysis of data subjected to fouling.*

In addition to the development of a novel method for the analysis of spatial data, original techniques for the analysis of temporal data were also developed. This analysis was designed to complement the spatial analysis described above and to provide a method of analysis for temporal data which may be subjected to fouling due to long deployment times. This technique may become increasingly relevant with the addition of optical instruments to the existing Argo float system and both the temporal and spatial analysis combined can provide increased analysis possibilities in the data collected from *AUV* systems. The data analysed is from the Liverpool Bay Coastal Observatory and was for *ac-s* data deployed for an average of six weeks. Due to fouling the attenuation was used as a measure of turbidity, rather

than attempting the analysis of the full *ac-s* data set ($c_{ac\text{-}s}(555)$ was used). In order to analyse the data, it had to be separated in to high and low frequency components. As the data was not continuous, the application of a fast Fourier transform (*FFT*) lead to edge effects at the start and end of each deployment and therefore the application of repeated smoothing was utilised instead, in order to separate the high frequency and low frequency components of the data. This removed the fouling from the data set and left the high frequency tidal components of the turbidity signal to be analysed. The application of an *FFT* on the high frequency signal showed a major peak coincident with the M_2 tidal component and a secondary peak at approximately 4 day^{-1}, which is approximately twice a tidal cycle. This "subsidiary peak" matched one found within the turbidity data. The use of cross correlation analysis to determine phase relationships graphically showed that the turbidity signal was out of phase with tidal height and salinity; in phase with fluorescence; and 45º out of phase with current velocity. All of this analysis coupled with the dynamics of Liverpool Bay (Appendix A) suggested that the turbidity signal was caused by the advection of sediment from the Mersey and Dee estuaries causing an increasing turbidity signal during the ebb tide and a decreasing turbidity signal during the flood tide. The "subsidiary peak" which was shown to be driven by current velocity is caused by offsite re-suspension causing a small turbidity peak during the flood tide. All of the proposed analysis techniques were tested using previously published work on the dynamics of Liverpool Bay and in each case the results from the novel analysis in this thesis were confirmed by previously published results, including the turbidity analysis which utilised all three novel approaches and was confirmed by known dynamics within Liverpool Bay. Therefore the temporal analysis methods proposed within this work have been shown to be effective tools for the analysis of poor quality data that would otherwise be discarded.

9.3 Suggestions for further work

In this thesis, measurement uncertainties have proved to be a major stumbling block to the development and validation of *IOP* inversion techniques. Improved validation of any of the methods presented here would require an intensive measurement campaign which concurrently measured optics, hydrography and *OSC* concentrations. All of the techniques for data analysis, with sub-optimal data quality, could then be refined and validated on clean data with minimal measurement uncertainties.

The analysis of optical signals could also be expanded to include the examination of optical structures on a finer (sub-metre) scale, with links to physical processes such as horizontal shear and vertical mixing coefficients (Lee et al., 2013; Sullivan et al., 2012; Sullivan et al., 2010).

The planned expansion of the Argo Float system to include the use of bio-optical sensors, such as chlorophyll fluorescence, and backscattering and beam attenuation coefficients means that optical data will soon be made available on the same scale as physical measurements such as temperature and salinity. These systems have been designed to reduce the amount of fouling on the optical instruments by flushing with deep ocean water and using the ocean-air interface on resurfacing (IOCCG, 2011). Optical sensors are also being increasingly fitted to autonomous underwater vehicles (*AUVs*) and glider systems to allow long term optical time series to be acquired at high spatial resolution. The analysis techniques developed in this thesis provide a relatively fault-tolerant means of analysing these optical data, which will not usually be accompanied by *OSC* measurements for validation purposes.

The Global Ocean Observing System (*GOOS*) which will combine physical, hydrological and optical oceanographic data will also provide an opportunity to apply the techniques prototyped in Liverpool Bay on a global scale.

There is ample scope for the refinement of the inversion techniques developed in this thesis to study regional differences in the interaction between physical, hydrological and optical parameters, and to interpret these differences in terms of marine ecosystem function.

References

Aas, E., Høkedal, J. & Sørensen, K., 2005. Spectral backscattering coefficient in costal waters. *International Journal of Remote Sensing*, 26(2), pp.331-43.

Allali, K., Bricaud, A., Babin, M., Morel, A. & Chang, P., 1995. A new method for measuring spectral absorption coefficients of marine particles. *Limnology & Oceanography*, 40, pp.1526-32.

Allen, J.I., Blackford, J., Holt, J., Proctor, R., Ashworth, M. & Siddorn, J., 2001. A highly spatially resolved ecosystem model for the north west European continental shelf. *Sarisa*, 86, pp.423-40.

Allen, J.I., Holt, J., Blackford, J. & Proctor, R., 2007. Error quantification of a high-resolution coupled hydrodynamic-ecosystem coastal-ocean model: Part 2. Chlorophyll-a, nutrients and SPM. *Journal of Marine Systems*, 68, pp.381-404.

Amoudry, L.O. & Souza, A.J., 2011a. Deterministic coastal morphological and sediment transport modelling: a review and discussion. *Review of Geophysics*, 49.

Amoudry, L.O. & Souza, A.J., 2011. Impact of sediment induced stratification and turbulence closures on sediment transport and morphological modelling. *Continental Shelf Research*, 13(9), pp.912-28.

Apel, J.R., 1987. *Principles of Ocean Physics*. London: Academic.

Arbones, B., Figueras, F.G. & Zapata, M., 1996. Determination of phytoplankton absorption coefficient in natural seawater samples: evidence of a unique equation to correct the pathlength amplification on glass fibre filters. *Marine Ecology Progress Series*, 137, pp.293-304.

Babin, M. & Stramski, D., 2002. Light absorption by aquatic particles in the near infra-red spectral region. *Limnology & Oceanography*, 47, pp.911-15.

Babin, M., Stramski, D., Giovanni, M., Claustre, H., Bricaud, A., Obolenski, G. & Hoepffner, N., 2003. Variations in the light absorption coefficients of phytoplankton,

nonalgal particles, and dissolved organic matter in coastal waters around Europe. *Journal of Geophysical Research*, 108(C7).

Barillé-Boyer, A.L., Barillé, L., Massé, H., Razet, D. & Héral, M., 2003. Correction for particulate organic matter as estimated by loss on ignition in estuarine ecosystems. *Estuarine, Coastal & Shelf Science*, 58, pp.147-53.

Binding, C.E., Bowers, D.G. & Mitchelson-Jacob, G., 2003. An algorithm for the vertical retrieval of suspended sediment concentrations in the Irish Sea from SeaWiFs ocean colour satellite imagery. *International Journal of Remote Sensing*, 24, pp.3791-806.

Boss, E., Slade, W.H., Behrenfield, M. & Dall'Olmo, G., 2009. Acceptance angle effects on the beam attenuation in the ocean. *Optics Express*, 17(3), pp.1535-50.

Boss, E., Taylor, L., Gilbert, S., Gundersen, K., Hawley, N., Jansen, C., Johengen, T., Purcell, H., Robertson, C., Schar, D.W., Smith, G.J. & Tamburri, M.N., 2009a. Comparison of inherent optical properties as a surrogate for particulate matter concentration in coastal waters. *Limnology & Oceanography: Methods*, 7, pp.803-10.

Bricaud, A., Babin, M., Morel, A. & Claustre, H., 1995. Variability in the chlorophyll-specific absorption coefficients of natural phytoplankton: analysis and parameterisation. *Journal of Geophysical Research: Oceans*, 100, pp.13321-32.

Bricaud, A., Claustre, H., Ras, J. & Oubelkheir, K., 2004. Natural variability of phytoplanktonic absorption in oceanic waters: Influence of the size struture of algal populations. *Journal of Geophysical Research*, 109, p.C11010.

Bricaud, A., Morel, A. & Prieur, L., 1981. Absorption by dissolved organic matter of the sea (yellow substance) in the UV and visible domains. *Limnology and Oceanography*, 26, pp.43-53.

Bricaud, A., Morel, A. & Prieur, L., 1983. Optical efficiency factors of some phytoplankters. *Limnology & Oceanography*, 28(5), pp.816-32.

Bricaud, A. & Stramski, D., 1990. Spectral absorption coefficients of living phytoplankton and non-algal biogenous matter: a comparisson between the Peru upwelling area and the Sargasso Sea. *Limnology and Oceanography*, 35, pp.562-82.

Brown, I.C., 2010. *The inversion of in situ Inherent Optical Property Measurements in Shelf Seas*. Glasgow: University of Strathclyde Thesis.

Brown, J.M., Bolaños, R., Howarth, M.J. & Souza, A.J., 2012. Extracting sea level residual in tidally dominated estuarine environments. *Ocean Dynamics*, 62, pp.969-82.

Bukata, R.P., Jerome, J.H., Kondratyev, K.Y. & Pozdnyakov, D.V., 1995. *Optical Properties and Remote Sensing of Inland Waters*. 1st ed. Florida: CRC Press LLC, Chapter 1.

Cannizzaro, J.P., Carder, K.L., Chen, R.F., Heil, C.A. & Vargo, G.A., 2008. A novel technique for the detection of the toxic dioflagellate, Karenia brevis, in the Gulf of Mexico from remotely sensed ocean colour data. *Continental Shelf Research*, 28, pp.137-58.

Capuzzo, E., Painting, S.J., Forster, R.M., Greenwood, N., Stephens, D.T. & Mikkelsen, O.A., 2013. Variability in the sub-surface light climate at ecohydrodynamically distinct sites in the North Sea. *Biogeochemistry*, 113, pp.85-103.

Carder, K.L., Steward, R.G., Harvey, G.R. & Ortner, P.B., 1989. Marine humic and fulvic acids: their effects on remote sensing of ocean chlorophyll. *Limnology & Oceanography*, 34, pp.68-81.

Chami, M., McKee, D., Leymarie, E. & Khomenko, G., 2006. Influence of the angular shape of the volume scattering function and multiple scattering on remote sensing reflectance. *Applied Optics*, 45, pp.9210-20.

Chami, M., Shybanov, E.B., Khomenko, G.A., Lee, M.E.G., Martynov, O.V. & Korotaev, G.K., 2006. Spectral variation of the volume scattering function over the

full range of scattering angles in the coastal environment. *Applied Optics*, 45(15), pp.3605-19.

Chang, G.C. & Dickey, T.D., 1999. Partitioning in situ total spectral absorption by use of moored spectral absorption-attenuation meters. *Applied Optics*, 38(18), pp.3876-87.

Chen, Z., Hu, C., Muller-Karger, F.E. & Luther, M.E., 2010. Short-term variability of suspended sediment and phytoplankton in Tampa Bay, Florida: Observations from a coastal oceanographic tower and ocean color satellites. *Estuarine, Coastal & Shelf Science*, 89, pp.62-72.

Cleveland, J.S. & Weidemann, A.D., 1993. Quantifying absorption by aquatic particles: A multiple scattering correction for glass-fiber filters. *Limnology & Oceanography*, 38(6), pp.1321-27.

Coble, P., Hu, C., Gould, R.W., Chang, G. & Wood, A.M., 2004. Colored Dissolved Organic Matter in the Coastal Ocean: An Optical Tool for Coastal Zone Environmental Assessment and Mangement. *Oceanography*, June. pp.50-59.

Creanor, D.E. & Cunningham, A., 2010. Origins of ambiguity in the inversion of remote sensing reflectance signals by spectral matching in optically complex shelf seas. *Journal of the European Optical Society - Rapid Publications*, 5(10018), pp.1990-2573.

Cunningham, A., Ramage, L. & McKee, D., 2013. Relationships between inherent optical properties and the depth of penetration of solar radiation in optically complex coastal waters. *Journal of Geophysical Research: Oceans*, 118, pp.2310-17.

Dickey, T., Lewis, M. & Chang, G., 2006. Optical Oceanography: Recent advances and future directions using global remote sensing and in situ observations. *Reviews of Geophysics*, 44, p.RG1001.

Doerffer, R., Sørensen, K. & Aiken, J., 1999. MERIS potential for coastal zone applications. *International Journal of Remote Sensing*, 20(9), pp.1809-18.

Doron, M., Brasseur, P. & Brankart, J.M., 2011. Stochastic estimation of biogeochemical parameters of a 3D ocean coupled physical-biogeochemical model: Twin experiments. *Journal of Marine Systems*, 87, pp.194-207.

Doxaran, D., Ruddick, K., McKee, D., Gentili, B., Tailliez, D., Chami, M. & Babin, M., 2009. Spectral variations of light scattering by marine particles in coastal waters, from visible to near infrared. *Limnology & Oceanography*, 54, pp.1257-71.

D'Sa, E.J., Miller, R.L. & McKee, B.A., 2007. Suspended particulate matter dynamics in coastal waters from ocean color: Application to the northern Gulf of Mexico. *Geophysical Research Letters*, 34, p.LE23611.

Fabricus, K.E., De'ath, G., Humphrey, C., Zagorskis, I. & Schaffelke, B., 2013. Intra-annual variation in turbidity in response to terrestrial runoff on near-shore coral reefs of the Great Barrier Reef. *Estuarine, Coastal and Shelf Science*, 116, pp.57-65.

Fang, L.G., Chen, S.S., Li, D. & Li, H.L., 2009. Use of reflectance ratios as a proxy for coastal water constituent monitoring in the Pearl River estuary. *Sensors*, 9, pp.656-73.

Ferrari, G.M. & Dowell, M.D., 1998. CDOM absorption characteristics with relation to fluorescence and salinity in coastal areas of the Southern Baltic Sea. *Estuarine, Coastal & Shelf Science*, 47, pp.91-105.

Field, C.B., Behrenfeld, M.J., Randerson, J.T. & Falkowski, P., 1998. Primary production of the biosphere: integrating terrestrial and oceanic components. *Science*, 281, pp.237-40.

Foster, P., Voltolina, D., Spencer, C.P., Miller, I. & Beardall, J., 1983. A seasonal study of the distribution of surface state variables in Liverpool Bay. V. Summer. *Journal of Experimental Marine Biology & Ecology*, 73, pp.151-65.

Gallegos, C.L., 2005. Optical water quality of blackwater river estuary: the lower St Johns river, Florida USA. *Estuarine, Coastal & Shelf Science*, 63, pp.57-72.

Gallegos, C.L. & Neale, P.J., 2002. Partitioning spectral absorption in case 2 waters: discrimination of dissolved and particulate components. *Applied Optics*, 41(21), pp.4220-33.

Geiger, E.F., Grossi, M.D., Trembanis, A.C., Kohut, J.T. & Oliver, M.J., 2011. Satellite-derived coastal ocean and estuarine salinity in the Mid-Atlantic. *Continental Shelf Research*.

Golub, G.H., 1968. Least squares, singular values and matrix approximations. *Aplikace Matematiky*, 13(1), pp.44-51.

Golub, G.H. & Reinsch, C., 1970. Singular Value Decomposition and Least Squares Solutions. *Numerische Mathematik*, 14, pp.403-20.

Gordon, R.L., 1996. *Acoustic Doppler Current Profilier Principles of Operation A Practical Primer. 2nd Edition for Broadband ADCPs*. San Diago, California: RD Instruments.

Gordon, H.R. & McCluney, W.R., 1975. Estimation of the depth of sunlight penetration in the sea from remote sensing. *Applied Optics*, 14, pp.413-16.

Greenwood, N., Hydes, D.J., Mahaffey, C., Wither, A., Barry, J., Sivyer, D.B., Pearce, D.J., Hartman, S.E., Andres, O. & Lees, H.E., 2011. Spatial and temporal variability in nutrient concentrations in Liverpool Bay, a temperate latitude region of freshwater influence. *Ocean Dynamics*, 61(12), pp.2181-99.

Heaps, N.S., 1972. Estimation of density currents in the Liverpool Bay area of the Irish Sea. *Geophysical Journal of the Royal Astronomical Society of London*, 30, pp.415-32.

Holt, J., 2008. *POLCOMS User Guide, Version 6.4*. [Online] Available at: cobs.noc.ac.uk/modl/polcoms/POLCOMS_user_guide.pdf [Accessed 12 April , 2014].

Holt, J.T., Allen, J.I., Proctor, R. & Gilbert, F., 2005. Error quantification of a high resolution coupled hydrodynamic-ecosystem coastal-ocean model: Part 1. Model

overview and assessment of the hydrodynamics. *Journal of Marine Systems*, 57, pp.167-88.

Holt, J., Hughes, J., Hopkins, J., Wakelin, S.L., Holliday, N.P., Dye, S., González-Pola, C., Hjøllo, S.S., Mork, K.A., Nolan, G., Proctor, R., Read, J., Shammon, T., Sherwin, T., Smyth, T., Tattershall, G., Ward, B. & Wiltshire, K.H., 2012. Mulit-decadal variability and trends in the temperature of the northwest European continental shelf: A model-data synthesis. *Progress in Oceanography*, 106, pp.96-117.

Howarth, M.J., Proctor, R., Balfour, C., Knight, P., Palmer, M. & Player, R., 2008. The Liverpool Bay Coastal Observatory. Liverpool, UK, , 2008. Physics of Estuaries & Coastal Seas.

Howarth, M.J., Proctor, R., Knight, P.J., Smithson, M.J. & Mills, D.K., 2006. The Liverpool Bay Coastal Observatory - towards the goals. In *Proceedings Oceans '06*. 18-21 September 2006, Boston, , 2006. IEEE.

Howlett, E.R., Rippeth, T.P. & Howarth, M.J., 2011. Processes contributing to the evolution and destruction of stratification in the Liverpool Bay ROFI. *Ocean Dynamics*, 167, pp.191-94.

IOCCG, 2011. *Bio-Optical Sensors on Argo Floats*. Reports of the International Ocean-Colour Coordinating Group, No 11. Dartmouth, Canada: IOCCG.

Jeffrey, S.W. & Humphrey, G.F., 1975. New spectrophotometric equations for determining chlorophylls a, b, c1 and c2 in higher plants, algae and natural phytoplankton. *Biochemie und Physiologie der Pflanzen*, 167, pp.191-94.

Jeffrey, S.W., Mantoura, R.F.C. & Wright, W.W., 1996. *Phytoplankton pigments in oceanography: guidelines to modern methods*. Paris: UNESCO.

Jerlov, N.G., 1975. A transparency meter for ocean water. *Tellus*, 9, pp.229-33.

Jerlov, N.G., 1976. Marine Optics. In R.J. Gibbs, ed. *Suspended Solids in Water*. Amsterdam: Plenum Press, Elsevier.

Kiefer, D.A., Chamberlin, W.S. & Booth, C.R., 1989. Natural fluorescence of chlorophyll a: Relationship to photosynthesis and chlorophyll concentration in the western South Pacific gyre. *Limnology & Oceanography*, 34(5), pp.868-81.

Kirk, J.T.O., 1992. Monte Carlo modelling of the performance of a reflective tube absorption meter. *Applied Optics*, 31, pp.6463-68.

Kirk, J.T.O., 1994. *Light and Photosynthesis in Aquatic Ecosystems*. 2nd ed. Cambridge: Cambridge University Press.

Kishino, M., Takahashi, M., Okami, N. & Ichimura, S., 1985. Estimation of the spectral absorption coefficients of phytoplankton in the sea. *Bulletin of Marine Science*, 37, pp.634-42.

Kowalczuk, P., Cooper, W.J., Whitehead, R.F., Durako, M.J. & Sheldon, W., 2003. Characterization of CDOM in an organic rich river and surrounding coastal ocean in the South Atlantic Bight. *Aquatic Science*, 65, pp.381-98.

Krivstov, V., Howarth, M.J., Jones, S.E., Souza, A.J. & Jago, C.F., 2008. Monitoring and modelling of the Irish Sea and Liverpool Bay: An overview and SPM case study. *Ecological Modelling*, 212, pp.37-52.

Kromkamp, J.C., Morris, E.P., Forster, R.M., Honeywill, C., Hagerthey, S. & Paterson, D.M., 2006. Relationship of intertidal surface sediment chlorophyll concentration to hypertidal reflectance and chlorophyll fluorescence. *Estuaries & Coasts*, 29(2), pp.183-96.

Lahet, F. & Stramski, D., 2010. MODIS imagery of turbid plumes in San Diego coastal waters during rainstorm events. *Remote Sensing of Environment*, 114, pp.332-44.

Lawson, C.L. & Hanson, R.J., 1995. *Solving Least Squares Problems*. Philadelphia, PA: SIAM.

Lee, J.H., Churnside, J.H., Marchbanks, R.D., Donaghay, P.L. & Sullivan, J.M., 2013. Oceanographic lidar profiles compared with estimates from in situ optical measurements. *Applied Optics*, 52(4), pp.786-94.

Lee, Z.P., Du, K.P. & Arnone, R., 2002. Deriving inherent optical properties from water color: A mulit-band quasi-analytical algorithm for optically deep waters. *Applied Optics*, 41, pp.5755-72.

Le, C.F., Hu, C.M., Cannizzaro, J. & Duan, H.T., 2013. Long-term distribution patterns of remotely sensed water quality parameters in Chesapeake Bay. *Estuarine, Coastal & Shelf Science*, 128, pp.93-103.

Leymarie, E., Doxaran, D. & Babin, M., 2010. Uncertainties associated to measurements of inherent optical properties in natural waters. *Applied Optics*, 49, pp.5415-36.

Lide, D.R., 1997. Physical and optical properties of minerals. In D.R. Lide, ed. *CRC Handbook of Chemistry and Physics (77th Edition)*. Boca Raton, Florida: CRC Press. p.2496.

Llope, M., Daskalov, G.M., Rouyer, T.A., Mihnevas, V., Chan, K.S., Grishin, A.N. & Strenseth, N.C., 2011. Overfishing of top predators eroded the resilience of the Black Sea system regardless of the climate and anthropogenic conditions. *Global Change Biology*, 17, pp.1251-56.

Lohrenz, S.E., 2000. A novel theoretical approach to correct for pathlength amplification and variable sample loading in measurements of particulate spectral absorption by the quantitative filter technique. *Journal of Plankton Research*, 22, pp.639-57.

Lohrenz, A.D., Weidman, A.D. & Tuel, M., 2003. Phytoplankton spectral absorption as influenced by community size structure and pigment composition. *Journal of Plankton Research*, 25(1), pp.35-61.

Loisel, H., Mériaux, X., Berthon, J. & Poteau, A., 2007. Investigation of the optical backscattering to scattering ratio of marine particles in relation to their biogeochemical composition in the eastern English Channel and southern North Sea. *Limnology & Oceanography*, 52(2), pp.739-52.

Lorenzen, C.J., 1966. A method for the continuous measurement of in vivo chlorophyll concentration. *Deep Sea Research & Oceanographic Abstracts*, 13(2), pp.223-27.

Los, F.J., Villars, M.T. & Van der Tol, M.W.M., 2008. A 3-dimentional primary production model (BLOOM/GEM) and its applications to the (Southern) North Sea (coupled physical-chemical-ecological model). *Journal of Marine Systems*, 74, pp.259-94.

Lynch, J.F., Irish, J.D., Sherwood, C.R. & Agrawal, Y.C., 1994. Determining suspended sediment particle size information from acoustical and optical backscatter measurements. *Continental Shelf Research*, 14(10/11), pp.1139-65.

Maffione, R.A. & Dana, D.R., 1997. Instruments and methods for measuring the backwards-scattering coefficient of ocean waters. *Applied Optics*, 36(24), pp.6057-67.

McKee, D., Piskozub, J. & Brown, I., 2008. Scattering error corrections for in situ absorption and attenuation measurements. *Optics Express*, 16, pp.19480-92.

McKee, D., Piskozub, J., Röttgers, R. & Reynolds, R.A., 2013. Evaluation and improvement of an iterative scattering correction scheme for in situ absorption and attenuation measurements. *Journal of Atmospheric and Oceanic Technology*, 30, pp.1527-41.

Menon, H.B. & Sangekar, N.P., 2010. Measurement of salinity of Mandovi and Zuari estuarine waters from OCM data. *Indian Journal of Geo-Marine Science*, 39(4), pp.504-08.

Miller, 1985. *Nutrient dynamics in relation to a thermocline discontinuity in the NE Irish Sea*. Bangor, Wales: Ph.D Thesis. University of Wales.

Mitchell, B.G., 1990. Algorythms for determining the absorption coefficient of aquatic particles using the quantitative filter technique (QFT). *SPIE*, 1302, pp.137-48.

Mitchell, C., Cunningham, A. & McKee, D., 2014. Remote sensing of shelf sea optical properties: evaluation of a quasi-analytical approach for the Irish Sea. *Remote Sensing of Environment*, 143, pp.142-53.

Mobley, C.D., 1994. *Light and Water: Radiative Transfer in Natural Waters*. New York: Academic.

Möllmann, C., Diekmann, R., Müller-Karulis, B., Kornilovs, G., Plikshs, M. & Axe, P., 2009. Reorganisation of a large marine ecosystem due to atmospheric and anthropogenic pressure: a discontinuous regime shift in the Central Baltic Sea. *Global Change Biology*, 15, pp.1377-93.

Moore, L.R., Goericke, R. & Chisholm, S.W., 1995. Comparative physiology of Synechococcus and Prochlorococcus: influence of light and temperature on growth, pigments, fluorescence and absorptive properties. *Marine Ecology Progress Series*, 116, pp.259-75.

Morel, A. & Prieur, L., 1977. Analysis of variations in ocean colour. *Limnology & Oceanography*, 22, pp.709-22.

Morrison, J.R. & Sosik, H.M., 2002. Inherent optical properties in New England Coastal Waters: Decomposition into contributions from optically important constituents. Santa Fe, New Mexico, , 2002. Proceedings of Ocean Optics XVI.

Morrow, J.H., Chamberlin, W.S. & Kiefer, D.A., 1989. A two-component description of spectral absorption by marine particles. *Limnology & Oceanography*, 34, pp.1500-09.

Neil, C., Cunningham, A. & McKee, D., 2011. Relationship between suspended mineral concentrations and red-waveband reflectances in moderately turbid shelf seas. *Remote Sensing Environment*, 115, pp.3719-30.

Neil, C., Cunningham, A., McKee, D. & Polton, J.A., 2012. Remote Sensing of seasonal stratification dynamics in the Southern Irish Sea. *Remote Sensing of Environment*, 127, pp.288-97.

Oguz, T., 2005. Long term anthropogenic forcing of the Black Sea ecosystem. *Oceanography*, 18(2), pp.112-21.

O'Neill, C.K., Polton, J.A., Holt, J.T. & O'Dea, E.J., 2012. Modelling temperature and salinity in Liverpool Bay and the Irish Sea: sensitivity to model type and surface forcing. *Ocean Science*, 8, pp.903-13.

Palmer, M.R., 2010. The modification of current ellipses by stratification in the Liverpool Bay ROFI. *Ocean Dynamics*, 60, pp.219-26.

Palmer, M.R. & Polton, J.A., 2011. A strain-induced fresh water pump in the Liverpool Bay ROFI. *Ocean Dynamics*, 61, pp.1905-15.

Parsons, T.R., Maita, Y. & Lalli, C.M., 1984. *A manual of chemical and biological methods for seawater analysis*. Oxford: Pergamon Press.

Pegau, S., Ceaveland, J.S., Doss, W., Kennedy, C.D., Maffione, R.A., Mueller, J.L., Stone, R., Trees, C.C., Weidemann, A.D., Wells, W.H. & Zaneveld, J.R.V., 1995. A comparison of methods for the absorption coefficient in natural waters. *Journal of Geophysical Research*, 100(C7), pp.13201-20.

Pegau, W.S., Grey, D. & Zaneveld, J.R.V., 1997. Absorption and attenuation of visible and near-infrared light in water: dependance on temperature and salinity. *Applied Optics*, 36, pp.6035-46.

Pegau, S., Zaneveld, J.R.V., Mitchell, B.G., Mueller, J.L., Kahru, M., Weiland, J. & Stramska, M., 2002. Ocean optics protocols for Satellite Ocean Colour Sensor Validation, revision 4, Volume IV: Inherent Optical Properties: Instruments, Characterizations, Field Measurements and Data Analysis Protocols. In J.L. Mueller, G.S. Fargion & C.R. McClain, eds. *NASA/TM-2003-211621/Rev4.-Vol.IV*. Greenbelt, Maryland 20771, USA: NASA, NASA Goddard Space Flight Centre.

Peng, F., Effler, S.W., O'Donnel, D., Weidemann, A.D. & Auer, M.T., 2009. Characterisations of minerogenic particles in support of modelling light scattering in Lake Superior through a two-component approach. *Limnology & Oceanography*, 54, pp.1369-81.

Platt, T., Hoepffner, N., Stuart, V. & Brown , C., 2008. *Why Ocean Colour? The societal benefits of ocean colour technology*. Dartmouth, Canada: Report Number 7, International Ocean Colour Coordinating Group.

Polton, J.A., Palmer, M.R. & Howarth, M.J., 2011. Physical and Dynamical Oceanography in Liverpool Bay. *Ocean Dynmics*, 61, pp.1421-39.

Pope, R.M. & Fry, E.S., 1997. Absorption spectrum (380 - 700nm) of pure water: II. Integrating cavity measurements. *Applied Optics*, 36, pp.8710-23.

Press, W.H., Teukolsky, S.A., Vetterling, W.T. & Flannert, B.P., 2007. *Numerical Recipes: The Art of Scientific Computing*. 3rd ed. New York: Cambridge University Press.

Robinson, I.S., Antoine, D., Darecki, M., Gorringe, P., Pettersson, L., Ruddick, K., Santoleri, R., Siegel, H., Vincent, P., Wernand, M.R., Westbrook, G. & Zibordi, G., 2008. *Remote Sensing of Shelf Sea Ecosystems State of the Art Perspectives*. Ostend, Belgum: Marine Board - European Science Foundation Marine Board - European Science Foundation.

Roesler, C.S., 1998. Theoretical and experimental approaches to improve the accuracy of particle absorption coefficients derived from the quantitative filter technique. *Limnology & Oceanography*, 43(7), pp.1649-60.

Roesler, C.S., Perry, M.J. & Carder, K.L., 1989. Modelling in situ phytoplankton absorption from total absorption spectra in productive inland marine waters. *Limnology and Oceanography*, 34(8), pp.1510-23.

Röttgers, R. & Gehnke, S., 2012. Measurement of light absorption by aquatic particles: improvement of the quantitative filter technique by use of an integrating sphere approach. *Applied Optics*, 51(9), pp.1336-51.

Schofield, O., Bergmann, T., Oliver, M.J., Irwin, A., Kirkpatrick, G., Bissett, W.P., Moline, M.A. & Orrico, C., 2004. Inversion of spectral absorption in the optically complex coastal waters of the Mid-Atlanic Bight. *Journal of Geophysical Research: Oceans*, 109.

Seabird, 2008. *SBE19 plus User's Guide (Version 17)*. Washington: Sea-Bird Electronics Inc.

Simpson, J.H., Brown , J., Matthews, J. & Allen, G., 1990. Tidal Straining, density currents and stirring in the control of estuarine stratification. *Estuaries*, 13, pp.125-32.

Simpson, J.H., Burchard, H., Fisher, N.R. & Rippeth, T.P., 2002. The semi-diurnal cycle of dissipation in a ROFI: model-measurement comparisons. *Continental Shelf Research*, 22, pp.1615-28.

Slade, W.H. & Boss, E., 2006. Calibrated Near-Forward Volume Scattering Function Obtained from the LISST Particle Sizer. *Optics Express*, 14, pp.3602-15.

Slade, W.H., Boss, E., Dall'Omo, G., Langner, M.R., Loftin, J., Behrenfeld, M.J., Roesler, C. & Westberry, T.K., 2010. Underway and moored methods for improving accuracy in measurement of spectral particulate absorption and attenuation. *Journal of Atmospheric & Oceanic Technology*, 27, pp.1733-46.

Smith, R.C., Ainley, D., Baker, K., Domak, E., Emslie, S., Fraser, B., Kennett, J., Leventer, A., Mosley-Thompson, E., Stammerjohn, S. & Vernet, M., 1999. Marine ecosystem sensitivity to climate change. *BioScience*, 49(5), pp.393-404.

Smith, R.C. & Baker, K.S., 1981. Optical properties of the clearest natural waters (200 - 800 nm). *Applied Optics*, 20(2), pp.177-84.

Sokolov, A., Chami, M., Dmitriev, E. & Khomenko, G., 2010. Parameterisation of volume scattering function of coastal waters based on the statistical approach. *Optics Express*, 18(5), pp.4615-36.

Spinrad, R.W., Carder, K.L. & Perry, M.J., 1994. *Ocean Optics*. 1st ed. New York: Oxford University Press.

Stavn, R.H. & Richter, S.J., 2008. Biogeo-optics: particle optical properties and the partitioning of the spectral scattering coefficient of ocean waters. *Applied Optics*, 47(14), pp.2660-79.

Stavn, R.H., Rick, H.J. & Falster, A.V., 2009. Correcting the errors from variable sea salt retention and water of hydration in loss on ignition analysis: implications for studies of estuarine and coastal waters. *Estuarine, Coastal & Shelf Science*, 81, pp.575-82.

Stramski, D., Wozniak, S.B. & Flatau, P.J., 2004. Optical properties of Asian mineral dust suspended in seawater. *Limnology & Oceanography*, 49, pp.749-55.

Sullivan, J.M., Donaghay, P.L. & Rines, J.E.B., 2010. Coastal thin layer dynamics: Consequences to biology & optics. *Continental Shelf Research*, 30, pp.50-65.

Sullivan, J.M., Twardowski, M.S., Donaghay, P.L. & Freeman, S.A., 2005. Using optical scattering to discriminate particle types in coastal waters. *Applied Optics*, 44(9), pp.1667-80.

Sullivan, J.M., Twardowski, M., Donaghay, p.L., Rines, J., McFarland, M., Talapatra, S., Katz, J., Churnside, J. & Weidemann, A., 2012. Biological Thin Layers: history, ecological significance and consequences to oceanographic sensing systems. In Hou, W.W. & Arnone, R., eds. *Conference on Ocean Sensing and Monitoring IV*. Baltimore, MD, , 2012. Proceedings of SPIE.

Sullivan, J.M., Twardowski, M.S., Zaneveld, J.R.V. & Moore, C.M., 2006. Hyperspectral temperature and salt dependencies of absorption by water and heavy water in the 400–750 nm spectral range. *Applied Optics*, 45, pp.5294-309.

Tassan, S. & Ferrari, G.M., 1998. Measurement of light absorption of minerals retained on filters: Determination of the pathlength amplification factor by the 'transmittance-reflectance' method. *Journal of Plankton Research*, 20, pp.1699-709.

Tassan, S. & Ferrari, G.M., 2003. Variability of light absorption by aquatic particles in the near infra-red spectral region. *Applied Optics*, 42, pp.4802-10.

Tassan, S., Ferrari, G.M., Bricaud, A. & Babin, M., 2000. Variation of the amplification factor of light absorption by filter-retained aquatic particles in the coastal environment. *Journal of Plankton Research*, 22, pp.659-68.

Taylor, J.R., 1997. *An Introduction to Error Analysis*. 2nd ed. Sausalito, California: University Science Books.

Timms, R.M. & Moss, B., 1984. Prevention of growth of potentially dense phytoplankton populations by zooplankton grazing, in the presence of zooplankton fish, in shallow wetland ecosystem. *Limnology & Oceanography*, 29(3), pp.472-86.

Trüper, H.G. & Yentsch, C.S., 1967. Use of glass fibre filters for the rapid preperation of in vivo absorption spectra of photosynthetic bacteria. *Journal of bacteriology*, 94, pp.1255-56.

Tzortziou, M., Herman, R., Gallegos, C.L., Neale, P.J., Subramaniam, A., Harding Jr., L.W. & Ahmad, Z., 2006. Bio-optics from the Chesapeake Bay from measurements and radiative transfer closure. *Estuarine, Coastal and Shelf Science*, 68, pp.348-62.

Verspecht, F., Rippeth, T.P., Simpson, J.H., Souza, A.J., Burchard, H. & Howarth, M.J., 2009. Residual circulation and stratification in the Liverpool Bay region of freshwater influence. *Ocean Dynamics*, 59, pp.765-79.

Vodacek, A., Blough, N.V., DeGrandpre, M.D., Peltzer, E.T. & Nelson, R.K., 1997. Seasonal variation of CDOM and DOC in the Middle Atlantic Bight: Terrestrial inputs and photooxidation. *Limnology & Oceanography*, 42(4), pp.674-86.

Voss, K.J. & Austin, R.W., 1993. Beam attenuation measurement error due to small-angle scattering acceptance. *Journal of Atmospheric and Oceanic Technology*, 10, pp.113-21.

WET Labs, 2006. *ac-s Users Guide (Revision F)*. Philomath Oregon: WETLabs Inc.

WET Labs, 2011. *ECO Fluorometer Users Guide*. Philomath, Oregon: WETLabs Inc.

WETLabs, 2006a. *WET Labs Archive File Processing (Revision E4)*. Philomath, Oregon: WETLabs Inc.

Whitmire, A.L., Pegau, W.S., Karp-Boss, L., Boss, E. & Cowles, T.J., 2010. Spectral backscattering properties of marine phytoplankton. *Optics Express*, 18(14), pp.15073-93.

Yensch, C.S. & Menzel, D.W., 1963. A method for the determination of phytoplankton chlorophyll and phaeophytin by fluorescence. *Deep Sea Research & Oceanographic Abstracts*, 10(3), pp.221-31.

Yentsch, C.S., 1962. Measurement of visible light absorption by particle matter in the ocean. *Limnology & Oceanography*, 7, pp.207-17.

Zaneveld, J.R.V., Kitchen, J.C. & Moore, M., 1994. The scattering error correction of reflecting-tube absorption meters. In *Ocean Optics XII*. Bergen, Norway, , 1994. SPIE.

Appendix A The Liverpool Bay Coastal Observatory

A.1 Objectives

The Liverpool Bay Coastal Observatory *COBS* was a collaboration between several marine institutes in the UK headed by the National Oceanography Centre (NOC) with two major objectives;

1. To understand, through effective continuous measurement and modelling, the response of a coastal sea to natural and anthropogenic forcing.

2. To provide a framework for research into the functioning of a shelf sea in a changing climate.

During the lifetime of the project, integrated (near) real-time measurements were coupled to the Proudman Oceanographic Laboratory Coastal Ocean Modelling System (*POLCOMS*) and results were displayed on the web (*http://cobs.noc.ac.uk/*).

Site A is located in Liverpool Bay in the eastern Irish Sea, Figure A.1. The site was chosen as it is located in an area that experiences large amounts of anthropogenic and natural forcing with large wind farm developments and river outflows in the area.

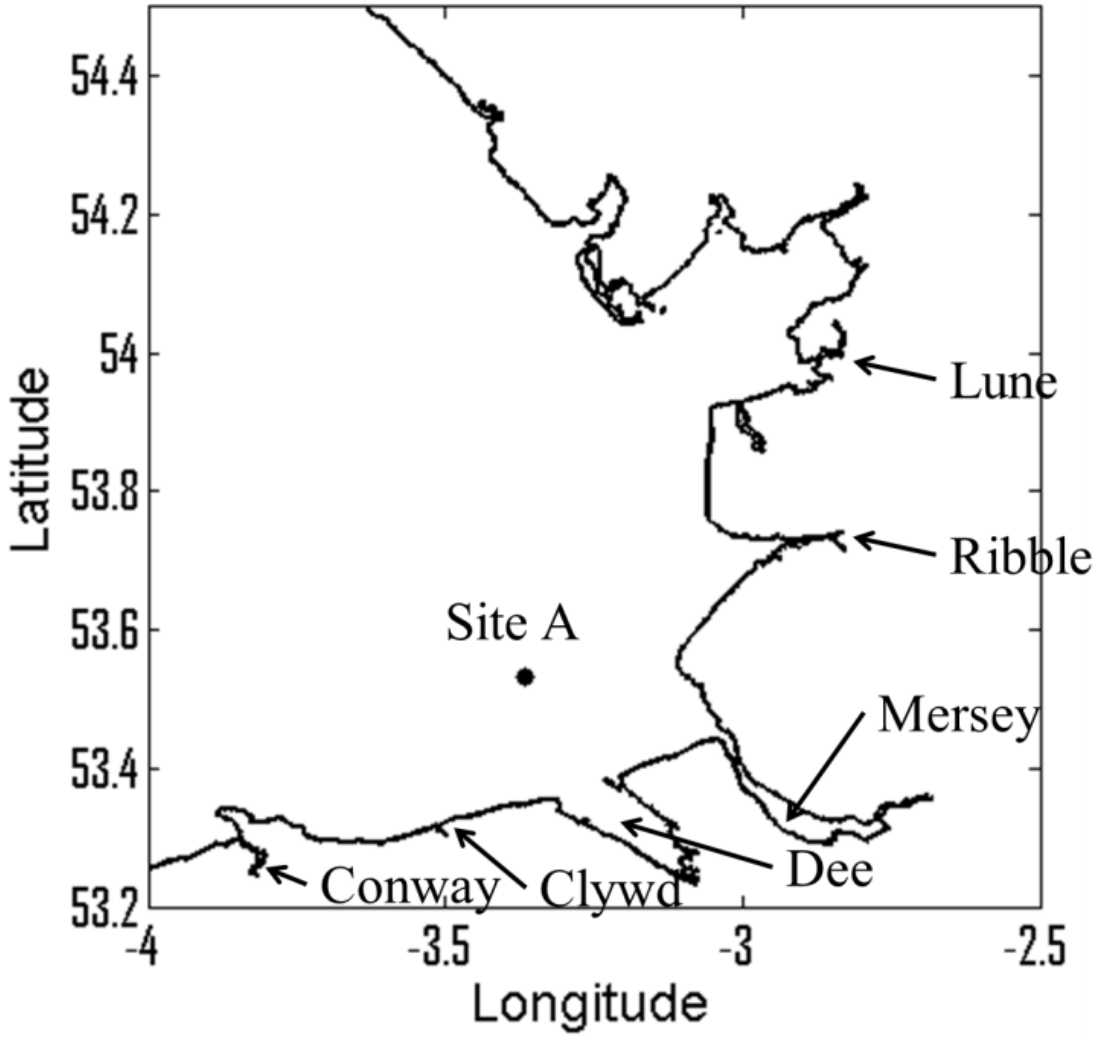

Figure A.1: Map of Liverpool Bay showing the position of the mooring site. Marked on the map with arrows are the major river outflows in the area, these are the sources of freshwater to Liverpool Bay.

A.2 Measurements and Instrumentation

Measurements in Liverpool Bay include (Howarth et al., 2008);

1. Current, temperature and salinity profiles at the fixed mooring site (Site A) from
    a. *CTD* at surface, 5 m and 10 m below the surface.
    b. Bottom mounted *ADCP*.

2. Wave height at Site A
3. Weather from the Hilbre Island and Bidston Observatory weather station
4. Surface temperature, salinity, turbidity, nutrients, irradiance and fluorescence from *CEFAS* SmartBuoy, also daily water samples at Site A
5. Instrumented Ferries (Liverpool to Douglas and Liverpool to Dublin) for near surface temperature, salinity, turbidity, chlorophyll and nutrients
6. Glider operations to measure currents, temperature and salinity.
7. Tide gauge network, with additional sensors for waves, temperature and salinity.
8. A 12-16MHz WERA high frequency radar system to observe sea surface currents and waves with a range of approximately 50 km.
9. Satellite Data – infra-red for sea surface temperature and visible for chlorophyll and suspended sediment.
10. River flow monitors for freshwater input into Liverpool Bay.
11. Optical Instruments (*ac-s* and *ECO* fluorometer) 5 m below surface at Site A. Operational since July 2010.

A.2.1 POLCOMS

The Proudman Oceanographic Laboratory Coastal Ocean Modelling System (*POLCOMS*) is a nested 3D baroclinic hydrodynamic coastal ocean model covering the ocean/shelf of northwest Europe (at 12 km resolution), the Irish Sea (at 1 km resolution) and Liverpool Bay (at 100 - 300 m resolution). Boundary conditions for Liverpool Bay are taken from the Irish Sea model, which in turn uses boundary conditions from Forecast Ocean Atmosphere Model (*FOAM*) from the Met Office. Local river discharges are included through a link-up with the Environment Agency river-flow network. Implementation was initially hydrodynamic with 3D wave-current interaction provided by two way linking between wave (*WAM*) and current models with performance checked against the *in situ* and coastal sea-level measurements. *POLCOMS* also includes a sediment transport model for estimating

concentrations of *SPM* an important influence on light attenuation and hence biological processes. Biological dynamics were simulated by coupling *POLCOMS* to the European Seas Regional Ecosystem Model (*ERSEM*) and validation was provided by *CEFAS* SmartBuoy data and the SeaWiFS satellite ocean colour sensor.

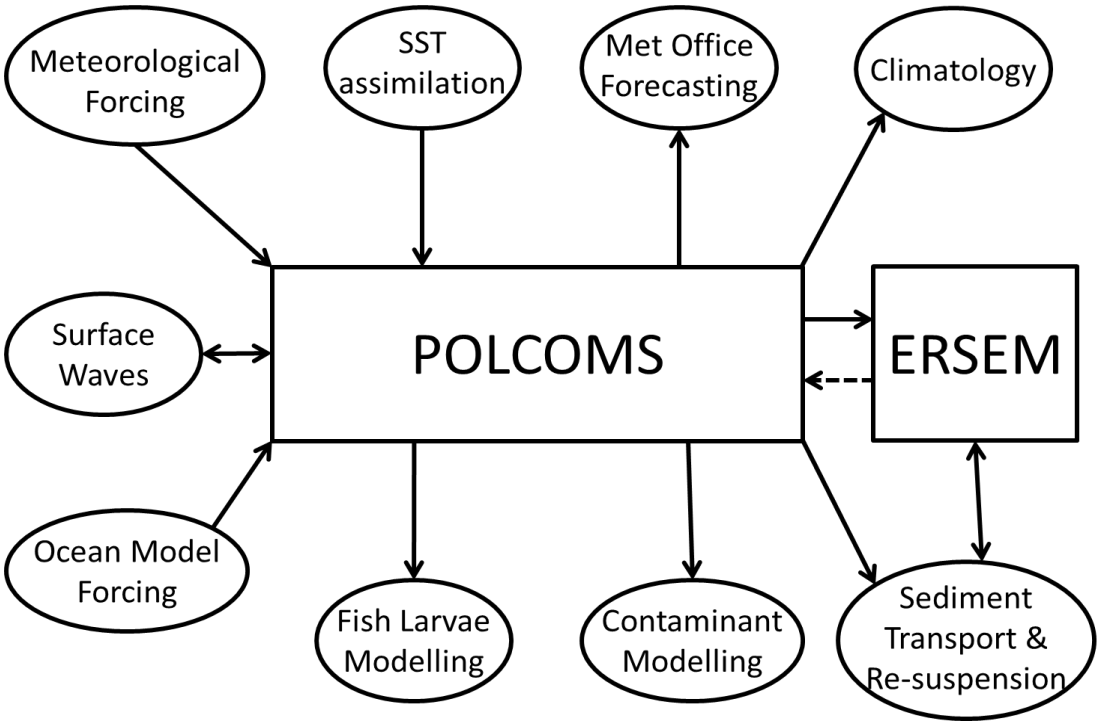

Figure A.2: Inputs and Outputs from *POLCOMS* model

Models are run daily in near-real time. Daily mean sea surface and bed temperature, salinity, chlorophyll, oxygen, nitrate, currents, waves and sea surface height are displayed on the *COBS* website (Brown et al., 2012; Holt et al., 2012; O'Neill et al., 2012; Holt, 2008).

An optical analysis of Liverpool Bay is relevant to the future development of the *POLCOMS* model as ocean colour satellite imagery is used to estimate sea surface temperature for validation. Also optical data can provide information regarding the biological activity of Liverpool Bay which is also of interest and great importance to the study site. Sediment transport modelling can also be completed using optical data and this can be used for model validation and development (Amoudry & Souza, 2011; Amoudry & Souza, 2011a).

A.3 Initial Outline for Work

The initial aim for this PhD was to take the *IOP* inversion method (*AAC*) detailed in Chapter 6 and apply it to the optical data collected in Liverpool Bay. This would recover optically significant constituent (*OSC*) concentrations that could be used to model the underwater light field which would then be coupled to the *POLCOMS* model to improve the accuracy of the *POLCOMS-ERSEM* model.

It became apparent however, that the *ac-s* was not well maintained; cleaning and calibration were not completed as outlined in Chapter 4 (WET Labs, 2006), fouling of the optical surfaces was severe, and the data obtained were therefore not amenable to processing or analysing using standard techniques. An alternative methodology using signal processing techniques was therefore developed, and conclusions that can be drawn from this analysis are presented in the current chapter.

A.4 Additional Data Assessment

As well as the optical time series, water samples were collected to measure coloured dissolved organic material (*CDOM*), Chlorophyll-a (*CHL*) and mineral suspended solids (*MSS*), at the site at the start of each deployment. Known problems with sample analyses include inadequate cleaning of the cuvettes used in the *CDOM* analysis and no inclusion of blank filter pads to monitor errors in *SPM* measurements (Pegau et al., 2002).

Depth profiles were taken concurrently with *OSC* samples in order to calculate *SIOPs* for the site, but there were problems with *ac-s* calibration and data logging which rendered the profiling data unusable. Initial plans for the generation of *SIOPs* at Site A could not therefore be realised.

A.5 Dynamics of Liverpool Bay

A.5.1 Tidal Dynamics

Liverpool Bay is characterised by strong tidal currents (0.75 - 1 ms^{-1} at springs). The tides take the form of a standing wave, resulting from the reflection of a Kelvin wave at the Lancashire coast located at the east of the bay (Simpson et al., 2002). Tidal ranges are considerable, and reach approximately 10 m at Site A. Maximum currents occur 3 hours before and after high water (Miller, 1985). Tidal currents are principally rectilinear, oriented with the major axis near east-west, at approximately 98° from north (Verspecht et al., 2009). Depth-averaged major-axis currents reach up to 1 m s^{-1} on springs and 0.3 m s^{-1} on neaps. Slack water occurs at high tide and low tide. There is also a residual estuarine-type circulation with surface currents directed toward the north and those at the bed directed towards the southeast (Heaps, 1972).

A.5.2 Region of Freshwater Influence

Three major rivers, the Mersey, the Dee and the Ribble, discharge into the south east corner of Liverpool Bay with average flow rates of 40 - 80 m^3 s^{-1}. Liverpool Bay also receives freshwater from the Lune, Clwyd and Conway. The average total input of freshwater is approximately 220 m^3 s^{-1} (Greenwood et al., 2011; Howlett et al., 2011). Figure A.1 shows the location of the major freshwater sources into Liverpool Bay. Site A is therefore located in a region of freshwater influence (*ROFI*).

A.5.3 Strain Induced Periodic Stratification

The freshwater input into Liverpool Bay causes stratification to occur. Freshwater brought out by the ebb tide is more buoyant than the higher salinity shelf sea water causing a horizontal gradient in Liverpool Bay. Increased friction at the bed coupled with the horizontal salinity gradient causes Site A to be fully mixed at high tide and vertically stratified at low tide. This is demonstrated in the schematic diagram in Figure A.3.

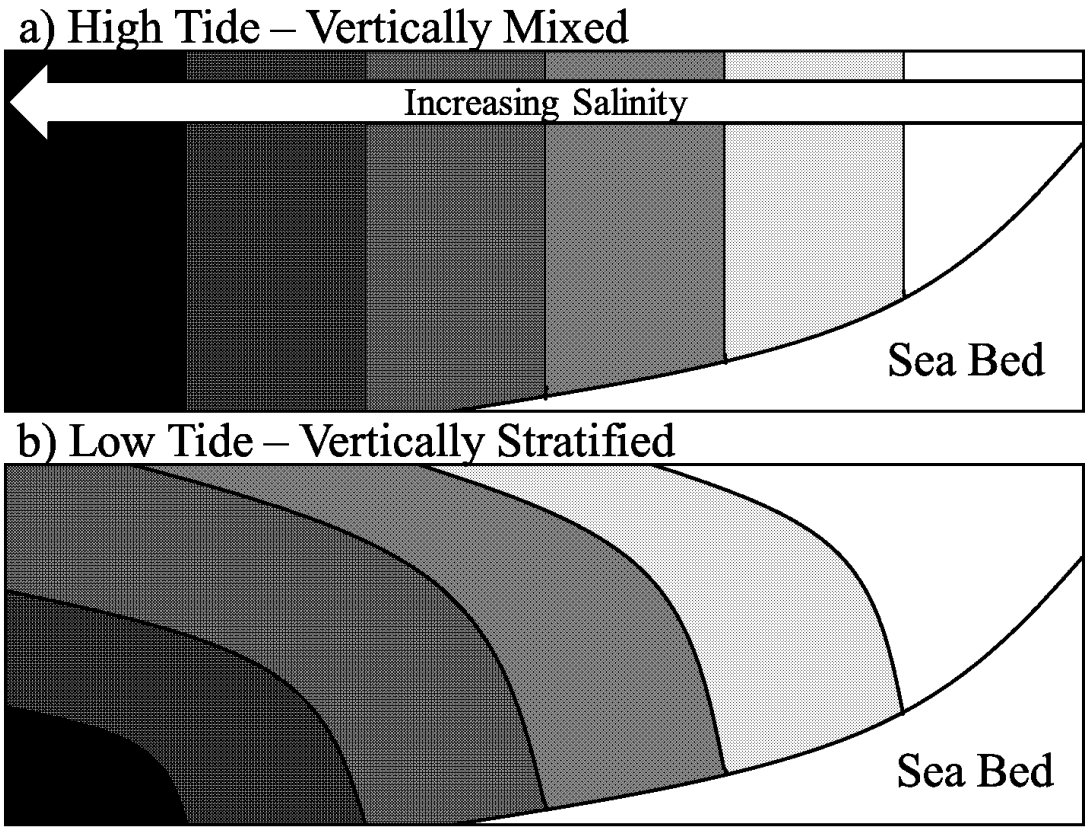

Figure A.3: Schematic showing creation of vertical stratification in Liverpool Bay. Stratification increases on the ebb tide and is broken down during the flood tide.

Tidal straining results from the differential advection of the off-shore salinity gradient by the sheared tidal flow. In regions where the tide is a standing wave, such as Site A, it results in the formation and intensification of stratification on the ebb phase of the tide and the removal of stratification on the flood (Simpson et al., 1990). This periodic stratification is referred to as strain induced periodic stratification (*SIPS*) and has a semi-diurnal periodicity at Site A.

A.5.4 Anthropogenic Forcing and Eutrophication

The location of Site A was chosen as it experiences both natural and anthropogenic forcing. The anthropogenic inputs at the site are varied, with urban outputs from Liverpool and rural outputs from the North Wales coast. The bay is also widely used for commercial shipping, including the Liverpool-Dublin ferry which collects data as part of the *COBS* research. Offshore wind farms are operational at North Hoyle and

Burbo Bank at the mouth of the Dee and Mersey Rivers respectively and also at Rhyl Flats further along the North Wales coastline.

Elevated levels of nutrient inputs from the human activity at the coast have given rise to fears that Liverpool Bay is eutrophic and government interest in the area has consequently increased. The *CEFAS* SmartBuoy is located at Site A for this reason (Howarth et al., 2006).

Appendix B University of Strathclyde Archive UK Shelf Data Set

Loch Etive 2000

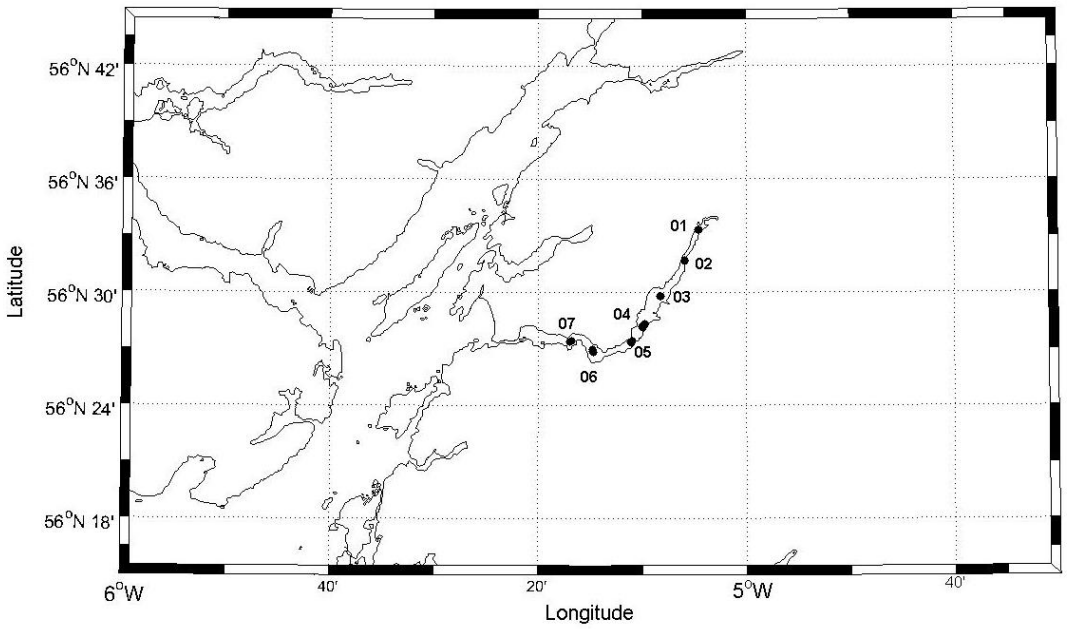

Figure B.1: Station map of the Loch Etive cruises from March to July 2000.

Table B.1: List of station IDs, coordinates and dates occupied during the Loch Etive 2000 cruises shown in Figure B.1

Cruise Duration Vessel	**Loch Etive (LE00) 30th – 31st March, 27th – 28th April, 13th July 2000 R.V. Calanus**		
ID	**Date**	**Latitude (°N)**	**Longitude (°W)**
LE00-01	30/03/00	56.5553	5.0756
LE00-02	30/03/00	56.5285	5.0985
LE00-03	30/03/00	56.4965	5.1377
LE00-04	30/03/00	56.4696	5.1665
LE00-05	31/03/00	56.4689	5.1663
LE00-06	31/03/00	56.4565	5.1839
LE00-07	31/03/00	56.4479	5.2458
LE00-08	31/03/00	56.4564	5.2820
LE00-09	27/04/00	56.5548	5.0765
LE00-10	27/04/00	56.5275	5.0988
LE00-11	27/04/00	56.4962	5.1369
LE00-12	27/04/00	56.4723	5.1618
LE00-13	27/04/00	56.4567	5.1820
LE00-14	28/04/00	56.4571	5.2797
LE00-15	28/04/00	56.4472	5.2445
LE00-16	28/04/00	56.4556	5.1844
LE00-17	28/04/00	56.4717	5.1623
LE00-18	13/07/00	56.4702	5.1661
LE00-19	13/07/00	56.4564	5.1856
LE00-20	13/07/00	56.4493	5.2466

Clyde Sea 2000

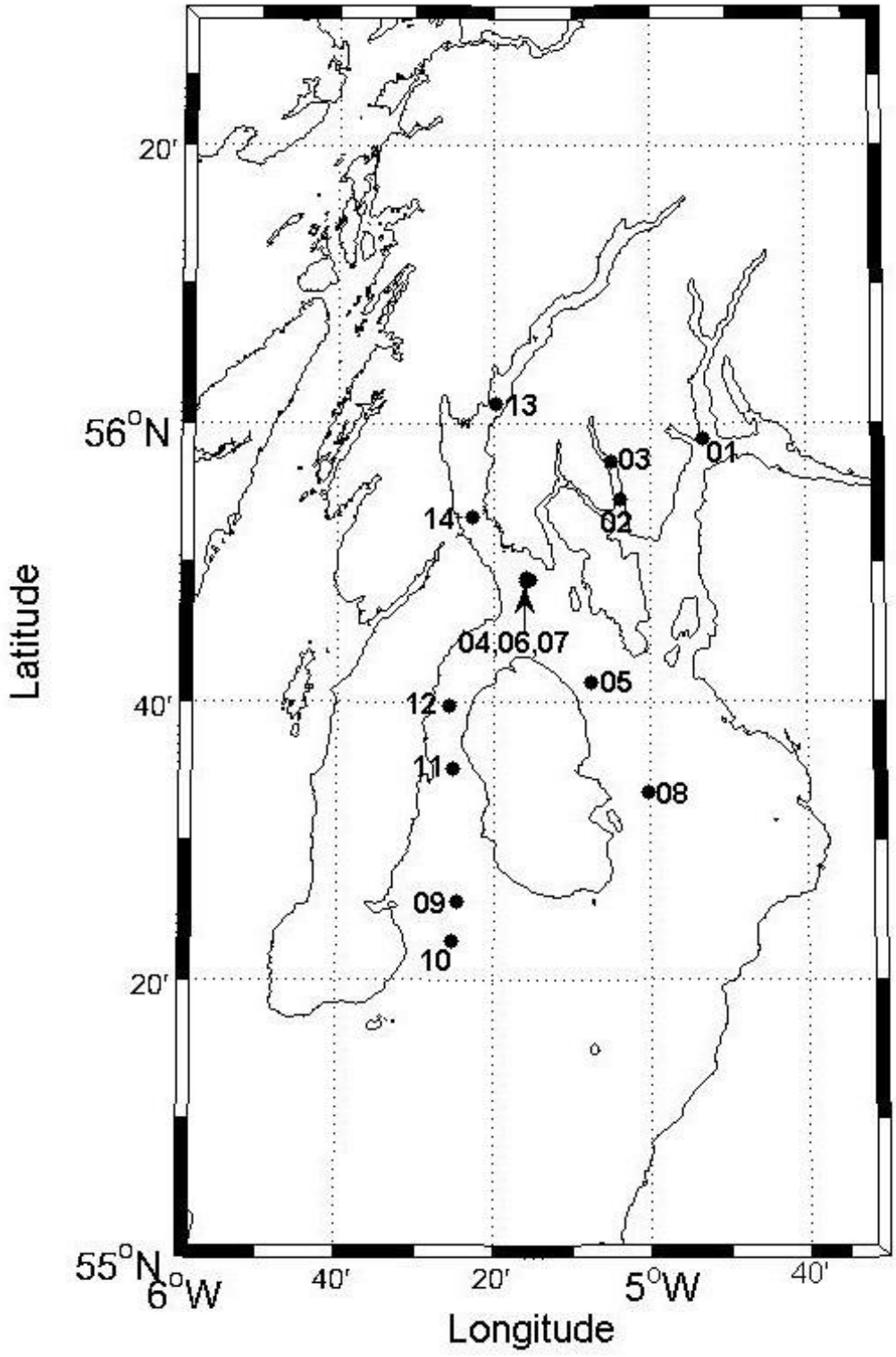

Figure B.2: Station map of the Clyde Sea May 2000 cruise.

Table B.2: List of station IDs, coordinates and dates occupied during the Clyde Sea 2000 cruise shown in Figure B.2

Cruise	**Clyde Sea 1 (CL00)**		
Duration	**16th – 19th May 2000**		
Vessel	**R.V. Calanus**		
ID	**Date**	**Latitude (°N)**	**Longitude (°W)**
CL00-01	16/05/00	55.9817	4.8864
CL00-02	16/05/00	55.9083	5.0630
CL00-03	16/05/00	55.9544	5.0838
CL00-04	17/05/00	55.8117	5.2557
CL00-05	17/05/00	55.6908	5.1265
CL00-06	17/05/00	55.8140	5.2651
CL00-07	18/05/00	55.8103	5.2636
CL00-08	18/05/00	55.5576	5.0044
CL00-09	18/05/00	55.4275	5.4128
CL00-10	19/05/00	55.3086	5.4234
CL00-11	19/05/00	55.5869	5.4193
CL00-12	19/05/00	55.6626	5.4290
CL00-13	19/05/00	56.0223	5.3287
CL00-14	19/05/00	55.8885	5.3788

Clyde Sea 2001

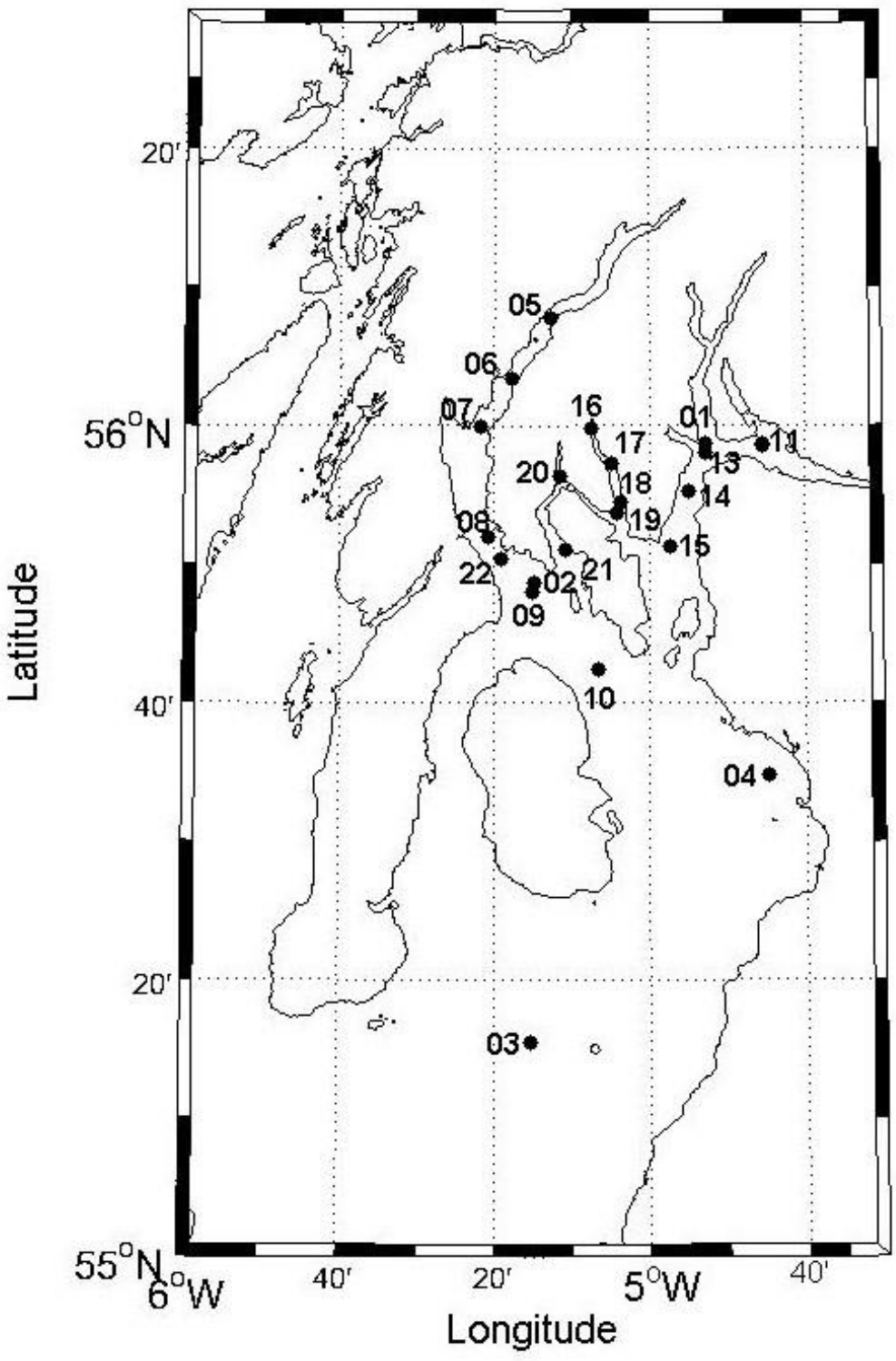

Figure B.3: Station map of the Clyde Sea April 2001 cruise.

Table B.3: List of station IDs, coordinates and dates occupied during the Clyde Sea April 2001 cruise shown in Figure B.3.

Cruise **Duration** **Vessel**	**Clyde Sea 2 (CL01)** **10th – 27th April 2001** **R.V. Calanus**		
ID	**Date**	**Latitude (°N)**	**Longitude (°W)**
CL01-01	10/04/01	55.9782	4.8813
CL01-02	11/04/01	55.8115	5.2491
CL01-03	19/04/01	55.2585	5.2546
CL01-04	20/04/01	55.5792	4.7458
CL01-05	23/04/01	56.1304	5.2127
CL01-06	23/04/01	56.0555	5.2956
CL01-07	23/04/01	55.9988	5.3621
CL01-08	24/04/01	55.8652	5.3456
CL01-09	24/04/01	55.7996	5.2519
CL01-10	24/04/01	55.7071	5.1101
CL01-11	25/04/01	55.9773	4.7563
CL01-12	25/04/01	55.9759	4.7592
CL01-13	25/04/01	55.9683	4.8820
CL01-14	25/04/01	55.9200	4.9163
CL01-15	25/04/01	55.8538	4.9549
CL01-16	26/04/01	55.9977	5.1239
CL01-17	26/04/01	55.9546	5.0829
CL01-18	26/04/01	55.9089	5.0619
CL01-19	26/04/01	55.8937	5.0714
CL01-20	26/04/01	55.9400	5.1923
CL01-21	27/04/01	55.8513	5.1819
CL01-22	27/04/01	55.8407	5.3193

Irish Sea August 2001

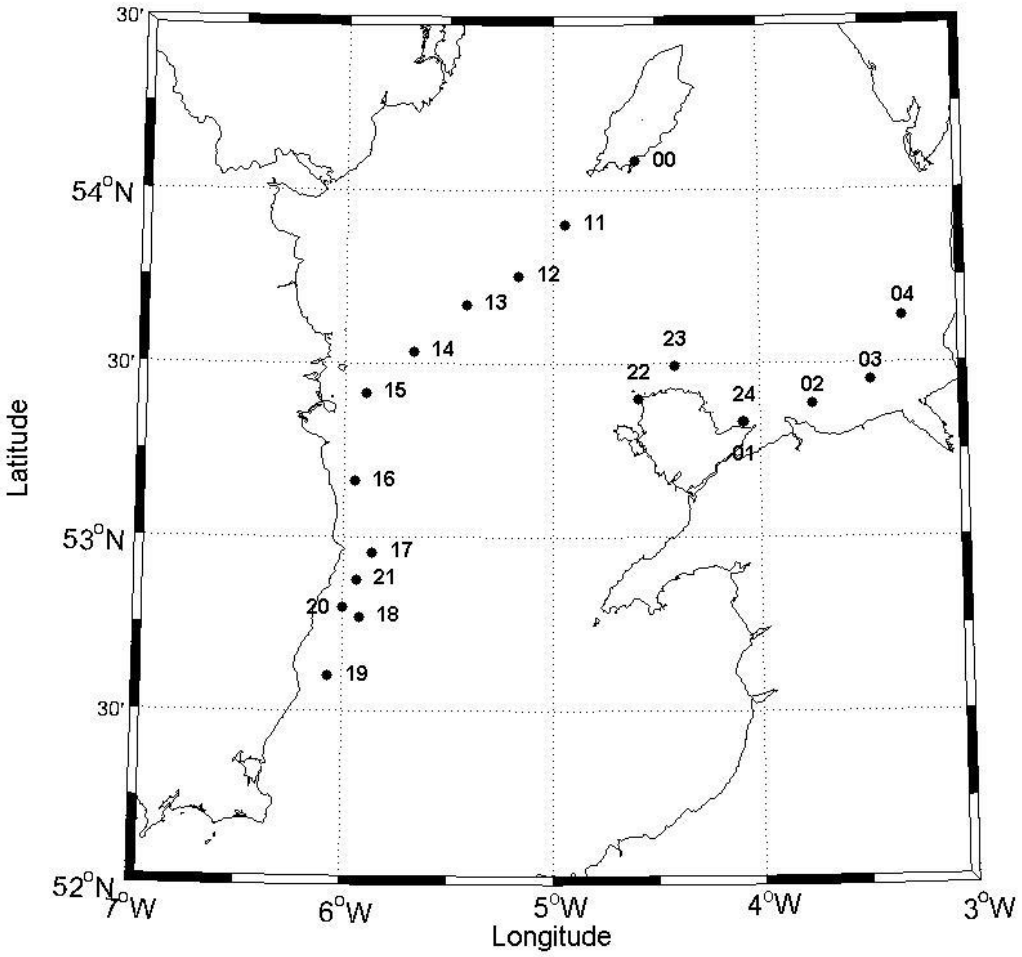

Figure B.4: Station map of the Irish Sea August 2001 cruise.

Table B.4: List of station IDs, coordinates and dates occupied during the Irish Sea August 2001 cruise shown in Figure B.4

Cruise	**Irish Sea (IS01)**		
Duration	**7th – 10th August 2001**		
Vessel	**R.V. Prince Madog**		
ID	**Date**	**Latitude (°N)**	**Longitude (°W)**
IS02-01	02/04/02	53.4698	4.5308
IS02-02	02/04/02	53.4725	4.5196
IS02-03	02/04/02	53.4688	4.5117
IS02-04	02/04/02	53.4705	4.5225
IS02-05	02/04/02	53.4696	4.5295
IS02-06	02/04/02	53.4722	4.5333
IS02-07	02/04/02	53.4677	4.5458
IS02-08	02/04/02	53.4609	4.5345
IS02-09	02/04/02	53.4696	4.5518
IS02-10	02/04/02	53.4638	4.5446
IS02-11	03/04/02	53.7627	5.2122
IS02-12	03/04/02	53.7941	5.2854
IS02-13	03/04/02	53.8322	5.3653
IS02-14	03/04/02	53.8674	5.4466
IS02-15	03/04/02	53.9043	5.5292
IS02-16	03/04/02	53.9643	5.6476
IS02-17	03/04/02	53.9089	5.7655
IS02-18	03/04/02	53.9348	5.8557
IS02-19	03/04/02	53.8808	5.9109
IS02-20	04/04/02	53.8518	5.8440
IS02-21	04/04/02	53.7978	5.7483
IS02-22	04/04/02	53.7681	5.6819
IS02-23	04/04/02	53.7315	5.6073
IS02-24	04/04/02	53.7043	5.5397
IS02-25	04/04/02	53.8666	5.6858
IS02-26	04/04/02	53.8386	5.6192
IS02-27	04/04/02	53.7952	5.5497
IS02-28	04/04/02	53.7735	5.4783
IS02-29	04/04/02	53.7354	5.4144
IS02-30	05/04/02	53.4799	4.3942
IS02-31	05/04/02	53.4622	4.2789
IS02-32	05/04/02	53.3718	4.1969
IS02-33	05/04/02	53.3431	4.0566

Irish Sea November 2001

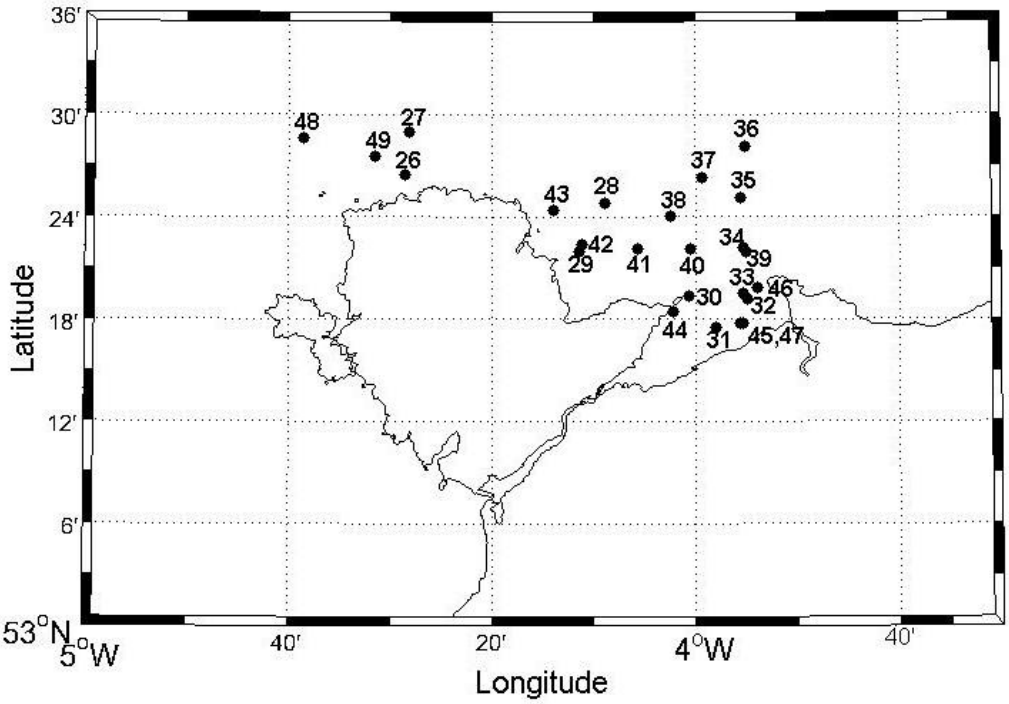

Figure B.5: Station map of the Irish Sea November 2001.

Table B.5: List of station IDs, coordinates and dates occupied during the Irish Sea November 2001 cruises shown in Figure B.5

Cruise **Duration** **Vessel**	**Irish Sea (IS01)** **26th – 30th November 2001** **R.V. Prince Madog**		
ID	**Date**	**Latitude (°N)**	**Latitude (°W)**
IS01-26	26/11/01	53.4589	4.5256
IS01-27	26/11/01	53.4413	4.4757
IS01-28	26/11/01	53.4828	4.4682
IS01-29	27/11/01	53.4137	4.1482
IS01-30	27/11/01	53.3662	4.1895
IS01-31	27/11/01	53.3220	4.0106
IS01-32	27/11/01	53.2915	3.9658
IS01-33	27/11/01	53.3201	3.9162
IS01-34	28/11/01	53.3256	3.9223
IS01-35	28/11/01	53.3695	3.9223
IS01-36	28/11/01	53.4192	3.9258
IS01-37	28/11/01	53.4691	3.9191
IS01-38	28/11/01	53.4389	3.9891
IS01-39	28/11/01	53.4002	4.0405
IS01-40	29/11/01	53.3660	3.9171
IS01-41	29/11/01	53.3688	4.0079
IS01-42	29/11/01	53.3686	4.0945
IS01-43	29/11/01	53.3734	4.1854
IS01-44	29/11/01	53.4059	4.2314
IS01-45	30/11/01	53.3074	4.0355
IS01-46	30/11/01	53.2956	3.9267
IS01-47	30/11/01	53.3309	3.8978
IS01-48	30/11/01	53.2956	3.9222
IS01-49	26/11/01	53.4772	4.6415

Irish Sea April 2002

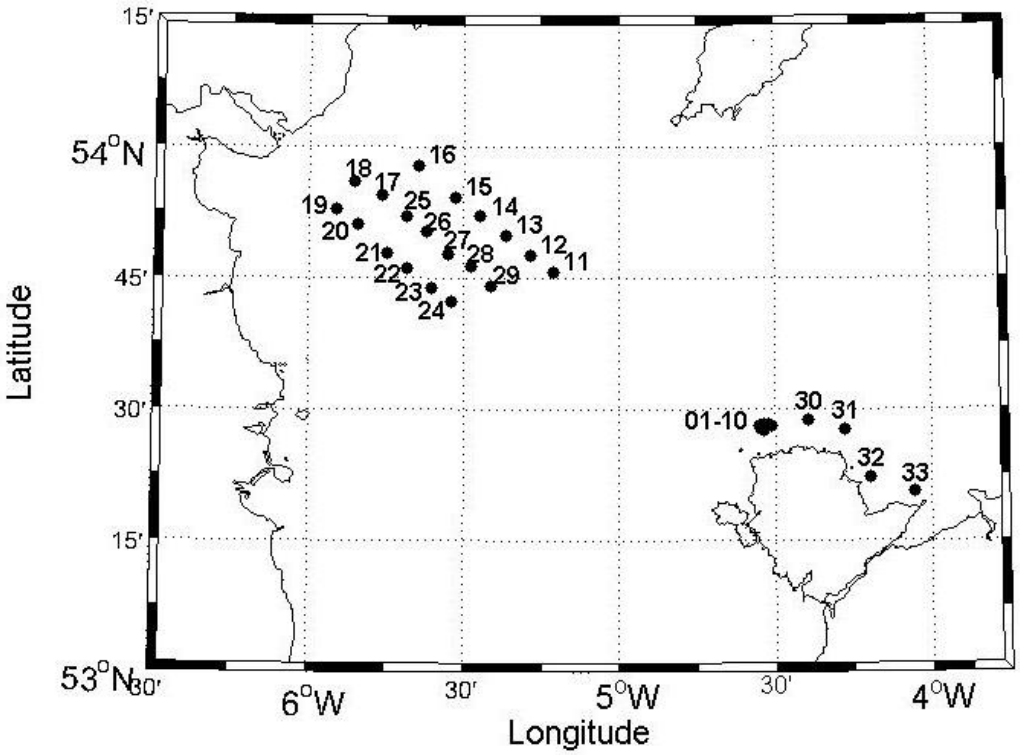

Figure B.6: Station map of the Irish Sea April 2002.

Table B.6: List of station IDs, coordinates and dates occupied during the Irish Sea April 2002 cruises shown in Figure B.6

Cruise **Duration** **Vessel**	**Irish Sea (IS02)** **2nd – 5th April 2002** **R.V. Prince Madog**		
ID	**Date**	**Latitude (°N)**	**Latitude (°W)**
IS02-01	02/04/02	53.4698	4.5308
IS02-02	02/04/02	53.4725	4.5196
IS02-03	02/04/02	53.4688	4.5117
IS02-04	02/04/02	53.4705	4.5225
IS02-05	02/04/02	53.4696	4.5295
IS02-06	02/04/02	53.4722	4.5333
IS02-07	02/04/02	53.4677	4.5458
IS02-08	02/04/02	53.4609	4.5345
IS02-09	02/04/02	53.4696	4.5518
IS02-10	02/04/02	53.4638	4.5446
IS02-11	03/04/02	53.7627	5.2122
IS02-12	03/04/02	53.7941	5.2854
IS02-13	03/04/02	53.8322	5.3653
IS02-14	03/04/02	53.8674	5.4466
IS02-15	03/04/02	53.9043	5.5292
IS02-16	03/04/02	53.9643	5.6476
IS02-17	03/04/02	53.9089	5.7655
IS02-18	03/04/02	53.9348	5.8557
IS02-19	03/04/02	53.8808	5.9109
IS02-20	04/04/02	53.8518	5.8440
IS02-21	04/04/02	53.7978	5.7483
IS02-22	04/04/02	53.7681	5.6819
IS02-23	04/04/02	53.7315	5.6073
IS02-24	04/04/02	53.7043	5.5397
IS02-25	04/04/02	53.8666	5.6858
IS02-26	04/04/02	53.8386	5.6192
IS02-27	04/04/02	53.7952	5.5497
IS02-28	04/04/02	53.7735	5.4783
IS02-29	04/04/02	53.7354	5.4144
IS02-30	05/04/02	53.4799	4.3942
IS02-31	05/04/02	53.4622	4.2789
IS02-32	05/04/02	53.3718	4.1969
IS02-33	05/04/02	53.3431	4.0566

Irish Sea July 2002

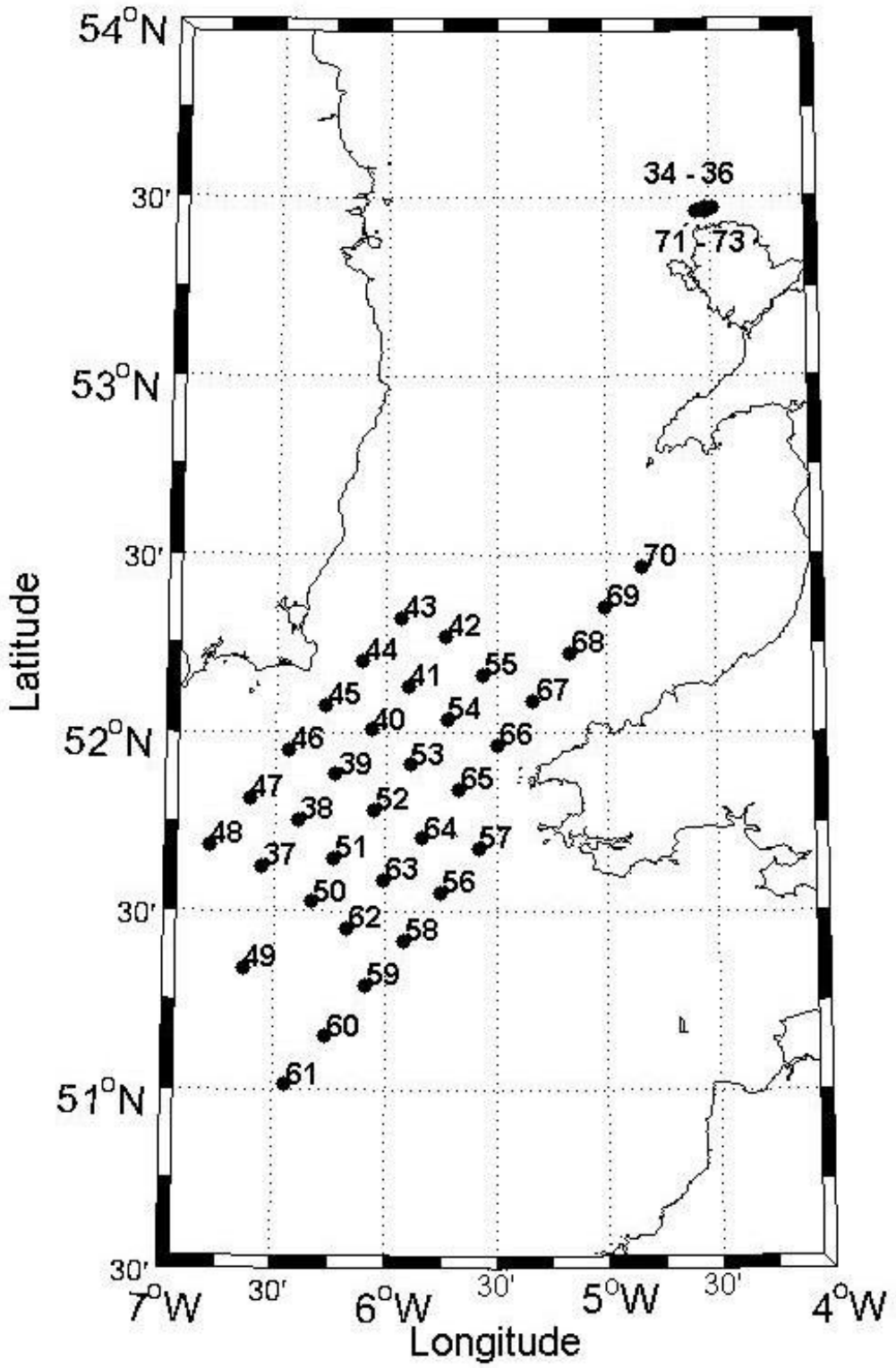

Figure B.7: Station map of the Irish Sea July 2002.

Table B.7: List of station IDs, coordinates and dates occupied during the Irish Sea July 2002 cruises shown in Figure B.7.

Cruise	**Irish Sea (IS02)**		
Duration	**13th – 20th July 2002**		
Vessel	**R.V. Prince Madog**		
ID	**Date**	**Latitude (°N)**	**Latitude (°W)**
IS02-34	13/07/02	53.4696	4.4913
IS02-35	13/07/02	53.4705	4.5242
IS02-36	13/07/02	53.4662	4.5442
IS02-37	14/07/02	51.6244	6.5623
IS02-38	14/07/02	51.7553	6.4004
IS02-39	14/07/02	51.8836	6.2311
IS02-40	14/07/02	52.0082	6.0665
IS02-41	14/07/02	52.1309	5.9005
IS02-42	14/07/02	52.2677	5.7284
IS02-43	15/07/02	52.3219	5.9367
IS02-44	15/07/02	52.2019	6.1142
IS02-45	15/07/02	52.0752	6.2798
IS02-46	15/07/02	51.9523	6.4457
IS02-47	15/07/02	51.8163	6.6202
IS02-48	15/07/02	51.6859	6.7998
IS02-49	15/07/02	51.3407	6.6410
IS02-50	16/07/02	51.5274	6.3337
IS02-51	16/07/02	51.6497	6.2364
IS02-52	16/07/02	51.7826	6.0545
IS02-53	16/07/02	51.9116	5.8938
IS02-54	16/07/02	52.0382	5.7260
IS02-55	16/07/02	52.1632	5.5619
IS02-56	17/07/02	51.5500	5.7500
IS02-57	17/07/02	51.6776	5.5815
IS02-58	18/07/02	51.4174	5.9217
IS02-59	18/07/02	51.2915	6.0928
IS02-60	18/07/02	51.1487	6.2741
IS02-61	18/07/02	51.0155	6.4464
IS02-62	19/07/02	51.4539	6.1766
IS02-63	19/07/02	51.5863	6.0115
IS02-64	19/07/02	51.7064	5.8396
IS02-65	19/07/02	51.8407	5.6678
IS02-66	19/07/02	51.9674	5.4991
IS02-67	19/07/02	52.0913	5.3319
IS02-68	19/07/02	52.2248	5.1652
IS02-69	19/07/02	52.3509	5.0032
IS02-70	19/07/02	52.4633	4.8376
IS02-71	20/07/02	53.4597	4.5258
IS02-72	20/07/02	53.4595	4.5258
IS02-73	20/07/02	53.4606	4.5692

Oban 2003

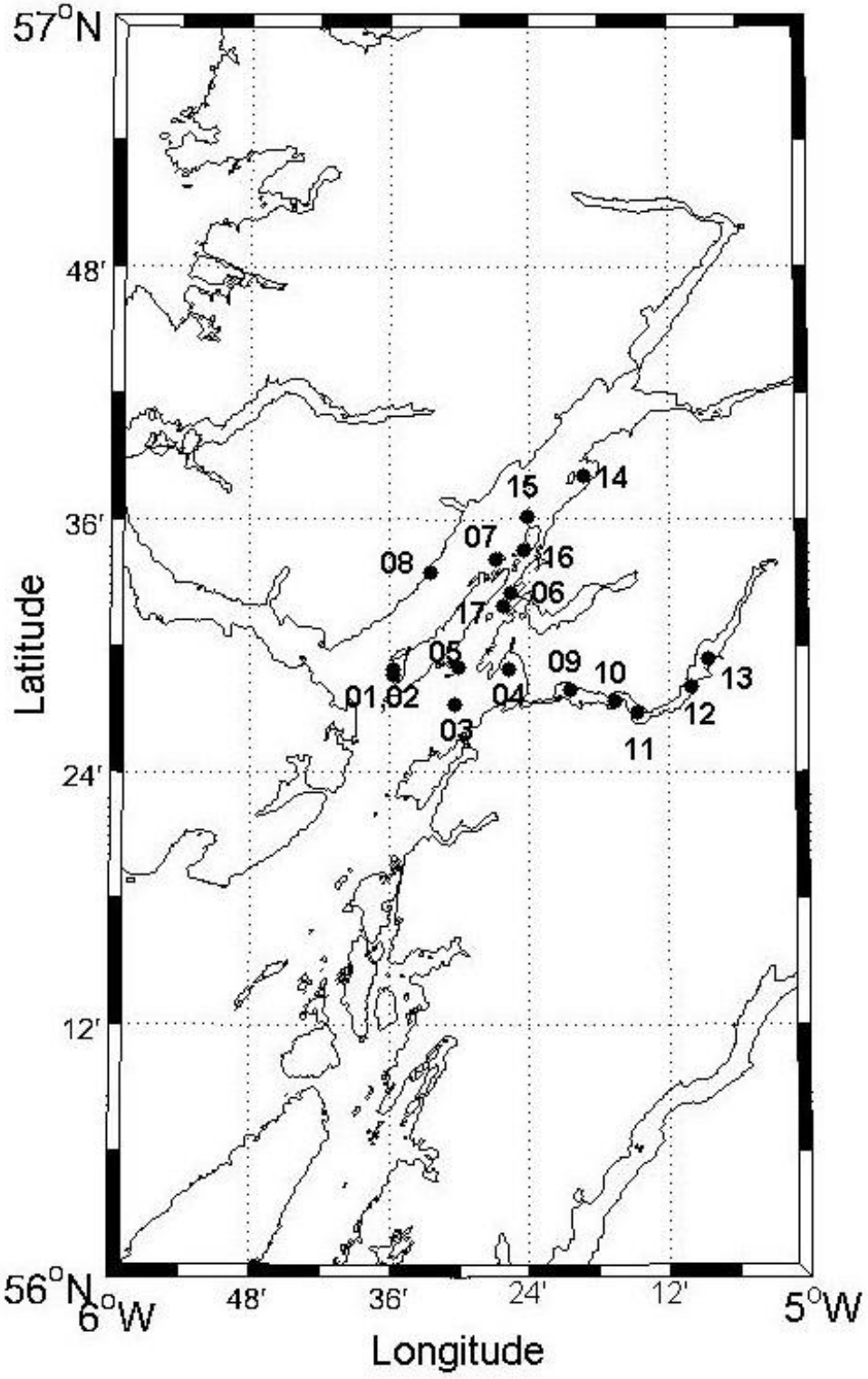

Figure B.8: Station map of the Oban April 2003 cruise.

Table B.8: List of station IDs, coordinates and dates occupied during the Oban April 2003 cruise shown in Figure B.8

Cruise Duration Vessel	**Oban (OB03) 22nd – 25th April 2003 R.V. Calanus**		
ID	**Date**	**Latitude (°N)**	**Latitude (°W)**
OB03-01	22/04/03	56.4812	5.5936
OB03-02	22/04/03	56.4767	5.5947
OB03-03	22/04/03	56.4533	5.5074
OB03-04	23/04/03	56.4809	5.4285
OB03-05	23/04/03	56.4822	5.5021
OB03-06	23/04/03	56.5425	5.4261
OB03-07	23/04/03	56.5678	5.4477
OB03-08	23/04/03	56.5581	5.5403
OB03-09	24/04/03	56.4654	5.3425
OB03-10	24/04/03	56.4565	5.2775
OB03-11	24/04/03	56.4475	5.2452
OB03-12	24/04/03	56.4680	5.1667
OB03-13	24/04/03	56.4895	5.1444
OB03-14	25/04/03	56.6345	5.3230
OB03-15	25/04/03	56.6026	5.4021
OB03-16	25/04/03	56.5762	5.4084
OB03-17	25/04/03	56.5319	5.4359

Oban 2004

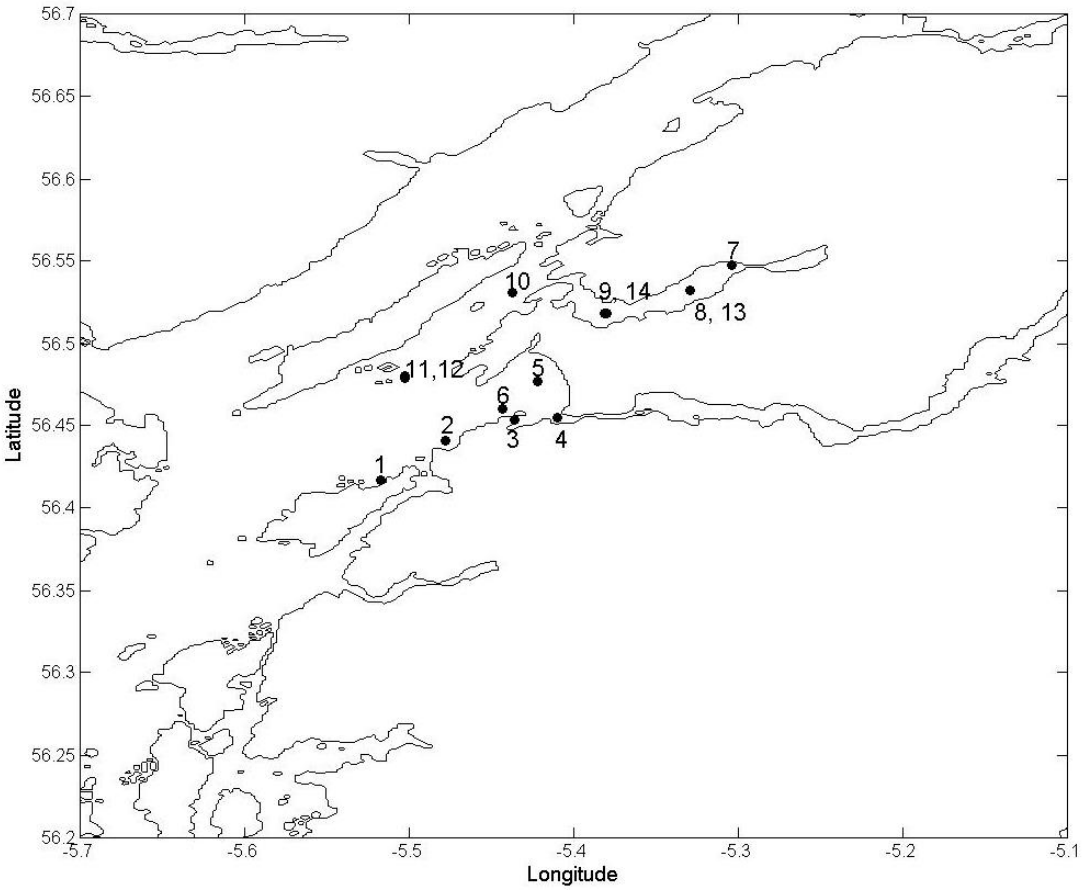

Figure B.9: Station map of the Oban April 2004 cruise.

Table B.9: List of station IDs, coordinates and dates occupied during the Oban April 2004 cruises shown in Figure B.9

Cruise Duration Vessel	**Oban (OB04) 14th – 16th April 2004 R.V. Calanus**		
ID	**Date**	**Latitude (°N)**	**Latitude (°W)**
OB04-01	14/04/04	56.4172	5.5170
OB04-02	14/04/04	56.4410	5.4778
OB04-03	14/04/04	56.4534	5.4363
OB04-04	14/04/04	56.4548	5.4099
OB04-05	14/04/04	56.4771	5.4220
OB04-06	14/04/04	56.4603	5.4433
OB04-07	15/04/04	56.5475	5.3042
OB04-08	15/04/04	56.5325	5.3294
OB04-09	15/04/04	56.5184	5.3798
OB04-10	15/04/04	56.5310	5.4371
OB04-11	16/04/04	56.4806	5.5030
OB04-12	16/04/04	56.4788	5.5025
OB04-13	16/04/04	56.5326	5.3293
OB04-14	16/04/04	56.5186	5.3810

Sound of Jura 2004

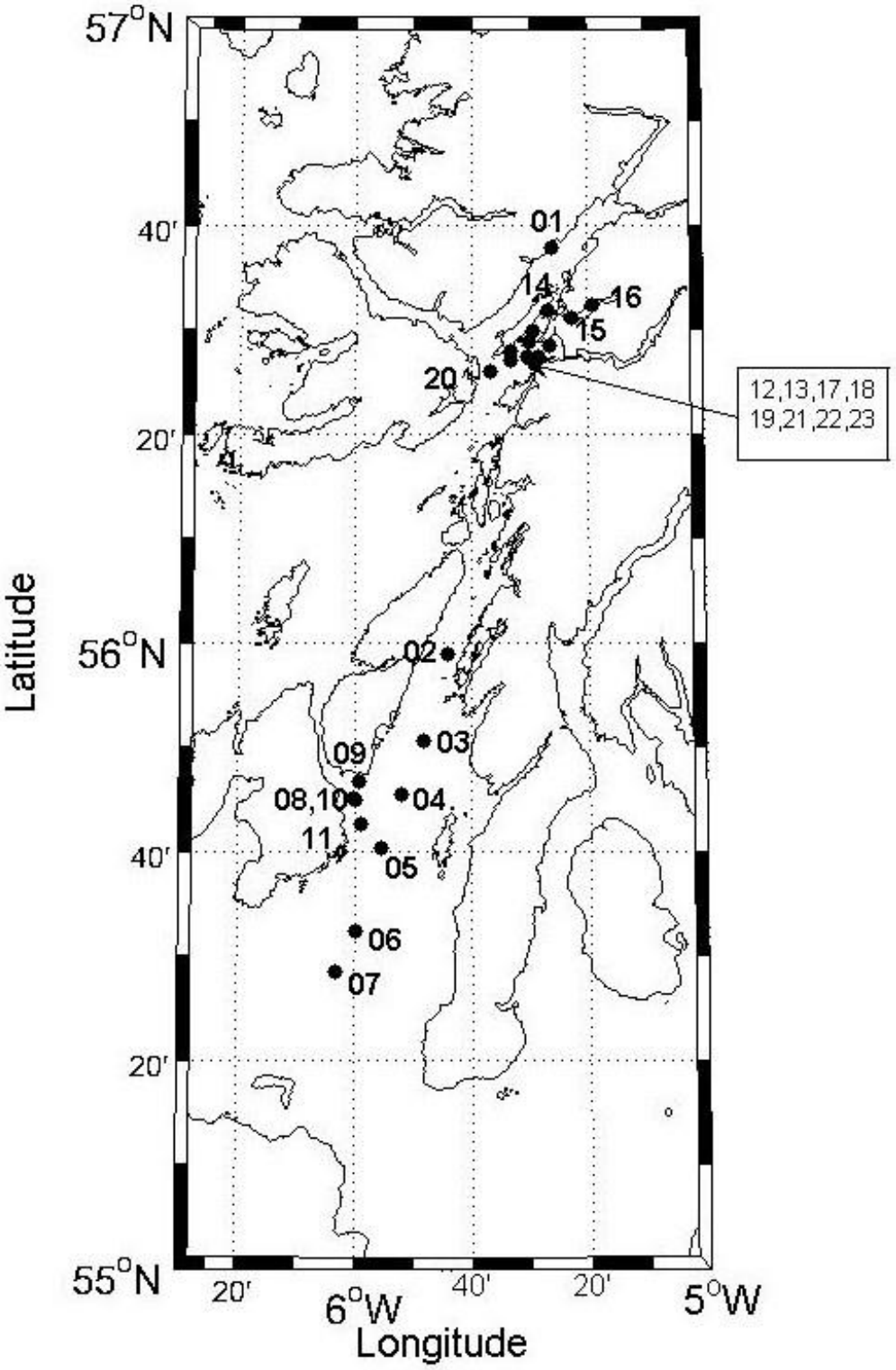

Figure B.10: Station map of the Sound of Jura June 2004 cruise.

Table B.10: List of station IDs, coordinates and dates occupied during the Sound of Jura June 2004 cruises shown in Figure B.10

Cruise **Duration** **Vessel**	**Sound of Jura (SJ04)** **21st – 25th June 2004** **R.V. Calanus**		
ID	**Date**	**Latitude (°N)**	**Latitude (°W)**
SJ04-01	21/06/04	56.6318	5.4358
SJ04-02	21/06/04	55.9826	5.7374
SJ04-03	21/06/04	55.8457	5.8034
SJ04-04	22/06/04	55.7594	5.8685
SJ04-05	22/06/04	55.6723	5.9263
SJ04-06	22/06/04	55.5406	5.9989
SJ04-07	22/06/04	55.4768	6.0527
SJ04-08	22/06/04	55.7519	6.0016
SJ04-09	23/06/04	55.7792	5.9898
SJ04-10	23/06/04	55.7502	6.0007
SJ04-11	23/06/04	55.7119	5.9810
SJ04-12	24/06/04	56.4744	5.4424
SJ04-13	24/06/04	56.4823	5.5004
SJ04-14	24/06/04	56.5321	5.4472
SJ04-15	24/06/04	56.5184	5.3801
SJ04-16	24/06/04	56.5407	5.3209
SJ04-17	24/06/04	56.4578	5.5067
SJ04-18	25/06/04	56.4449	5.4883
SJ04-19	25/06/04	56.4525	5.5564
SJ04-20	25/06/04	56.4346	5.6120
SJ04-21	25/06/04	56.4664	5.5540
SJ04-22	25/06/04	56.4988	5.4930
SJ04-23	25/06/04	56.4585	5.4761

Bristol Channel 2005

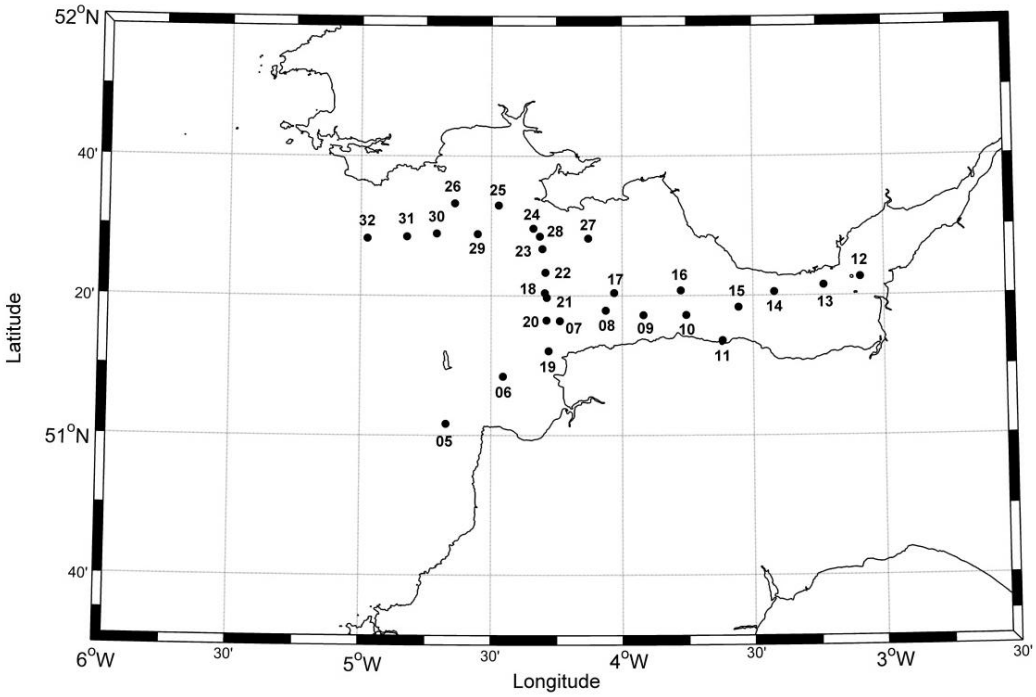

Figure B.11: Station map of the Bristol Channel April/May 2005 cruise.

Table B.11: List of station IDs, coordinates and dates occupied during the Bristol Channel April/May 2005 cruises shown in Figure B.11

Cruise **Duration** **Vessel**	**Bristol Channel (BC05)** **29th April – 3rd May 2005** **R.V. Prince Madog**		
ID	**Date**	**Latitude (°N)**	**Latitude (°W)**
BC05-01	29/04/05	53.2229	4.7621
BC05-02	29/04/05	53.0834	4.8474
BC05-03	29/04/05	52.9906	4.8632
BC05-04	29/04/05	52.8504	4.9441
BC05-05	30/04/05	51.0277	4.6721
BC05-06	30/04/05	51.1405	4.4545
BC05-07	30/04/05	51.2732	4.2380
BC05-08	30/04/05	51.2981	4.0631
BC05-09	30/04/05	51.2871	3.9189
BC05-10	30/04/05	51.2872	3.7553
BC05-12	01/05/05	51.3777	3.0902
BC05-13	01/05/05	51.3585	3.2304
BC05-14	01/05/05	51.3425	3.4192
BC05-15	01/05/05	51.3059	3.5561
BC05-16	01/05/05	51.3456	3.7757
BC05-17	01/05/05	51.3399	4.0304
BC05-18	01/05/05	51.3399	4.2951
BC05-19	02/05/05	51.2012	4.2807
BC05-20	02/05/05	51.2744	4.2889
BC05-21	02/05/05	51.3288	4.2881
BC05-22	02/05/05	51.3888	4.2932
BC05-23	02/05/05	51.4449	4.3045
BC05-24	02/05/05	51.4937	4.3392
BC05-25	02/05/05	51.5489	4.4723
BC05-26	02/05/05	51.5537	4.6402
BC05-27	03/05/05	51.4701	4.1294
BC05-28	03/05/05	51.4748	4.3146
BC05-29	03/05/05	51.4805	4.5525
BC05-30	03/05/05	51.4818	4.7092
BC05-31	03/05/05	51.4743	4.8231
BC05-32	03/05/05	51.4705	4.9747

Bristol Channel 2006

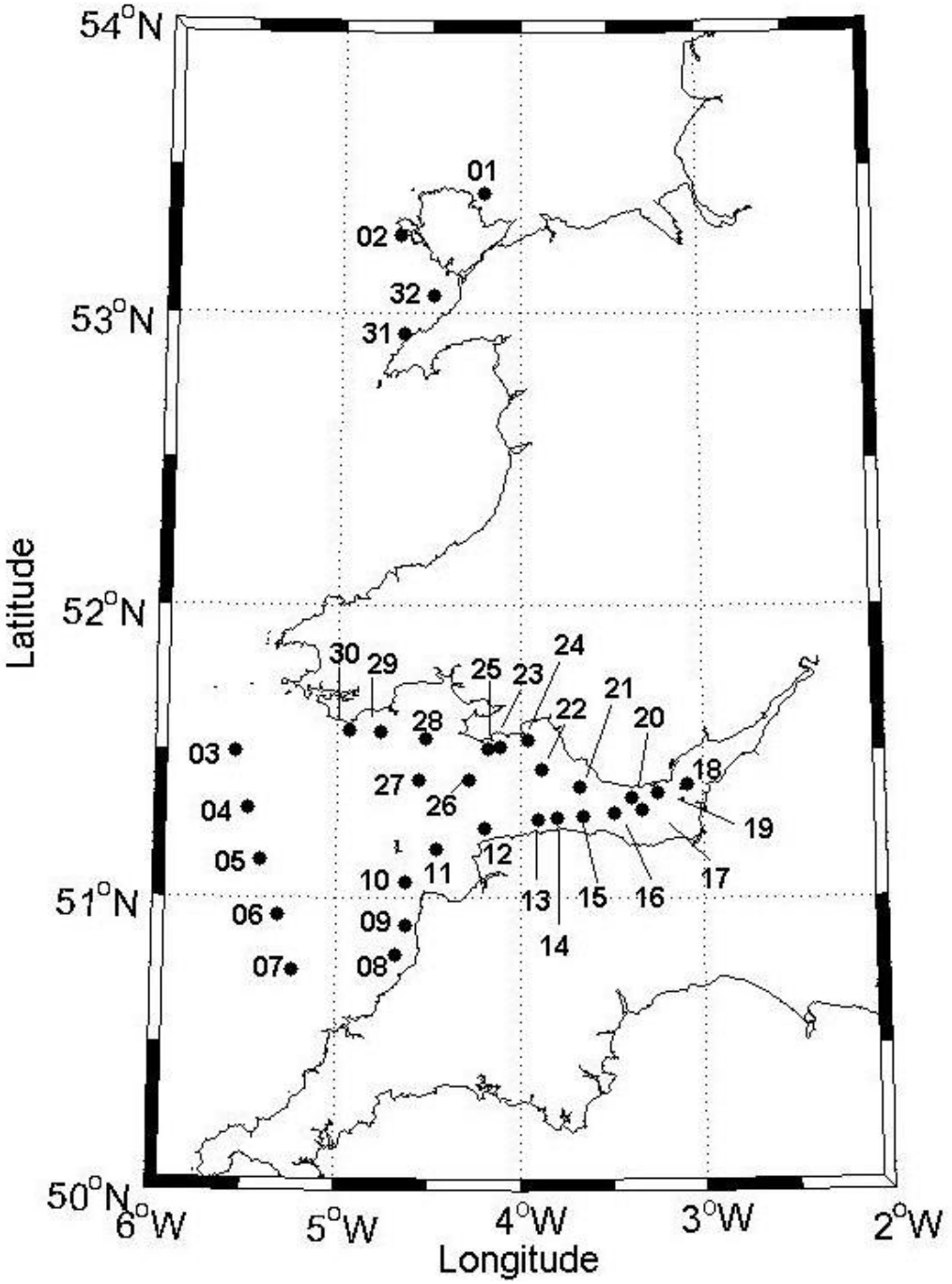

Figure B.12: Station map of the Bristol Channel August 2006 cruise.

Table B.12: List of station IDs, coordinates and dates occupied during the Bristol Channel August 2006 cruises shown in Figure B.12

Cruise **Duration** **Vessel**	**Bristol Channel (BC06)** **7th – 13th August 2006** **R.V. Prince Madog**		
ID	**Date**	**Latitude (°N)**	**Latitude (°W)**
BC06-01	07/08/06	53.4120	4.1995
BC06-02	07/08/06	53.2641	4.6818
BC06-03	08/08/06	51.5031	5.5669
BC06-04	08/08/06	51.3086	5.4947
BC06-05	08/08/06	51.1325	5.4166
BC06-06	08/08/06	50.9426	5.3236
BC06-07	08/08/06	50.7520	5.2383
BC06-08	09/08/06	50.8041	4.6746
BC06-09	09/08/06	50.9063	4.6247
BC06-10	09/08/06	51.0535	4.6281
BC06-11	09/08/06	51.1651	4.4570
BC06-12	09/08/06	51.2412	4.1894
BC06-13	10/08/06	51.2678	3.9003
BC06-14	10/08/06	51.2764	3.7958
BC06-15	10/08/06	51.2774	3.6593
BC06-16	10/08/06	51.2904	3.4831
BC06-17	10/08/06	51.3012	3.3307
BC06-18	10/08/06	51.3890	3.0814
BC06-19	11/08/06	51.3581	3.2443
BC06-20	11/08/06	51.3436	3.3854
BC06-21	11/08/06	51.3799	3.6752
BC06-22	11/08/06	51.4387	3.8778
BC06-23	11/08/06	51.5144	4.1126
BC06-24	11/08/06	51.5403	3.9527
BC06-25	12/08/06	51.5081	4.1754
BC06-26	12/08/06	51.4070	4.2797
BC06-27	12/08/06	51.4045	4.5530
BC06-28	12/08/06	51.5453	4.5229
BC06-29	12/08/06	51.5658	4.7693
BC06-30	12/08/06	51.5704	4.9414
BC06-31	13/08/06	52.9308	4.6488
BC06-32	13/08/06	53.0581	4.4890

Acknowledgements

I would like to thank my supervisor, Professor Alex Cunningham, whose infinite patience is probably the only reason I ever got this far. To David McKee for scaring the life out of me on numerous occasions, honestly David, if you hadn't told me I was wasting my time so often I probably would have been. Everyone at NOC: Liverpool, thank you for continuing to send data, even though I was mean about it repeatedly, especially to Andy Lane your company was always greatly appreciated. To all of the current PhD students in the MORSE Group, I wish all of you the best of luck when the challenge of writing comes your way. Thanks is also due to NERC for the financing me throughout my PhD research.

Danielle, your idea of "Wine Friday" didn't take off after you left; it makes me sad but I would have been drinking alone. I am grateful for the time we spent together in the office, even if it was slightly detrimental to our work ethic at times. The people on Level 2 (you know who you are, even if your office isn't there), the coffee and chat meant more to me than I could ever explain. Carol Trager-Cowan, thank you so much for the opportunity to work with you on that endless list of outreach work, I loved every minute of it and my current career path would not be possible without it (and the references of course).

Finally, I wish to thank my family; Simon you have given me so much and it would not be a cliché to say that this would not be possible without you. Teaching me how to program must have taken more patience than I could ever dream of possessing. Thank you to Simon's parents (Cilli and Jörg) for babysitting and so much more. Zoë, you are the world's best distraction but without you I could have procrastinated forever, so I thank you for keeping me focused. My siblings Christopher, John David and Elizabeth (Tiny), you all keep me laughing – even when I'm not. Thank you to Charles for, somewhat unknowingly, financing my full 9 years at university, as Mum would say multiply it by five (sorry). To save the best for last, to my Mum, I don't even know where to begin thanking you for the unwavering support and help over the last 31 years, my best for now is to say that this is yours and if they let me put your name on it I would.